Title

Investigations into Redox Carriers for Electrochemical Carbon Dioxide Capture and Concentration

Permalink

https://escholarship.org/uc/item/8x76d1ht

Author

Zito, Alessandra Mary

Publication Date

2023

Copyright Information

Peer reviewed|Thesis/dissertation

UNIVERSITY OF CALIFORNIA,
IRVINE

Investigations into Redox Carriers for Electrochemical Carbon Dioxide Capture and

Concentration

DISSERTATION

submitted in partial satisfaction of the requirements
for the degree of

DOCTOR OF PHILOSOPHY

in Chemistry

by

Alessandra Mary Zito

Dissertation Committee:
Professor Jenny Y. Yang, Chair
Assistant Professor Maxx Arguilla
Distinguished Professor A. S. Borovik

2023

DEDICATION

For my family.

TABLE OF CONTENTS   Page

CHAPTER 1. Introduction………………………………………..……………1

CHAPTER 2. Computational and Experimental Design of Quinones for Electrochemical CO_2 Capture and Concentration………………………………………………35

LIST OF FIGURES

LIST OF TABLES

LIST OF SCHEMES

Scheme 2.1. (**A**.) Electrochemical CO_2 capture and concentration using quinone-based carriers. A quinone in the neutral oxidation state (**Q**) is singly reduced at the cathode to yield quinone radical anion (**Q$_{RA}$**) and singly reduced again to yield quinone dianion (**Q$_{DA}$**) with increased affinity (nucleophilicity) to bind CO_2. The carrier is regenerated by oxidation of **Q$_{DA}$(CO$_2$)** to **Q$_{RA}$(CO$_2$)**, leading to the release and concentration of CO_2 at the anode. (**B**.) To avoid unwanted side-reactions and deactivation of **Q$_{DA}$**, the $E°_{cathodic}$ potential should be positive of the $O_2/O_2^{\bullet-}$ redox couple. (**C**.) Selection of suitable CO_2 capture molecules is limited by the observed linear relationship between $\log(K_{CO2(DA)})$ and $E°_{cathodic}$. Note that the series of plotted systems also contains the same redox carriers measured in different solvents…………………………………37

Scheme 2.2. *Left*: A participation of HOMO(Q$_{DA}$) vs. in-plane(Q$_{DA}$) orbitals requires a different approach of the CO_2 molecule. The geometry optimizations of the CO_2-bound quinone dianions suggest that both orbitals are involved in the CO_2 binding; however, the perpendicular orientation of the benzene and CO_2 plane of the adduct suggests a higher contribution from the in-plane(Q$_{DA}$). Additionally, an out-of-plane bending of the CO_2 molecule in the adduct (illustrated by the angle 'Ω') indicates the presence of weak interaction with the HOMO(Q$_{DA}$). *Right*: The benzoquinone (BQ) substituents can affect the energies of HOMO(Q$_{DA}$) and in-plane(Q$_{DA}$) to the same extent – resulting in a linear correlation between $E_{1/2}$ and $\log(K_{CO2(DA)})$ – or the MOs energies can be influenced unequally. Since the higher in-plane(Q$_{DA}$) energy is required for the better energetic overlap with the LUMO(CO_2), reducing the energy gap between HOMO(Q$_{DA}$) and in-plane(Q$_{DA}$) can produce a more favorable CO_2 capture behavior at the lower $E_{1/2}$…………………………………63

Scheme 2.3. The library of substituted BQs was generated as follows: (i) SMILES representation was used to generate all of the unique-structure combinations of the mono-, bis-, tris-, and tetra-substituted 1,4-BQ by introducing 24 different substituents (-F, -Cl, -Br, -CF$_3$, -Me, -Et, -tBu, -Ph, -Bn, -OH, -OCH$_3$, -CH$_2$OH, -OPh, -OCOCH$_3$, -COOCH$_3$, -NH$_2$, -NHCH$_3$, -N(CH$_3$)$_2$, -NHCOCH$_3$, -NHPh, -CN, -NO$_2$, -N(CH$_3$)$_3^+$, -CH$_2$N(CH$_3$)$_3^+$), (ii) SMILES codes were transformed into the 3D structures XYZ coordinates, (iii) MD simulation at the GFN0-xTB level was performed to capture the conformational flexibility of the species, (iv) 500 snapshots along each trajectory were fully optimized at the GFN2-xTB level with the GBSA solvation model, (v) resulting optimized structures were then clustered by energy and geometry (RMSD), (vi) structures with altered bonding were removed using a connectivity filter, and (vii) from the ensemble of GFN2-xTB optimized geometries, we have selected only the lowest-lying conformer that was further optimized using DFT (PBE0/def2-SVP), and for which we have calculated the HOMO(Q$_{DA}$) and

ACKNOWLEDGEMENTS

To my advisor, Jenny – I cannot thank you enough. You gave me the freedom to pursue interesting science and the encouragement to keep going, even when that interesting science wasn't working so well. You have taught me so much, and I am thankful for your mentorship, motivation, and inspiration.

Maxx, Andy, and Sara – thank you for your patience and for encouraging me to look at my work from a different angle; I am lucky to have had the chance to work with you.

Thank you to my group members, who made me look forward to going to work every day, and who I am grateful to consider part of my chemistry family: Dr. Annie Chantarojsiri, Dr. Zach Thammavongsy, Dr. Brian Lydon, Dr. Steven Chabolla, Dr. Alex Reath, Dr. Bianca Ceballos, Dr. Caitlin Hanna, Dr. Drew Cunningham, Dr. Jeffrey Barlow, Ian Mercer, MS, Amanda Kummeth, MS, Dr. Carina Jette, Dr. Tyler Kerr, Dr. Kelsey Collins, Dr. Sarah Wang, Dr. Nadia Léonard, Dr. Ryan King, Dr. Ana Garcia, Dr. Ab Qayoom Mir, Dr. Magy Mikhail, Alissa Matus, Clarabella Li, Andrew Cypcar, Colleen Miller, Elise Payong, Jared Stanley, Faith Flinkingshelt, Ciara Gillis, Ute Petri, and Claire Zimmerman. Bye forever; I'll miss you terribly. Make good choices.

Jesus, Jaclyn, Natalia, Roman – I am so lucky to have mentored you; thank you for making the science fun.

To my inorganic cohort, Rachel, Amanda, Sierra, Ian – I am grateful to have gone through classes and exams by your sides. Thank you for being there for and with me.

Meghen, Jen, Bonnie, Mariana, Dave – thank you for the lunches, for listening to me talk for hours about nothing, and for being my friends. You made hard days a little easier, and I am so glad to have you in my life.

Christina, Cat, Jodi, Sondra – thank you for the encouragement from afar; I am so happy to have found sincere friends in you.

Mom, Dad, Mike, Matt – you have continuously supported me through all of my life, and I couldn't have done this without you. Thank you for everything.

Marie – thank you for being there for me every day.

<div align="center">

VITA

Alessandra Mary Zito

</div>

Education

2018 – 2023	University of California, Irvine	Irvine, CA
	PhD, Inorganic Chemistry	
2014 – 2018	Johns Hopkins University	Baltimore, MD
	B. A., Chemistry	

Research Experience

2018 – 2023   Graduate Student Researcher

University of California, Irvine   *Advisor: Jenny Y. Yang*

- Designing and synthesizing redox-active molecules to be used for carbon dioxide capture in collaboration with the Alexandrova lab at UCLA

- Investigation the effects secondary sphere interactions on the reduction potentials and CO_2 binding affinities of redox-active molecules to be used for carbon dioxide capture

- Building an electrochemical system capable of carbon dioxide capture in collaboration with the Brushett lab at MIT

- Ensuring the lab is adhering to all safety regulations as graduate safety representative

2016 – 2018   Undergraduate Student Researcher

Johns Hopkins University, Baltimore, MD   *Advisor: V. Sara Thoi*

- Synthesized and characterized a manganese-benzimidazole complex to be used for homogeneous CO_2 reduction

2017   Undergraduate Student Researcher

University of Pittsburgh, Pittsburgh, PA   *Advisor: Haitao Liu*

- Conducted a study involving the effect of contamination of carbon materials on capacitance of a supercapacitor

Publications

1   Zito, A.,[†] Bim, D.,[†] Clarke, L.,[†] Barlow, J. M.,[†] Kummeth, A., Li, C., Leonard, M., Ripley, K., Zhang, Z., Brushett, F.,* Alexandrova, A.,* Yang, J. Y.* Review: Electrochemical Carbon Dioxide Capture and Concentration. *Chem. Rev.* Accepted. [†]*indicates the authors contributed equally*

2   Singh, K., Gerke, C., Saund, S., Zito, A., Siegler, M., Thoi, V. S.* CO_2 Activation with Manganese Tricarbonyl Complexes via an H-Atom Responsive Benzimidazole Ligand. *In review.*

3   Zito, A.,[†] Bím, D.,[†] Alexandrova, A.,* Yang, J. Y.* Computational and Experimental Design of Quinones for Electrochemical CO2 Capture and Concentration. *ACS Sustainable Chem. Eng.* **2022.** https://doi.org/10.1021/acssuschemeng.2c03463 [†]*indicates the authors contributed equally*

4   Barlow, J. M.,[†] Clarke, L.,[†] Zhang, Z.,[†] Bim, D., Ripley, K., Zito, A., Brushett, F.,* Alexandrova, A.,* Yang, J. Y.* Molecular Design of Redox Carriers for Electrochemical CO_2 Capture and Concentration. *Chem. Soc. Rev.* **2022.** https://doi.org/10.1039/D2CS00367H [†]*indicates the authors contributed equally*

5   Tolman, N. L., Mukai, J., Wang, S., Zito, A., Luo, T., and Liu, H.* The Effect of Physical Adsorption on the Capacitance of Activated Carbon Electrodes. *Carbon.* **2019**, *150*, 334–339. https://doi.org/10.1016/j.carbon.2019.05.005

6   Zito, A., Yang, J. Y.* Exploring Electrolyte Effects on Reduction Potential and Carbon Dioxide Binding Affinity of Quinones. *In preparation.*

7   Galeana, J. M., Jette, C. Yang, J. Y.,* Zito, A.* Benzoquinone Imines for Carbon Dioxide Capture. *In preparation.*

8   Zito, A., Yang, J. Y.* Using a Zinc-1,10-Phenanthroline-5,6-dione Eomplex for Electrochemical Carbon Dioxide Capture. *In preparation.*

Presentations

1   **Zito, A.** and Yang, J. Y.; American Chemical Society Spring Meeting; Indianapolis, IN; March 28, 2023; Oral and Poster presentations.

2   **Zito, A.** and Yang, J. Y.; Southern California Inorganic Photochemistry Conference; Catalina Island, CA; October 14-16, 2022; Oral presentation.

3   **Zito, A.** and Yang, J. Y.; Gordon Research Seminar and Conference: Electrochemistry; Ventura, CA; September 10-16, 2022; Poster presentation.

4   **Zito, A.** and Yang, J. Y.; Gordon Research Seminar and Conference: Carbon Capture, Utilization, and Storage; Ventura, CA; April 2-8, 2022; Poster presentation.

5   **Zito, A.** and Yang, J. Y.; University of California Chemical Symposium; Virtual Meeting; March 25, 2022; Oral presentation.

6   **Zito, A.** and Yang, J. Y.; American Chemical Society Spring Meeting; San Diego, CA; March 20, 2022; Poster presentation.

7   **Zito, A.** and Yang, J. Y.; University of California Chemical Symposium; Virtual Meeting; March 25, 2021; Poster presentation.

8   **Zito, A.** and Yang, J. Y.; American Chemical Society Spring Meeting; Virtual Meeting; April 14, 2021; Oral presentation.

9   **Zito, A**. and Yang, J. Y.; International School of Chemistry; Virtual Meeting; September 5, 2020, Oral presentation.

10 **Zito, A.** and Yang, J. Y.; Southern California Bioinorganic Meeting; University of California, Los Angeles; December 7, 2019; Poster presentation.

Awards

Gordon Research Seminar Chair – Electrochemistry	2024
ACS Women Chemists Committee Eli Lilly Travel Award	2023
DARPA Innovation Fellowship	2023
NRC Research Associateship with NRL (declined)	2023
Chemistry Department Travel Grant	2022
ACS Division of Inorganic Chemistry Award for Undergraduate Research – Preceptor	2022
Chemistry Departmental Service Award	2021
ACS Division of Inorganic Chemistry Travel Award	2021
Next Generation Electrochemistry Participant	2020
National Science Foundation – Graduate Research Fellowship	2020
Loh Down on Science – Science Communication Fellowship	2020-2022
UCI – Graduate Recruitment Fellowship	2020

Teaching Experience

2018-2020   **Laboratory Teaching Assistant**
Department of Chemistry, University of California-Irvine
Instructed multiple lower and upper division laboratory classes including general chemistry and advanced inorganic chemistry. Responsible for supervision of all lab activities, including but not limited to: preparation and presentation of pre-laboratory lectures, enforcement of all safety practices, assisting students with laboratory procedures, teaching students how to use air-free techniques, and grading all assignments.

2018-2020   **Lecture Teaching Assistant**
Department of Chemistry, University of California-Irvine
Instructed upper division lectures classes focused on advanced inorganic chemistry. Responsible for preparation and presentation of discussion sections of 20-40 students, creating problem sets, test study guides, and grading assignments.

ABSTRACT OF THE DISSERTATION

Investigations into Redox Carriers for Electrochemical Carbon Dioxide Capture and

Concentration

by

Alessandra Mary Zito

Doctor of Philosophy in Chemistry

University of California, Irvine, 2023

Professor Jenny Y. Yang, Chair

The development of carbon dioxide capture and concentration technologies is vital to mitigate anthropogenic carbon dioxide emissions. Nearly all of the illustrative mitigation pathways to decarbonization depend upon CO_2 capture. Current state-of-the-art technologies for carbon capture are predominantly thermal based. However, the practical applications of this technology have been limited by low overall energetic inefficiency due to Carnot limitations and thermal sorbent degradation. Electrochemical CO_2 capture and concentration has been presented as an alternative technology that may address the concerns of energetic efficiency by bypassing the need for temperature swings and instead using more energetically-efficient redox swings. A fully reversible system would fully reform the sorbent, further addressing the concerns of thermal degradation.

This dissertation describes the investigation and implementation into organic and inorganic redox carriers for CO_2 capture and concentration. Chapter 1 describes electrochemical CO2 capture and concentration (eCCC) topics, with a specific focus on systems that utilize redox carrier species. Relevant equations and thermodynamic considerations for efficient eCCC process are

discussed in detail. Additionally, reported examples of eCCC systems utilizing redox carriers are discussed and evaluated. Chapter 2 discusses a computational and experimental approach to tuning the CO_2 binding affinity and reduction potential required for forming the CO_2-reactive species of quinones functionalized with electron withdrawing and electron donating groups. Chapter 3 delves into investigations on the effect of supporting electrolyte on the CO_2 binding affinity and reduction potential of various quinones, using Lewis acids and cation size to investigate their effects on the reduction potential of the dianion and the CO_2 binding affinity. Chapter 4 describes investigations on a cobalt macrocycle and a metal-supported quinone that are both capable of CO_2 capture and concentration. Chapter 5 introduces a new redox carrier, the benzoquinone di-imine, and is an experimental study on the effect of functionalization of the pendant redox-active amine. Chapter 6 describes investigations of intermolecular and intramolecular interactions and the effects they have on the reduction potential of the dianion and the CO_2 binding affinity. The appendix features a detailed discussion of the reactor design used for electrochemical cycling experiments.

Chapter 1

Introduction

1.1 Introduction

A burgeoning population with industrialization have resulted in significantly increased global energy demand and fossil fuel consumption. As a result, anthropogenic carbon dioxide (CO_2) emissions have quickly grown to unsustainable levels. Despite aggressive targets and policies implemented globally to reduce emissions over the last several years, our annual rate of net CO_2 released has reached record levels, exceeding 36 Gt CO_2/year from fossil fuels and industry in both 2019 and 2021.[1–3] To limit global temperature rise to well below 2°C, as called for by the 2015 Paris agreement,[4] rapid and widespread decarbonization efforts are needed across all sectors of our economy.

In 2020, the power (i.e., electricity, heat) and industrial (e.g., cement production, chemicals/petrochemicals manufacturing) sectors accounted for over 50% of total emissions worldwide.[5] Within these sectors, large scale stationary "point sources" make up the majority of these emissions, which are generated from burning fossil fuels or as chemical process byproducts.[6] The remaining generators of CO_2 emissions consist of a combination of small, disperse, and often mobile sources, primarily from the transportation, waste, and agricultural sectors, which are often called "non-point sources.[2,5] The transition towards decarbonizing all of these sectors will need to be driven by a significant expansion of renewables and electrification, coupled with energy efficiency improvements. However, pathways towards decarbonization also call for large scale carbon capture and storage (CCS) or utilization/conversion (CCU). The proposed suite of carbon capture technologies can specifically address emissions from existing fossil-fuel based infrastructure, account for hard-to-decarbonize sectors (e.g., industrial byproducts), and enable net-negative applications.[1,4,7]

Considerable progress has been made in the development and optimization of carbon capture systems, particularly for coal and natural gas power plant applications.[1] According to the Global CCS institute, more than 100 commercial scale CCS facilities are operational, in construction, or in development stages as of 2021, most of which capture CO_2 from the power and industrial sectors.[8] However, in order to meet the Paris agreement, not only would all "point-source" processes need to approach net-zero carbon emissions, but emissions from other distributed sources also need to be significantly reduced or eliminated.[9] Direct air capture (DAC) of CO_2 represents a carbon-negative technology that could further act to lower emissions from non-point-source emitters.[10,11] There are currently fewer commercialized DAC processes (19 plants operating worldwide), and those that do exist are relatively small-scale, although DAC is currently receiving increased levels of attention and monetary support from both public- and private-sector organizations.[12]

Despite the role CCS is projected to play in emissions reduction, a major drawback to current technologies is that carbon capture and concentration (CCC) methods remain energy-intensive and costly, preventing widespread implementation.[13–17] One of the most mature CCC technologies is the utilization of amine-based absorbent solutions for capture from power plant flue gas. Such a process exploits the natural affinity of amines for absorbing CO_2 at room temperature to form the corresponding ammonium carbamate, followed by the thermal regeneration of the absorber to enable cyclic use.[18] A weakness of this approach, and thermally driven separation in general, is the Carnot limitation incurred by the temperature swings necessary for absorption and desorption. As a result, a typical alkanolamine capture process operating between ~37–117 °C can only approach a maximum of ~21% energetic efficiency.[19] After decades of research, most state-of-the-art amine capture systems still have high heating demands of > 2.3

GJ/ton CO_2 (>110 kJ/mol CO_2). Therefore, current systems are limited to ca. < 20% of the Carnot efficiency, or < 5% overall energetic efficiency, upon optimization at scale.[20–23] To put this efficiency into context, 20–30% of the entire power output of a typical coal-fired power plant is required to power a retrofitted CCC process alone.[24,25] Using these systems, every ton of captured CO_2 would cost an estimated $50-100 for power generation plants and $40-120 for industrial sources (i.e., cement, iron, or steel).[26–29] CCC systems for DAC are further underdeveloped, and the heating demands are much higher due to the significantly lower CO_2 concentrations. Typical thermochemical DAC systems require > 5 GJ/ton CO_2 (or > 240 kJ/mol CO_2), operating at < 10% of the energetic efficiency, resulting in higher system costs; however, it is important to note that due to the early development stage of DAC technologies, these energy estimates are generated with less certainty than point-source capture facilities.[14,30] Reported DAC cost estimates are in the range of $130–1000/ton CO_2, dependent upon the source of heat to drive regeneration (i.e., waste heat or generated heat) and the carbon footprint associated with this heat.[14,29–32] Specifically, methods which fall on the lower end of this cost range typically assume access to a source of waste heat to carry out process heating needs. Reaching net-zero emissions by 2040 is estimated to require about 2,000 large-scale CCS facilities worldwide.[33] While most current commercial demonstrations primarily use thermochemical approaches, achievement of large-scale carbon capture will likely require a diverse portfolio of options. Development of methods which offer higher energetic efficiencies than thermally-driven processes and are operated with low-carbon energy sources could enable more widespread deployment of CCC.

More efficient CO_2 separation strategies would specifically enable operation closer to the thermodynamic minimum for system energy requirements. To separate a species from a gaseous mixture, the minimum energy is equal to the difference in Gibbs free energy before and after

separation. In the limit of "skimming", where an infinitesimal quantity of CO_2 is removed from a feed gas mixture at ambient pressures, the Gibbs free energy of separation (ΔG) is given by eq. 1.1.[34]

$$\Delta G = -RT \ln \left(\frac{P_{CO_2}}{P_0} \right) \tag{1.1}$$

where R is the ideal gas constant (8.314 J mol^{-1} K^{-1}), T is the absolute temperature (K), P_{CO_2} is the partial pressure of CO_2 in the feed gas mixture, and P_0 is the ambient pressure. The relationship between the change in free energy and partial pressure demonstrates that CO_2 separation is an endergonic process whose energetics depend on the reaction conditions as well as the required changes in concentration. For example, for DAC, separating 400 ppm CO_2 from air at standard temperature (T = 298.15 K) and pressure (1 bar) to generate a pure CO_2 stream at 1 bar will require at least 19.4 kJ/mol CO_2. However, concentration from a flue gas stream containing 15 mol% CO_2 at ambient conditions requires a minimum work of separation of 4.7 kJ/mol CO_2. Note that "skimming" considered in eq. 1.1 represents a lower bound of energy requirements, which will increase with the fraction of CO_2 removed from the feed gas. Considering 90% removal of CO_2 from a flue gas mixture (15 mol% CO_2), and using expressions demonstrated in previous work,[14,34] at least 6.4 kJ/mol CO_2 is required. The minimum thermodynamic work constitutes a limit which is unachievable under practical conditions due to irreversible losses (e.g., entropic losses); however, all processes, whether they are thermochemical, electrochemical, or otherwise, aim to balance these losses with process efficiency, selectivity, and yield, with a goal of minimizing cost.

Electrochemical carbon capture and concentration (eCCC) offers a promising alternative to thermochemical processes as it circumvents the limitations of temperature-driven capture and release.[35–39] More specifically, electrochemical carbon capture systems are not bounded by Carnot efficiencies, and can theoretically approach operation at the thermodynamic minimum energy

requirement (i.e., 100% energetic efficiencies).[37] As such, in electrochemical systems, the minimum cell potential (E_{cell}) is related to the minimum separation work (represented by the change in Gibbs free energy).

$$E_{cell} = -\frac{\Delta G}{nF} \qquad (1.2)$$

where n is the moles of electrons transferred per mole of CO_2 captured, F is the Faraday constant (96485 C mol^{-1}), and together, they describe the charge transferred during the reaction. As CO_2 separation is a nonspontaneous process ($\Delta G > 0$), the cell potential, or difference between the potential of the cathode and anode, is negative ($E_{cell} < 0$). This minimum cell potential is directly related to the relative CO_2 concentrations at the two electrodes via the Nernst equation. To perturb the reaction equilibrium and drive the process toward favorable CO_2 separation, the actual cell voltage magnitude ($|V_{cell}|$) must be greater than $|E_{cell}|$, resulting in energetic losses. This deviation from E_{cell} is dependent on the thermodynamic cycle of the separation system and overpotentials that result from resistive losses in the electrochemical cell(s). These cell resistances arise from a summation of inefficiencies associated with kinetic, ohmic, and transport phenomena that underlie system operation and their magnitudes are influenced by the chosen cell materials and reactor operating conditions (i.e., current density). Thus, cell potential and associated energy requirements are influenced by several design and operational factors. Despite these potential energetic penalties, an advantage of electrochemical systems is their ability to apply electric currents (via polarized electrode surfaces) that directly act on target redox-active molecules rather than on the entire capture medium via heating and cooling, thus reducing or eliminating sensible heat losses. Due to these differences in process energetics, electrochemical systems can potentially operate with reduced energy requirements over thermochemical systems and are therefore particularly attractive. Additionally, eCCC systems present an opportunity to operate at milder conditions (i.e.,

at or near room temperature), allow for modular designs that can more readily be scaled up or down, and can run on electricity from renewable sources. There is an inherent energy loss within the nonaqueous flow systems; experimentally determined iR drops are within the range of 300-1200 ohms. However, the iR drop is dependent upon cell design parameters such as electrodes, separators, and supporting electrolyte, and thus the energy losses associated with cell resistance are expected to change with each system.

1.2 Redox-Active Capture Molecules

The approach to eCCC of interest for this work is the use of redox-active capture molecules, or redox carriers, that directly bind and release CO_2 upon oxidation or reduction (i.e., direct eCCC methods). **Scheme 1.1**

Scheme 1.1. Redox-active capture molecules for electrochemically-mediated CO_2 separation, adapted from Ref. 39.
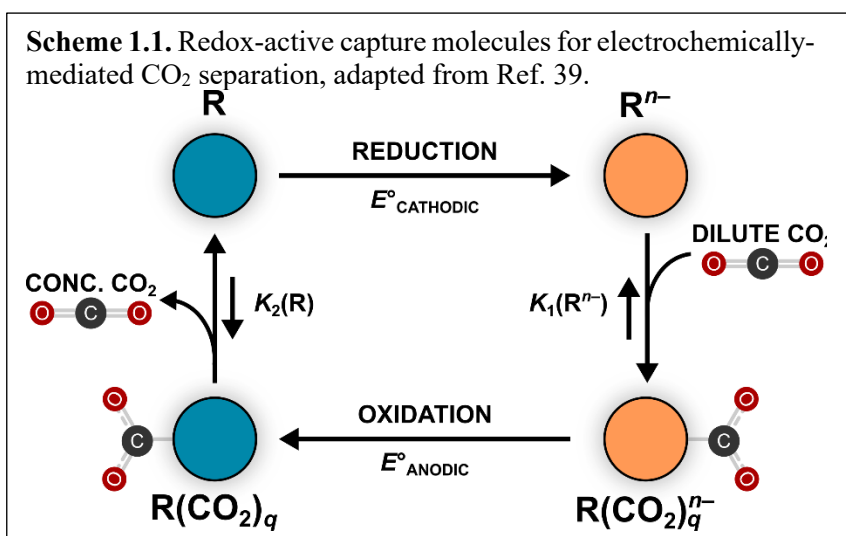
illustrates a generalized direct eCCC cycle featuring a redox carrier.[39] In the cycle, the molecule in the resting state (R) is reduced to form the active state carrier species (R^{n-}), where n is the number of electrons transferred. The reduced species has a high affinity for CO_2 ($K_{1(R^{n-})}$), which results in capture from a dilute inlet stream to form the CO_2-bound adduct, $R(CO_2)_q^{n-}$. Here, q represents the number of CO_2 molecules that bind to each capture molecule. Release is triggered by the oxidation of $R(CO_2)_q^{n-}$ to form $R(CO_2)_q$, which has a much lower affinity for CO_2 ($K_{2(R)}$),

7

resulting in liberation of CO_2 to reform the resting-state carrier (R) to complete the cycle. This approach takes advantage of the difference between the binding affinity of the oxidized ($K_{2(R)}$) and reduced ($K_{1(R^{n-})}$) states of the carrier (R and R^{n-}, respectively).

DuBois and coworkers were the first to publish the use of redox-active capture molecules for eCCC applications.[40] Several classes of redox-active capture molecules were assessed using spectroscopic, voltametric, and controlled potential electrolysis approaches to determine both the electrochemical reversibility of CO_2 binding and the CO_2 equilibrium constants of the oxidized and reduced forms.[40,41] In these works, they outline desirable molecular properties of efficient CO_2 capture molecules. They propose that a capture molecule for direct eCCC must have a site capable of CO_2 binding and must also be able to undergo chemically reversible oxidation and reduction in the presence and absence of CO_2. Regarding these two points, they identified the importance of proximity of the redox center to the CO_2 binding site. Shorter distances between the two sites resulted in larger changes in the binding affinity between oxidized and reduced states of the capture molecule. This is important because the difference in CO_2 binding affinity between the oxidized and reduced forms must be sufficiently large to enable sufficient CO_2 capture from a given feed gas. One metric that can be utilized to evaluate if sufficient CO_2 is captured from the feed gas is the Faradaic efficiency ($\eta_{Faradaic}$), or the moles of CO_2 separated per mole of electron transferred. Assuming complete activation/deactivation of a redox-active capture molecule (with total concentration $[R]_T$), the upper bound on $\eta_{Faradaic}$ for a redox-active carrier / solvent system can be determined using eq. 1.3. This expression was derived using equations presented by Clarke et al., and aligns with other previous works.[41–43]

$$\eta_{Faradaic} = \frac{q}{n}\left(\frac{K_{1(R^{n-})}(K_H P_i)^q}{1 + K_{1(R^{n-})}(K_H P_i)^q} - \frac{K_{2(R)}(K_H P_f)^q}{1 + K_{2(R)}(K_H P_f)^q}\right) - \frac{K_H}{n[R]_T}(P_f - P_i) \tag{1.3}$$

In the above equation, K_H is the Henry's law constant for CO_2 in the electrolyte solution (M atm^{-1}), P_i is the initial CO_2 partial pressure before separation (atm), and P_f is the final CO_2 partial pressure after separation and recovery (typically 1 atm). For any capture molecule, the upper bound on achievable faradaic efficiencies is q/n. Then, considering an example system with a 10% CO_2 feed gas (within the typical concentration range for a coal-fired power plant flue gas) [19,24] and the following constant parameters ($[R]_T = 1$ M, $K_H = 0.175$ M atm^{-1}, $K_{2(R)} \ll 1$, $n = 2$, and $q = 1$), a $K_{1(R^{n-})}$ value of at least 6.3×10^2 is required to obtain $\geq 90\%$ of the maximum Faradaic efficiency (q/n) according to eq. 1.3. Using the same equation, a $K_{1(R^{n-})}$ value of at least 1.6×10^5 is necessary to capture from atmospheric CO_2 sources ($P_i = 410$ ppm) with the same efficiency.

In addition to impacting the Faradaic efficiency, binding coefficients can also influence system energy requirements due to their direct relation to the difference in standard potentials for the binding and release steps ($\Delta E = E^{\circ}_{cathodic} - E^{\circ}_{anodic}$). More specifically, the ratio between the activated and deactivated capture molecule binding affinities, i.e., $K_{1(R^{n-})}/K_{2(R)}$, is intrinsically proportional to ΔE according to eq. 1.4.

$$-RT \ln \left(\frac{K_{1(R^{n-})}}{K_{2(R)}} \right) = nF(\Delta E) \tag{1.4}$$

Therefore, a higher binding affinity ratio, $K_{1(R^{n-})}/K_{2(R)}$, will lead to higher cell voltages and thus greater energy requirements. To further assess this tradeoff between system energy requirements and Faradaic efficiency, Clarke et al. defined a combined efficiency metric to highlight molecular properties (such as $K_{1(R^{n-})}$) that may be effective to adequately balance this tradeoff.[43] Their work also explores how these effective properties are dependent upon other system properties, such as system configuration.

The effect of resistance in the cell has been studied using the MacMullin number (N_m), a ratio of the resistivity of the separator to the electrolyte.[44] It has been noted that a larger N_m value leads to a higher system voltage and operating current density, but the overall energetics are lower. The opposite is true when the N_m value is smaller; crossover will lower the system energy, leading to higher overall energetics.

Beyond having adequate CO_2 binding affinities while maintaining a minimal potential difference between binding and release steps, additional desirable characteristics of capture molecules include rapid electron transfer kinetics, high solubility, stability of the carrier species towards other compounds present in a given feed gas composition (e.g., oxygen, water vapor), among others.[38,39,42] Overall, several different classes of molecules have been identified and assessed as capture molecule candidates. Quinones are the most studied group of molecules, [42,45–50] but other redox-active capture species have been assessed as well, including transition-metal complexes,[51] bipyridines,[52–54] and thiols.[55]

1.3 Quinones

Reduced *ortho*- and *para*-benzoquinones can bind CO_2 directly under aprotic conditions. CO_2 reacts with reduced quinones at one or more anionic oxygen atoms via an ECEC (electron transfer, chemical reaction, electron transfer, chemical reaction) EECC (two electron transfers followed by two chemical reactions), or EEC (electron transfer, electron transfer, chemical reaction) mechanism.[48] An ECEC mechanism may be desirable because the quinone captures two CO_2 molecules, increasing the sorbent capacity. Additionally, capturing two CO_2 molecules per two electron transfers results in a theoretical maximum Faradaic efficiencies of 100%. ECEC or EEC mechanisms depend on whether CO_2 molecules bind to the reduced species in its radical

anion (Q_{RA}) and/or dianion (Q_{DA}) forms (**Scheme 1.2**).[47–49] In general, quinones have a wide range of affinity for CO_2; reported CO_2 binding constants for quinone dianions ($K_{CO_2(DA)}$) have been reported between ca. $10 – 10^{20}$ which is summarized in **Table 1.1.** Numerous quinones also bind CO_2 in their radical anion state (Q_{RA}). However to date, $K_{CO_2(RA)}$ values have only been reported for 9,10-phenanthrenequinone and 2,6-di-*tert*-butyl-1,4-benzoquinone.[40,41] The binding constants for both radical anions ($K_{CO_2(RA)}$) are several orders of magnitude smaller than the corresponding values for the dianions ($K_{CO_2(DA)}$). Although no other values of $K_{CO_2(RA)}$ have been quantitatively determined, cyclic voltammetry suggests that $K_{CO_2(RA)}$ is always much smaller than $K_{CO_2(DA)}$,[40,41,48,49,56,57] likely due to increased nucleophilicity of the oxygen atoms in the dianion. The specific value for $K_{CO_2(RA)}$, which represents the thermodynamic favorability of CO_2 binding to a quinone radical anion species, causes the disparity in reported mechanisms (EEC or ECEC). A complication to this assessment, however, is if disproportionation of two Q_{RA} molecules transpires to create Q and Q_{DA}, which then reacts with CO_2; this may result in inflated values for $K_{CO_2(RA)}$ and falsely suggest an ECEC mechanism if not properly considered.[41,58,59]

Scheme 1.2. Direct electrochemical capture by quinones by EEC mechanism (black), EECC (red) or ECEC mechanisms (blue).
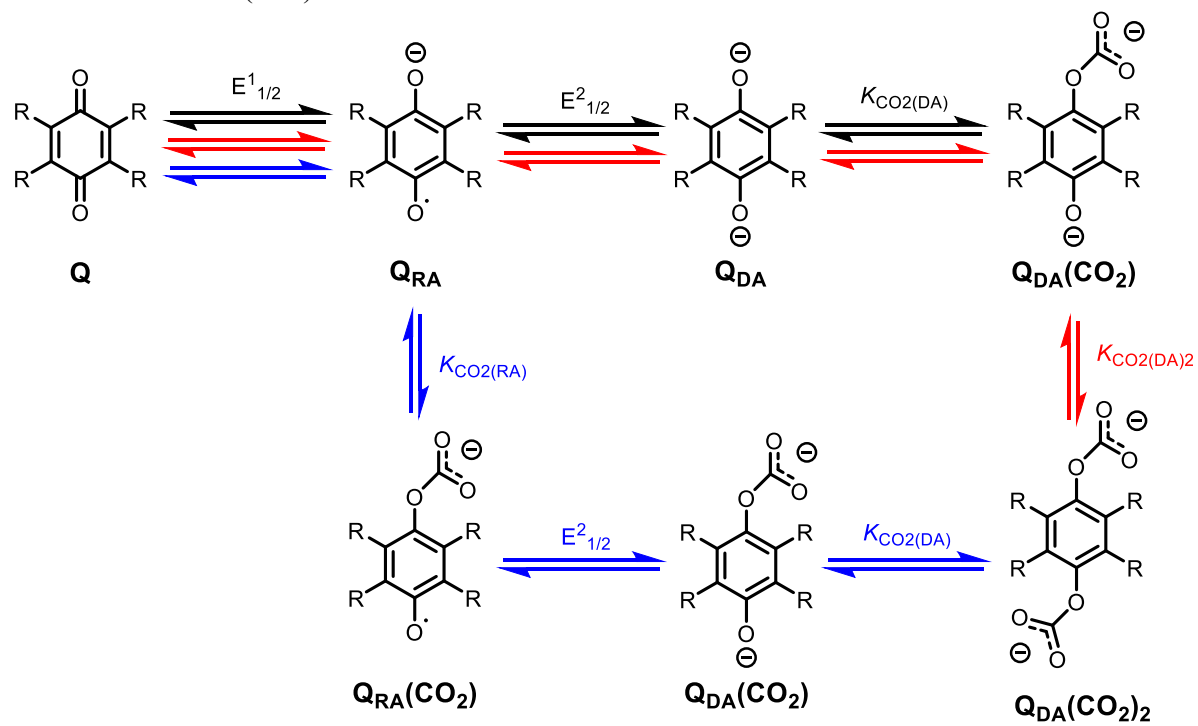
Table 1.1. Reported reduction potentials for various quinone radical anion / dianion redox pairs ($E^2_{1/2}$) and associated CO_2 binding constants of the dianion species ($K_{CO_2(DA)}$).

Quinone	Solvent	$E^2_{1/2(N_2)}$[a]	$E^2_{1/2(CO_2)}$[a]	$\Delta E_{1/2}$[b]	Log($K_{CO_2(DA)}$)	Ref.
tetrafluoro-1,4-benzoquinone	DMF	–1.20	–0.90	0.30	4.3	[56]
tetrachloro-1,4-benzoquinone	MeCN	–1.12	N/A	N/A	3.8	[40]
2,6-di-tert-butyl-1,4-benzoquinone	MeCN	–1.86	N/A	N/A	15.0	[40]
9,10-phenanthrenequinone	MeCN	–1.59	N/A	N/A	11.8	[40]
2,3-dicyano-1,4-benzoquinone[c]	MeCN	–0.87	N/A	N/A	3.8	[41]
2, 6-dichloro- 1,4-benzoquinone	MeCN	–1.34	–1.00	0.34	6.0	[48]
2- chloro-1,4-benzoquinone	MeCN	–1.47	–0.98	0.49	10.0	[48]
tetrafluoro-1,4-benzoquinone	MeCN	–1.20	–1.02	0.18	3.8	[48]
tetrachloro-1,4-benzoquinone	MeCN	–1.14	–1.03	0.11	2.5	[48]
5-hydroxy-NQ[c]	MeCN	–1.34	–1.11	0.23	3.3	[48]
1, 8-dihydroxy-AQ[c]	MeCN	–1.60	–1.34	0.26	5.4	[48]
1, 2-dihydroxy-AQ[c]	MeCN	–1.69	–1.48	0.21	4.6	[48]
5, 8-dihydroxy-NQ[c]	MeCN	–1.38	–1.31	0.07	2.1	[48]
anthraquinone	MeCN	–1.96	–1.02	0.46	9.0	[60]
1-hydroxy-AQ[c]	MeCN	–1.70	–1.58	0.20	5.1	[60]
1,4-dihydroxy-AQ[c]	MeCN	–1.55	–1.54	0.01	1.1	[60]
1-amino-AQ[c]	MeCN	–1.98	N/A	N/A	8.3	[60]
1,4-diamino-AQ[c]	MeCN	–2.03	N/A	N/A	9.7	[60]
1-amino-4-hydroxy-AQ[c]	MeCN	–1.81	–1.60	0.21	4.8	[60]

[a]Potentials are reported as V vs. Fe(C$_5$H$_5$)$_2^{+/0}$. Potentials recorded versus SCE were converted with Ref. [61]
[b]Reported in units of volts and equal to the shift in half-wave potential in the presence and absence of CO_2 ($\Delta E_{1/2} = E^{o\prime} - E_{1/2}$ in eq. 1.4).
[c]Features intramolecular hydrogen-bonding interactions.

Among the multiple classes of redox-active molecules first considered by DuBois and coworkers, quinones were the most promising because the CO_2 binding site is close to the redox site, have reversible reduction and oxidation events in both the presence and absence of CO_2, and have more significant CO_2 binding affinity in the activated form and little to no binding affinity in the deactivated form.[40] A wide variety of quinone candidates were screened in acetonitrile (MeCN) and dimethylformamide (DMF) using both cyclic voltammetry and bulk electrolysis techniques. Of the large number investigated, only five had reversible CO_2 binding and release with sufficient CO_2 binding affinities: 2,6-di-*tert*-butyl-1,4-benzoquinone (DtBBQ), 9,10-phenanthrenequinone (PAQ), tetrachloro-1,4-benzoquinone (TCQ), 2,3-dicyano-1,4-benzoquinone, and 2,3-dicyano-5,6-dichloro-1,4-benzoquinone (DDQ). Reduction potentials and values of $K_{CO_2(DA)}$ (and some values of $K_{CO_2(RA)}$) were reported for each of the five quinones, however little mechanistic information was determined beyond the number of CO_2 molecules bound per quinone dianion. A significant observation in this work was that the log of the CO_2 binding affinity of the quinone dianions ($\log(K_{CO_2(DA)})$) is linearly correlated with the second reduction potential to the dianion species under an N_2 atmosphere. This trend has since been observed among a wider selection of quinones,[39,41,48,62–64] bipyridines,[62] and more recently with NHC-analogues (using DFT-derived binding constants).[65]

In 1989, Mizen and Wrighton reported the first mechanistic study of CO_2 binding to quinone dianions.[47] Chemical reduction of PAQ was used to characterize the CO_2-active species. PAQ was reduced by one or two electrons with cobaltocene or sodium metal (to form PAQ[•–] or PAQ[2–], respectively), followed by addition of CO_2 resulted in the formation of a new species. This species featured a ^{13}C NMR peak between 156-158 ppm in CD_3CN or DMSO-d_6, suggesting formation of an alkyl carbonate. Infrared spectroscopy further confirmed this assessment,

exhibiting carbonyl stretches at 1646 and 1686 cm^{-1} when cobaltocene was used as the reductant. Spectroelectrochemical infrared (SEC-IR) spectroscopy indicates the formation of a single carbonyl stretch at 1646 cm^{-1} upon reduction of PAQ to PAQ^{2-}. The stretch observed at 1686 cm^{-1} was attributed to interactions with cobaltocenium cation, which is more likely to interact and stabilize the CO_2 adduct than the tetrabutylammonium cations present in SEC-IR studies. When the same experiments were repeated in the absence of CO_2, the ^{13}C NMR and IR signals were not observed, which indicated CO_2 binding occurs at one or both anionic oxygen atoms upon reduction of PAQ to PAQ^{2-}. With this information, along with the experimentally determined 2:1 ratio of CO_2:PAQ^{2-}, Mizen and Wrighton proposed an ECEC mechanism for the reaction, whereby two molecules of CO_2 are bound through the two oxygen atoms of PAQ^{2-}.

Shortly thereafter, Ogura and coworkers reported a mechanistic study with several other quinones and CO_2 in MeCN.[48] This study expanded upon the work of Mizen and Wrighton by including 11 different quinones of varying electron density. Like PAQ, the quinones with more nucleophilic oxygen atoms bind two molecules of CO_2 via an ECEC mechanism. In contrast, the less electron dense quinones did not bind CO_2 in the radical anionic state and thus undergo an EEC to bind one molecule of CO_2 upon reduction to the dianion. Interestingly, the authors observed that there appeared to be a specific threshold potential for the first reduction (to form the radical anion) where the quinones switched between EEC and ECEC mechanisms. The proposed ECEC mechanism for 1,4-anthraquinone (AQ), 1,4-napthoquinone (NQ), duroquinone (DQ), and 2,6-dimethylbenzoquinone (DMQ) in MeCN by Ogura and coworkers contrasts with the mechanism previously reported in dimethylsulfoxide by Simpson and Durand.[57] Simpson and Durand proposed an ECE mechanism for each of these quinones based on cyclic voltammetry; however the authors did not determine how many CO_2 molecules were bound to the reduced quinone

species. Due to the difficulty of differentiating ECE and ECEC mechanisms by cyclic voltammetry and without knowledge of either reaction stoichiometry or products formed,[66] it is likely that the mechanism was incorrectly assigned and is in fact ECEC for these quinones. In more recent work, naphthoquinones have been determined to undergo ECEC or EEC mechanisms in ionic liquid solvents, similar to what has been previously observed in aprotic organic solvents.[49]

To study the redox behavior and the reactivity toward CO_2 capture of p-benzoquinone (BQ) and tetrafluoro-p-benzoquinone (TFBQ), Namazian et al. employed both experiments (cyclic voltammetry) and theory (ab initio calculations with the G3MP2//B3LYP composite method with the CPCM solvation model).[56] Their cyclic voltammetry results in DMF solvent indicated that BQ is likely to capture CO_2 after the first reduction to BQ semiquinone ($BQ^{\bullet-}$), whereas the TFBQ was proposed to react with CO_2 only after the two-electron reduction ($TFBQ^{2-}$) is accomplished (note that this corresponds to the ECE and EEC mechanisms for BQ and TFBQ, respectively). In the article, the lower reactivity of the TFBQ semiquinone was explained based on the lower nucleophilicity of the quinone's oxygen atoms due to the presence of the electron-withdrawing fluorine atoms. The calculation of the lower charge on the oxygen atoms in $TFBQ^{\bullet-}$ was performed as a confirmation. The BQ and TFBQ were also compared in the regioselectivity of CO_2 binding. Both theory and experimental work indicate that $TFBQ^{2-}$ binds CO_2 at the oxygen atom, forming a carbonate product (note that the carbonate was calculated to be favored by ~ 88 kJ/mol over the carboxylate). Comparatively, theory predicts that BQ prefers carboxylate (carbon-bound CO_2) over the carbonate product by ~ 10 kJ/mol.[59] However, these findings conflict with previous experimental observations, and they speculated that this difference may be due to kinetics, as the formation of the carbonate product may be a faster reaction than the that to form the more stable carboxylate product. While formation of a carboxylate versus a carbonate

does not affect the overall mechanism (i.e., EEC or ECE) in theory, it is unclear if and how the resulting product would impact overall performance of a redox active capture molecule. Fan et al. revisited the BQ reactivity by comparing the properties of the most stable carboxylate species obtained from the calculations with the experimental infrared absorption, and notably, the authors' findings were in agreement.[67]

Naphthoquinones undergo ECEC or EEC mechanisms in ionic liquid solvents, similar to what has been observed in aprotic organic solvents.[49] Jin and coworkers used a spectroelectrochemical approach to elucidate the mechanism and site of binding for CO_2 capture with NQ, 2-chloro-1,4-napthoquinone (CNQ), and 2,3-dichloro-1, 4-napthoquinone (DCNQ). Upon two electron reductions of NQ to the dianion (NQ^{2-}) under CO_2, a carbonyl stretch is observed at 1634 cm^{-1} via spectroelectrochemical infrared spectroscopy (SEC-IR). The IR band is consistent with a carbonate species and is not present when the experiment is repeated in an inert N_2 atmosphere. This result suggests that CO_2 binds to NQ^{2-} through the anionic oxygen atoms, similar to what was previously observed with PAQ^{2-} in MeCN.[47] Using cyclic voltabsorptometry (CVA) and derivative cyclic voltabsorptometry (DCVA), the authors concluded that reaction of CO_2 with NQ follows an ECEC mechanism. Monitoring the IR spectrum during CVA and DCVA experiments, it was observed that the CO_2 binds to the radical anion ($NQ^{\bullet-}$) prior to being reduced to the dianion, where it could then bind a second molecule of CO_2. The overall reaction stoichiometry of NQ with CO_2 was further confirmed using a similar method used by Ogura and coworkers.[48] When the solution was oxidized, the carbonate stretch at 1634 cm^{-1} disappeared, with the growth of a peak at 1671 cm^{-1} corresponding to NQ. This pattern was observed across multiple consecutive scans, indicating that binding and release is reversible. When these experiments were

repeated for CNQ and DCNQ, similar results were observed; however, both quinones only bind one molecule of CO_2 through a proposed EEC mechanism.

The effects of hydrogen bond donors was probed by Barlow et al. who demonstrated that use of such additives indeed shifts the reduction potential of the redox-active capture molecule to more positive potentials.[62] Different alcohols were added to tetrachloroquinone (TCQ) in DMF to study the effect of these hydrogen-bond donors on the reduction potential and the CO_2 binding affinity. Although all alcohol additives resulted in a positive shift of the reduction potential, stronger hydrogen-bonding interactions inhibited CO_2 binding, leading to smaller CO_2 binding affinities, while moderate interactions resulted in larger CO_2 binding affinities. Ethanol was identified as a hydrogen-bond donor that did not have deleterious effects on the CO_2 binding affinity but enabled a favorable shift in the reduction potential to values greater than that of O_2 reduction. TCQ was tested via controlled potential electrolysis with the presence and absence of ethanol in the electrolyte mixture, where the reduced form of TCQ (TCQ^{2-}) was oxidized and re-reduced in the presence of a simulated flue gas mixture (87:10:3 N_2:CO_2:O_2). With ethanol as an additive, Barlow et al. showed improvements in the extent of electrochemical CO_2 capture and concentration from flue gas concentrations in the presence of O_2. More specifically, with the addition of ethanol, the estimated Faradaic efficiencies during both oxidation/release and reduction/recapture steps were improved from 84% to 95% and 27% to 73%, respectively. The TCQ/ethanol pair was not tested over multiple cycles, so long term stability of this specific chemistry is unclear. However, this work demonstrates that hydrogen-bond donors can be added to an electrolyte to anodically shift the reduction potentials of the quinone (or another redox active capture agent) and improve O_2 stability.

1.4 Transition Metals

Figure 1.1. Carbonate adduct, $[Cu_2(tpmc)(\mu\text{-}CO_3)]^{2+}$ formed from $[Cu_2(tpmc)(\mu\text{-}OH)]^{3+}$.
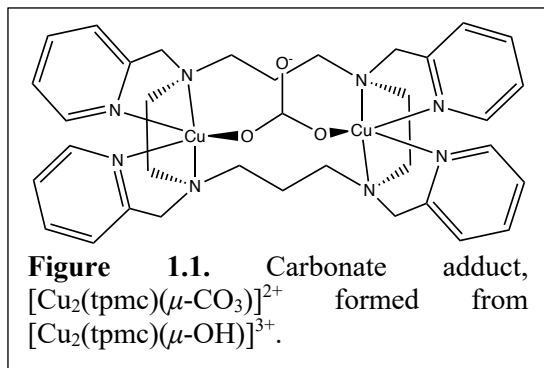
Redox-active transition metal (TM) centers paired with specific ligands can also serve as CO_2 capture agents in direct eCCC systems. DuBois and coworkers suggested that TM complexes with ligands that contain a CO_2 binding site (i.e., a nucleophilic nitrogen or oxygen) could effectively concentrate CO_2.[41] The metal center as the active redox site would alter the electron density of the compound and thus the CO_2 binding affinity. Their study found that the distance between the redox metal center to CO_2 binding site significantly impacts the compound's ability to capture and release CO_2. The assayed compounds contained one, two, or five atoms separating the binding site to the redox active metal center of Co, Fe, or Ru. CO_2 capture activity was only observed in the Co^{3+} cyclopentadienyl indenyl complex with a one-atom separation of metal from the binding site.

A few binuclear TM complexes explored in other works were demonstrated to trap the CO_2 dissolved in aqueous media as a bound carbonate ion.[68–71] In these, specific bridging ligands orient two metals (Zn, Co, Ni, or Cu) to issue strong carbonate binding interactions. However, studies examining the electrochemical behavior of these compounds and their application to reversibly pumping CO_2 are limited.

DuBois and coworkers examined binuclear Ni and Cu complexes with varied bridging ligands for the reversible capture and release of bicarbonate, and found that more flexible ligands resulted in enhanced binding.[51,71] However, the reduction potentials of the nickel complexes were too negative for electrochemical pumping. Of the copper complexes surveyed, the $[Cu_2(tpmc)(\mu\text{-}$

OH)]$^{3+}$ complex (tpmc = bridging *N,N',N'',N'''*-tetrakis(2-pyridylmethyl)-1,4,8,11-tetraazacyclotetradecane ligand), demonstrated a viable reduction potential for CO_2 pumping and successful electrochemical CO_2 capture and concentration from 10% to 75% (**Figure 1.1)**. Cycling resulted in partial precipitation of the Cu^+ complex, an outcome which could potentially be improved upon with variation of supporting electrolytes or ligand. Contrary to typical increased CO_2 binding affinity upon reduction, these systems bind carbonate upon *oxidation*, and *reduction* results in CO_2 release.

1.5 Bipyridine

Bipyridines also become more nucleophilic upon reduction, making them suitable candidates as CO_2 capture redox carriers. A study by Ishida et al. described the reversible capture and release of CO_2 by *N*-propyl-4,4'-bipyridinium (Prbipy$^+$).[52] More recently, Buttry and coworkers explored the reactivity of the related *N*-methyl-4,4'-bipyridinium (Mebipy$^+$) with experimental data and theoretical calculations.[53] The electrochemical behavior and DFT calculations indicate the following mechanism of CO_2 binding for Mebipy$^+$ and the related Prbipy$^+$ (**Scheme 1.3**). First, the Mebipy$^+$ is reduced by one electron to form a neutral Mebipy. In the presence of CO_2, Mebipy$^•$ species undergoes disproportionation to form Mebipy$^+$ and Mebipy$^-$. The latter reacts with CO_2 to form Mebipy–CO_2^-, which results in a disappearance of the more cathodic redox event. The CO_2 adduct can then be electrochemically oxidized by two electrons to return the parent Mebipy$^+$ cation. For these monoalkylated bipyridinium species, the stoichiometry thus requires two electrons due to the disproportionation event that occurs to capture one molecule of CO_2.

Scheme 1.3. Reduction of MeBipy$^+$, disproportionation of Mebipy$^\bullet$, and CO$_2$ binding to Mebipy$^-$.
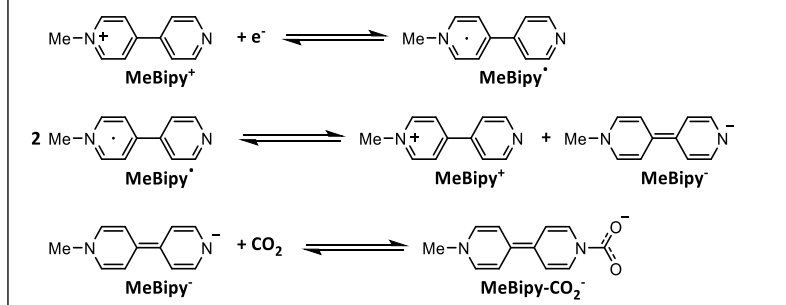
Buttry and coworkers also studied the related non-alkylated compound, 4-,4'-bipyridine (bipy).[54] The one electron reduction of bipy produces the radical anion, bipy$^{\bullet-}$, which quickly binds to CO_2. Following oxidation of the bipy–$CO_2^{\bullet-}$ adduct, CO_2 is released and bipy is regenerated. This mechanism differs from the monoalkylated bipyridinium compounds. One equivalent of electrons is sufficient to capture a single equivalent of CO_2 due to the more nucleophilic radical anion, which readily binds to CO_2 after a single reduction. In the ionic liquid BMF TFSI under a N_2 atmosphere, reduction of bipy to bipy$^{\bullet-}$ is a one electron reversible couple at -2.25 V vs. $Fe(C_5H_5)_2^{+/0}$. In a solution saturated with CO_2, the reduction peak for bipy$^{\bullet-}$ shifts from -2.3 V to -2.05 V vs. $Fe(C_5H_5)_2^{+/0}$ displaying strong binding between bipy$^{\bullet-}$ CO_2. The bipy–$CO_2^{\bullet-}$ is oxidized at -1.35 V vs. $Fe(C_5H_5)_2^{+/0}$, a substantial positive shift due to the very stable N–C bond formed in the adduct. The large potential difference between reduction and oxidation of this adduct is a crucial component as it can impact the total energy for the bipy–CO_2 capture release cycle.

1.6 Experimental Methods for Measuring CO$_2$ Binding Affinities

The CO_2 binding affinity of the reduced and oxidized forms of the capture species ($K_{1(R^{n-})}$ and $K_{2(R)}$, respectively) must be sufficiently large to enable CO_2 capture and release, respectively. Thus, determination of $K_{1(R^{n-})}$ and $K_{2(R)}$ values for the active and resting states of redox carriers is important. There are several methods used to measure binding coefficients; however, unique to

redox carriers, electrochemical methods specific to the reaction mechanism can be employed to measure these equilibrium constants. For a system with an EC mechanism (electron transfer followed by chemical step), or EEC mechanism (where a chemical step follows two electron transfer steps), carrier CO_2 binding constants (for $K_{1(R^{n-})}$ values between 100 and 10^{15}) can be measured using the observed shift in the half-wave potential, $E_{1/2}$, recorded in the presence and absence of a known concentration of CO_2 by applying eq. 1.5.[50,72]

$$E_{1/2} = E^{o\prime} + \frac{R_u T}{nF} \ln\left(K_{1(R^{n-})}\right) + q\frac{RT}{nF} \ln [CO_2] \qquad (1.5)$$

In the above equation, R_u is the universal gas constant, T is temperature, F is Faraday's constant, and n is the number of electrons being passed in the redox event. The number of CO_2 molecules that are bound during the chemical step is represented by the term q (which can be determined via other spectroscopic or voltammetric techniques[40,41,73]). $E^{o\prime}$ is the half-wave potential in the absence of CO_2, while $E_{1/2}$ represents the half-wave potential in the presence of a known CO_2 concentration in solution ($[CO_2]$). This approach does not require isolation of the active-state carrier, which can often be unstable or difficult to isolate cleanly. For an EC mechanism where $K_{1(R^{n-})}$ values are larger than 10^{15}, the change in potential can be measured using the open circuit potential, with a varied range of CO_2 concentrations. In this case, the active state carrier must be formed chemically or electrochemically. The $E_{1/2}$ value from eq. 1.4 would refer to the open circuit potential under a known concentration of CO_2. The $E^{o\prime}$ value would refer to the open circuit potential in the absence of CO_2. The y-intercept of the linear relationship of the change in open circuit potential versus the natural log of the concentration of CO_2 in solution can be used to find the binding constant. Values of $K_{1(R^{n-})}$ for redox carriers can be also be determined using more common spectroscopic or physical techniques, depending on the magnitude of $K_{1(R^{n-})}$ and solubility of the carrier. These techniques include, but are not limited to: NMR and electronic

absorption spectroscopy, gravimetry, and gas uptake experiments.[40,41,74,75] An example of one of these methods is measuring the electronic absorption spectrum of an eCCC carrier under various concentrations of CO_2.[41] In order to utilize this method however, the active state carrier must be used, meaning that it must be isolable and stable over the course of the experiments. The resulting spectra can be analyzed using a variety of approaches to assess the equilibrium constant; for example the Benesi-Hildebrand method.[76]

1.7 Conclusions

The use of electrochemical CO_2 capture and concentration was initially reported in literature in the 1960's. In the intervening time frame, several different concepts and architectures have been proposed, with significant advancements occurring over the last decade. Some of these systems already operate in the laboratory setting with estimated energetic efficiencies rivaling state-of-the-art thermal systems. These results have demonstrated the promise of eCCC, but also outline scientific challenges that, if addressed, would accelerate implementation and widespread use.

Long term stability still presents a challenge in most eCCC systems. Most redox carrier systems are specifically sensitive to oxygen, which is commonly present in dilute CO_2 streams. A combination of modifying these systems to work at milder electrochemical potentials and implementing engineering design approaches (e.g., pre-separating O_2 or water vapor from the inlet streams) could be used to address current issues surrounding instability in the presence of O_2 and/or water vapor (for non-aqueous systems). The stability of current chemistries towards other components in CO_2-containing streams (i.e., sulfur oxides, nitrous oxides, etc.) is also not clear. Within this thesis, strategies to control the CO_2 binding affinity and reduction potentials were

investigated with the goal of finding an O_2-stable electrochemical carbon dioxide capture system. Strategies included usage of synthetic handles through exchanging functionalization on the quinone ring and inclusion of intramolecular hydrogen bonding groups. There were also studies performed that focused on control of the solvent environment through changing the electrolyte salt and the use of additives that would stabilize the dianion.

1.8 References

(1)   IPCC. *Climate Change 2022: Mitigation of Climate Change. Contribution of Working Group III to the Sixth Assessment Report of the Intergovernmental Panel on Climate Change*; Cambridge, UK and New York, NY, 2022. https://doi.org/10.1017/9781009325844.

(2)   *Global Energy Review: CO2 Emissions in 2021*; Paris, 2022.

(3)   Friedlingstein, P.; Jones, M. W.; O'Sullivan, M.; Andrew, R. M.; Bakker, D. C. E.; Hauck, J.; Le Quéré, C.; Peters, G. P.; Peters, W.; Pongratz, J.; et al. Global Carbon Budget 2021. *Earth Syst. Sci. Data* **2022**, *14* (4), 1917–2005. https://doi.org/10.5194/ESSD-14-1917-2022.

(4)   Rogelj, J.; den elzen, M.; Höhne, N.; Fransen, T.; Fekete, H.; Winkler, H.; Schaeffer, R.; Sha, F.; Riahi, K.; Meinshausen, M. Paris Agreement Climate Proposals Need a Boost to Keep Warming Well below 2 °C. **2016**. https://doi.org/10.1038/nature18307.

(5)   Ritchie, H.; Roser, M.; Rosado, P. CO₂ and Greenhouse Gas Emissions. *Our World Data* **2020**.

(6)   Metz, B.; Davidson, O.; de Coninck, H.; Loos, M.; Meyer, L. *IPCC Special Report on Carbon Dioxide Capture and Storage*; Cambridge, UK, 2005.

(7)   International Energy Agency. *Net Zero by 2050*; Paris, 2021.

(8)   Facilities - Global CCS Institute https://co2re.co/FacilityData (accessed Sep 1, 2022).

(9)   Tavoni, M.; van der Zwaan, B. Nuclear Versus Coal plus CCS: A Comparison of Two Competitive Base-Load Climate Control Options. *Environ. Model. Assess.* **2011**, *16* (5), 431–440. https://doi.org/10.1007/S10666-011-9259-1.

(10)   Chu, S.; Majumdar, A. Opportunities and Challenges for a Sustainable Energy Future. **2012**. https://doi.org/10.1038/nature11475.

(11)   Lackner, K. S.; Brennan, S.; Matter, J. M.; Park, A. H. A.; Wright, A.; Van Der Zwaan, B. The Urgency of the Development of CO 2 Capture from Ambient Air. *Proc. Natl. Acad. Sci. U. S. A.* **2012**, *109* (33), 13156–13162. https://doi.org/10.1073/PNAS.1108765109.

(12)   IEA. *Direct Air Capture*; Paris, 2022.

(13)   Hammond, G. P.; Akwe, O. S. O.; Williams, S. Techno-Economic Appraisal of Fossil-Fuelled Power Generation Systems with Carbon Dioxide Capture and Storage. *Energy* **2011**, *36* (2), 975–984. https://doi.org/10.1016/j.energy.2010.12.012.

(14)   House, K. Z.; Baclig, A. C.; Ranjan, M.; Van Nierop, E. A.; Wilcox, J.; Herzog, H. J. Economic and Energetic Analysis of Capturing CO2 from Ambient Air. *Proc. Natl. Acad. Sci. U. S. A.* **2011**, *108* (51), 20428–20433. https://doi.org/10.1073/pnas.1012253108.

(15)   Chao, C.; Deng, Y.; Dewil, R.; Baeyens, J.; Fan, X. Post-Combustion Carbon Capture. *Renew. Sustain. Energy Rev.* **2021**, *138*, 110490. https://doi.org/10.1016/J.RSER.2020.110490.

(16)   Raza, A.; Gholami, R.; Rezaee, R.; Rasouli, V.; Rabiei, M. Significant Aspects of Carbon Capture and Storage – A Review. *Petroleum* **2019**, *5* (4), 335–340. https://doi.org/10.1016/J.PETLM.2018.12.007.

(17)   Wang, X.; Song, C. Carbon Capture From Flue Gas and the Atmosphere: A Perspective. *Front. Energy Res.* **2020**, *8* (December 2019). https://doi.org/10.3389/fenrg.2020.560849.

(18)   Yu, C. H.; Huang, C. H.; Tan, C. S. A Review of CO2 Capture by Absorption and Adsorption. *Aerosol Air Qual. Res.* **2012**, *12* (5), 745–769. https://doi.org/10.4209/AAQR.2012.05.0132.

(19)   House, K. Z.; Harvey, C. F.; Aziz, M. J.; Schrag, D. P. The Energy Penalty of Post-Combustion CO 2 Capture & Storage and Its Implications for Retrofitting the U.S. Installed Base. https://doi.org/10.1039/b811608c.

(20)   Abu-Zahra, M. R. M.; Schneiders, L. H. J.; Niederer, J. P. M.; Feron, P. H. M.; Versteeg, G. F. CO2 Capture from Power Plants: Part I. A Parametric Study of the Technical Performance Based on Monoethanolamine. *Int. J. Greenh. Gas Control* **2007**, *1* (1), 37–46. https://doi.org/10.1016/S1750-5836(06)00007-7.

(21)   Goto, K.; Kodama, S.; Okabe, H.; Fujioka, Y. Energy Performance of New Amine-Based Solvents for CO 2 Capture from Blast Furnace Gas. **2012**.

(22)   Singh, A.; Stéphenne, K. Shell Cansolv CO2 Capture Technology: Achievement from First Commercial Plant. *Energy Procedia* **2014**, *63*, 1678–1685. https://doi.org/10.1016/J.EGYPRO.2014.11.177.

(23)   Yulia, F.; Sofianita, R.; Prayogo, K.; Nasruddin, N. Optimization of Post Combustion CO2 Absorption System Monoethanolamine (MEA) Based for 320 MW Coal-Fired Power Plant Application – Exergy and Exergoenvironmental Analysis. *Case Stud. Therm. Eng.* **2021**, *26*, 101093. https://doi.org/10.1016/J.CSITE.2021.101093.

(24)   Rochelle, G.; Chen, E.; Freeman, S.; Van Wagener, D.; Xu, Q.; Voice, A. Aqueous Piperazine as the New Standard for CO2 Capture Technology. *Chem. Eng. J.* **2011**, *171* (3),

725–733. https://doi.org/10.1016/j.cej.2011.02.011.

(25)   Boot-Handford, M. E.; Abanades, J. C.; Anthony, E. J.; Blunt, M. J.; Brandani, S.; Mac Dowell, N.; Fernández, J. R.; Ferrari, M. C.; Gross, R.; Hallett, J. P.; et al. Carbon Capture and Storage Update. *Energy Environ. Sci.* **2013**, *7* (1), 130–189. https://doi.org/10.1039/C3EE42350F.

(26)   Rochelle, G. T. Amine Scrubbing for CO2 Capture. *Science (80-.).* **2009**, *325* (5948), 1652–1654. https://doi.org/10.1126/science.1176731.

(27)   Wilcox, J. *Carbon Capture*; Springer New York, 2012. https://doi.org/10.1007/978-1-4614-2215-0.

(28)   Mirza, N.; Kearns, D. *State of the Art: CCS Tchnologies 2022*; 2022.

(29)   Baylin-Stern, A.; Berghout, N. Is carbon capture too expensive? – Analysis https://www.iea.org/commentaries/is-carbon-capture-too-expensive (accessed Feb 21, 2023).

(30)   Fasihi, M.; Efimova, O.; Breyer, C. Techno-Economic Assessment of CO2 Direct Air Capture Plants. *J. Clean. Prod.* **2019**, *224*, 957–980. https://doi.org/10.1016/J.JCLEPRO.2019.03.086.

(31)   Mcqueen, N.; Psarras, P.; Ne, H.; Pilorgé, P.; Liguori, S.; He, J.; Yuan, M.; Woodall, C. M.; Kian, K.; Pierpoint, L.; et al. Cost Analysis of Direct Air Capture and Sequestration Coupled to Low-Carbon Thermal Energy in the United States. *Cite This Environ. Sci. Technol* **2020**, *54*, 7551. https://doi.org/10.1021/acs.est.0c00476.

(32)   Lackner, K. S.; Azarabadi, H. Buying down the Cost of Direct Air Capture. *Ind. Eng. Chem. Res.* **2021**, *60* (22), 8196–8208. https://doi.org/10.1021/ACS.IECR.0C04839.

(33)   Page, B.; Turan, G.; Zapantis, A.; Beck, L.; Consoli, C.; Havercroft, I.; Liu, H.; Loria, P.;

Schneider, A.; Tamme, E.; et al. *Global Status of CCS Report: 2019*; 2019.

(34)   Lackner, K. S. The Thermodynamics of Direct Air Capture of Carbon Dioxide. *Energy* **2013**, *50* (1), 38–46. https://doi.org/10.1016/j.energy.2012.09.012.

(35)   Stern, M. C.; Simeon, F.; Herzog, H.; Hatton, T. A. Post-Combustion Carbon Dioxide Capture Using Electrochemically Mediated Amine Regeneration. *Energy Environ. Sci.* **2013**, *6*, 2505. https://doi.org/10.1039/c3ee41165f.

(36)   Stern, M. C.; Simeon, F.; Hammer, T.; Landes, H.; Herzog, H. J.; Hatton, T. A. Electrochemically Mediated Separation for Carbon Capture. *Energy Procedia* **2011**, *4*, 860–867. https://doi.org/10.1016/j.egypro.2011.01.130.

(37)   Shaw, R. A.; Hatton, T. A. Electrochemical CO2 Capture Thermodynamics. *Int. J. Greenh. Gas Control* **2020**, *95* (June 2019), 102878. https://doi.org/10.1016/j.ijggc.2019.102878.

(38)   Rheinhardt, J. H.; Singh, P.; Tarakeshwar, P.; Buttry, D. A. Electrochemical Capture and Release of Carbon Dioxide. *ACS Energy Lett.* **2017**, *2* (2), 454–461. https://doi.org/10.1021/acsenergylett.6b00608.

(39)   Barlow, J. M.; Clarke, L. E.; Zhang, Z.; Bím, D.; Ripley, K. M.; Zito, A.; Brushett, F. R.; Alexandrova, A. N.; Yang, J. Y. Molecular Design of Redox Carriers for Electrochemical CO2 Capture and Concentration. *Chem. Soc. Rev.* **2022**, *51* (20), 8415–8433. https://doi.org/10.1039/D2CS00367H.

(40)   Bell, W. L.; Miedaner, A.; Smart, J. C.; DuBois, D. L. Synthesis and Evaluation of Electroactive CO2 Carriers. *SAE Technical Paper Series*. 1988, pp 1–10. https://doi.org/10.4271/881078.

(41)   Dubois, D. L.; Miedaner, A.; Bell, W.; Smart, J. C. Electrochemical Concentration of Carbon Dioxide. In *Electrochemical and Electrocatalytic Reactions of Carbon Dioxide*;

Sullivan, B. R., Ed.; Elsevier: Amsterdam, 1993; pp 94–117.

(42)   Koval, C.; Poshusta, J.; Scovazzo, P.; Noble, R.; DuBois, D. Electrochemical Separation and Concentration of <1% Carbon Dioxide from Nitrogen. *J. Electrochem. Soc.* **2003**, *150* (5), D91–D98. https://doi.org/10.1149/1.1566962.

(43)   Clarke, L. E.; Leonard, M. E.; Hatton, T. A.; Brushett, F. R. Thermodynamic Modeling of CO2 Separation Systems with Soluble, Redox-Active Capture Species. *Ind. Eng. Chem. Res.* **2022**, *61* (29), 10531–10546. https://doi.org/10.1021/acs.iecr.1c04185.

(44)   Wang, M.; Hatton, T. A. Flue Gas CO2 Capture via Electrochemically Mediated Amine Regeneration: Desorption Unit Design and Analysis. *Ind. Eng. Chem. Res* **2020**, *59*, 10120–10129. https://doi.org/10.1021/acs.iecr.0c00790.

(45)   Guido, C. A.; Pietrucci, F.; Gallet, G. A.; Andreoni, W. The Fate of a Zwitterion in Water from Ab Initio Molecular Dynamics: Monoethanolamine (MEA)-CO2. *J. Chem. Theory Comput.* **2013**, *9* (1), 28–32. https://doi.org/10.1021/CT301071B/.

(46)   Ma, C.; Pietrucci, F.; Andreoni, W. Capture and Release of CO2 in Monoethanolamine Aqueous Solutions: New Insights from First-Principles Reaction Dynamics. *J. Chem. Theory Comput.* **2015**, *11* (7), 3189–3198. https://doi.org/10.1021/acs.jctc.5b00379.

(47)   Mizen, M. B.; Wrighton, M. S. Reductive Addition of CO2 to 9,10-Phenanthrenequinone. *J. Electrochem. Soc.* **1989**, *136* (4), 941. https://doi.org/10.1149/1.2096891.

(48)   Nagaoka, T.; Nishii, N.; Fujii, K.; Ogura, K. Mechanisms of Reductive Addition of CO2 to Quinones in Acetonitrile. *J. Electroanal. Chem.* **1992**, *322* (1–2), 383–389. https://doi.org/10.1016/0022-0728(92)80090-Q.

(49)   Qiao, X.; Li, D.; Cheng, L.; Jin, B. Mechanism of Electrochemical Capture of CO2 via Redox Cycle of Chlorinated 1,4-Naphthoquinone in BMIMBF4: An in-Situ FT-IR

Spectroelectrochemical Approach. *J. Electroanal. Chem.* **2019**, *845*, 126–136. https://doi.org/10.1016/j.jelechem.2019.05.057.

(50) Schmidt, M. H.; Miskelly, G. M.; Lewis, N. S. Effects of Redox Potential, Steric Configuration, Solvent, and Alkali Metal Cations on the Binding of Carbon Dioxide to Cobalt(I) and Nickel(I) Macrocycles. *J. Am. Chem. Soc.* **1990**, *112* (9), 3420–3426. https://doi.org/10.1021/ja00165a027.

(51) Appel, A. M.; Newell, R.; DuBois, D. L.; Rakowski DuBois, M. Concentration of Carbon Dioxide by Electrochemically Modulated Complexation with a Binuclear Copper Complex. *Inorg. Chem.* **2005**, *44* (9), 3046–3056. https://doi.org/10.1021/ic050023k.

(52) Ishida, H.; Ohba, T.; Yamaguchi, T.; Ohkubo, K. Interaction between CO_2 and Electrochemically Reduced Species of N-Propyl-4,4′-Bipyridinium Cation. *Chem. Lett.* **1994**, *23* (5), 905–908. https://doi.org/10.1246/cl.1994.905.

(53) Singh, P.; Tarakeshwar, P.; Buttry, D. A. Experimental, Simulation, and Computational Study of the Interaction of Reduced Forms of N-Methyl-4,4'-Bipyridinium with CO2. *ChemElectroChem* **2020**, *7* (2), 469–475. https://doi.org/10.1002/CELC.201901884.

(54) Ranjan, R.; Olson, J.; Singh, P.; Lorance, E. D.; Buttry, D. A.; Gould, I. R. Reversible Electrochemical Trapping of Carbon Dioxide Using 4,4′-Bipyridine That Does Not Require Thermal Activation. *J. Phys. Chem. Lett.* **2015**, *6* (24), 4943–4946. https://doi.org/10.1021/acs.jpclett.5b02220.

(55) Singh, P.; Rheinhardt, J. H.; Olson, J. Z.; Tarakeshwar, P.; Mujica, V.; Buttry, D. A. Electrochemical Capture and Release of Carbon Dioxide Using a Disulfide-Thiocarbonate Redox Cycle. *J. Am. Chem. Soc.* **2017**, *139* (3), 1033–1036. https://doi.org/10.1021/jacs.6b10806.

(56) Namazian, M.; Zare, H. R.; Yousofian-Varzaneh, H. Electrochemical Behavior of Tetrafluoro-p-Benzoquinone at the Presence of Carbon Dioxide: Experimental and Theoretical Studies. *Electrochim. Acta* **2016**, *196*, 692–698. https://doi.org/10.1016/J.ELECTACTA.2016.02.159.

(57) Comeau Simpson, T.; Durand, R. R. Reactivity of Carbon Dioxide with Quinones. *Electrochim. Acta* **1990**, *35* (9), 1399–1403. https://doi.org/10.1016/0013-4686(90)85012-C.

(58) Gupta, N.; Linschitz, H. Hydrogen-Bonding and Protonation Effects in Electrochemistry of Quinones in Aprotic Solvents. *J. Am. Chem. Soc.* **1997**, *119* (27), 6384–6391. https://doi.org/10.1021/JA970028J.

(59) De Sousa Bulhõesw, L. O.; Zara, A. J. The Effect of Carbon Dioxide on the Electroreduction of 1,4-Benzoquinone. *J. Electroanal. Chem. Interfacial Electrochem.* **1988**, *248* (1), 159–165. https://doi.org/10.1016/0022-0728(88)85158-1.

(60) Schimanofsky, C.; Wielend, D.; Kröll, S.; Lerch, S.; Werner, D.; M. Gallmetzer, J.; Mayr, F.; Neugebauer, H.; Irimia-Vladu, M.; Portenkirchner, E.; et al. Direct Electrochemical CO2 Capture Using Substituted Anthraquinones in Homogeneous Solutions: A Joint Experimental and Theoretical Study. *J. Phys. Chem. C* **2022**, *126* (33), 14138–14154. https://doi.org/10.1021/acs.jpcc.2c03129.

(61) Connelly, N. G.; Geiger, W. E. Chemical Redox Agents for Organometallic Chemistry. *Chem. Rev.* **1996**, *96* (2), 877–910. https://doi.org/10.1021/cr940053x.

(62) Barlow, J. M.; Yang, J. Y. Oxygen Stable Electrochemical CO2 Capture and Concentration with Quinones through Alcohol Additives. *J. Am. Chem. Soc.* **2022**, *144* (31), 14161–14169.

(63) Bui, A. T.; Hartley, N. A.; Thom, A. J. W.; Forse, A. C. Trade-Off between Redox Potential

and the Strength of Electrochemical CO2 Capture in Quinones. *J. Phys. Chem. C* **2022**, *126* (33), 14163–14172. https://doi.org/10.1021/ACS.JPCC.2C03752.

(64)   Alherz, A. W.; Petersen, H. A.; Singstock, N. R.; Sur, S. N.; Musgrave, C. B.; Luca, O. R. Predictive Energetic Tuning of Quinoid O-Nucleophiles for the Electrochemical Capture of Carbon Dioxide. *Energy Adv.* **2022**, *1* (11), 900–907. https://doi.org/10.1039/D2YA00114D.

(65)   Petersen, H. A.; Alherz, A. W.; Stinson, T. A.; Huntzinger, C. G.; Musgrave, C. B.; Luca, O. R. Predictive Energetic Tuning of C-Nucleophiles for the Electrochemical Capture of Carbon Dioxide. *iScience* **2022**, *25* (4), 103997. https://doi.org/10.1016/J.ISCI.2022.103997.

(66)   Zanello, P. *Inorganic Electrochemistry*; Royal Society of Chemistry: Cambridge, 2003. https://doi.org/10.1039/9781847551146.

(67)   Fan, H.; Cheng, L.; Jin, B. Investigation on Electrochemical Capture of CO2 in P-Benzoquinone Solutions by in Situ FT-IR Spectroelectrochemistry. *Electrochim. Acta* **2019**, *324*, 134882. https://doi.org/10.1016/j.electacta.2019.134882.

(68)   Kajiwara, T.; Yamaguchi, T.; Kido, H.; Kawabata, S.; Kuroda, R.; Ito, T. A Dinucleating Bis(Dimethylcyclam) Ligand and Its Dinickel(II) and Dizinc(II) Complexes with the Face-to-Face Ring Arrangement. *Inorg. Chem.* **1993**, *32* (23), 4990–4991. https://doi.org/10.1021/IC00075A003.

(69)   Murase, I.; Vučkovic, G.; Kodera, M.; Harada, H.; Matsumoto, N.; Kida, S. Synthesis and Characterization of Copper(II), Nickel(II), and Cobalt(II) Binuclear Complexes with a New Tricyclic Octadentate Ligand, 1,5,8,12,15,19,22,26-Octaazatricyclo[17.9.2.25,5]Dotriacontane (Tcoa): Trapping of CO2 in a Neutral Aqueous

Solution. *Inorg. Chem.* **1991**, *30* (4), 728–733. https://doi.org/10.1021/IC00004A024.

(70) Harada, H.; Kodera, M.; Vučković, G.; Matsumoto, N.; Kida, S. Preparation and Redox
Chemistry of Novel Carbonato-Bridged Cobalt(II) Complexes with 1,4,8,11 -Tetrakis (2-
Aminoethyl)-1,4,8,11 -Tetraazacyclotetradecane and 1,4,8,11-Tetrakis(Pyridylmethyl)-
1,4,8,11-Tetraazacyclotetradecane. *Inorg. Chem.* **1991**, *30* (6), 1190–1194.
https://doi.org/10.1021/IC00006A007.

(71) Newell, R.; Appel, A.; DuBois, D. L.; DuBois, M. R. Studies of Bicarbonate Binding by
Dinuclear and Mononuclear Ni(II) Complexes. *Inorg. Chem.* **2005**, *44* (2), 365–373.
https://doi.org/10.1021/IC049202C.

(72) Gangi, D. A.; Durand, R. R. Binding of Carbon Dioxide to Cobalt and Nickel Tetra-Aza
Macrocycles. *J. Chem. Soc., Chem Commun.* **1986**, 697–699.
https://doi.org/10.1039/C39860000697.

(73) Bard, A. J.; Faulkner, L. R. *Electrochemical Methods: Fundamentals and Applications*, 2nd
ed.; Wiley, 2001.

(74) Creutz, C. Carbon Dioxide Binding To Transition-Metal Centers. In *Electrochemical and
Electrocatalytic Reactions of Carbon Dioxide*; Sullivan, B. R., Ed.; Elsevier: Amsterdam,
1993; pp 19–67. https://doi.org/10.1016/B978-0-444-88316-2.50006-1.

(75) Creutz, C.; Schwarz, H. A.; Wishart, J. F.; Fujita, E.; Sutin, N. Thermodynamics and
Kinetics of Carbon Dioxide Binding to Two Stereoisomers of a Cobalt(I) Macrocycle in
Aqueous Solution. *J. Am. Chem. Soc.* **2002**, *113* (9), 3361–3371.
https://doi.org/10.1021/JA00009A022.

(76) Benesi, H. A.; Hildebrand, J. H. A Spectrophotometric Investigation of the Interaction of
Iodine with Aromatic Hydrocarbons. *J. Am. Chem. Soc.* **1949**, *71* (8), 2703–2707.

https://doi.org/10.1021/JA01176A030.

Chapter 2

Computational and Experimental Design of Quinones for Electrochemical CO₂ Capture and Concentration

2.1 Introduction

Many of the redox carriers that have been examined for electrochemical CO_2 capture and concentration are either not air-stable or lack a sufficient binding affinity to capture CO_2 from dilute streams, such as flue gas (~10-15% CO_2), or the atmosphere (0.04%).[4,7–14] The electrochemical concentration of CO_2 with 90% capture efficiency would require a redox carrier binding constant of ~10^4 M^{-1} from flue gas and ~10^6 M^{-1} from air.[15,16] Additionally, for CO_2 release, the ideal carrier should exhibit a negligible binding constant in its inactive redox state (**Scheme 2.1A**). The air instability of the redox carriers for electrochemical CO_2 capture and concentration systems originates from the presence of molecular oxygen in the air, which is reduced to superoxide ($O_2^{\bullet-}$) at ~ -1.2 V vs. ferrocene in organic solvents. This electron transfer reaction to form superoxide is an unfavorable side reaction at reduced redox carriers if their reduction potential is negative of the $O_2/O_2^{\bullet-}$ couple (**Scheme 2.1B**). Dioxygen reactivity not only reduces the efficiency of the process by removing electron equivalents, lowering the Faradaic yield, but the redox carrier can also undergo further deleterious reactivity with superoxide.[17,18] Therefore, the second requirement for a capture agent the reduction potential ($E_{1/2}$) to activate it is positive of -1.2 V.

Unfortunately, redox carriers investigated thus far do not meet these requirements. The most extensively studied class of redox carriers are quinones. Quinones lack binding affinity to CO_2 in their neutral state and enhanced affinity towards CO_2 upon two-electron and, in some cases, one-electron reduction (**Scheme 2.1A**). However, previously measured CO_2 binding affinities of quinones display a linear relationship between the logarithm of the binding constant ($\log(K_{CO_2})$) and the reduction potential of dianion formation ($E_{1/2}$) (**Scheme 2.1C**),[7] suggesting that the "Goldilocks" quinone (one that has both a desirable $E_{1/2}$ and K_{CO_2}) might not exist.

In order to determine how the steric and electronic effects of substituents influence these two key redox carrier properties, $\log(K_{CO_2})$ and the reduction potential ($E_{1/2}$), quantum-chemical calculations were used. The computational model was benchmarked on prior experimental data to identify the molecular orbitals that are most closely tied to these properties. A computational screen of over 60,000 quinone derivatives determined quinone candidates that were most likely to have favorable properties for air-stable CO_2 binding. Seven synthetically accessible or commercially available quinones were selected and examined experimentally. Within these compounds, the properties did not improve substantially over the previously observed linear relationship between $\log(K_{CO_2})$ and reduction potential.

Scheme 2.1. (**A**.) Electrochemical CO_2 capture and concentration using quinone-based carriers. A quinone in the neutral oxidation state (**Q**) is singly reduced at the cathode to yield quinone radical anion (**Q$_{RA}$**) and singly reduced again to yield quinone dianion (**Q$_{DA}$**) with increased affinity (nucleophilicity) to bind CO_2. The carrier is regenerated by oxidation of **Q$_{DA}$(CO$_2$)** to **Q$_{RA}$(CO$_2$)**, leading to the release and concentration of CO_2 at the anode. (**B**.) To avoid unwanted side-reactions and deactivation of **Q$_{DA}$**, the $E°_{cathodic}$ potential should be positive of the $O_2/O_2^{•-}$ redox couple. (**C**.) Selection of suitable CO_2 capture molecules is limited by the observed linear relationship between $\log(K_{CO_2(DA)})$ and $E°_{cathodic}$.[15] Note that the series of plotted systems also contains the same redox carriers measured in different solvents.

2.2 Results (Sections 2.2.1 – 2.23 were performed by Dr. Daniel Bim)

2.2.1 Computational Studies

The computational methodology (density functional theory; DFT) was first calibrated on

the set of quinones with known $E_{1/2}$ and $\log(K_{CO_2})$ values. Then, we used the computed data to

identify the molecular orbitals (MOs) that are involved in the electron-transfer (reduction) and

CO_2-binding steps for use as the direct descriptors of the quinone molecular properties. The

descriptors are then used in DFT calculations of ~60,000 individual quinone structures to evaluate

the consistency of the trend between $E_{1/2}$ and $\log(K_{CO_2})$ over the extensive range of the redox

carriers, as well as to identify structural/electronic handles for designing quinones with desired

functionalities.

2.2.2 Calibration of DFT for $E_{1/2}$ and K_{CO_2} predictions

We used quantum chemical calculations to predict $E_{1/2}$ and $\log(K_{CO_2})$ of several quinones

with experimentally determined properties (**Table 2.1**). DFT calculations at the PBE0/CPCM

level (see details in the Experimental Section) correlate reasonably well with the experiments. In

detail, the calculated $E_{1/2}$ are systematically shifted by ca. 0.20 V to more positive values, giving

Table 2.1. Reduction potentials and CO_2 binding affinities of quinones previously reported in the literature. All reported data were measured in MeCN.

Compound No.	Compound Name	$E_{1/2}$ [V] (vs. $Fe(C_5H_5)_2^{+/0}$)	$\log(K_{CO_2})$
1	2,6-tBu-*p*-benzoquinone[a]	–1.83 V (–1.56 V)	15 (13)
2	9,10-phenanthraquinone[a]	–1.57 V (–1.66 V)	12 (11)
3	2,3,5,6-tetrafluoro-*p*-benzoquinone[b]	–1.14 V (–1.13 V)	3.8 (6)
4	2,3,5,6-tetrachloro-*p*-benzoquinone[a]	–1.10 V (–1.02 V)	3.7 (4)
5	2,3-dicyano-*p*-benzoquinone[a]	–0.85 V (–0.62 V)	3.7 (0.4)
6	2,3-dichloro-5,6-dicyano-*p*-benzoquinone[a]	–0.63 V (–0.41 V)	0.55 (–2)

Calculated values in parentheses.
[a]from reference 15
[b]from reference 39

the regression line of $E_{1/2}$(calc.) = 1.07 x $E_{1/2}$(expt.) + 0.20 V, and R^2 = 0.92; the log(K_{CO_2}) values

are also predicted with respectable accuracy, with log(K_{CO_2}(calc.)) = 0.97 x log(K_{CO_2}(expt.)) –

0.85, and R^2 = 0.88 (*cf.* **Figure 2.15** for correlations). Both slopes are thus close to unity, while

the shifts are systematic and thus do not affect the results on the relative scale. A moderate

systematic shift of the reduction potentials can be associated either with the inaccurate computed

value of the absolute potential of the reference electrode, $Fe(C_5H_5)_2^{+/0}$, affecting all of the reported

reduction potentials through the relationship in eq. 1; or the scaling of the experimental values to

the absolute potentials, which depend on the experimental setup, surface potential, calibration of

the used electrode, etc. Note that a similar methodology (B3LYP/CPCM) was recently applied to

a broad series of quinones one-electron and proton-coupled electron potentials by Huynh et al.,

also demonstrating an adequate overall performance.[19]

2.2.3 Molecular Orbitals Analysis

We found an excellent correlation between $E_{1/2}$ and HOMO(Q_{DA}) energy (**Figure 2.1A),**

informing the use of HOMO(Q_{DA}) energy as an estimate for the quinone redox properties.

Interestingly, the correlation is significantly worse for log(K_{CO_2}) vs. HOMO(Q_{DA}) energy (**Figure**

2.1B), and instead, the 'in-plane(Q_{DA})' orbital energy correlates much better with log(K_{CO_2})

(**Figure 2.1C**). The result suggests that the in-plane(Q_{DA}) (which is usually the HOMO-1) is

primarily responsible for CO_2 binding, which is consistent with the geometries obtained from the

DFT optimizations of the CO_2-bound structures and analysis of the bonding MOs (see **Scheme**

2.2). In other words, the HOMO(Q_{DA}) serves as electron donor for oxidation, whereas the CO_2

binding involves the electron donation from the in-plane(Q_{DA}) to CO_2. Hence, we propose using

these orbital energies as descriptors of $E_{1/2}$ and log(K_{CO_2}) to avoid the quantum chemical

calculations of the full thermodynamic cycles, which allows us to investigate otherwise unfeasibly

large series of prospective redox carriers. Importantly, the involvement of different MOs suggests that we might isolate the electrochemical (redox) and chemical (CO_2 binding) steps by independently tuning the energy levels of these MOs, to break the unfavorable linear relationship (see detailed discussion in section **2.5.7**). Yet, persistent pronounced correlation between $log(K_{CO_2})$ and the HOMO(Q_{DA}) energy (**Figure 2.1B**) suggests that the energies of the HOMO(Q_{DA}) and the in-plane(Q_{DA}) are not entirely decoupled, and the task of molecular design might be non-trivial.

Figure 2.1. (**A.**) Correlation between the experimental reduction potentials ($E_{1/2}$) and calculated HOMO(Q_{DA}) energies of various quinone dianions. (**B.**) Correlations between the experimental $log(K_{CO_2})$ and calculated HOMO(Q_{DA}) energies. (**C.**) Correlations between the experimental $log(K_{CO_2})$ and calculated in-plane(Q_{DA}) energies. All experimental values can be found in **Table 2.1**.
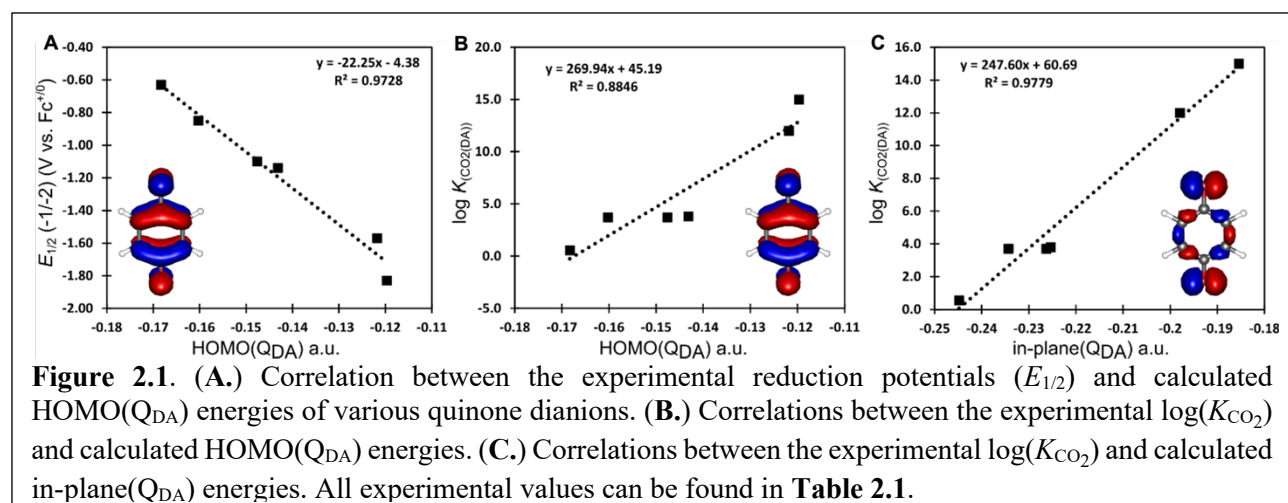
2.2.4 Selection of Quinones for Electrochemical CO_2 Capture

To interpret how the distinct structural perturbations of the *p*-benzoquinone (BQ) scaffold influence the corresponding HOMO(Q_{DA}) and in-plane(Q_{DA}) orbital energies (and thus $E_{1/2}$ and K_{CO_2}), we calculated MO energies of an extensive library of ca. 60,000 substituted BQs (**Scheme 2.3**). In **Figure 2.2A**, the energies of the HOMO(Q_{DA}) and in-plane(Q_{DA}) orbitals are translated into $E_{1/2}$ and $log(K_{CO_2})$ using the regression lines from **Figure 2.1**, and plotted against each other for each compound. Noticeably, an overall linear correlation is observed (i.e., the two orbitals are coupled and simultaneously altered in energy, while the energy gap between them remains essentially constant, indicating the linear relationship between $E_{1/2}$ and $log(K_{CO_2})$ witnessed in the

experiments). Interestingly, it appears the relationship holds over this extensive series of redox carriers. It should be noted that the slope observed in **Figure 2.2A** plot matches reasonably the experimentally observed trend from **Scheme 2.1C**. As discussed in detail in section **2.5.7**, the deviations from the linear trend suggest the correlation could be violated for particular substituent classes, forming the basis for the compounds to be synthesized and tested for improved CO_2 capture in the experimental part of the study (*vide infra*).

The HOMO(Q_{DA}) orbital energies also correlate well with the substituents Hammett σ parameters (**Figure 2.2B**): the electron-withdrawing/electron-donating substituents decrease/increase the energies of the HOMO(Q_{DA}) orbitals and thus increase/decrease the $E_{1/2}$. A good overall correlation suggests that using Hammett σ parameters might represent an intuitive handle for rational design of quinone-based redox carriers.

Figure 2.2. A. A trend between in-plane(Q_{DA}) and HOMO(Q_{DA}) orbital energies (corresponding to log(K_{CO_2}) and $E_{1/2}$) indicates the linear relationship exists over an extended series of quinone reduction potentials; exceeding ~2 V. B. Second reduction potentials ($E_{1/2}$) correlate well with the Hammett substituent σ parameters. Note that Hammett σ parameters were taken unchanged from ref. [19], with the σ_m values for halogen substituents, the σ_p^- values for substituents capable of conjugating with the reaction center, and the σ_p values for all other substituents.

For the experimental evaluation of '$E_{1/2}$ vs. log(K_{CO_2})' trend, we have selected quinones with previously described syntheses and the predicted second reduction potentials that range over ~1.5 V. Furthermore, we have limited the

selection to quinones for which the energy gap between HOMO(Q_{DA}) and in-plane(Q_{DA}) orbitals is lowered as compared to the unsubstituted BQ, which is proposed to favor CO_2 binding for the same $E_{1/2}$ potentials (Section **2.5.7**). Note that such improved CO_2 binding is proposed for the electron-withdrawing substituents, such as -NO_2, -COOR, -CF_3, -CN; sterically-demanding substituents, such as -tBu, -Ph, -OPh, -Bn; and -NMe_2 (note that -NMe_2 strongly donates electrons into the system; however, the steric profile of the alkyl groups prevents the facile overlap of its unshared electron pairs with the HOMO(Q_{DA}) π system, lowering the HOMO(Q_{DA}) vs. in-plane(Q_{DA}) energy gap (see section **2.5.7**)).

2.2.5 Experimental Evaluation of the Electrochemical CO_2 Capture

To evaluate the theoretical model and to broaden the scope of the experimentally-derived CO_2 binding affinities, seven quinones with largely varied $E_{1/2}$ values were selected, synthesized, and characterized (**Table 2.2**). All quinones were synthesized in the neutral benzoquinone form. To avoid possible photochemical decomposition pathways, all quinones were made and stored

Figure 2.3. Correlation between experimentally measured $E_{1/2}$ and Hammett σ parameters. Points highlighted in black are quinones that were previously studied (**Table 2.1**) and points in red are values from this work (**Table 2.2**). Note that Hammett σ parameters were taken unchanged from ref. [19].
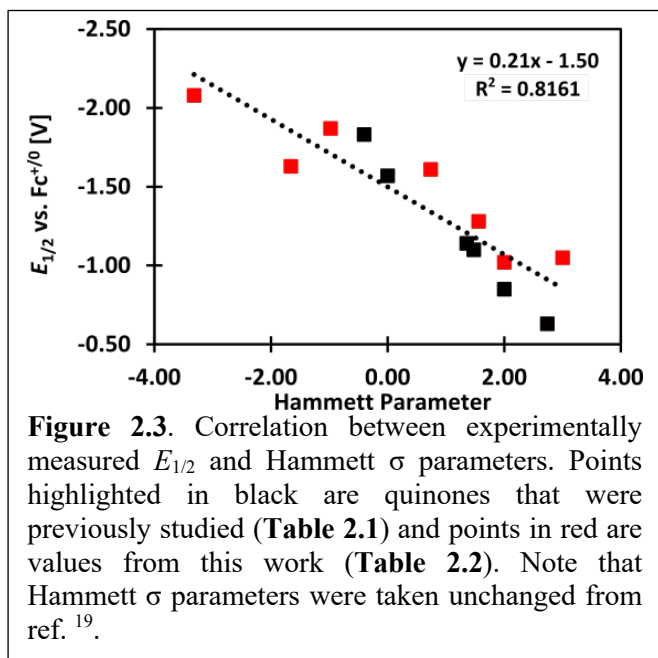
in the dark. These quinones were probed in detail using electrochemical techniques to gain insight about the correlation between their reduction potentials and CO_2 binding affinities. Notably, the experimental reduction potentials for the quinones previously published and studied here correlate with the Hammett substituent σ parameters in **Figure 2.3**. The regression line ($E_{1/2}$ = 0.21 x

"Hammett σ parameter" – 1.50 V) is in an excellent agreement with the one obtained from the large-scale theoretical calculations ($E_{1/2}$ = 0.22 x "Hammett σ parameter" – 1.67 V).

2.2.6 Determination of Experimental CO_2 Binding Constant Using Cyclic Voltammetry

In this study, CO_2 binding affinity was determined electrochemically. For compounds **7-10** (**Table 2.2**), the K_{CO_2} was determined using cyclic voltammetry (CV). In the CVs, addition of CO_2 does not impact the first reduction to the semiquinone. However, the second reductive peak (**Figure 2.4**) to form the dianion shifts anodically, indicating the species reacts with CO_2 in a chemical step. These voltametric data indicate an EEC mechanism (electron transfer, electron transfer, chemical reaction). The shift of the half-wave potential ($\Delta E_{1/2}$) to form the dianion between a N_2 and CO_2 atmosphere and the concentration of ($[CO_2]$) was used to find the binding constant, K_{CO_2}, using relationships derived from the Nernst equation and equilibrium constant (eqns. 2.1-2.2):

$$Q_{DA} + CO_2 \overset{K_{CO2}}{\rightleftharpoons} Q_{DA}CO_2 \tag{2.1}$$

$$\Delta E_{1/2} = \frac{0.0592}{n}\log(K_{CO2}) + q\frac{0.0592}{n}\log[CO_2] \tag{2.2}$$

where *n* refers to the number of electrons involved in the reduction or oxidation and *q* is the number of CO_2 molecules bound to the reduced quinone dianion, Q_{DA}.

Figure 2.4. Cyclic voltammetry of dicyano-*p*-naphthoquinone (**7**) under an atmosphere of dinitrogen (black solid trace) and carbon dioxide (red dashed trace). The potential for each voltammogram is referenced to ferrocene.
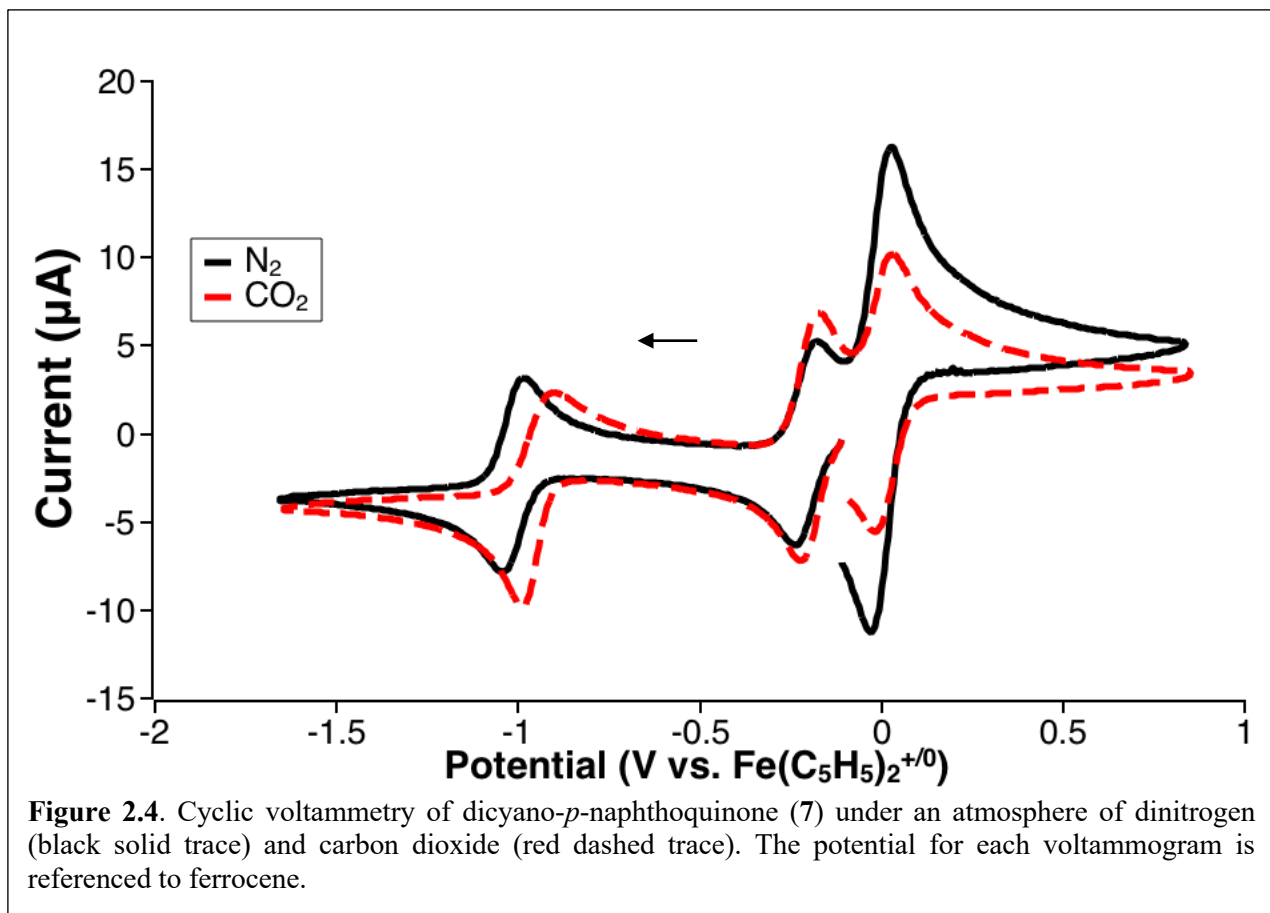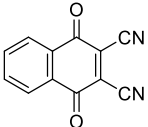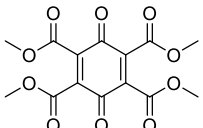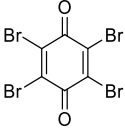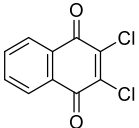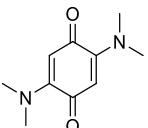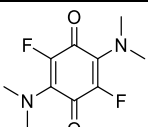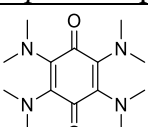
2.2.7 Determination of Experimental CO_2 Binding Constant Using Open Circuit Potential

For compounds **11-13**, another form of measuring K_{CO_2} was necessary due to the absence of a second reductive peak in the presence of CO_2 (**Figure S4**). This voltametric behavior has been reported previously by Mizen and Wrighton, and it is believed to be indicative of an ECEC binding mechanism (electron transfer, chemical reaction, electron transfer, chemical reaction).[12] Upon reduction of the neutral quinone to the radical anion, it binds a CO_2 molecule (eqns. 2.3-2.4). Further reduction of the CO_2-bound radical anion to the dianion results in the binding of another CO_2 molecule (eqns. 2.5-2.6).

$$Q + e^- \rightleftharpoons Q^{\cdot-} \tag{2.3}$$

$$Q^{\cdot-} + CO_2 \rightleftharpoons Q(CO_2)^{\cdot-} \tag{2.4}$$

$$Q(CO_2)^{\cdot-} + e^- \rightleftharpoons Q(CO_2)^{2-} \tag{2.5}$$

$$Q(CO_2)^{2-} + CO_2 \rightleftharpoons Q(CO_2)_2^{2-} \tag{2.6}$$
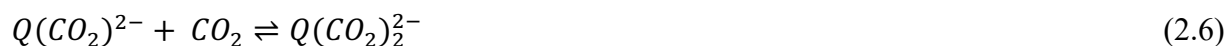
In such cases, the K_{CO_2} values were measured by forming a 1:1 solution of the radical anion and dianion species through controlled potential electrolysis. The change in the open circuit potential (OCP) of the solution with varying concentrations of CO_2 was plotted versus $\log[CO_2]$ (Figures **2.10-2.13**). From this plot, the y-intercept can be used to calculate K_{CO_2}, based on eq. 2. The slope of the line can be used to derive the q value, which is the number of CO_2 molecules bound to the quinone. The n term is representative of the number of electrons.

Table 2.2. Reduction potentials and CO_2 binding affinities of quinones synthesized and studied in this work.

Compound No.	Compound	$E_{1/2}$ [V] (vs. $Fe(C_5H_5)_2^{+/0}$)	$\log(K_{CO_2})$	Solvent
7	2,3-dicyano-*p*-naphthoquinone	-1.02	1.7	MeCN
8	Tetramethylester-*p*-benzoquinone	-1.05	2.5	Chloroform
9	Tetrabromo-*p*-benzoquinone	-1.28	3.3	DMF
10	2,3-dichloro-*p*-naphthoquinone	-1.61	5.7	DMF
11	2,5-bis(dimethylamino)-*p*-benzoquinone	-1.63	$12.1 \pm 0.6^{\dagger}$	MeCN
12	2,5-bis(dimethylamino)-3,6-difluoro-*p*-benzoquinone	-1.87	$4.82 \pm 0.1^{\dagger}$	DMF
13	Tetra(dimethylamino)-*p*-benzoquinone	-2.08	$11.6 \pm 0.8^{\dagger}$	MeCN

*binding constants measured using cyclic voltammetry, †binding constants measured using open circuit potential

2.2.8 Comparison of Solvent Effects

Chloroform was used as a solvent for tetramethylester-*p*-benzoquinone (**8**) due to its insolubility in MeCN or DMF. To examine how the solvent selection might affect K_{CO2} values, the CO_2 binding to tetrabromo-*p*-benzoquinone (**9**) and 2,3-dichloro-*p*-naphthoquinone (**10**) were measured in DMF, MeCN, and dimethylsulfoxide (DMSO). The binding affinity was similar in these solvents (**Tables 2.3** and **2.4**). However, the reduction potential differed more than expected. For 2,3-dichloro-*p*-naphthoquinone (**10**), there was a 100 mV difference in reduction potential between DMF and MeCN, despite their nearly identical dielectric constants, indicating other properties, such as solvent donor strength, may be important to stabilizing the reduced quinone dianions.

Table 2.3. A comparison of reduction potentials and CO_2 binding affinities for 2,3-dichloro-*p*-naphthoquinone (**10**). All values found using cyclic voltammetry with 1 mM analyte and 0.1 M TBAPF$_6$ electrolyte.

Solvent	$E_{1/2}$ [V] (vs. Fe(C$_5$H$_5$)$_2^{+/0}$)	$\log(K_{CO2})$
DMSO	-1.50	5.5 ± 0.9
MeCN	-1.51	5.3 ± 0.6
DMF	-1.61	5.7 ± 0.8

2.3 Discussion

By combining the theory and experiment in the previous sections, we have attempted to review the existence of the proposed linear relationship between $E_{1/2}$ and $\log(K_{CO2})$ of the quinone redox carriers. Our goal was to break the relationship in order to find quinone-based systems capable of capturing CO_2 in the presence of oxygen. Using a set of both theoretical (~60,000 calculated species) and experimental (7 newly introduced quinones) data, we have demonstrated the trend holds relatively well over the large set of quinones. (**Figure 2.5**).
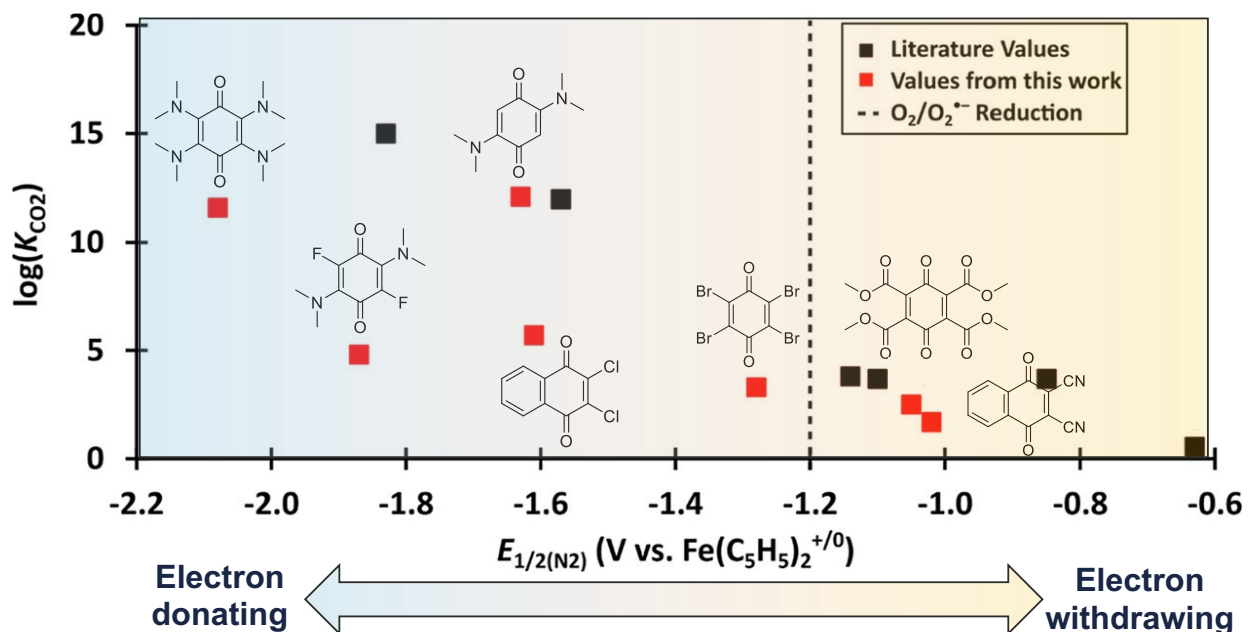
Figure 2.5. A summary of the relationship between the CO_2 binding affinity and the reduction potential to form the dianion, combining values from **Tables 2.1** (previously reported values, black points) and **2.2** (values from this work, red points).

Based on the theoretical predictions, we suggest that the redox and CO_2-binding steps could be separated by tuning the MOs of different quinones through variation of steric and electronic effects. Specifically, the reduction potentials were observed to correlate well with the energy of the HOMO(Q_{DA}) orbital in the substituted *p*-BQs, while the log(K_{CO_2}) values correlate better with the energy of the in-plane(Q_{DA}) orbital. All of the synthesized quinones followed this theoretical concept, however, we have not observed any improvement over the expected $E_{1/2}$ vs. log(K_{CO_2}) trend. In fact, we observed some deviations from the trend toward the lower CO_2 binding. The deviations may be due to steric hindrance of CO_2 binding due to large functional groups in the 2,5 positions. Based on the otherwise steady linear correlation in **Figure 2.5**, it appears that overcoming the trend toward the more positive CO_2 binding would be particularly difficult. Also, several quinones that were computationally predicted to improve the CO_2 binding were synthetically inaccessible, such as the nitro-substituted benzoquinones.

Several drawbacks of the theoretical modeling which complicate the design of CO_2 redox carriers should also be mentioned. Firstly, the reduction of quinone leads to a negative charge buildup at the quinone oxygen atoms, which requires significant solvent reorganization, and likely involves direct participation of the solvent. These solvent effects are probably *not* accurately described *via* a simple continuum-based solvation model. It is impossible to distinguish some organic solvents in our model, such as the MeCN and DMF used in the experiments, since their dielectric constants are similar ($\varepsilon = 36$ vs. $\varepsilon = 37$), although their redox potentials vary by ~100 mV (**Table 2.3**).[20] We also do not account for different experimental ionic strength, supporting electrolyte, quinone/CO_2 concentrations, etc.

Furthermore, in the simplified (large-scale) model, the reduction potentials and CO_2-binding constants are approximated by only a single value of the energy of the HOMO or in-plane orbitals of the quinone dianion. This approach can be hampered by the conformational flexibility of the studied quinones, which could break orbital symmetry and allow orbital mixing upon CO_2 binding, thereby disqualifying a single orbital as a uniformly reliable descriptor. The optimized structures from the large-scale modeling might not always represent the global energetic minimum for each compound. In the full thermodynamic cycle, such inconsistencies would likely cancel out from subtracting ΔG of radical anion and dianion species. In this study, we have selected only one geometry for each substituted BQ structure from the GFN2-xTB optimization, as the subsequent DFT optimization of more conformers would become prohibitively expensive. Optimistically, the errors from such simplification might be less pronounced in comparing the energy difference of HOMO(Q_{DA}) and in-plane (Q_{DA}) between *p*-BQ and different substituted quinones, rather than evaluating the absolute energies. Lastly, the positively charged ($-N(CH_3)_3^+$ and $-CH_2N(CH_3)_3^+$) substituents often lead to decomposition from the BQ scaffold at GFN2-xTB, and we thus

excluded such substituents from the analysis. All of these deficiencies might be responsible for an inadequate matching between the theory-estimated and measured properties for some quinones.

There may be shortcomings between the mapping of Hammett parameters to the prediction of $E_{1/2}$ values and thus the prioritization of groups for synthesis. To probe this more, we leveraged our large dataset to understand how trends might vary nonlinearly and cumulatively in further substituted quinones. We trained a random algorithm on the energy gap between the HOMO(Q_{DA}) and the in-plane (Q_{DA}) orbitals, using a one-hot encoded vector of the functional groups as an input. Using this trained regressor we performed permutation feature importance to determine which groups were more influential in determining the target energy gap. Spearman correlation between the count of each group in a given quinone and the gap energy (as opposed to the previously used Pearson correlation which strictly measures linear relationships between variables) was also used to understand the nonlinear relationship between these two variables.[21] These coupled techniques give a sense of importance and directionality to the count of each substituent and could explain the results from experiment. They showed that some substituents not included in the synthesized quinones (-CF$_3$, -OH, -C(CH$_3$)$_3$) were more important in closing the orbital energy gap and improving CO_2 binding performance. Quinones with these substituents could be candidates for future study. Additionally, the effects of halogenated substituents (-Br, -Cl) and nitrile groups may have not been as pronounced in shifting the energy gap, but their reduction potentials are close to the dioxygen reduction, so through electrolyte engineering, they may be useful for capture of CO_2 in the presence of O_2.

From the experimental perspective, quinones can be extremely sensitive to water, air, and light. The experimental determination of K_{CO_2} is particularly challenging using the OCP method as the fully reduced dianions are more sensitive to decomposition, although we take rigorous

precaution to exclude water, air, and light when working with the dianion form. K_{CO_2} values determined using cyclic voltammetry are more likely to be accurate because they do not depend on isolation of the sensitive dianion.

2.4 Conclusion

Although we have focused on quinone-based carriers in this work, the outcomes might not be limited to this class of compounds. Similar relationships between $E_{1/2}$ and $\log(K_{CO_2})$ values have been observed for other systems, such as metal-based complexes that reversibly bind to CO_2.[22] In these complexes, a neutral CO_2 molecule can reversibly bind to a metal cation, forming a new σ bond between the metal and electrophilic carbon of CO_2. Analogous to quinones, the metal-carboxylate adduct stability parallels the Brønsted basicities of relative metal ions as a measure of the metal half-wave reduction potentials. However, since the redox and binding processes take place at the same site in the metal complexes, the possibility of disrupting the $E_{1/2}$ and $\log(K_{CO_2})$ trend appears to be even more problematic. Notably, it was suggested that in the tetramethylcyclam (TMC)-based metal complexes, the hydrogen-bonding interactions between the amine hydrogens in the *d,l*-configuration of TMC and the CO_2 molecule might improve the CO_2 adduct stabilization, outlining a new avenue in designing viable electrochemical carbon capture carriers. A similar approach was documented in a recent application utilizing intermolecular hydrogen bonding to increase CO_2 binding by introducing protic solvents in conjunction with quinones carriers.[16]

While manipulation of the HOMO/in-plane orbitals gap did not improve the target properties, we have demonstrated the tunability of the electrochemical properties through substituents effects. To break the linear relationship, however, it appears that further work is

required. We speculate that stabilization of the CO_2 adducts via secondary interactions from the second sphere – either intermolecular through the interaction with solvent molecules, or intramolecular by attaching the substituents with the auxiliary binding groups – represents a potential approach that we are currently pursuing. In addition, the further statistical study of functional groups using generative models could see the inclusion of more groups in the space of computationally-explored molecules for screening.

2.5 Experimental and Computational Procedures

2.5.1 General Methods

Bromanil (**9**) and 2,3-dichloro-*p*-naphthoquinone (**10**) were purchased and used without further purification. Compounds 2,3-dicyano-1,4-naphthoquinone (**7**),[23,24] tetramethylester-*p*-benzoquinone (**8**),[25,26] 2,5-bis(dimethylamino)-*p*-benzoquinone (**11**),[27] 2,5-bis(dimethylamino)-3,6-difluoro-*p*-benzoquinone (**12**),[27] and tetra(dimethlyamino)-*p*-benzoquinone (**13**) [28] were all synthesized according to literature procedures. Synthesis and manipulation of compounds were carried out in open air unless otherwise noted. For air- and moisture-sensitive procedures, manipulations were carried out using standard Schlenk or glovebox techniques under an inert atmosphere of N_2. The glovebox used was a Vacuum Atmospheres Company (VAC) glovebox. All reagents and solvents were used as purchased without further purification unless otherwise noted. All non-deuterated solvents used for electrochemical study were degassed by sparging with argon and then dried by passage through an alumina column under argon pressure on a Solvent Drying System (JC Meyer Solvent Systems) and stored over activated 3Å molecular sieves. Deuterated solvents were purchased from Cambridge Isotopes Laboratories, Inc. and were used as received without further purification. Electrochemical studies were performed using high purity

(99.999%) carbon dioxide passed through a VICI carbon dioxide purification column to eliminate residual H_2O, O_2, CO, halocarbons, and sulfur contaminations.

Previously reported quinones were synthesized according to previously reported procedures. Tetrabromo-p-benzoquinone was purchased from Matrix Scientific. 2,3-dichloro-p-naphthoquinone was purchased from Thermo Scientific.

Nuclear magnetic resonance (NMR) spectroscopic measurements were carried out at 298 K. ^{1}H NMR spectra were recorded on a Bruker DRX500 spectrometer operating at 500.15 MHz. ^{13}C NMR spectra were recorded on Bruker AVANCE600 spectrometer operating at 150.92 MHz. All ^{1}H and ^{13}C NMR chemical shifts are reported in ppm relative to SiMe4 using [1]H (chloroform-*d*: 7.26 ppm) and [13]C (chloroform-*d*: 77.16 ppm) chemical shifts of the solvent as a standard. ^{1}H NMR data for diamagnetic compounds are reported as follows: chemical shift, multiplicity (s = singlet), integration, assignment.

Synthesis of tetramethylester-p-benzoquinone (8): Tetramethylester-*p*-hydroquinone was prepared using literature procedures.[1] A suspension of 20 mg of tetramethylester-*p*-hydroquinone in 10 mL of acetic acid was stirred in a steam bath. 30% aqueous nitric acid (1 mL) was added dropwise. After one hour, the solution was poured into ice and chilled at –20 ºC overnight. The resulting solid was filtered out and recrystallized from hot methanol to obtain **8** as colorless crystals. ^{1}H NMR (500 MHz, $CDCl_3$, ppm): 3.81 (s, –CH_3). ^{13}C NMR (151 MHz, $CDCl_3$, ppm): 170.3, 168.9, 168.4, 51.9.

For binding constants calculated using cyclic voltammetry, error was calculated using the resolution of the bipotentiostat. For binding constants calculated using open circuit potentials, error was calculated by taking the square root of the sum each component's error squared.

2.5.2 Electrochemistry

All electrochemical measurements were performed using a Pine Wavedriver 10 bipotentiostat with AfterMath software, using a 1 mm diameter glassy carbon disc working electrode and glassy carbon rod counter electrode. A $Ag^{+/0}$ pseudo-reference electrode containing a silver wire submerged in 0.1 M tetrabutylammonium hexafluorophosphate (TBAPF$_6$) separated from the bulk solution by a Vycor tip was used in addition to an internal $Fe(C_5H_5)_2^{+/0}$ reference. TBAPF$_6$ was recrystallized three times from hot ethanol and dried in a vacuum oven before use. All voltammograms were started at the open circuit potential. Scans included iR drop compensation and $Fe(C_5H_5)_2^{+/0}$ was added as an internal reference and each CV was carefully referenced individually. A scanrate of 100mV/s was used for all cyclic voltammetry.

Controlled potential electrolyses used either glassy carbon or carbon cloth working and counter electrodes with a $Ag^{+/0}$ reference electrode. Open circuit potential (OCP) measurements were performed using a 1 mm diameter glassy carbon disc working electrode, a $Ag^{+/0}$ reference electrode, and a glassy carbon counter electrode, and were taken over 15 seconds and values were averaged; individual experiments were conducted in triplicates. All electrochemical measurements were performed in non-aqueous solvents and referenced to an internal standard of ferrocenium/ferrocene couple ($Fe(C_5H_5)_2^{+/0}$) at 0.00 V. All experiments were performed in dry and degassed organic solvents using 1 mM analyte with 100 mM concentration of tetrabutylammonium hexafluorophosphate (TBAPF$_6$) supporting electrolyte. For electrochemical studies performed under CO_2 conditions, samples were prepared by sparging the analyte solution with carbon dioxide gas for 10 minutes prior to measurement.

2.5.3 Theoretical Calculations of Reduction Potentials and CO₂ Binding Constants

The standard one-electron reduction potential ($E°$ in V) is defined as a quantity reflecting Gibbs free energy change upon $1e^-$ reduction, Ox (aq) + e^- → Red (aq):

$$E° \text{ [V]} = G_{\text{Ox}} \text{ [eV]} - G_{\text{Red}} \text{ [eV]} + \Delta E°_{\text{abs}}(\text{reference}) \text{ [eV]}, \tag{2.7}$$

where $G_{\text{Ox}}/G_{\text{Red}}$ are the Gibbs free energies of the oxidized/reduced state of a solute, and $\Delta E°_{\text{abs}}$(reference) is the absolute potential of a reference electrode, required to compare computations with the experiment. The one-electron reduction of a solute corresponds to a *half-cell reaction*, i.e., the *absolute* half-cell potential is the quantity obtained in the calculations. However, by convention, the measured reduction potentials are referred *relative* to the half-cell potential of a reference electrode. Herein, we have referenced the potentials to the $Fe(C_5H_5)_2^{+/0}$ absolute potential calculated using the same methodology as for the calculations of the reduction potentials of quinones (*vide infra*), yielding a value of –4.46 eV in acetonitrile (MeCN) or *N,N*-dimethylformamide (DMF) (note that COSMO solvation model cannot distinguish well between these solvents as their dielectric constants are similar).

The affinity for CO₂ binding is calculated as the equilibrium constant of the CO₂ association in the reaction Q_{DA} + CO₂ → Q_{DA}CO₂. The binding constant (K_{CO_2}) is related to the Gibbs free energy of the reaction through:

$$\Delta G = G_{[Q_{DA}\text{CO}_2]} - (G_{Q_{DA}} + G_{\text{CO}_2}) = -RT \ln K_{\text{CO}_2}. \tag{2.8}$$

2.5.4 Quantum-Chemical Calculations of Gibbs Free Energies

To calculate Gibbs free energies from eqns. 7 and 8, all of the quinones were optimized in the oxidized (radical-anion/semiquinone), reduced (dianion), and CO₂-bound dianion states, using the BP86 functional,[29,30] the def2-TZVP basis set,[31] and the zero-damping dispersion correction (-D3),[32] with the inclusion of the effect of solvation on geometry optimizations by employing the

implicit conductor-like screening model (COSMO)[33] with $\varepsilon = 37.0$ dielectric constant. The calculations were expedited by expanding the Coulomb integrals in an auxiliary basis set, via the resolution-of-identity (RI-*J*) approximation.[34] The equilibrium geometries were then used to calculate all of the terms contributing to the Gibbs free energies in equations. 2.7 and 2.8, as:

$$G = E_{el} + [E_{ZPVE} + RT - RTlnQ] + G_{solv}, \tag{2.9}$$

where:

(*i*) the E_{el} is the *in vacuo* single-point energy of optimized geometries calculated using the PBE0 functional with the def2-TZVPP basis set,

(*ii*) temperature-dependent $[E_{ZPVE} + pV - RT\,lnQ]$ term was obtained from frequency calculations with the rigid rotor/harmonic oscillator approximation (for $p = 1$ bar).

(*iii*) G_{solv} term accounting for the free energy of solvation was taken from the conductor-like screening model (COSMO).

2.5.5 Large-Scale Calculations of Substituted *p*-Benzoquinone

For the analysis of the effect of the substituents of the *p*-benzoquinone (BQ) scaffold on the HOMO(Q_{DA}) and in-plane(Q_{DA}) orbital energies (see Molecular Orbitals Analysis section), we have generated an extensive library of substituted BQs (the procedure is explained in detail in **Scheme 2.3**). First, we used SMILES representation to generate all of the unique-structure combinations of the mono-, bis-, tris-, and tetra-substituted BQ by introducing 24 different substituents (-F, -Cl, -Br, -CF$_3$, -Me, -Et, -tBu, -Ph, -Bn, -OH, -OCH$_3$, -CH$_2$OH, -OPh, -OCOCH$_3$, -COOCH$_3$, -NH$_2$, -NHCH$_3$, -N(CH$_3$)$_2$, -NHCOCH$_3$, -NHPh, -CN, -NO$_2$, -N(CH$_3$)$_3^+$, -CH$_2$N(CH$_3$)$_3^+$). This represents ca. 100,000 individual structures. Then, the SMILES codes were transformed into the 3D structures XYZ coordinates using Open Babel.[35]

To find the lowest-lying conformation of each compound, we performed MD simulation at the GFN0-xTB level.[36] We have captured 50 ps trajectories with 2.5 fs steps at $T = 600$ K, with all of the bond lengths constrained, to select 500 snapshots along each trajectory for full optimization at the GFN2-xTB[37] level with the generalized Born solvation model with the surface area contributions (GBSA). The resulting structures were then clustered by energy and geometry (RMSD) using ISOSTAT module of the Molclus program.[38] It should be noted that some initial geometries generated in the molecular dynamics resulted in a change of the bonding pattern after the GFN2-xTB procedure. Therefore, we included a connectivity filter and removed all structures with the altered original connectivity.

From the ensemble of GFN2-xTB optimized geometries, we have selected only the lowest-lying conformer that was further optimized using DFT (PBE0/def2-SVP), and for which we calculated the HOMO(Q_{DA}) and in-plane(Q_{DA}) orbital energies using the same level of theory. Note that this simplified level of theory was compared to the protocol used above to calculate the reduction potentials, CO_2 binding constants, and the orbital energies in the series of experimentally obtained compounds from **Table 2.1** (see **Figure 2.16**)

2.5.6 Measurement of K_{CO_2} Using Open Circuit Potential

A 1:1 ratio of the quinone dianion and radical anion was formed electrochemically using controlled potential electrolysis. To achieve this ratio, a solution of 5 mM of the selected benzoquinone in 0.1M TBAPF$_6$ was electrochemically reduced by 1.5 electrons under an inert atmosphere.

The open circuit potential of the reduced solution is measured (E_{OCP}). Then, the solution is sparged with different concentrations of CO_2 mixed with N_2. At each concentration of CO_2, the open circuit potential is measured (E_{CO2}). The change in the open circuit potential is then graphed

against the concentration of CO_2 in solution to yield a linear relationship. The K_{CO_2} can be calculated using y-intercept from the linear regression and the following adaptation of the Nernst equation.[2]

$$\left(E_{CO_2} - E_{OCP}\right) = \frac{0.0592}{n}\log(K_{CO2}) + q\frac{0.0592}{n}\log[CO_2] \qquad (2.10)$$

Error values for the CO_2 binding affinity values measured using CV were determined using the standard instrumental error. Error values for the CO_2 binding affinity values measured using OCP were calculated using the standard deviation of the y-intercept value that was found during the linear fit as well as the standard instrumental error; these values were combined using the square root of the sum of the squares method.
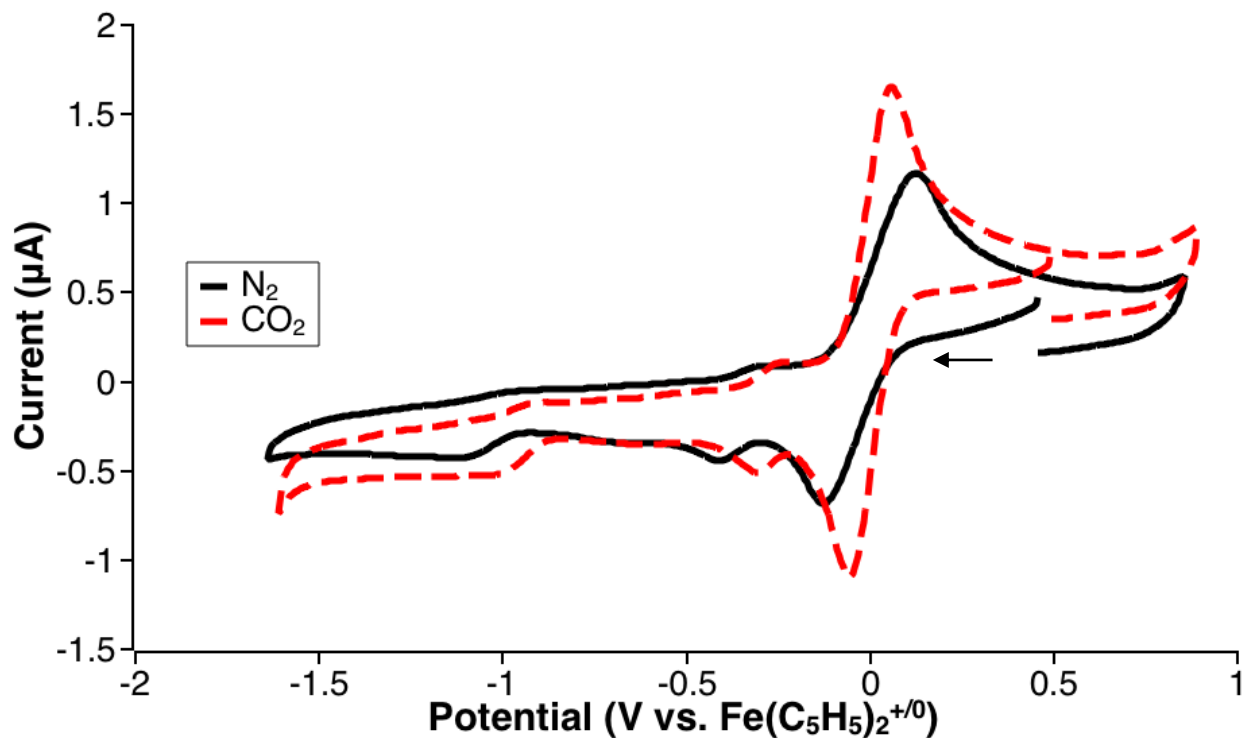
Figure 2.6. CV data of tetramethylester-*p*-benzoquinone **(8)** under N_2 (black solid trace) and CO_2 (red dashed trace) in chloroform.
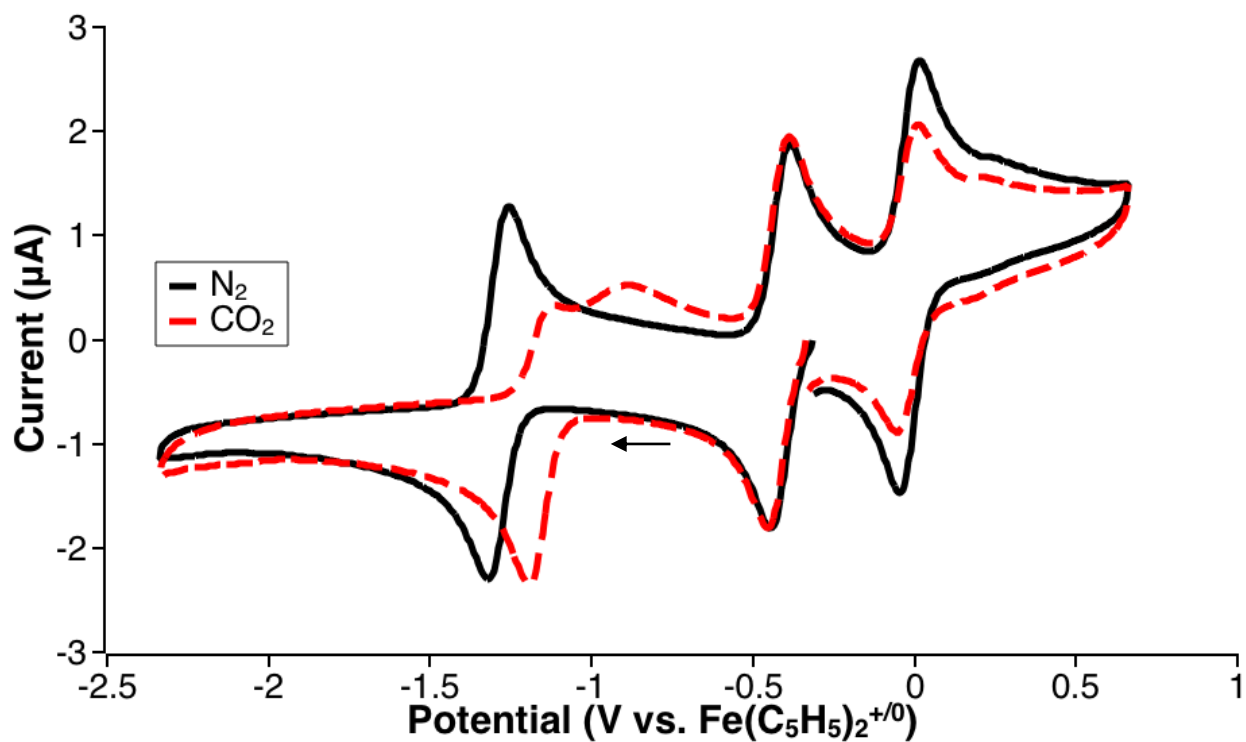
Figure 2.7. CV data of tetrabromo-*p*-benzoquinone **(9)** under N_2 (black solid trace) and CO_2 (red dashed trace) in DMF.
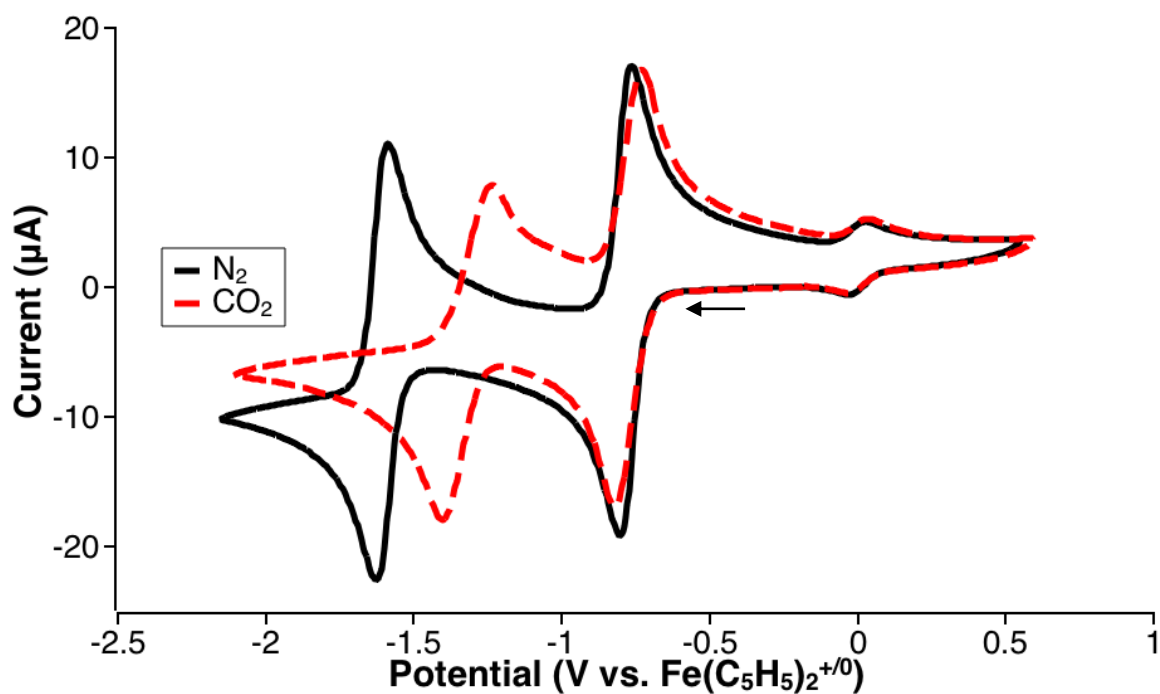
Figure 2.8. CV data of 2,3-dichloro-*p*-naphthoquinone **(10)** under N_2 (black solid trace) and CO_2 (red dashed trace) in DMF.
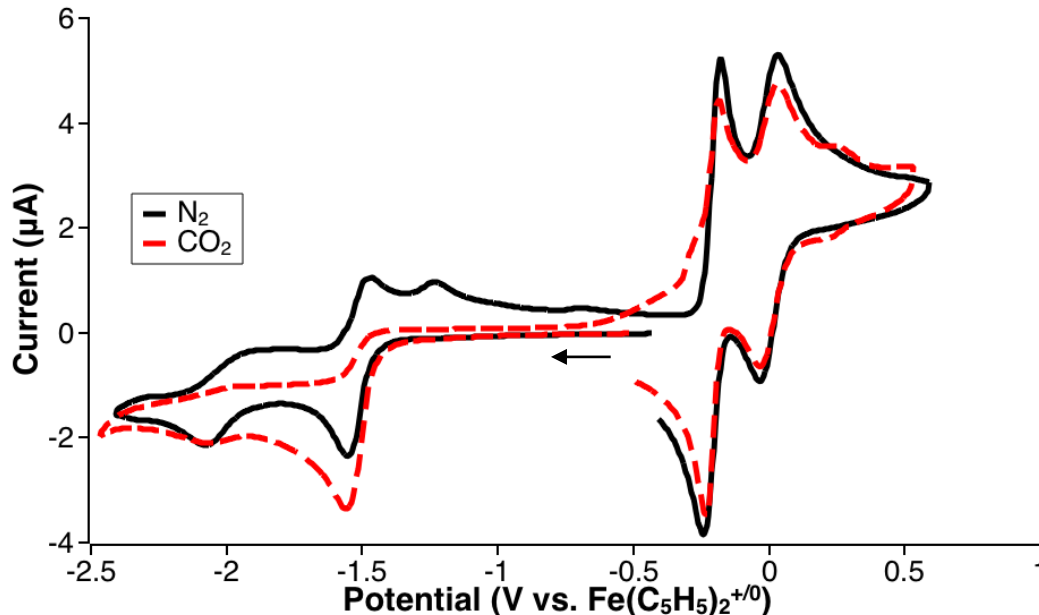
Figure 2.9. CV data of tetra(dimethylamino)-*p*-benzoquinone **(13)** under N_2 and CO_2 in MeCN. Note that there is not a clear peak shift upon introduction of CO_2, but instead the disappearance of the oxidative features and an increase in current for the reductive feature.

y=0.0245x+0.1021
R²=0.9852
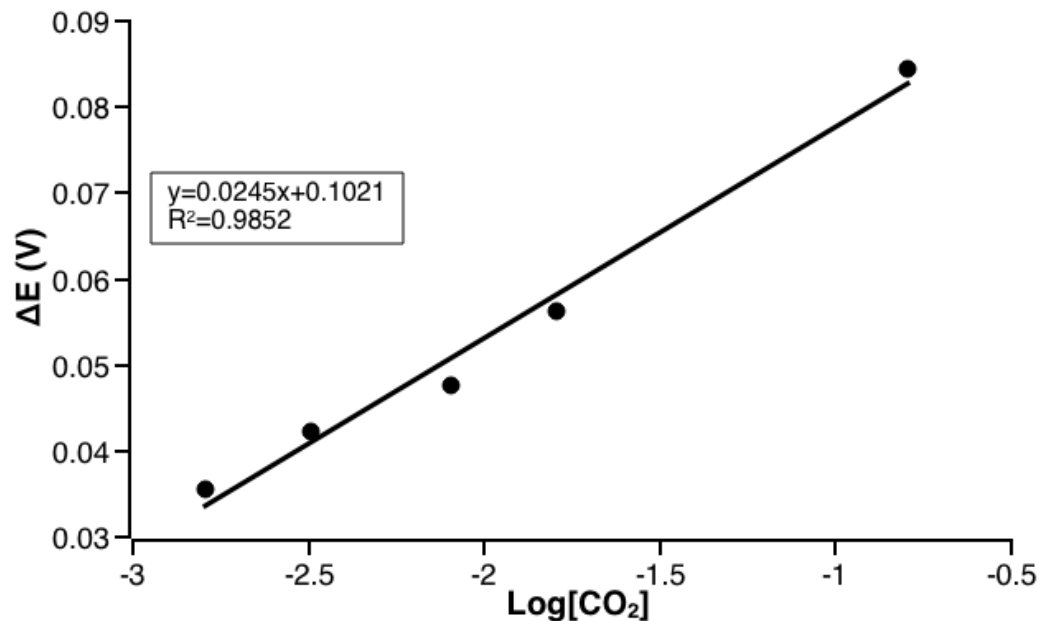
Figure 2.10. To confirm the binding constant found by CV, calculation of the binding constant for tetramethylester-*p*-benzoquinone **(8)** was done by measuring the change in open circuit potential versus the concentration of CO_2, data taken in MeCN. The log of the binding constant found with this method was 1.7 ± 0.1 M^{-1}, which falls into the range of the binding constant found using CV. Error bars for the x and y axes are too small to be seen in the graph.
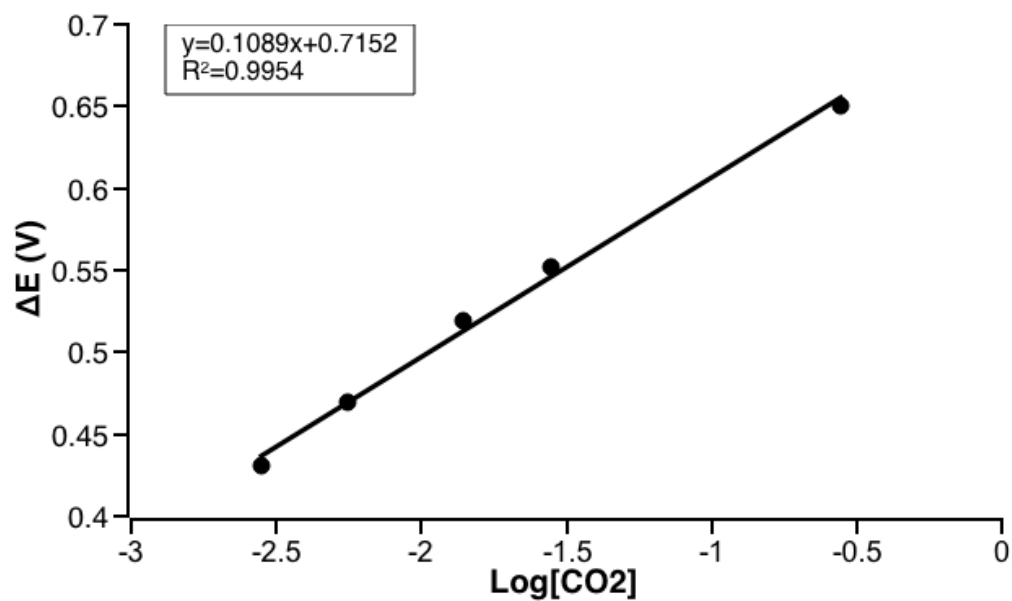
Figure 2.11. Calculation of the binding constant for bis(dimethylamino)-*p*-benzoquinone **(11)** was done by measuring the change in open circuit potential versus the concentration of CO_2, data taken in MeCN.
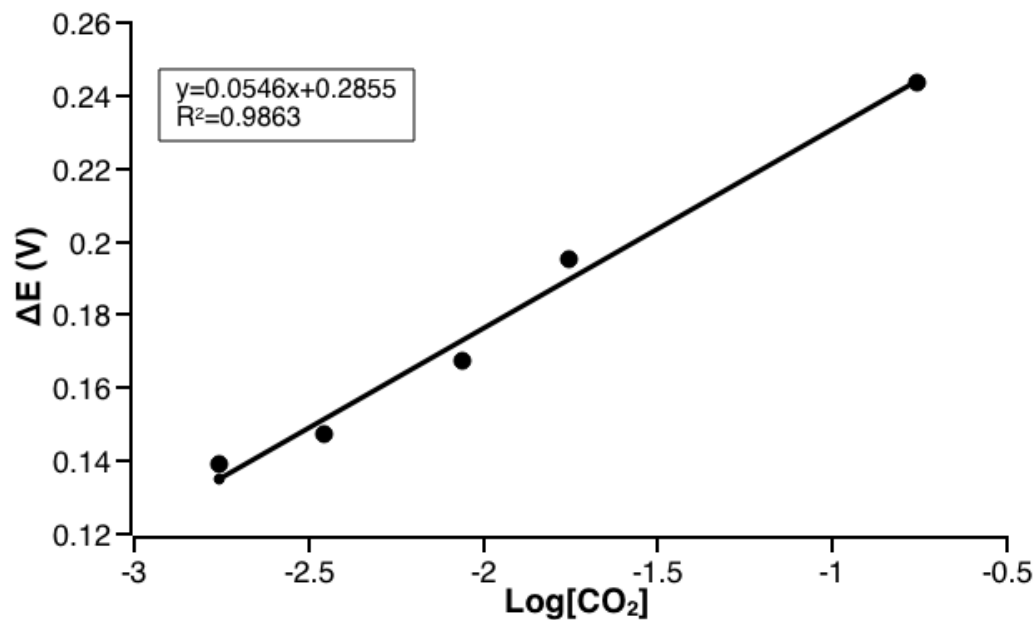
Figure 2.12. Calculation of the binding constant for difluoro-bis(dimethylamino)-*p*-benzoquinone **(12)** was done by measuring the change in open circuit potential versus the concentration of CO_2, data taken in DMF.
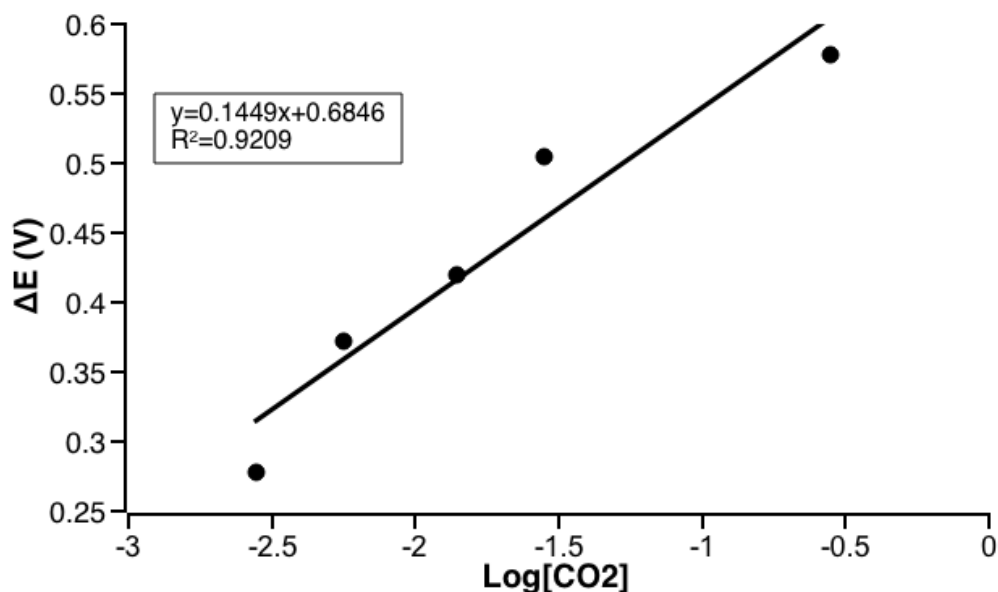
Figure 2.13. Calculation of the binding constant for tetra(dimethylamino)-*p*-benzoquinone **(13)** was done by measuring the change in open circuit potential versus the concentration of CO_2, data taken in MeCN.

Table 2.4. A comparison of reduction potentials and CO_2 binding affinities for tetrabromo-p-benzoquinone **(9)**. All values found using cyclic voltammetry with 1 mM analyte and 0.1 M TBAPF$_6$ electrolyte.

Solvent	$E_{1/2}$ [V] (vs. $Fe(C_5H_5)_2^{+/0}$)	$\log(K_{CO_2})$
DMSO	-1.14	3.0 ± 0.9
MeCN	-1.13	2.6 ± 0.6
DMF	-1.28	3.3 ± 0.8

2.5.7 Computational Studies

The involvement of different molecular orbitals (HOMO(Q_{DA}) and in-plane(Q_{DA})) for the electrochemical (redox) and chemical (CO_2 binding) steps suggests that the quinone properties might be isolable by regulating the energy levels of the particular MOs to improve the LFER in **Scheme 2.1** in the main text. Such a strategy is exemplified herein using the three model quinone systems in **Scheme 2.2** (*right*). We demonstrate that particular MO energies can be tuned by introducing the substituents in the benzoquinone (BQ) scaffold. In **Scheme 2.2**, the two modes of how the different substituents influence the Q_{DA} MO energies are recognized: *(i)* the whole

manifold of Q_{DA} MOs can be shifted in energy as the substituents change the quinone's electronic properties, or *(ii)* the energy gap between HOMO(Q_{DA}) and in-plane(Q_{DA}) can be increased or decreased as their energies are influenced unequally. Considering the LFER in **Scheme 2.2**, a transfer of the whole manifold of the MOs in energy corresponds to the movement along the LFER correlation line; i.e., simultaneous increase/decrease in the HOMO(Q_{DA}) and in-plane(Q_{DA}) energy equals to the decrease/increase of the $E_{1/2}$ and increase/decrease of the $\log(K_{CO_2(DA)})$. In contrast, changing the energy gap between the two participating MOs results in the movement out of the LFER correlation. Therefore, we propose that to achieve the same CO_2 binding at the more mild reduction potentials, the energy gap between HOMO(Q_{DA}) and in-plane(Q_{DA}) must be reduced.

Scheme 2.2. *Left*: A participation of HOMO(Q_{DA}) vs. in-plane(Q_{DA}) orbitals requires a different approach of the CO_2 molecule. The geometry optimizations of the CO_2-bound quinone dianions suggest that both orbitals are involved in the CO_2 binding; however, the perpendicular orientation of the benzene and CO_2 plane of the adduct suggests a higher contribution from the in-plane(Q_{DA}). Additionally, an out-of-plane bending of the CO_2 molecule in the adduct (illustrated by the angle 'Ω') indicates the presence of weak interaction with the HOMO(Q_{DA}). *Right*: The benzoquinone (BQ) substituents can affect the energies of HOMO(Q_{DA}) and in-plane(Q_{DA}) to the same extent – resulting in a linear correlation between $E_{1/2}$ and $\log(K_{CO_2(DA)})$ – or the MOs energies can be influenced unequally. Since the higher in-plane(Q_{DA}) energy is required for the better energetic overlap with the LUMO(CO_2), reducing the energy gap between HOMO(Q_{DA}) and in-plane(Q_{DA}) can produce a more favorable CO_2 capture behavior at the lower $E_{1/2}$.

Pursuing the goal to interpret how the distinct structural perturbations of the BQ scaffold influence the corresponding HOMO(Q_{DA}) and in-plane(Q_{DA}) orbital energies, we calculated MO

energies of an extensive library of ca. 60,000 substituted BQs. In **Figure 2.14**, the energies of the HOMO(Q_{DA}) and in-plane(Q_{DA}) orbitals are plotted for each compound. The two orbitals are coupled and simultaneously altered in energy, while the energy gap between them remains essentially constant, indicating the seemingly linear relationship between $E_{1/2}$ and $\log(K_{CO_2(DA)})$. However, some deviations from the trend, where the energy gap between the orbitals is changed, are also evident. Specifically, we demonstrate that by introducing various substituents, the energy gap between HOMO(Q_{DA}) and in-plane(Q_{DA}) can be reduced by ca. 0.4 a.u., corresponding to an increase in the $\log(K_{CO_2(DA)})$ by as much as 24 units for the same $E_{1/2}$ (*cf.* **Figure 2.14**, *left*). Finally, we identified several substituent classes with lower MOs energy gap than the unsubstituted BQ (**Figure 2.14**, *right*). The improved CO_2 binding is observed for the electron-withdrawing (EW) substituents, such as -NO$_2$, -COOR, -CF$_3$, -CN; sterically-demanding substituents, such as -tBu, -Ph, -OPh, -Bn; and interestingly, -NMe$_2$.
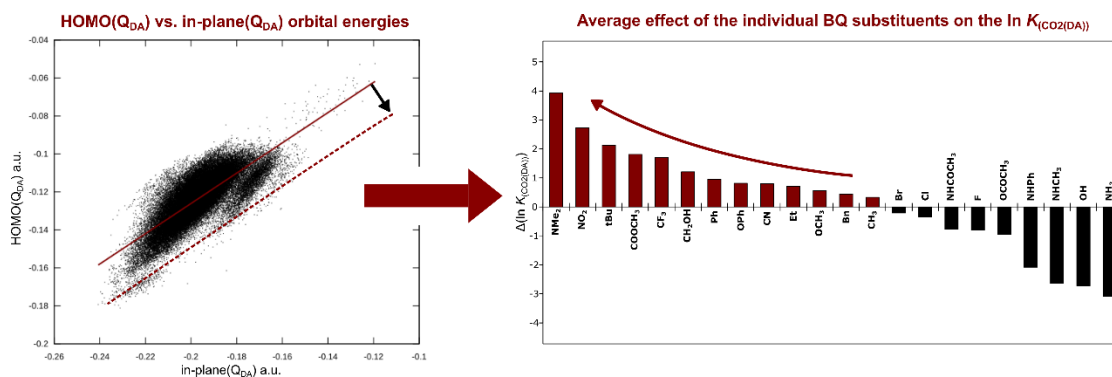
Figure 2.14. A correlation between the calculated HOMO(Q_{DA}) and in-plane(Q_{DA}) energies in a large series of quinone dianions. A favorable CO_2 binding at more mild reduction potentials is expected for the substituents reducing the HOMO(Q_{DA}) and in-plane(Q_{DA}) energy gap (exemplified by a dashed line). By analyzing the individual data points, the substituents with statistically significant effect on the CO_2 binding constants that goes beyond the LFER in **Scheme 2.1** are recognized in the plot on the right.

A linear correlation in **Figure 2.14** shows that BQ substitutions principally transfer the HOMO(Q_{DA}) and in-plane(Q_{DA}) energies in the same direction, whereas EW substituents decrease and electron-donating (ED) substituents increase the energy of both orbitals. At the same time,

owing to greater polarizability of the more delocalized HOMO(Q_{DA}), the HOMO(Q_{DA}) energy is affected more, which elucidates the decrease/increase of the energy gap utilizing EW/ED substituents. Additionally, we suggest that only the substituents that can participate in the resonance with HOMO(Q_{DA}) can significantly influence the HOMO(Q_{DA}) energy, while the in-plane(Q_{DA}) is always affected through the σ bonding. Therefore, in the case of, e.g., -tBu, -Ph, or -Bn substituents, their ED character without an unshared electron pair that could delocalize into the HOMO(Q_{DA}) π system leads to a higher increase in the in-plane(Q_{DA}), reducing the MOs energy gap. Similarly, the -NMe$_2$, -OPh, and -OCH$_3$ substituents strongly donate the electrons into the system. However, the steric bulk of the alkyl groups prevents the facile overlap of their unshared electron pairs with the HOMO(Q_{DA}) π system. This contrasts with the less bulky -NHR, -NH$_2$, and -OH substituents, which unfavorably decrease the energy gap between HOMO(Q_{DA}) and in-plane(Q_{DA}) by donating the electrons into both MOs. The effect of the number of individual substituents to the orbital energies is fairly additive; the plot in **Figure 2.15** shows the effect of individual substituents on the BQ scaffold.
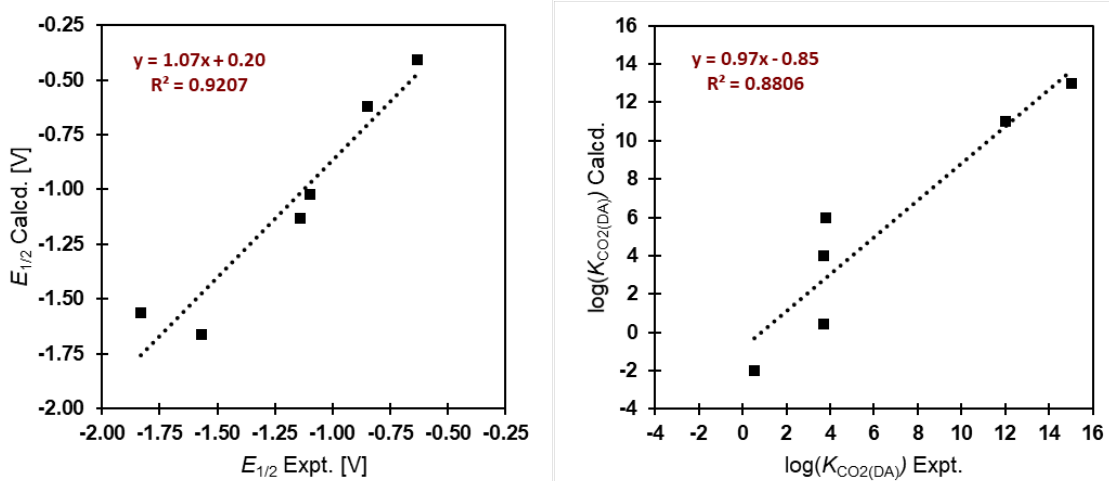
Figure 2.15. Correlations between the calculated and experimental reduction potentials ($E_{1/2}$) (left) and CO$_2$ binding constants ($\log(K_{CO_2})$) (right) of various quinone dianions from **Table 2.1**.

Scheme 2.3. The library of substituted BQs was generated as follows: (i) SMILES representation was used to generate all of the unique-structure combinations of the mono-, bis-, tris-, and tetra-substituted 1,4-BQ by introducing 24 different substituents (-F, -Cl, -Br, -CF$_3$, -Me, -Et, -tBu, -Ph, -Bn, -OH, -OCH$_3$, -CH$_2$OH, -OPh, -OCOCH$_3$, -COOCH$_3$, -NH$_2$, -NHCH$_3$, -N(CH$_3$)$_2$, -NHCOCH$_3$, -NHPh, -CN, -NO$_2$, -N(CH$_3$)$_3^+$, -CH$_2$N(CH$_3$)$_3^+$), (ii) SMILES codes were transformed into the 3D structures XYZ coordinates, (iii) MD simulation at the GFN0-xTB level was performed to capture the conformational flexibility of the species, (iv) 500 snapshots along each trajectory were fully optimized at the GFN2-xTB level with the GBSA solvation model, (v) resulting optimized structures were then clustered by energy and geometry (RMSD), (vi) structures with altered bonding were removed using a connectivity filter, and (vii) from the ensemble of GFN2-xTB optimized geometries, we have selected only the lowest-lying conformer that was further optimized using DFT (PBE0/def2-SVP), and for which we have calculated the HOMO(Q$_{DA}$) and in-plane(Q$_{DA}$) orbital energies using the same level of theory. For more details, see the Computational Details section in the main text.
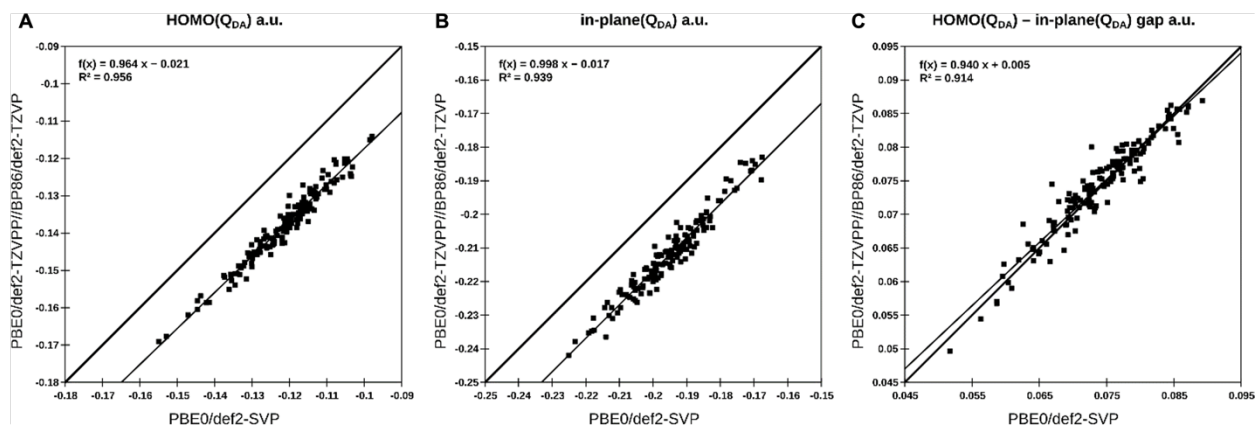
Figure 2.16. (**A**.) Calculated HOMO(Q$_{DA}$) orbital energies and (**B**.) in-plane(Q$_{DA}$) orbitals energies and (**C**.) their difference, compared at the 'full' and 'simplified' levels of theory (as described in the Computational Details section). The energies of the orbitals are systematically overestimated with the

66

smaller basis set (def2-SVP); however, the energetic gap between the orbitals appears to be relatively unaffected by the change.

References:

(1)   Rheinhardt, J. H.; Singh, P.; Tarakeshwar, P.; Buttry, D. A. Electrochemical Capture and Release of Carbon Dioxide. *ACS Energy Lett.* **2017**, *2* (2), 454–461. https://doi.org/10.1021/acsenergylett.6b00608.

(2)   Zhang, P.; Tong, J.; Huang, K. Electrochemical CO_2 Capture and Conversion. In *Materials and Processes for CO2 Capture, Conversion, and Sequestration*; Li, L., Wong-Ng, W., Huang, K., Cook, L. P., Eds.; John Wiley and Sons, 2018; pp 213–266. https://doi.org/10.1002/9781119231059.ch5.

(3)   Geothermal Power Generation. In *Advanced Renewable Energy Systems*; Bhatia, S. C., Ed.; WPI Publishing, 2014; pp 334–388. https://doi.org/10.1201/b18242.

(4)   Voskian, S.; Hatton, T. A. Faradaic Electro-Swing Reactive Adsorption for CO_2 Capture. *Energy Environ. Sci.* **2019**, *12*, 3530–3547. https://doi.org/10.1039/c9ee02412c.

(5)   Verley, G.; Esposito, M.; Willaert, T.; Van Den Broeck, C. The Unlikely Carnot Efficiency. *Nat. Commun.* **2014**, *5* (1), 1–5. https://doi.org/10.1038/ncomms5721.

(6)   Clarke, L. E.; Leonard, M. E.; Hatton, T. A.; Brushett, F. R. Thermodynamic Modeling of CO2 Separation Systems with Soluble, Redox-Active Capture Species. *Ind. Eng. Chem. Res.* **2022**, *61* (29), 10531–10546. https://doi.org/10.1021/acs.iecr.1c04185.

(7)   Bell, W. L.; Miedaner, A.; Smart, J. C.; DuBois, D. L. Synthesis and Evaluation of Electroactive CO_2 Carriers. *SAE Technical Paper Series*. 1988, pp 1–10. https://doi.org/10.4271/881078.

(8)   Hammond, G. P.; Akwe, O. S. O.; Williams, S. Techno-Economic Appraisal of Fossil-Fuelled Power Generation Systems with Carbon Dioxide Capture and Storage. *Energy*

2011, *36* (2), 975–984. https://doi.org/10.1016/j.energy.2010.12.012.

(9)   Stern, M. C.; Alan Hatton, T. Bench-Scale Demonstration of CO_2 Capture with Electrochemically-Mediated Amine Regeneration. *RSC Adv.* **2014**, *4* (12), 5906–5914. https://doi.org/10.1039/c3ra46774k.

(10)   Ranjan, R.; Olson, J.; Singh, P.; Lorance, E. D.; Buttry, D. A.; Gould, I. R. Reversible Electrochemical Trapping of Carbon Dioxide Using 4,4′-Bipyridine That Does Not Require Thermal Activation. *J. Phys. Chem. Lett.* **2015**, *6* (24), 4943–4946. https://doi.org/10.1021/acs.jpclett.5b02220.

(11)   Appel, A. M.; Newell, R.; DuBois, D. L.; Rakowski DuBois, M. Concentration of Carbon Dioxide by Electrochemically Modulated Complexation with a Binuclear Copper Complex. *Inorg. Chem.* **2005**, *44* (9), 3046–3056. https://doi.org/10.1021/ic050023k.

(12)   Mizen, M. B.; Wrighton, M. S. Reductive Addition of CO2 to 9,10-Phenanthrenequinone. *J. Electrochem. Soc.* **1989**, *136* (4), 941. https://doi.org/10.1149/1.2096891.

(13)   Gurkan, B.; Simeon, F.; Hatton, T. A. Quinone Reduction in Ionic Liquids for Electrochemical CO_2 Separation. *ACS Sustain. Chem. Eng.* **2015**, *3* (7), 1394–1405. https://doi.org/10.1021/acssuschemeng.5b00116.

(14)   Huang, C.; Liu, C.; Wu, K.; Yue, H.; Tang, S.; Lu, H.; Liang, B. CO_2 Capture from Flue Gas Using an Electrochemically Reversible Hydroquinone/Quinone Solution. *Energy & Fuels* **2019**, *33* (4), 3380–3389. https://doi.org/10.1021/acs.energyfuels.8b04419.

(15)   *Electrochemical and Catalytic Reactions of Carbon Dioxide*; Sullivan, B. R., Ed.; Amsterdam, 1993. https://doi.org/10.1002/9783527630295.fmatter.

(16)   Barlow, J. M.; Yang, J. Y. Oxygen Stable Electrochemical CO_2 Capture and Concentration with Quinones through Alcohol Additives. *J. Am. Chem. Soc.* **2022**, *144*

(31), 14161–14169.

(17)   Elhabiri, M.; Sidorov, P.; Cesar-Rodo, E.; Marcou, G.; Lanfranchi, D. A.; Davioud-
       Charvet, E.; Horvath, D.; Varnek, A. Electrochemical Properties of Substituted 2-Methyl-
       1,4-Naphthoquinones: Redox Behavior Predictions. *Chem. - A Eur. J.* **2015**, *21* (8), 3415–
       3424. https://doi.org/10.1002/chem.201403703.

(18)   Guin, P. S.; Das, S.; Mandal, P. C. Electrochemical Reduction of Quinones in Different
       Media: A Review. *Int. J. Electrochem.* **2011**, *2011*, 1–22.
       https://doi.org/10.4061/2011/816202.

(19)   Huynh, M. T.; Anson, C. W.; Cavell, A. C.; Stahl, S. S.; Hammes-Schiffer, S. Quinone 1
       E- and 2 e-/2 H+ Reduction Potentials: Identification and Analysis of Deviations from
       Systematic Scaling Relationships. *J. Am. Chem. Soc.* **2016**, *138* (49), 15903–15910.
       https://doi.org/10.1021/JACS.6B05797.

(20)   Shcherbakov, V. V.; Artemkina, Y. M. Dielectric Properties of Solvents and Their
       Limiting High-Frequency Conductivity. *Russ. J. Phys. Chem. A 2013 876* **2013**, *87* (6),
       1048–1051. https://doi.org/10.1134/S0036024413060241.

(21)   Géron, A. *Hands-On Machine Learning with Scikit-Learn, Keras, and TensorFlow:
       Concepts, Tools, and Techniques to Build Intelligent Systems*, 2nd ed.; O'Reilly Media,
       2019.

(22)   Schmidt, M. H.; Miskelly, G. M.; Lewis, N. S. Effects of Redox Potential, Steric
       Configuration, Solvent, and Alkali Metal Cations on the Binding of Carbon Dioxide to
       Cobalt(I) and Nickel(I) Macrocycles. *J. Am. Chem. Soc.* **1990**, *112* (9), 3420–3426.
       https://doi.org/10.1021/ja00165a027.

(23)   Ashwell, G. J.; Bryce, M. R.; Davies, S. R.; Hasan, M. Facile Isomerization of 2-

(Dicyanomethylene)-1,3-Indandione to 2,3-Dicyano-1,4-Naphthoquinone. *J. Org. Chem.* **1988**, *53* (19), 4585–4587. https://doi.org/10.1021/jo00254a034.

(24)   VanAllan, J. A.; Reynolds, G. A. The Reactions of 2,3-Dichloro-1,4-Naphthoquinone with Alkali Metal Cyanides. *J. Org. Chem.* **1964**, *29* (12), 3591–3593. https://doi.org/10.1021/jo01035a036.

(25)   Balachandran, A. L.; Sathi, V.; Deepthi, A.; Suneesh, C. V. A Convenient Method for the Synthesis of 3,6-Dihydroxybenzene-1,2,4,5-Tetracarboxylic Acid Tetraalkyl Esters and a Study of Their Fluorescence Properties. *Arkivoc* **2016**, *5*, 327–337. https://doi.org/10.3998/ark.5550190.p009.843.

(26)   Nef, J. U. Ueber Tautomere Körper. *Justus Liebig's Ann. der Chemie* **1890**, *258* (3), 261–318. https://doi.org/10.1002/jlac.18902580302.

(27)   Barbero, M.; Papillo, V. A.; Grolla, A. A.; Negri, R.; Travaglia, F.; Bordiga, M.; Condorelli, F.; Arlorio, M.; Giovenzana, G. B. Unprecedented Formation of 2,5-Diaminoquinones from the Reaction of Vanillin with Secondary Amines in Aerobic Conditions. *European J. Org. Chem.* **2020**, *2020* (1), 136–139. https://doi.org/10.1002/ejoc.201901553.

(28)   Bock, H.; Rupper, K.; Näther, C.; Havlas, Z. Structural Changes on Twofold Oxidation of Tetrakis(Dimethylamino)-p-Benzoquinone: A Sterically Overcrowded Electron-Rich "Chair" Compound Turns into a "Twist" Dicyanine Salt. *Angew. Chemie Int. Ed. English* **1991**, *30* (9), 1180–1183. https://doi.org/10.1002/anie.199111801.

(29)   Perdew, J. P. Density-Functional Approximation for the Correlation Energy of the Inhomogeneous Electron Gas. *Phys. Rev. B* **1986**, *33* (12), 8822–8824. https://doi.org/10.1103/PhysRevB.33.8822.

(30)   Becke, A. D. Density-Functional Exchange-Energy Approximation with Correct

Asymptotic Behavior. *Phys. Rev. A* **1988**, *38* (6), 3098–3100.

https://doi.org/10.1103/PhysRevA.38.3098.

(31)   Weigend, F.; Ahlrichs, R. Balanced Basis Sets of Split Valence, Triple Zeta Valence and

Quadruple Zeta Valence Quality for H to Rn: Design and Assessment of Accuracy. *Phys.*

Chem. Chem. Phys. **2005**, *7* (18), 3297–3305. https://doi.org/10.1039/b508541a.

(32)   Grimme, S.; Antony, J.; Ehrlich, S.; Krieg, H. A Consistent and Accurate Ab Initio

Parametrization of Density Functional Dispersion Correction (DFT-D) for the 94

Elements H-Pu. *J. Chem. Phys.* **2010**, *132* (15). https://doi.org/10.1063/1.3382344.

(33)   Klamt, A.; Schüürmann, G. COSMO: A New Approach to Dielectric Screening in

Solvents with Explicit Expressions for the Screening Energy and Its Gradient. *J. Chem.*

Soc. Perkin Trans. 2 **1993**, No. 5, 799–805. https://doi.org/10.1039/P29930000799.

(34)   Eichkorn, K.; Treutler, O.; Öhm, H.; Häser, M.; Ahlrichs, R. Auxiliary Basis Sets to

Approximate Coulomb Potentials. *Chem. Phys. Lett.* **1995**, *240* (4), 283–290.

https://doi.org/10.1016/0009-2614(95)00621-A.

(35)   O'Boyle, N. M.; Banck, M.; James, C. A.; Morley, C.; Vandermeersch, T.; Hutchison, G.

R. Open Babel: An Open Chemical Toolbox. *J. Cheminform.* **2011**, *3* (10), 1–14.

https://doi.org/10.1186/1758-2946-3-33.

(36)   Pracht, P.; Caldeweyher, E.; Ehlert, S.; Grimme, S. A Robust Non-Self-Consistent Tight-

Binding Quantum Chemistry Method for Large Molecules. **2019**.

https://doi.org/10.26434/chemrxiv.8326202.v1.

(37)   Bannwarth, C.; Ehlert, S.; Grimme, S. GFN2-XTB—An Accurate and Broadly

Parametrized Self-Consistent Tight-Binding Quantum Chemical Method with Multipole

Electrostatics and Density-Dependent Dispersion Contributions. *J. Chem. Theory Comput.* **2019**, *15* (3), 1652–1671. https://doi.org/10.1021/acs.jctc.8b01176.

(38)   Lu, T. Molclus Program.

(39)   Nagaoka, T.; Nishii, N.; Fujii, K.; Ogura, K. Mechanisms of Reductive Addition of CO_2 to Quinones in Acetonitrile. *J. Electroanal. Chem.* **1992**, *322* (1–2), 383–389. https://doi.org/10.1016/0022-0728(92)80090-Q.

Chapter 3

Exploring the Effect of Supporting Electrolyte on Reduction Potential and Carbon Dioxide Binding Affinity of Quinones

3.1 Introduction

The development of carbon capture and concentration technologies is vital to mitigate anthropogenic carbon dioxide (CO_2) emissions. In the 2022 IPCC report, nearly all of the illustrative mitigation pathways to decarbonization depend upon a carbon capture.[1] Current state-of-the-art technologies for carbon capture are predominantly thermal based. However, the practical applications of this technology have been limited by low overall energetic inefficiency due to Carnot limitations and thermal sorbent degradation.[2] Electrochemical CO_2 capture and concentration has been presented as an alternative technology that may address the concerns of energetic efficiency by bypassing the need for temperature swings and instead using more energetically-efficient redox swings. A reversible system would fully reform the sorbent, further addressing the concerns of thermal degradation. Electrochemical methods can also operate under ambient conditions.

Figure 3.1. A compilation of CO_2 binding affinity values and reduction potentials of various types of quinones. Data and references can be found in **Table 3.1**.
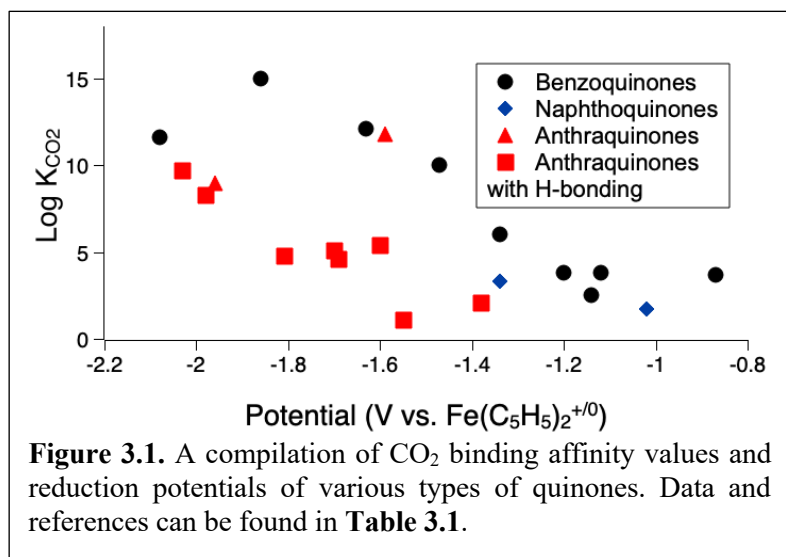
Quinones have been studied as redox carriers for electrochemical carbon dioxide capture since 1988.[3] The quinone scaffold is of interest due to its electrochemically-accessible 2-electron reduced state (dianion), which can reversibly bind CO_2. To capture CO_2 with 90% capture efficiency, a redox carrier binding constant of $\sim 10^4$ M^{-1} from flue gas and $\sim 10^6$ M^{-1} from air is required. Most redox carriers with sufficient binding constants to capture CO_2 from industrial streams or air have a sensitivity to reduced O_2.[4] This sensitivity is

Figure 3.2. (a) Quinones chosen for study because they represent a large range of reduction potentials and CO_2 binding affinities. **(b)** Supporting electrolytes chosen for study due to their varied size.
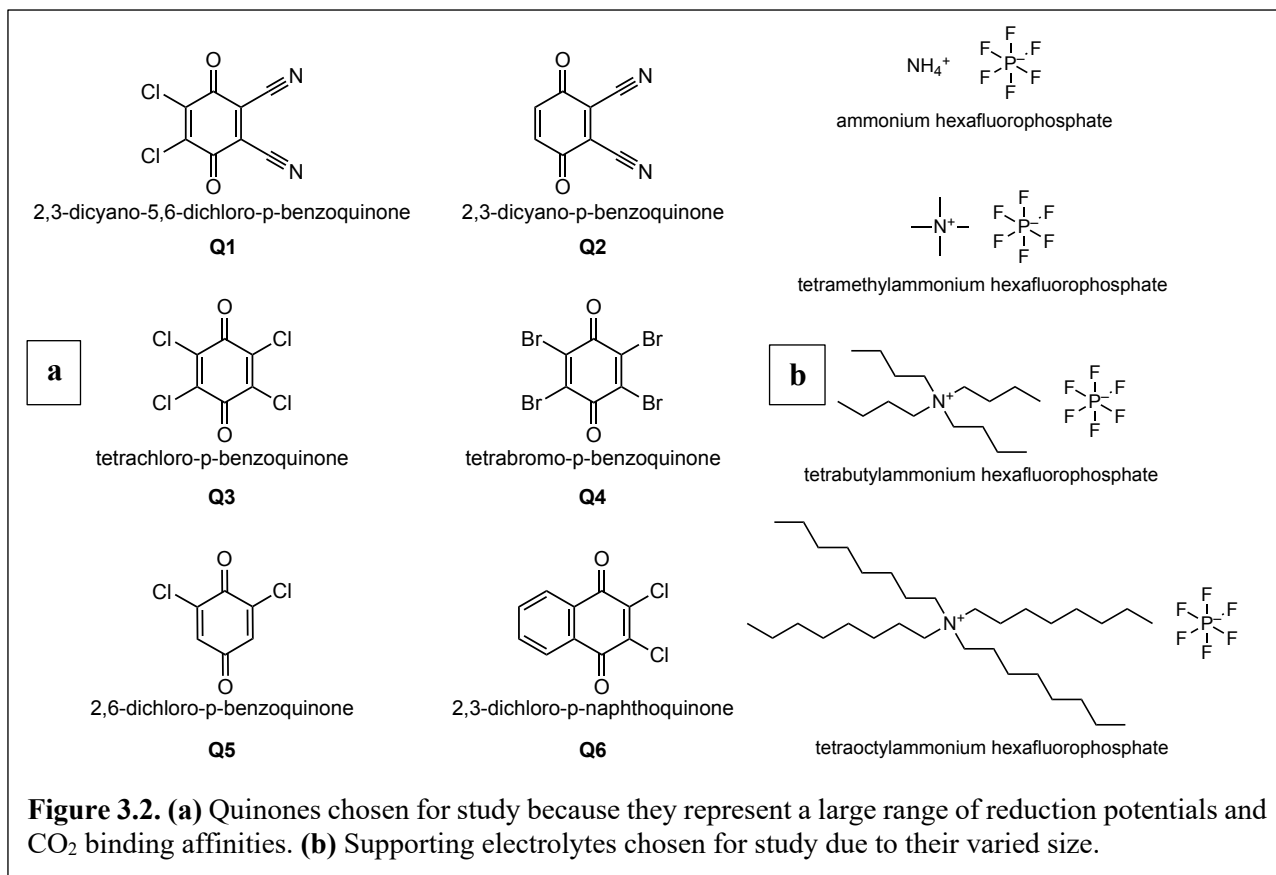
most commonly due to the reaction of the reduced carrier with O_2 to form superoxide ($O_2^{\bullet-}$). Thus, both the CO_2 binding constant for quinones, as well as their redox potential, are important to electrochemical CO_2 capture and release. However, there is a linear free energy relationship between the CO_2 binding affinity (K_{CO_2}) and the reduction potential for the formation of the quinone dianion in the absence of CO_2 ($E_{1/2}$) (**Figure 3.1**).[3,5,6]

Table 3.1. A compilation of CO_2 binding affinity values and reduction potentials of various types of quinones.

Quinone	$E_{1/2}^2$ under N_2 (V vs. $Fe(C_5H_5)_2^{+/0}$) [a]	Log K_{CO_2}	Reference
Tetrachloro-1,4-benzoquinone	−1.12	3.8	3
2,6-di-tert-butyl-1,4-benzoquinone	−1.86	15.0	3
9,10-phenanthrenequinone	−1.59	11.8	3
2,3-dicyano-1,4-benzoquinone[b]	−0.87	3.8	7
2, 6- dichloro-1,4-benzoquinone	−1.34	6.0	8
2- chloro- 1,4-benzoquinone	−1.47	10.0	8
tetrafluoro-1,4-benzoquinone	−1.20	3.8	8
tetrachloro-1,4-benzoquinone	−1.14	2.5	8
5-hydroxy-naphthoquinone[c]	−1.34	3.3	8
1, 8- dihydroxy-anthraquinone[c]	−1.60	5.4	8
1, 2- dihydroxy-anthraquinone[c]	−1.69	4.6	8
5, 8- dihydroxy-naphthoquinone[c]	−1.38	2.1	8
anthraquinone	−1.96	9.0	5
1-hydroxy-anthraquinone[c]	−1.70	5.1	5
1,4-dihydroxy-anthraquinone[c]	−1.55	1.1	5
1-amino-anthraquinone[c]	−1.98	8.3	5
1,4-diamino-anthraquinone[c]	−2.03	9.7	5
1-amino-4-hydroxy-anthraquinone[c]	−1.81	4.8	5
2,3-dicyano-1,4-naphthoquinone	−1.02	1.7	6
2,5-bis(dimethylamino)-1,4-benozquinone	−1.63	12.1	6
tetra(dimethylamino)-1,4-benzoquinone	−2.08	11.6	6

[a]Potentials are reported as V vs. $Fe(C_5H_5)_2^{+/0}$. Potentials recorded versus SCE were converted using Ref. [9].
[b]Undergoes Kolbe-Schmidt reaction with CO_2 as a decomposition pathway.
[c]Features intramolecular hydrogen-bonding interactions.

Tuning the microenvironment through solvent engineering can be an effective way of disrupting the linear free energy relationship. Barlow et. al previously demonstrated the impact of alcohol additives as hydrogen bond donors on redox potential and CO_2 binding of tetrachlorobenzoquinone in *N,N'*-dimethylformamide (DMF).[10] Different electrolytes have been used in the previously reported electrochemical CO_2 capture and concentration systems in aprotic solvent. Scovazzo et al. use tetrabutylammonium tetrafluoroborate.[11] Some systems also avoid the

use of an added electrolyte by using a deep eutectic solvent or ionic liquid.[11,12] Hatton and coworkers have used a Li supporting electrolyte.[13] Addition of alkali and alkaline earth metals to a quinone have been reported to cause an anodic shift in the quinone's reduction potential, but these electrolyte effects on the carbon dioxide binding affinity have not been quantified.[14–18] Herein, we seek to elucidate the effects of electrolyte on the reduction potential and K_{CO_2} of quinone redox carriers (**Figure 3.2a and b**).

3.2 Results and Discussion

The quinones (**Figure 3.2a**) were selected to have a range of reduction potentials and CO_2 binding affinities. Each quinone was studied by cyclic voltammetry (CV) in acetonitrile with a solution of 0.001 M quinone and 0.1 M electrolyte in the presence of N_2 and CO_2. The first series of electrolytes used were ammonium hexafluorophosphate (NH_4PF_6), tetramethylammonium hexafluorophoshate ($TMAPF_6$), tetrabutylammonium hexafluorophoshate ($TBAPF_6$), and tetraoctylammonium hexafluorophoshate ($TOAPF_6$). Additional studies were performed using lithium trifluoromethanesulfonate (LiOTf), sodium trifluoromethanesulfonate (NaOTf), potassium trifluoromethanesulfonate (KOTf), calcium trifluoromethanesulfonate (Ca $(OTf)_2$), barium trifluoromethanesulfonate (Ba $(OTf)_2$).

3.2.1 Ammonium Salts as Supporting Electrolyte

A series of ammonium cations were selected due to their differences in ionic radius: ammonium (146 pm), tetramethylammonium (292 pm), tetrabutylammonium (496 pm), and tetraoctylammonium (613 pm).[19,20]

In aprotic solvents, most quinones exhibit two reversible redox events. In contrast, when NH$_4$PF$_6$ was used as an electrolyte, only one redox event was present under N$_2$ (**Figure 3.3**). The behavior is similar to cyclic voltammetry of benzoquinones performed in water. The loss of the second reversible redox event is attributed to protonation.[21] In the presence of CO$_2$, there is a change in the cyclic voltammetry, but the data is inconclusive, as NH$_4$ may be interacting with the CO$_2$ in solution. Spectroelectrochemical studies were performed on Q1, Q4, and Q6; this representative set was chosen for study due to their variation of reduction potentials and CO$_2$ binding affinities (**Figures 3.4**). These studies consisted of electrochemically reducing the neutral quinone to the dianion using the selected supporting electrolyte salt. While the electrolysis is occurring, UV-visible spectra is taken. The spectra shown below are the dianion forms of the quinone generated *in-situ* in the presence and absence of CO$_2$.

The UV-visible spectra confirm the protonation of the dianion to form the hydroquinone with the emergence of absorptions at 300 nm.[22] Ammonium has a pK_a value of 16 in acetonitrile.[23] The pK_a values in acetonitrile are estimated to be ~26 for the hydroquinone and ~17 for the semiquinone,[24] indicating protonation to form the hydroquinone is favorable.
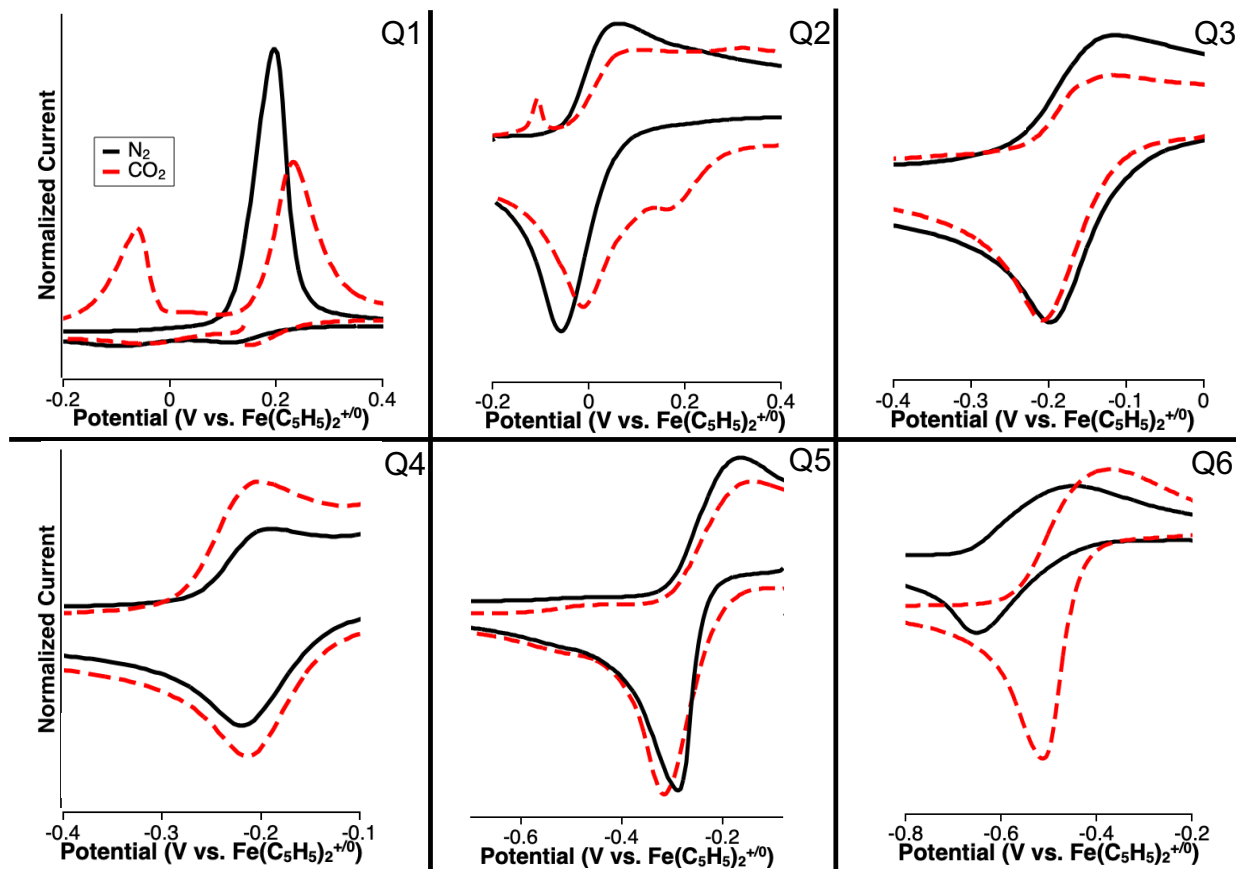
Figure 3.3. Cyclic voltammograms of Q1-Q6 and 0.1M NH_4PF_6 in MeCN. In the case of Q1, a stripping wave appears both under N_2 and CO_2, and it appears that there is some sort of side reaction. While it appears that there is a shift under CO_2, spectroelectrochemical UV-Vis studies (**Figure 3.4a**) indicate that binding is not occurring. There also appears to be a reaction occurring under CO_2 for Q6. To probe if CO_2 binding was truly occurring, spectroelectrochemical UV-Visible studies were performed, and there was no new species formed in the UV-Visible spectrum in the presence of CO_2 (**Figure 3.4c**).
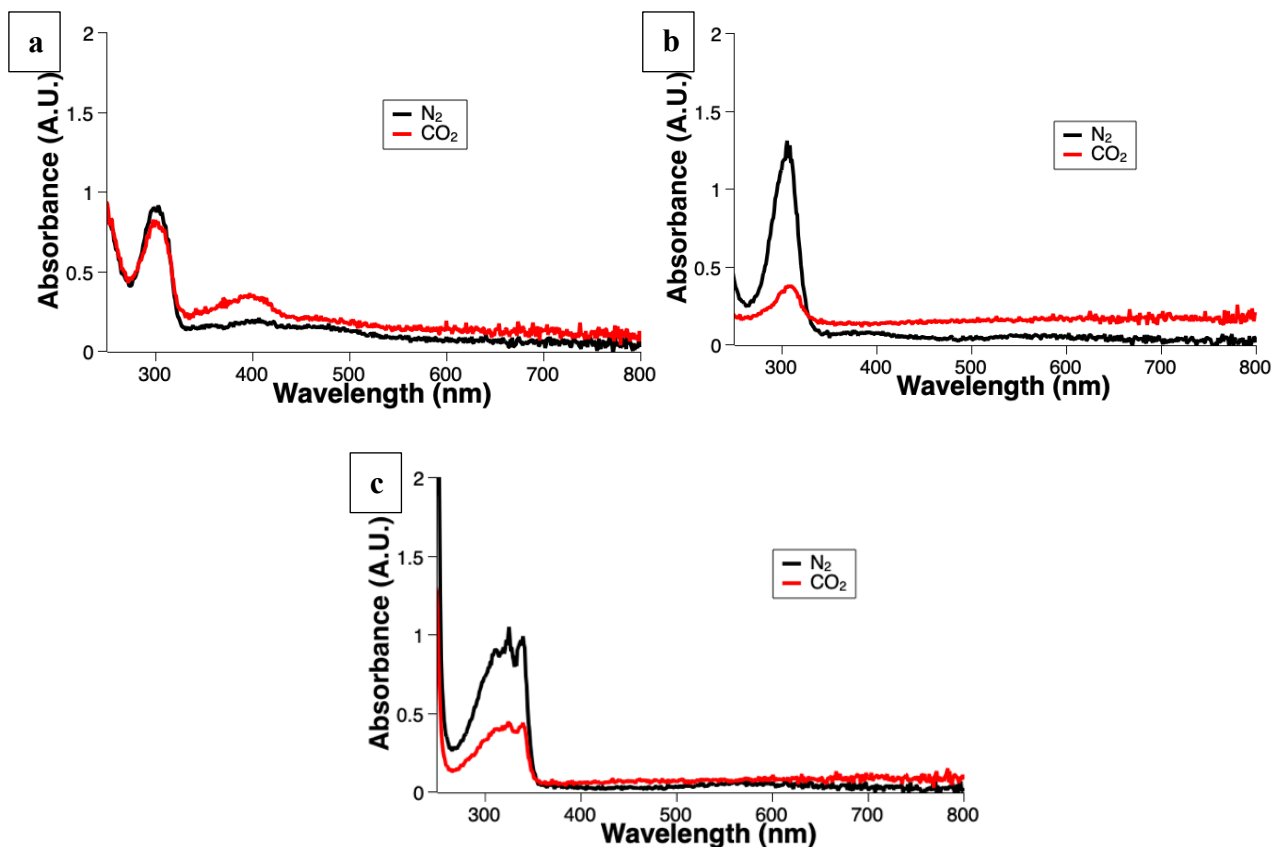
Figure 3.4. UV-visible spectra of Q1 dianion (**a**), Q4 dianion (**b**), and Q6 dianion (**c**) in NH_4PF_6 under N_2 (black trace) and CO_2 (red trace). The lack of appearance of new peaks between the N_2 and CO_2 spectra is indicative that there is no new species formed upon addition of CO_2.

The electrochemical and spectroelectrochemical studies with NH_4PF_6 as a supporting electrolyte were repeated in the presence of CO_2. There is no change in the either the CVs or the UV-visible spectrum upon reduction in comparison to the equivalent experiments run under N_2. The absence of change and the characteristic peak at $\lambda_{max} = 300$ nm indicates the inhibition of CO_2 binding which indicates formation of the hydroquinone inhibits CO_2 binding.

When TMA, TBA, and TOA were used as supporting electrolytes in acetonitrile, the characteristic two reversible reduction events were present in the CVs, however, their potentials were different depending on the electrolyte. The reduction potentials become more cathodic in the sequence $TMAPF_6$, $TBAPF_6$, $TOAPF_6$, with the latter leading to the most negative potentials

(**Figure 3.5**, black traces). However, the cathodic shift was most pronounced between $TMAPF_6$ and $TBAPF_6$ (30-90 mV) and much smaller between $TBAPF_6$ and $TOAPF_6$ (0-30 mV). From this data, it appears $TMAPF_6$ has the most significant effect on stabilizing the dianion, leading to more facile reduction.

Upon the addition of CO_2, an anodic potential shift of the second reduction was observed when $TMAPF_6$, $TBAPF_6$, and $TOAPF_6$ were used as the supporting electrolyte (**Figure 3.5,** red

Figure 3.5. Cyclic voltammograms of Q1, Q4, and Q6 for the alkylammonium supporting electrolytes.
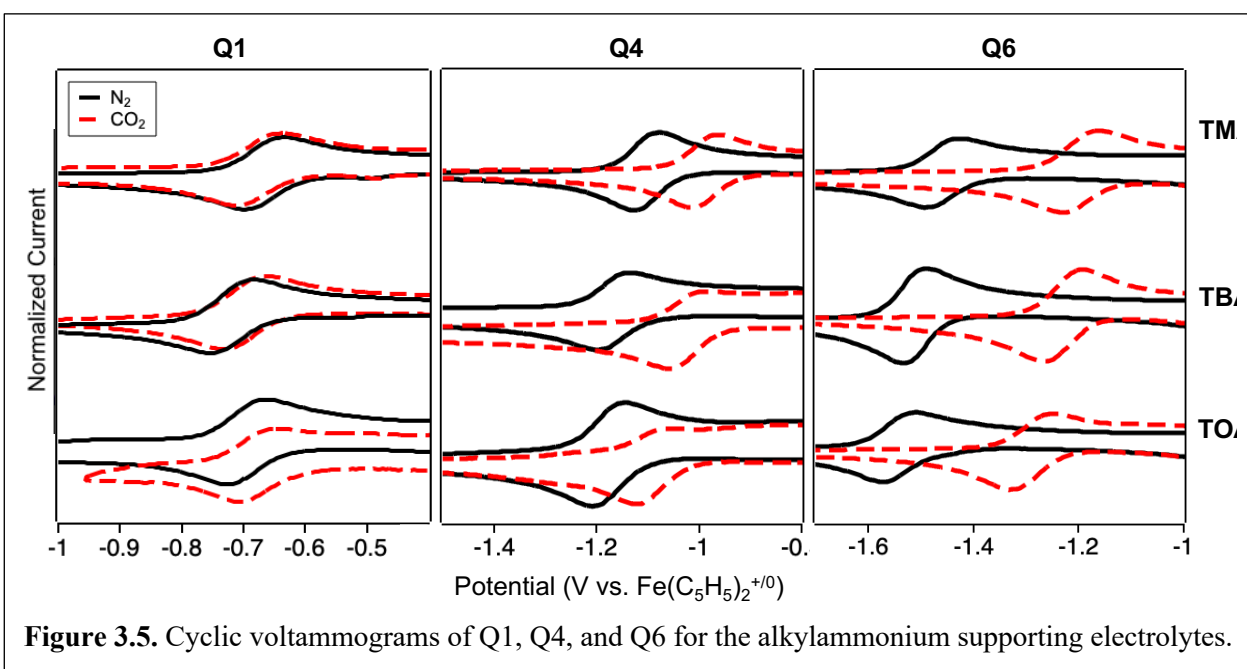
traces). The reduction potential shift indicates an EC event, where a chemical step (C, CO_2 binding) occurs upon reduction (E) to the dianion. CO_2 binding affinities were found for each of the quinone and supporting electrolyte pairs using a method similar to the open circuit potential.[6] Cyclic voltammograms were taken with varied concentrations of CO_2 counterbalanced with N_2 using a gas mixing apparatus (more information in Appendix A). The change in the reduction potential was plotted versus the log of the concentration of CO_2 to give a linear relationship. The y-intercept of the line correlated to the log K_{CO_2}, and the standard deviation of the y-intercept was used to find the associated error of each value. These values are reported in **Table 3.2**. This method is not

commonly used in literature but was used for these experiments to understand the significance of

the use of different supporting electrolyte salts with differing concentrations of CO_2.

Table 3.2. A comparison of reduction potential and CO_2 binding affinities when different chain lengths of alkylammonium are used as supporting electrolyte.

Compound		TMAPF$_6$	TBAPF$_6$	TOAPF$_6$
Q1	$E_{1/2}^2$ (V vs. Fe(C$_5$H$_5$)$_2^{+/0}$)	−0.67	−0.70	−0.70
	Log K_{CO_2} (M^{-1})	0	0.3	0.9
Q2	$E_{1/2}^2$ (V vs. Fe(C$_5$H$_5$)$_2^{+/0}$)	−0.90	−0.93	−0.95
	Log K_{CO_2} (M^{-1})	3.8 ± 0.2	4.0 ± 0.1	3.3 ± 0.3
Q3	$E_{1/2}^2$ (V vs. Fe(C$_5$H$_5$)$_2^{+/0}$)	−1.12	−1.15	−1.18
	Log K_{CO_2} (M^{-1})	2.3 ± 0.3	2.9 ± 0.5	3.0 ± 0.5
Q4	$E_{1/2}^2$ (V vs. Fe(C$_5$H$_5$)$_2^{+/0}$)	−1.10	−1.17	−1.17
	Log K_{CO_2} (M^{-1})	3.3 ± 0.3	3.0 ± 0.6	3.0 ± 0.4
Q5	$E_{1/2}^2$ (V vs. Fe(C$_5$H$_5$)$_2^{+/0}$)	−1.34	−1.41	−1.43
	Log K_{CO_2} (M^{-1})	6.3 ± 0.8	7.2 ± 0.7	7.3 ± 0.5
Q6	$E_{1/2}^2$ (V vs. Fe(C$_5$H$_5$)$_2^{+/0}$)	−1.46	−1.52	−1.54
	Log K_{CO_2} (M^{-1})	5.5 ± 0.5	6.2 ± 0.6	6.0 ± 0.2

To further investigate the CO_2 binding event observed in the CV, spectroelectrochemical

UV-visible measurements were taken using a representative set of quinones (Q1, Q4, and Q6,

Figures 3.2). of the quinone dianion changed in the presence of CO_2 compared to N$_2$ (**Figures 3.7-**

3.9). The dianionic species were formed electrochemically *in-situ*, and more information about how these experiments were performed can be found in section 3.4.2. The appearance of new peaks between the N_2 and CO_2 spectra is indicative that there is a new species formed upon addition of CO_2. These results are consistent with the formation of a CO_2-adduct. However, CO_2 binding affinity values cannot be extrapolated from this data. Because each of the dianion species are formed *in-situ*, while the initial concentrations of the neutral quinone are the same in each run, the dianion has different intensities. It is interesting to note that the electrolyte appears to have an effect on the UV-visible spectra of not only the CO_2 adduct species, but also the quinone dianion in the presence of N_2.
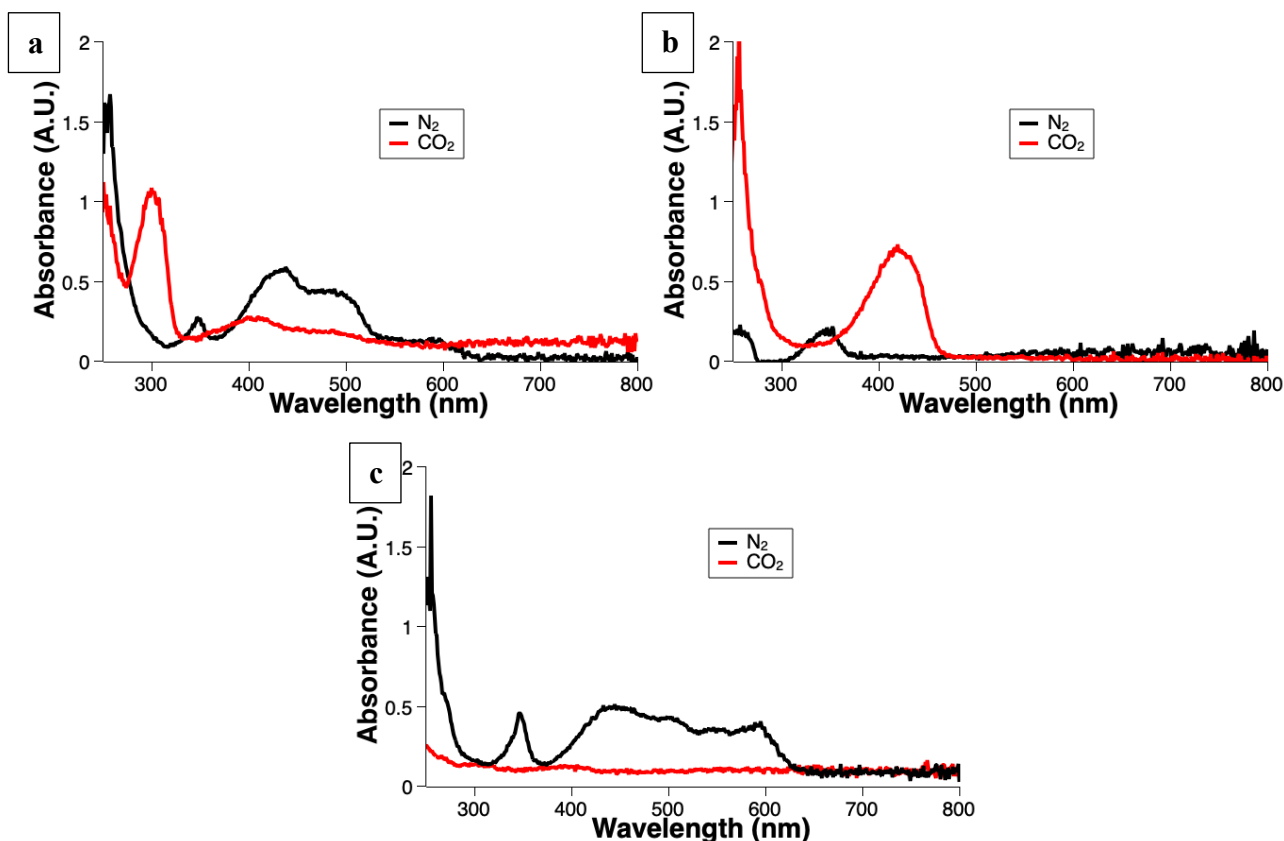
Figure 3.6. Spectroelectrochemical UV-visible spectra of **Q1** dianion in (**a**) TMAPF$_6$, (**b**) TBAPF$_6$, and (**c**) TOAPF$_6$ under N_2 (black trace) and CO_2 (red trace).
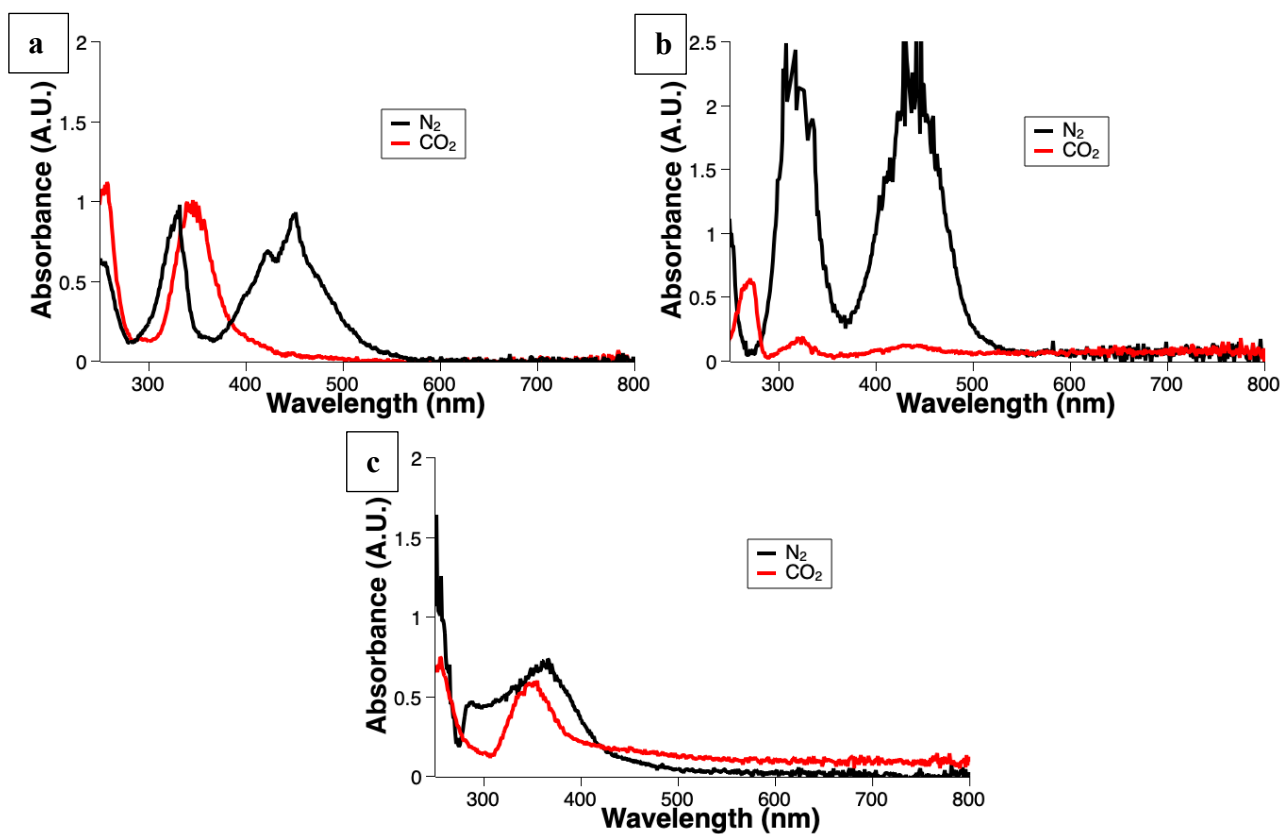
Figure 3.7. UV-Visible spectra of Q4 dianion in (**a**) TMAPF$_6$, (**b**) TBAPF$_6$, and (**c**) TOAPF$_6$ under N$_2$ (black trace) and CO$_2$ (red trace).
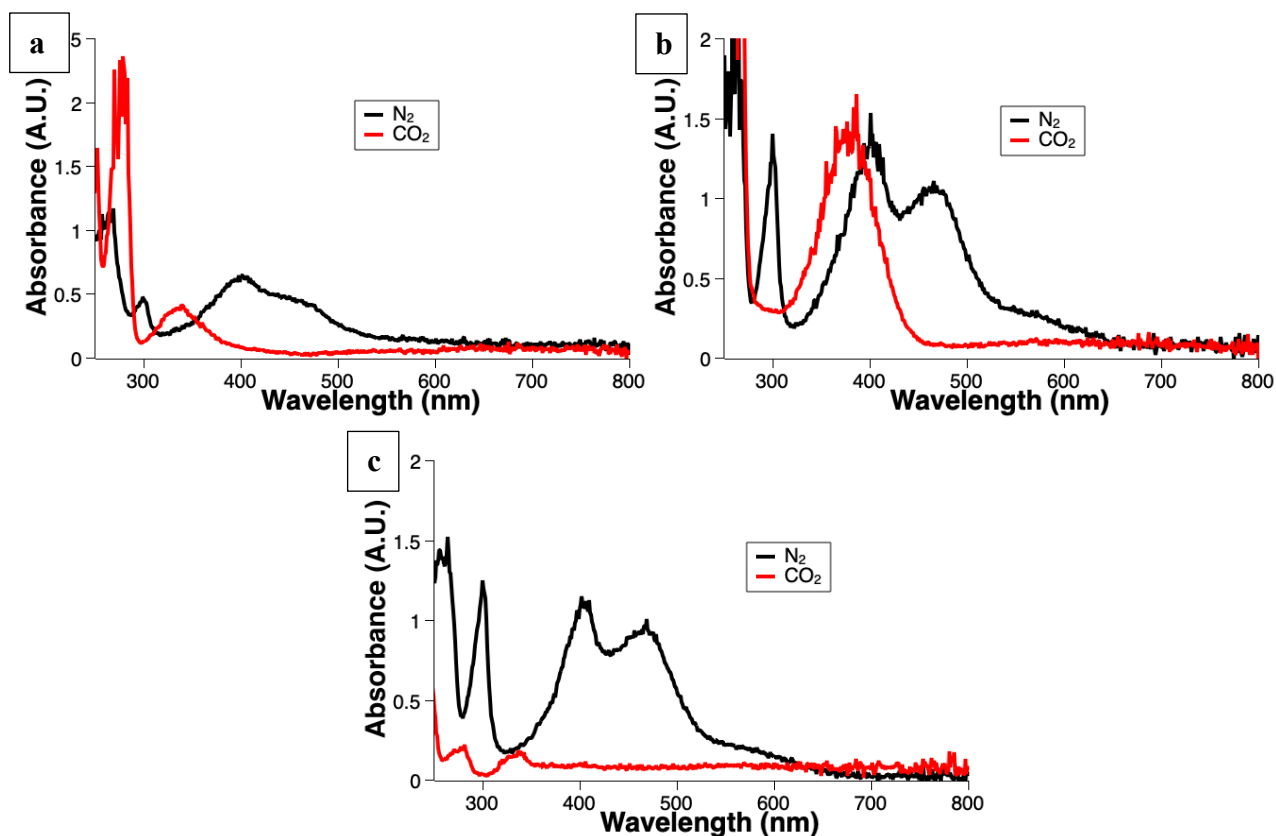
Figure 3.8. UV-visible spectra of Q6 dianion in (**a**) TMAPF$_6$, (**b**) TBAPF$_6$, and (**c**) TOAPF$_6$ under N$_2$ (black trace) and CO$_2$ (red trace).

3.2.2 Lewis acidic Alkali and Alkaline Earth Metals as Supporting Electrolyte

The addition of Lewis acids is known to anodically shift the reduction potential.[14–18] Nagaoka et al. studied the redox behavior of a series of carbonyl compounds, and they were able to quantify the binding affinity of sodium, lithium, and barium to the 9,10-phenanthrene-semi-quinone in DMF. It was found that the association constants ranged from log K = 3.2-6.2, with sodium having the weakest association and barium having the strongest association.[15] Dubois and coworkers measured a log K_{CO_2} of 2.7 for the 9,10-phenanthrene-semi-quinone.[7] These studies

suggests that the ion-pairing association would be stronger than the binding of CO_2. However, lithium and sodium have been used as electrolyte support in capture studies.[25]

Salts with lithium, sodium, potassium, calcium, and barium cations and trifluoromethanesulfonate anions were used as supporting electrolyte for electrochemical study of Q1, Q4, and Q6. CVs of all three quinones under N_2 with each of the alkali and alkaline earth ions resulted in positively shifted reduction potentials in comparison to tetrabutylammonium ion. However, the CVs lacked the characteristic two reversible redox events commonly seen in quinones (**Figure 3.10-3.24**); the loss of the two reversible redox events indicate binding of the alkali or alkaline earth metals to the semiquinone and/or quinone dianion.

Upon the addition of CO_2, the anodic shift in the reduction potential that indicates CO_2 binding is notably smaller. UV-visible study of the quinone dianion that was formed *in-situ* via spectroelectrochemistry suggests that a new species is formed in the presence of CO_2 in all cases of the Lewis acid.

When lithium trifluoromethanesulfonate was used as a supporting electrolyte, there was only one oxidative feature for all three of the quinones (**Figures 3.10-3.12**). Similar to what was reported in the case of 6QC (discussed further in Chapter 6), there was not a clear, reversible formation of the dianion. Under N_2, for Q6, a stripping wave appeared upon oxidation; this stripping feature was reproducible. Upon addition of CO_2, there were changes in the CV, but none were conclusive enough to calculate a binding affinity. The combination of quinones were studied using spectroelectrochemistry (**Figures 3.13-3.15**), and it was found that for Q1, there was a shift in the UV-visible spectrum, which indicates the formation of a CO_2 adduct; for Q4, there was no

detectable change; for Q6, the peak at 397 nm disappeared, indicating that a CO_2-adduct species was formed.
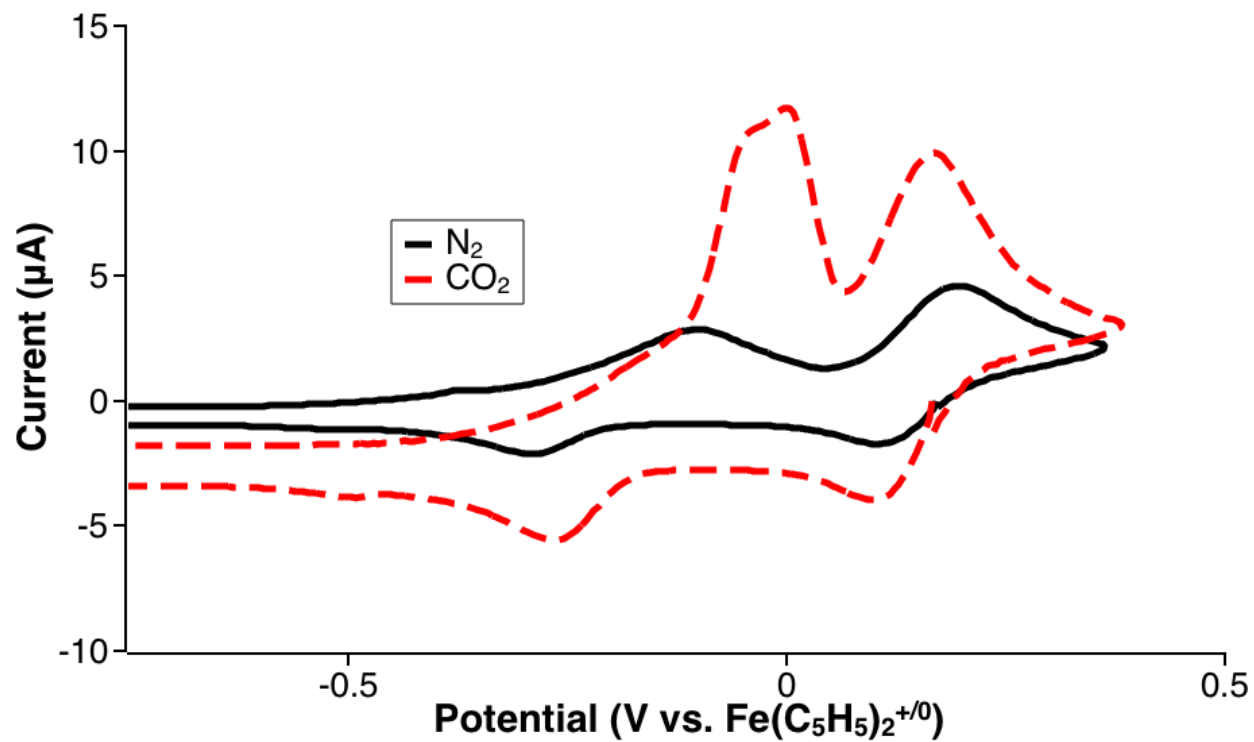
Figure 3.9. Cyclic voltammetry of 0.001M Q1 and 0.1M LiOTf in MeCN.
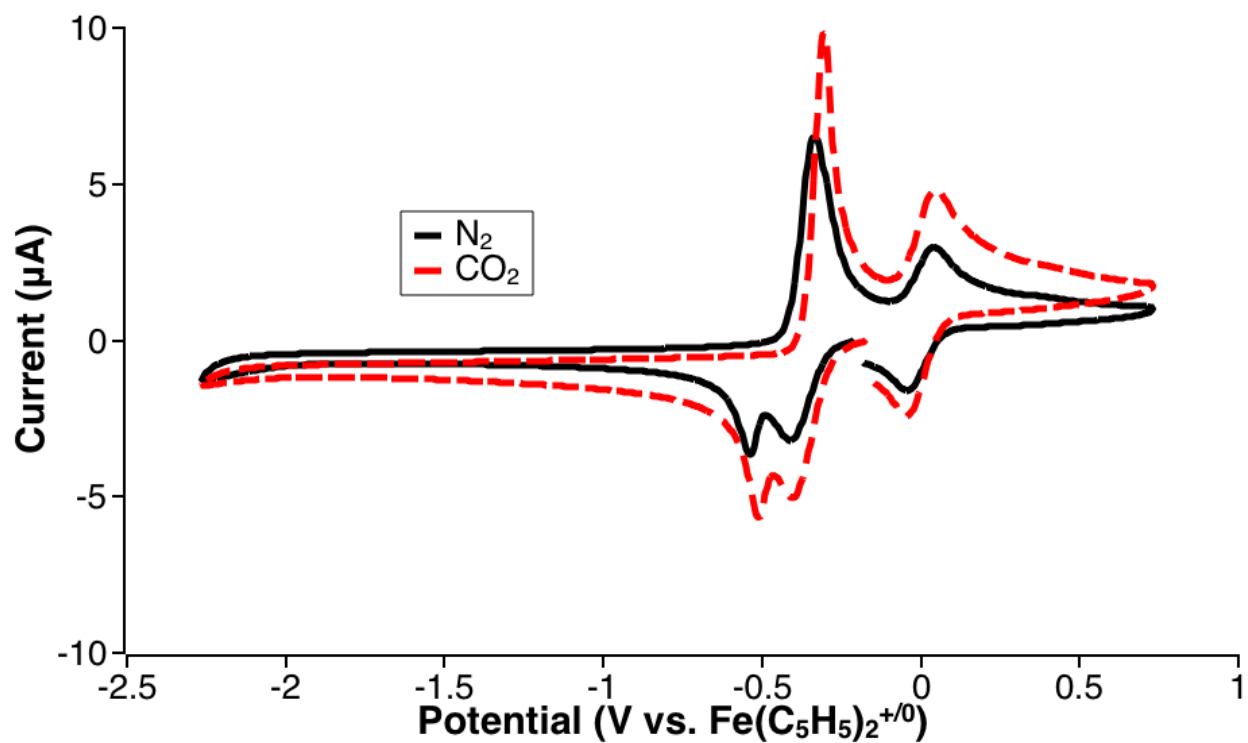
Figure 3.10. Cyclic voltammetry of 0.001M Q4 and 0.1M LiOTf in MeCN.
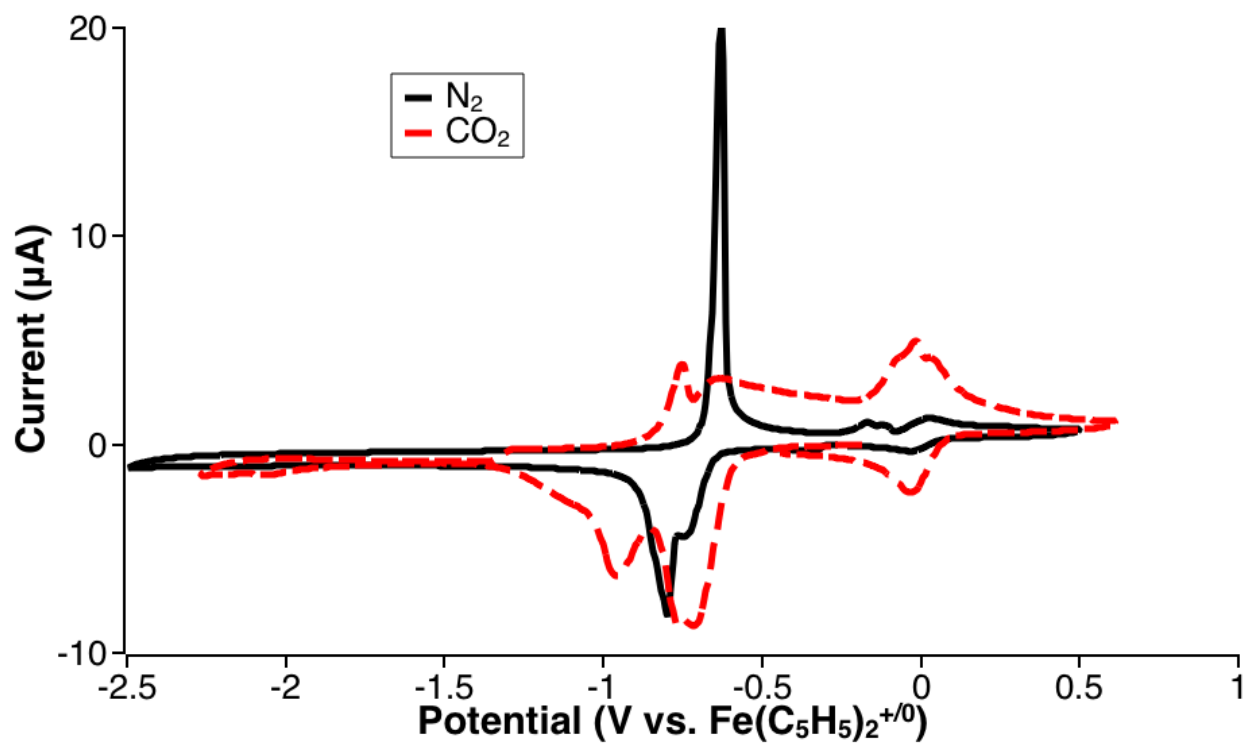
Figure 3.11. Cyclic voltammetry of 0.001M Q6 and 0.1M LiOTf in MeCN.
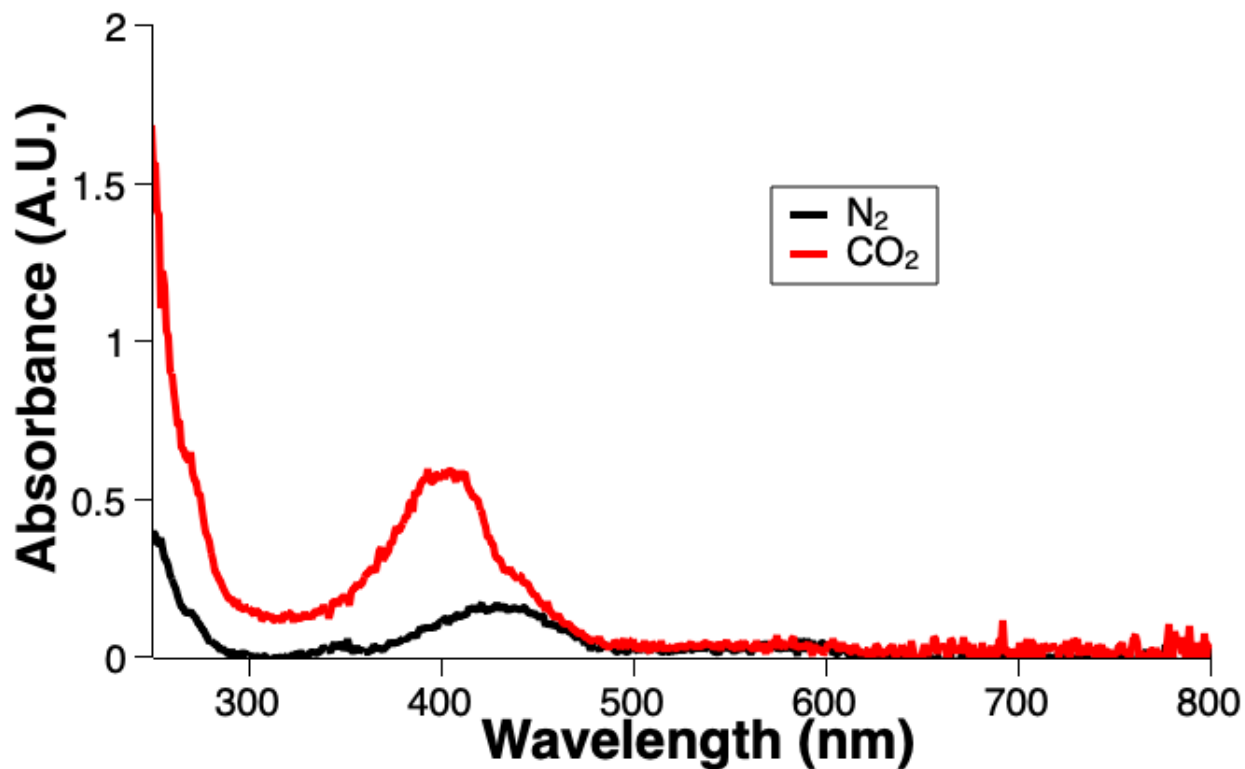
Figure 3.12. UV-visible spectra of Q1 dianion in LiOTf under N_2 (black trace) and CO_2 (red trace).
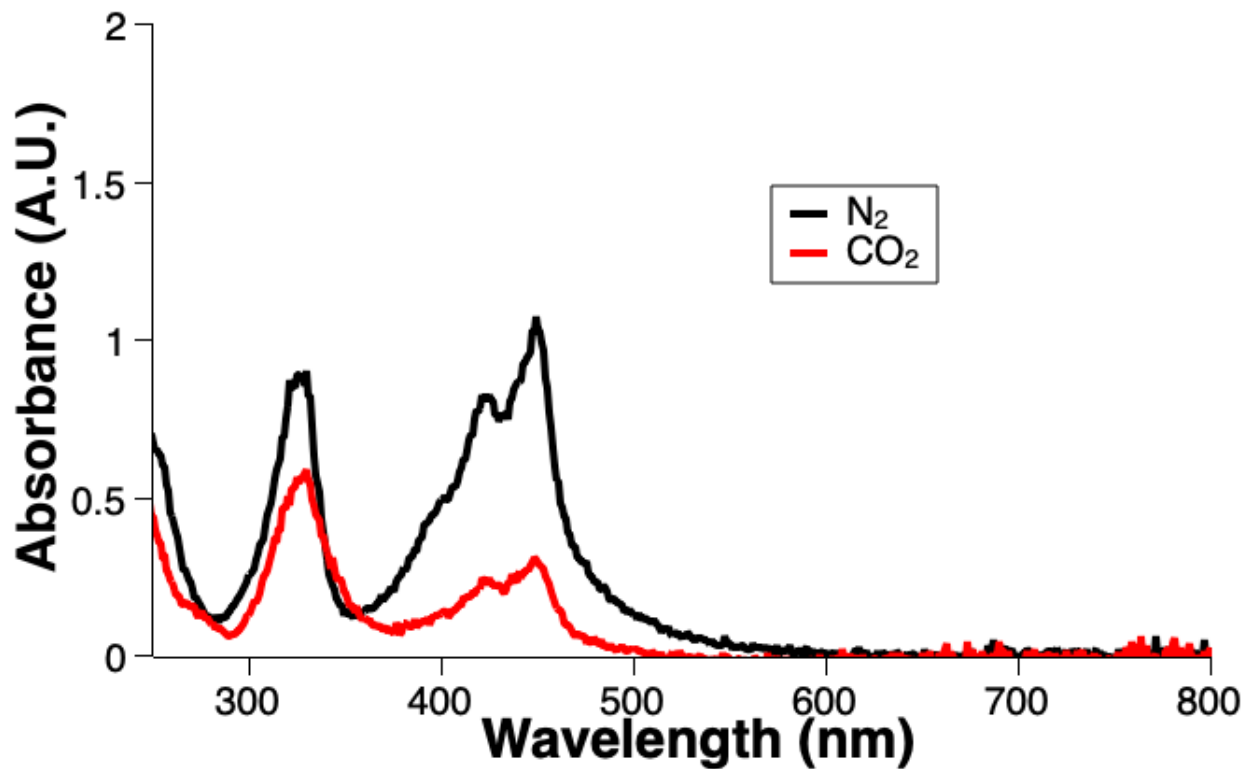
Figure 3.13. UV-visible spectra of Q4 dianion in LiOTf under N_2 (black trace) and CO_2 (red trace).
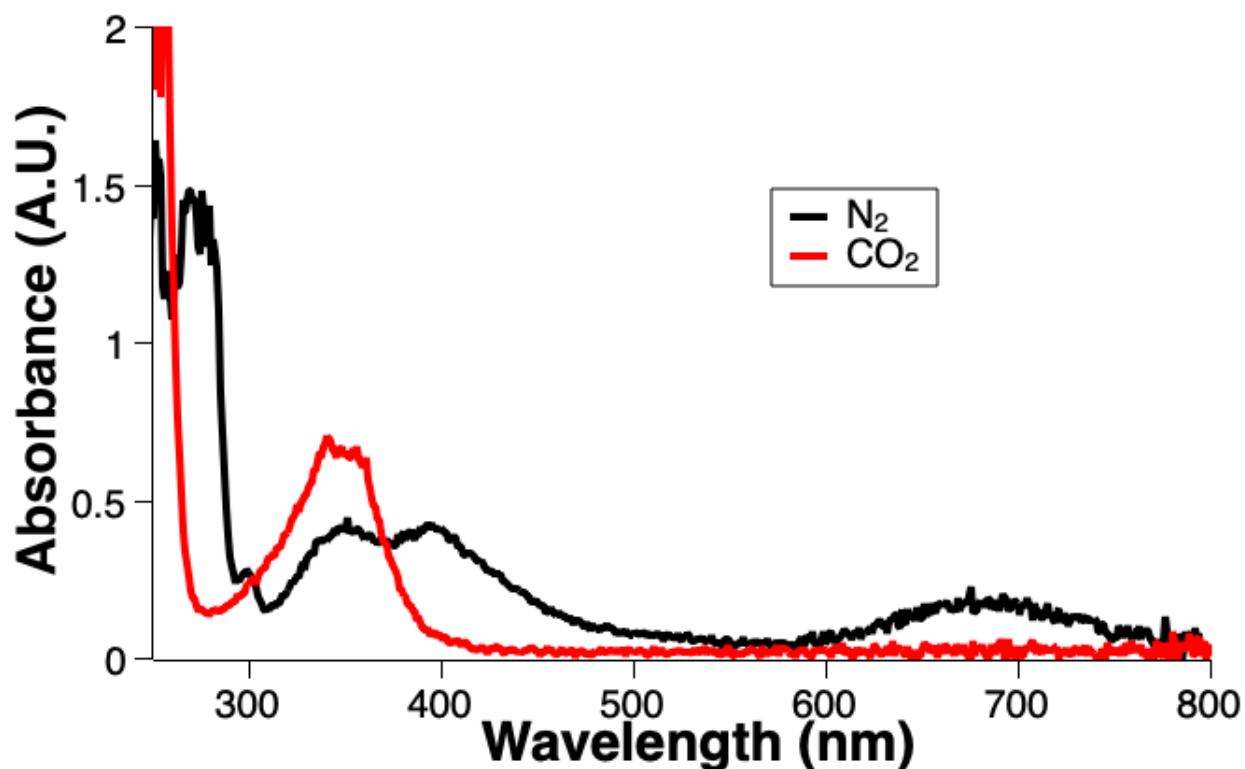
Figure 3.14. UV-visible spectra of Q6 dianion in LiOTf under N_2 (black trace) and CO_2 (red trace).

When sodium trifluoromethanesulfonate was used as a supporting electrolyte, Q1 only had one reductive peak and one oxidative peak by CV (**Figure 3.16**). Upon addition of CO_2, the peaks shifted slightly in opposite directions. Q4 and Q6 had CVs that looked more similar to the quinones shown throughout the rest of this thesis, and addition of CO_2 resulted in anodic shift of the second reductive event (**Figure 3.17 and 3.18**). When studied using spectroelectrochemical UV-visible spectroscopy, Q1 had a new peak at ~400 nm in the presence of CO_2, indicating the formation of a CO_2 adduct (**Figure 3.19**). For Q4, the peaks at 330, 422, and 450 nm were all present without CO_2, but when the experiment was repeated in the presence of CO_2, these peaks were not present and a new, broad peak at 300 nm appeared (**Figure 3.20**). When the dianion of Q6 was formed *in-situ*, it did not have any notable peaks, but when formed in the presence of CO_2, a peak appeared at 365 nm, indicating CO_2 binding.
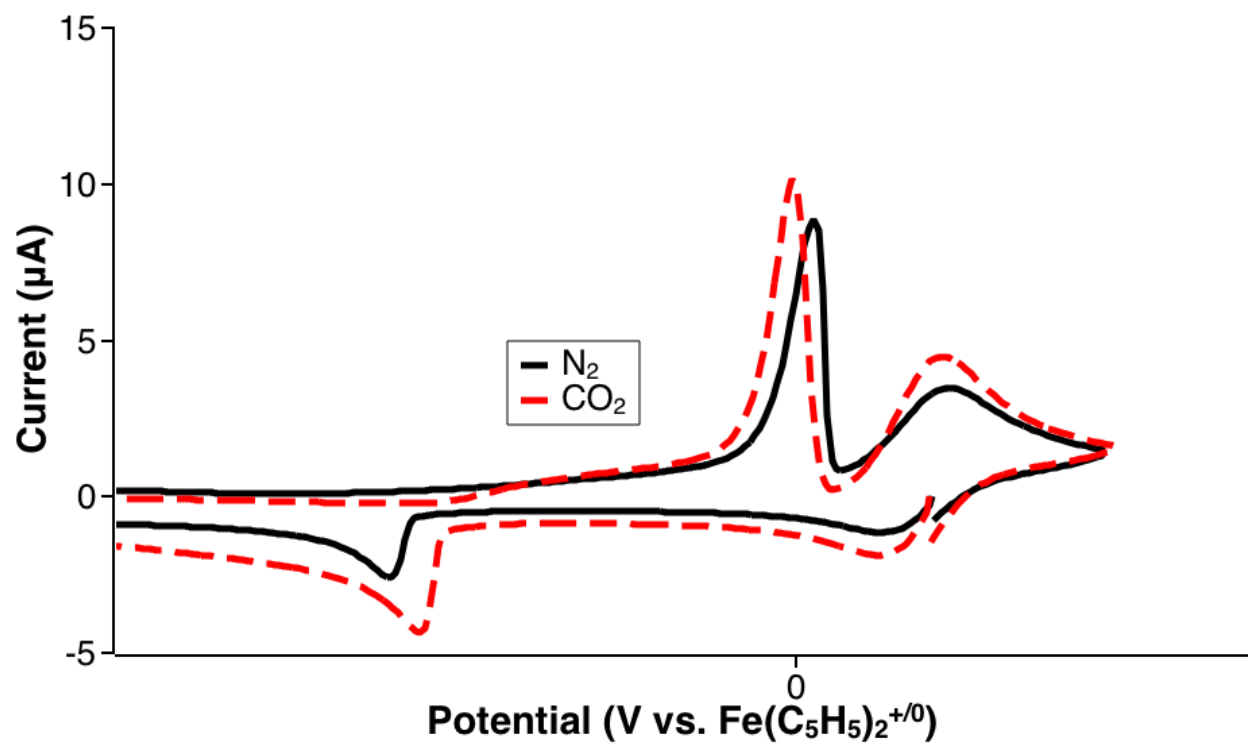
Figure 3.15. Cyclic voltammetry of 0.001M Q1 and 0.1M NaOTf in MeCN.
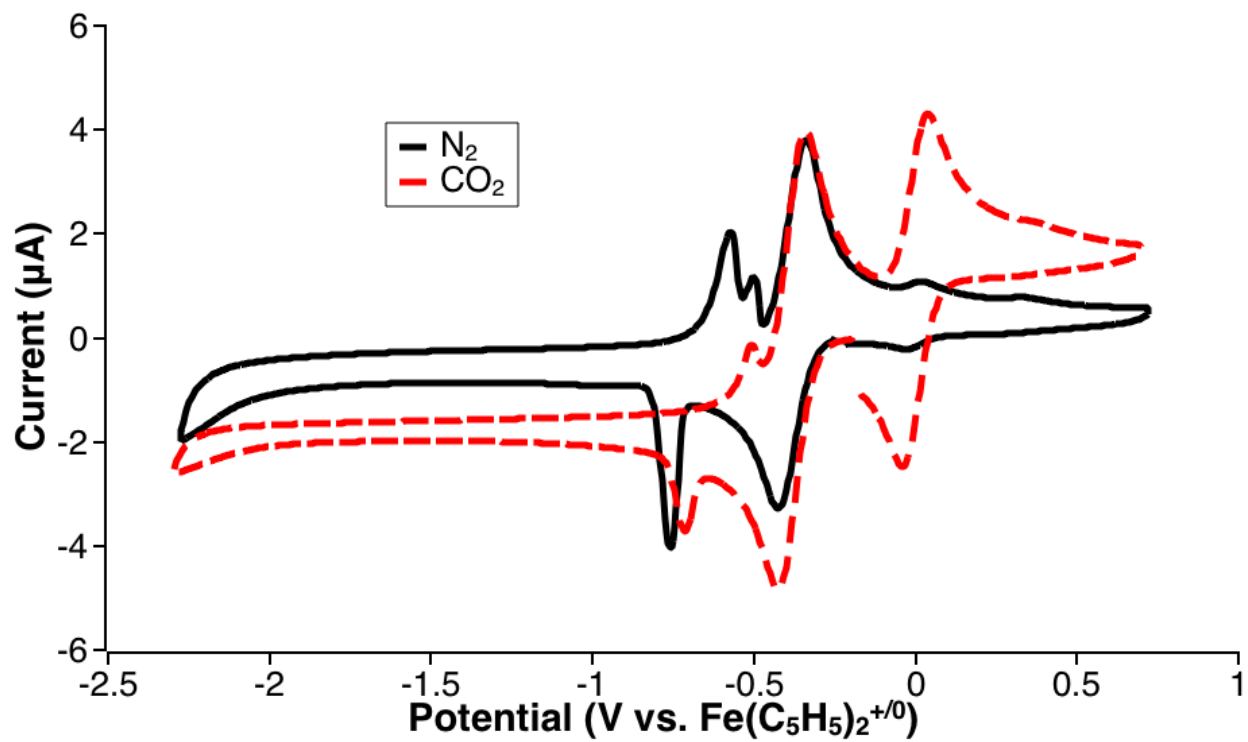
Figure 3.16. Cyclic voltammetry of 0.001M Q4 and 0.1M NaOTf in MeCN.
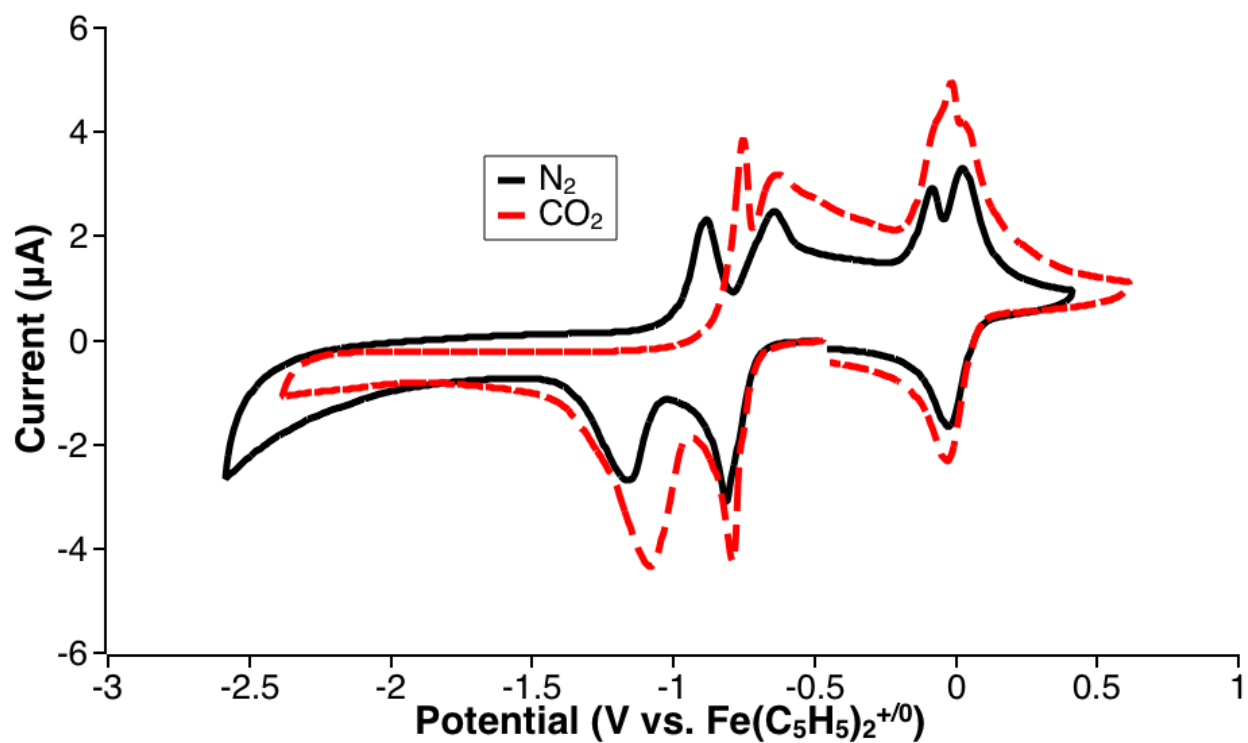
Figure 3.17. Cyclic voltammetry of 0.001M Q6 and 0.1M NaOTf in MeCN.
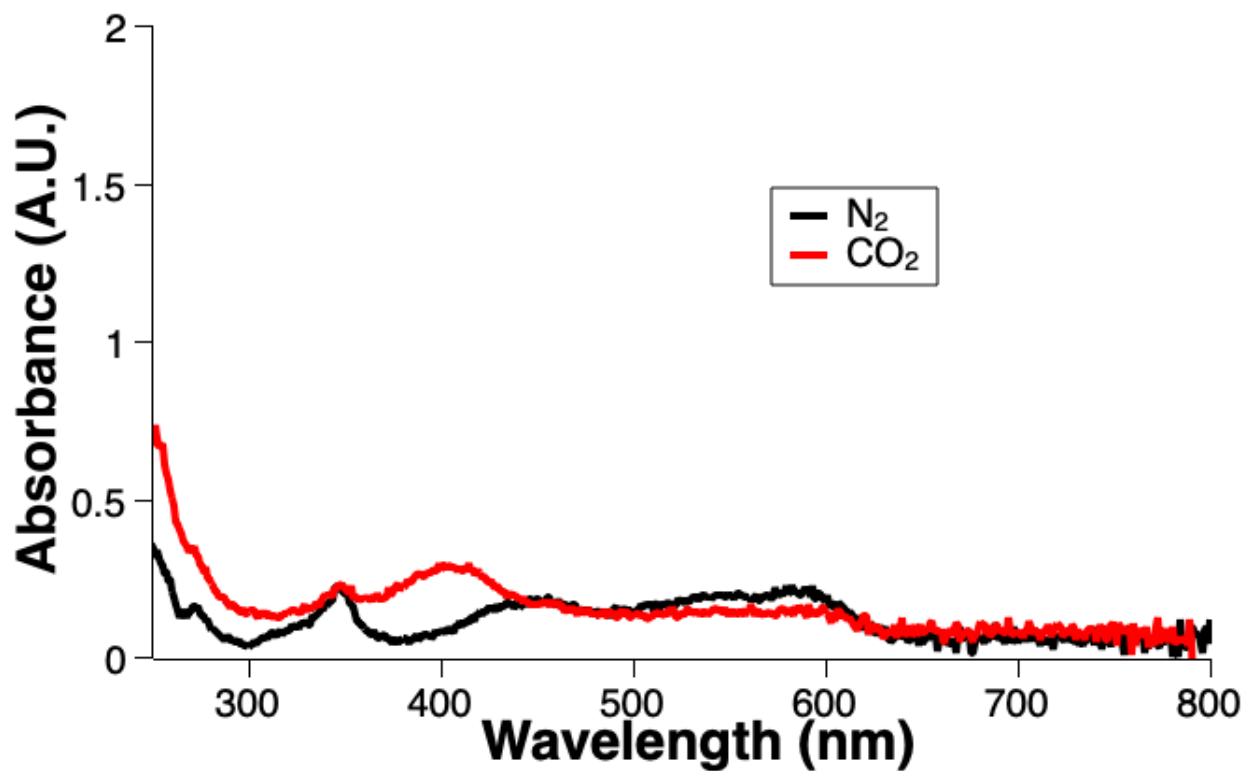
Figure 3.18. UV-visible spectra of Q1 dianion in NaOTf under N_2 (black trace) and CO_2 (red trace).
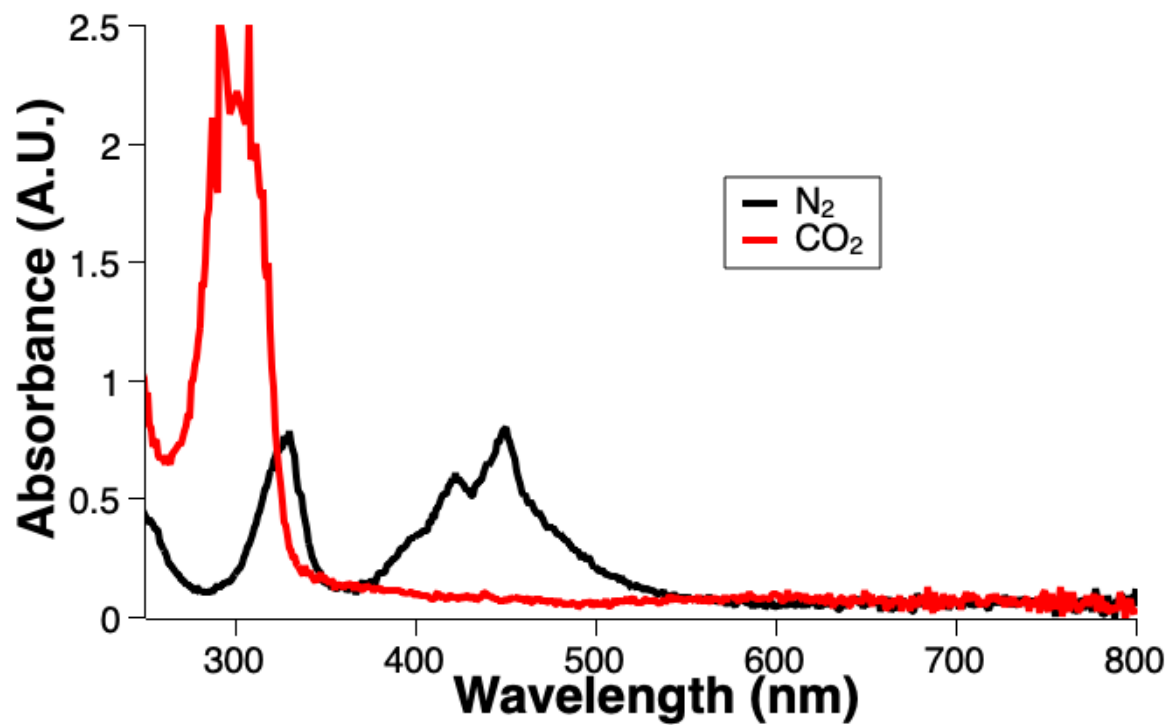
Figure 3.19. UV-visible spectra of Q4 dianion in NaOTf under N_2 (black trace) and CO_2 (red trace).
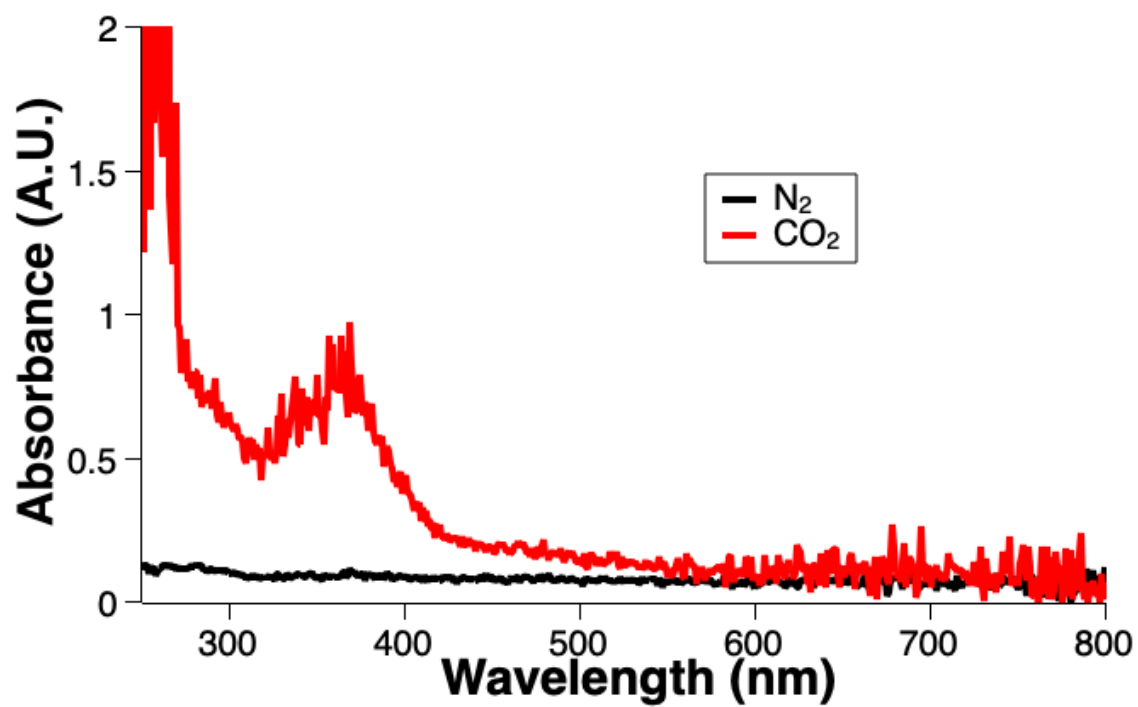
Figure 3.20. UV-visible spectra of Q6 dianion in NaOTf under N_2 (black trace) and CO_2 (red trace).

When potassium trifluoromethanesulfonate was used as a supporting electrolyte, Q1 only had one reductive peak and one oxidative peak by CV, however, it also featured another, much smaller reduction and oxidation as well (**Figure 3.22**). Upon addition of CO_2, the peaks shifted slightly in opposite directions, similarly to the CV of Q1 in the presence of sodium. Q4 and Q6 had one reversible feature that appeared similar to the peak commonly associated with formation of the radical anion, and another, smaller redox feature that looked to be the formation of the dianion (**Figure 3.23 and 3.24**). Addition of CO_2 resulted in a slight anodic shift of the second reductive event. When studied using spectroelectrochemical UV-visible spectroscopy, Q1 and Q4 both had a new, broad peak at ~300 nm in the presence of CO_2, indicating the formation of a CO_2 adduct (**Figure 3.25 and 3.26**). When the dianion of Q6 was formed *in-situ*, the UV-visible spectra in the presence and absence of CO_2 were completely different, showing that a CO_2 adduct had formed (**Figure 3.27**). Under N_2, there was a broad peak at 320 nm that was not at all present under CO_2, which had a peak at 390 nm.
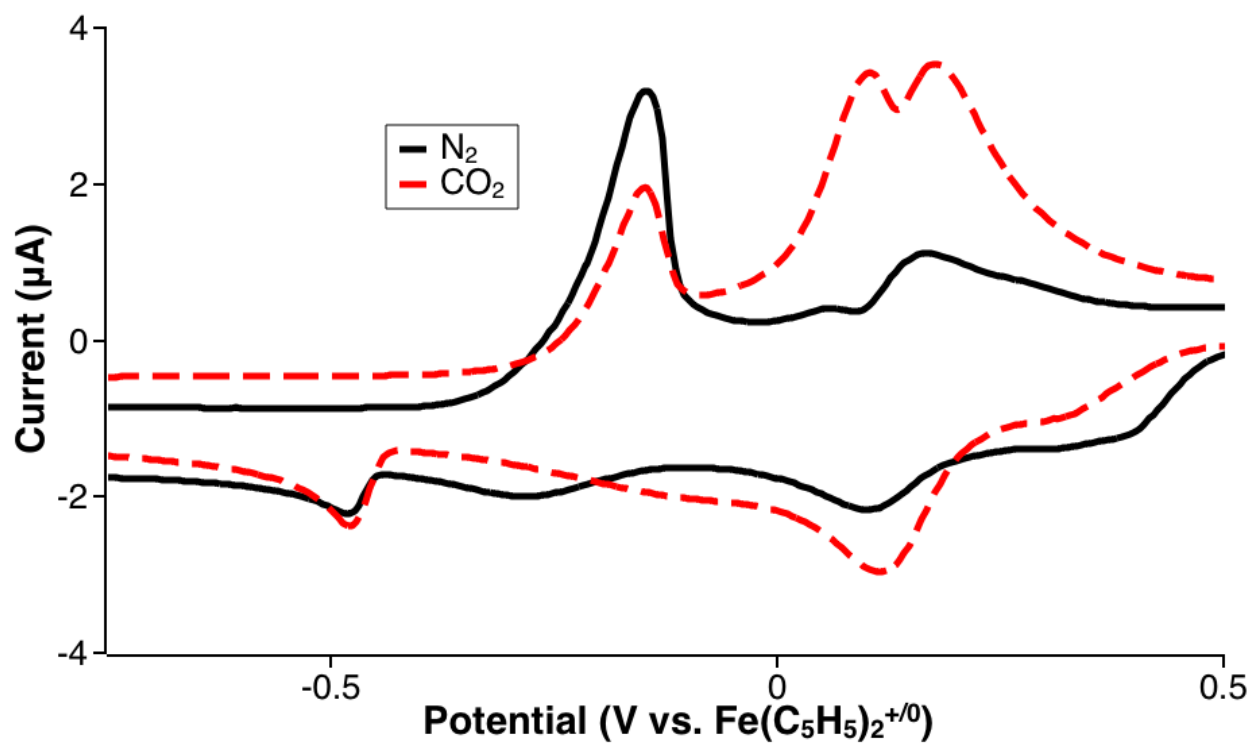
Figure 3.21. Cyclic voltammetry of 0.001M Q1 and 0.1M KOTf in MeCN.
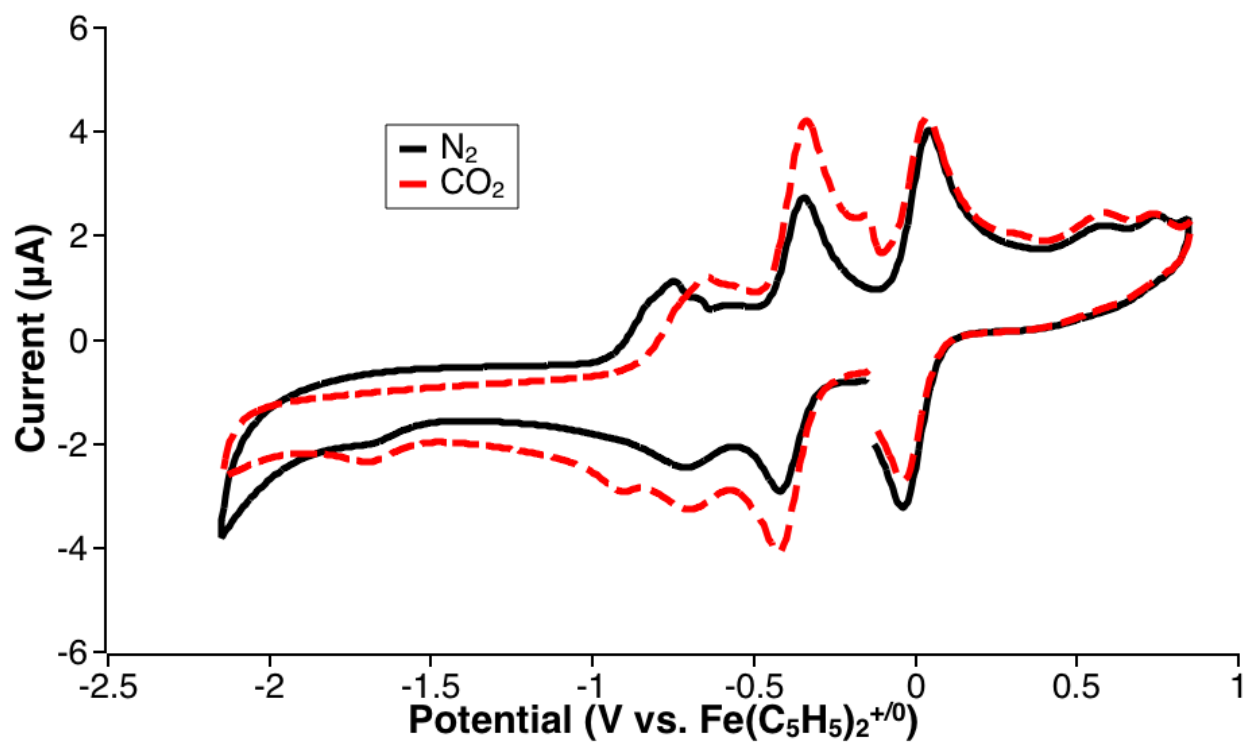
Figure 3.22. Cyclic voltammetry of 0.001M Q4 and 0.1M KOTf in MeCN.
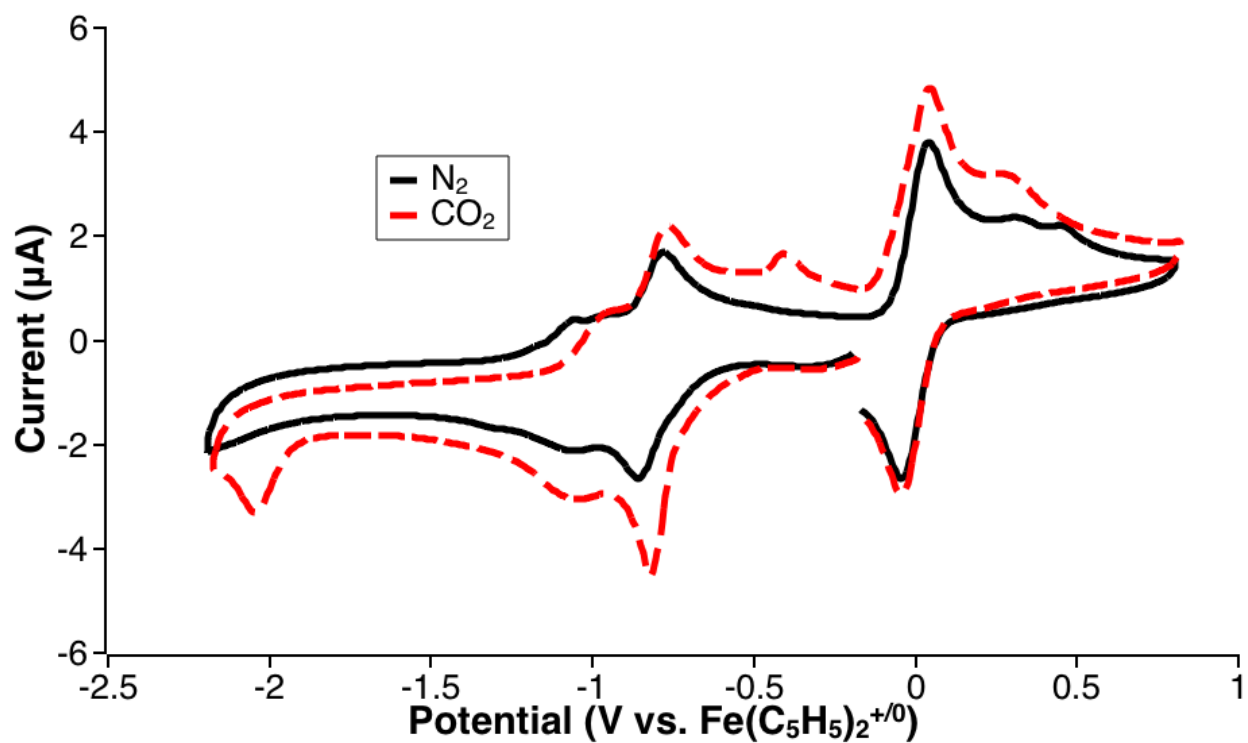
Figure 3.23. Cyclic voltammetry of 0.001M Q6 and 0.1M KOTf in MeCN.
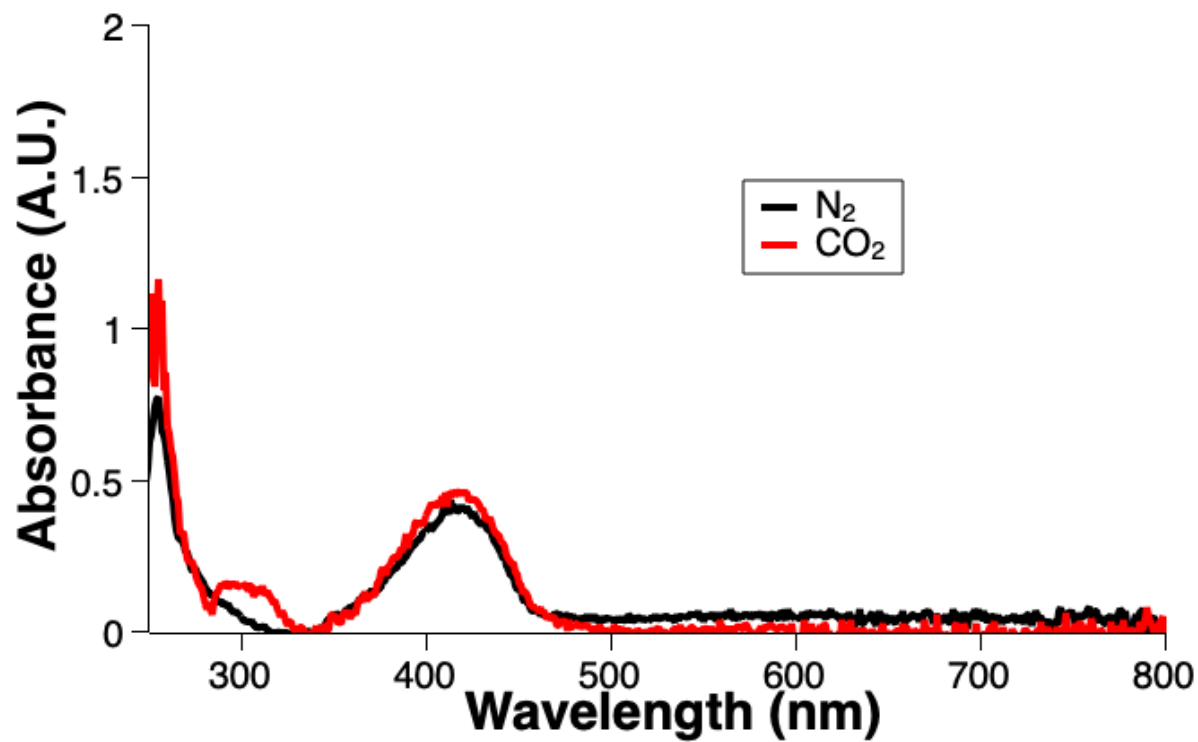
Figure 3.24. UV-visible spectra of Q1 dianion in KOTf under N_2 (black trace) and CO_2 (red trace).
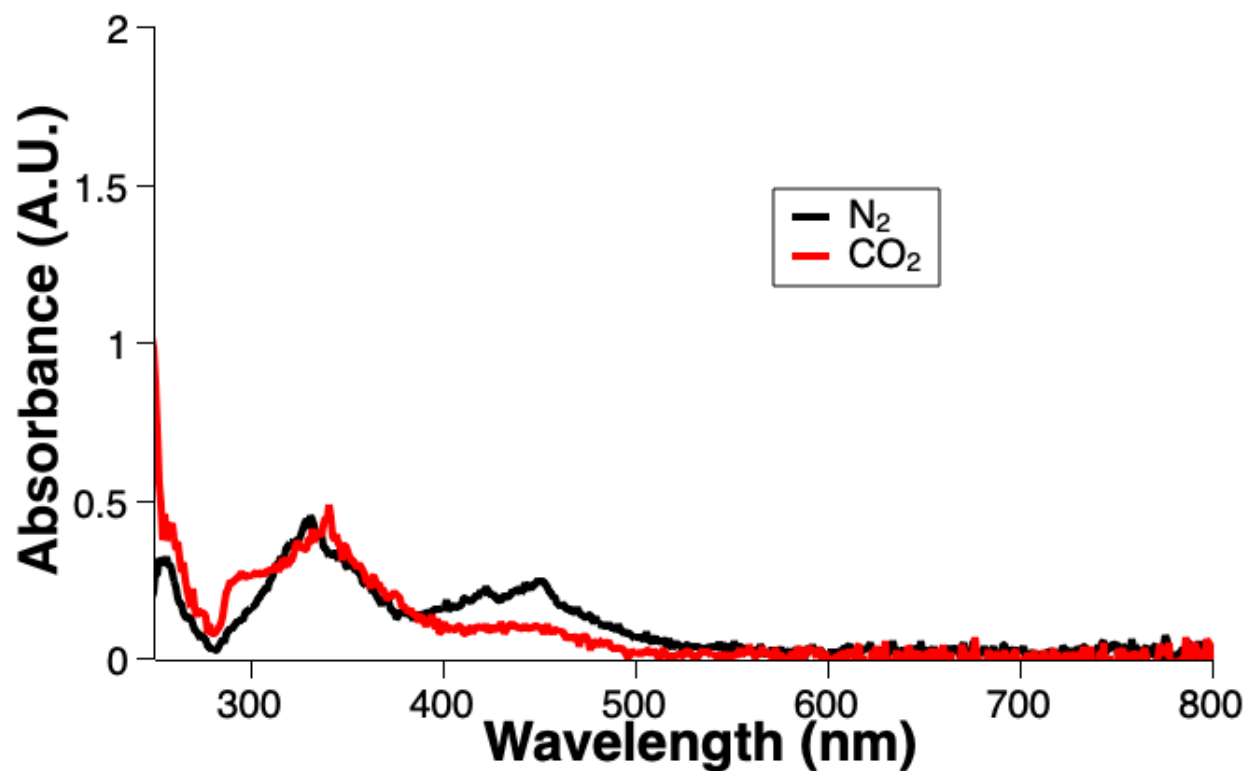
Figure 3.25. UV-visible spectra of Q4 dianion in KOTf under N_2 (black trace) and CO_2 (red trace).
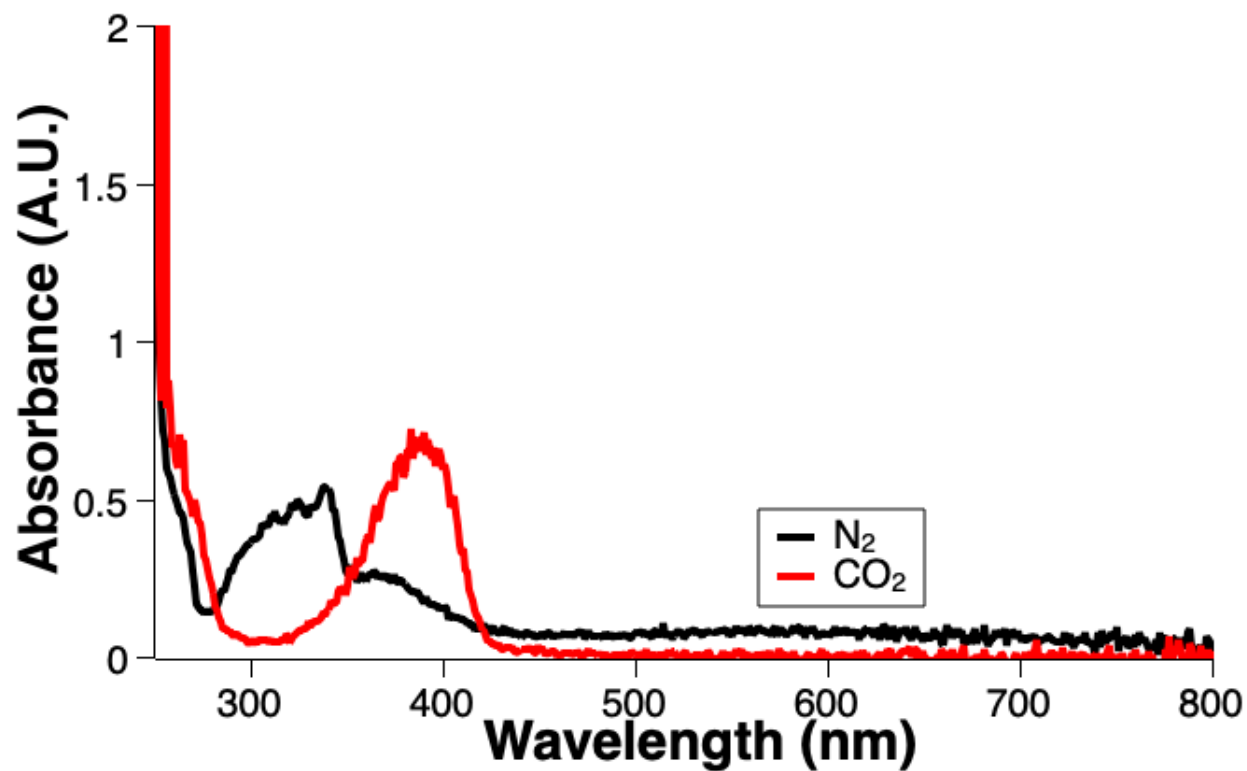
Figure 3.26. UV-visible spectra of Q6 dianion in KOTf under N_2 (black trace) and CO_2 (red trace).

When calcium trifluoromethanesulfonate was used as a supporting electrolyte, the cyclic voltammograms of Q1 and Q4 did not have notable changes in the presence of CO_2 (**Figure 3.28 and 3.29**). Q6 had CVs two reduction features (**Figure 3.30**). Addition of CO_2 resulted in one reversible redox event, similarly to the diamino-substituted quinone discussed in Chapter 2. When studied using spectroelectrochemical UV-visible spectroscopy, Q1 both had just one peak at ~395 nm in the presence of CO_2, indicating the formation of a CO_2 adduct (**Figure 3.31**). For Q4, a new peak appears at 345 nm, which is indicative of the CO_2 adduct. When the dianion of Q6 was formed *in-situ*, the UV-visible spectra in the presence and absence of CO_2 were once again completely different, showing that a CO_2 adduct had formed (**Figure 3.32**). Under N_2, there was a broad peak at 360 nm that was not at all present under CO_2, which had a peak at 330 nm.
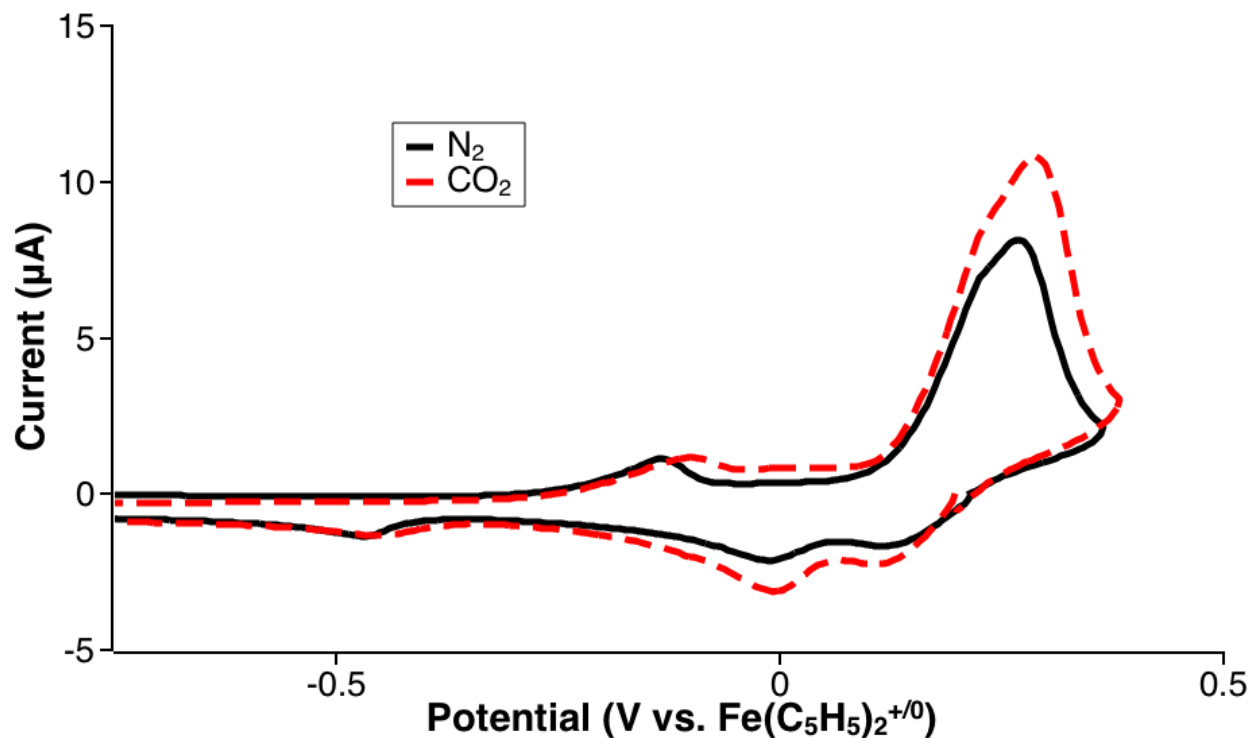
Figure 3.27. Cyclic voltammetry of 0.001M Q1 and 0.1M Ca (OTf)$_2$ in MeCN.
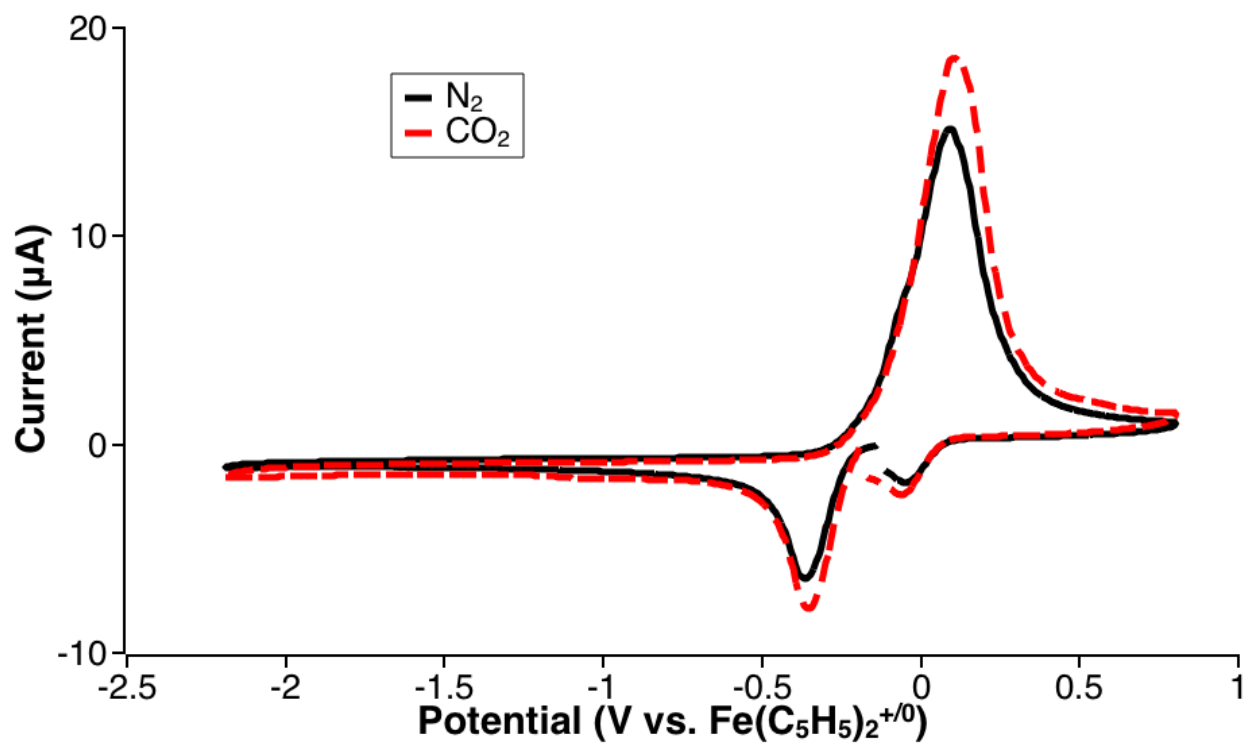
Figure 3.28. Cyclic voltammetry of 0.001M Q4 and 0.1M Ca $(OTf)_2$ in MeCN.
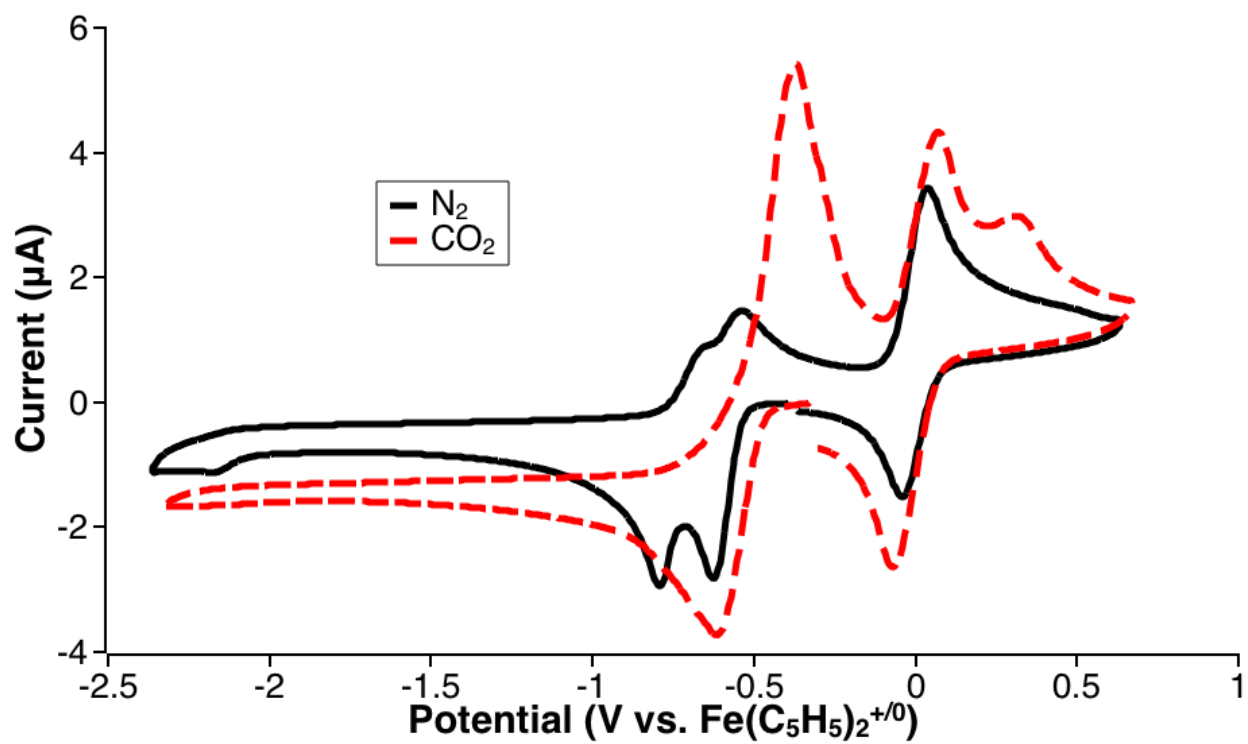
Figure 3.29. Cyclic voltammetry of 0.001M Q6 and 0.1M Ca $(OTf)_2$ in MeCN.
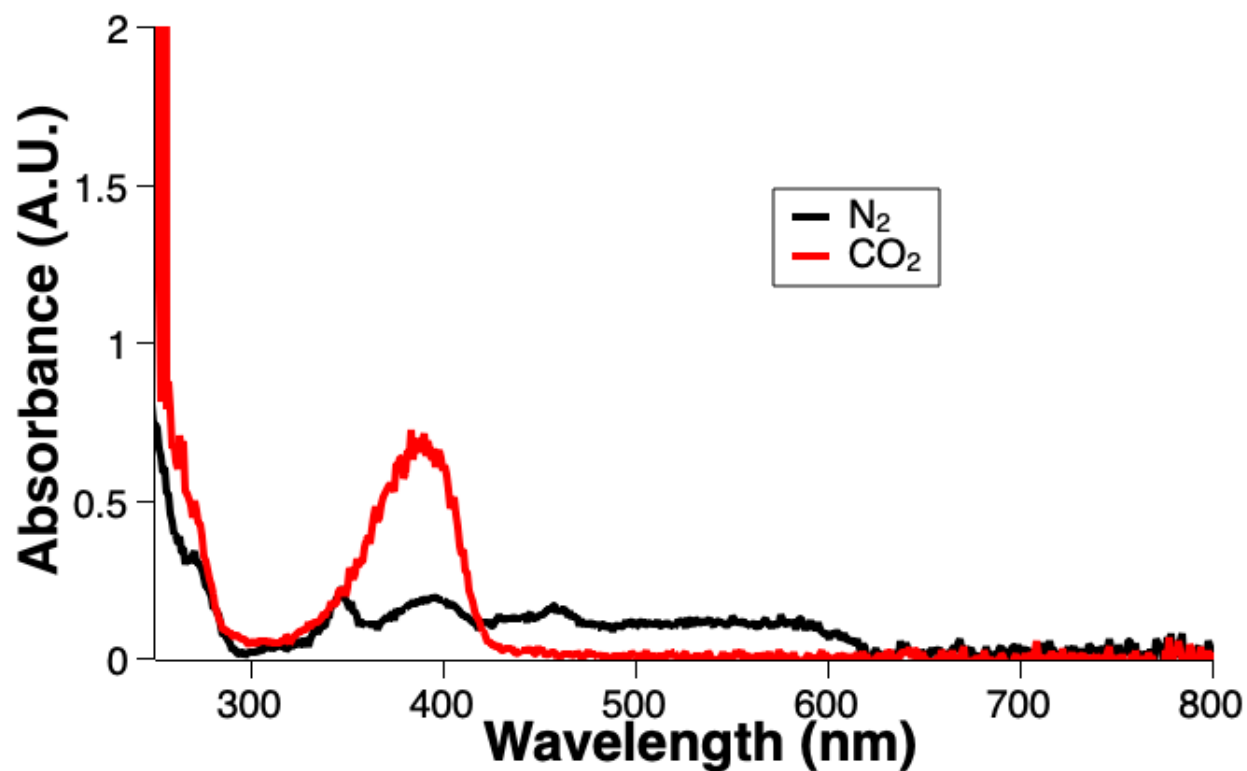
Figure 3.30. UV-visible spectra of Q1 dianion in Ca (OTf)$_2$ under N$_2$ (black trace) and CO$_2$ (red trace).
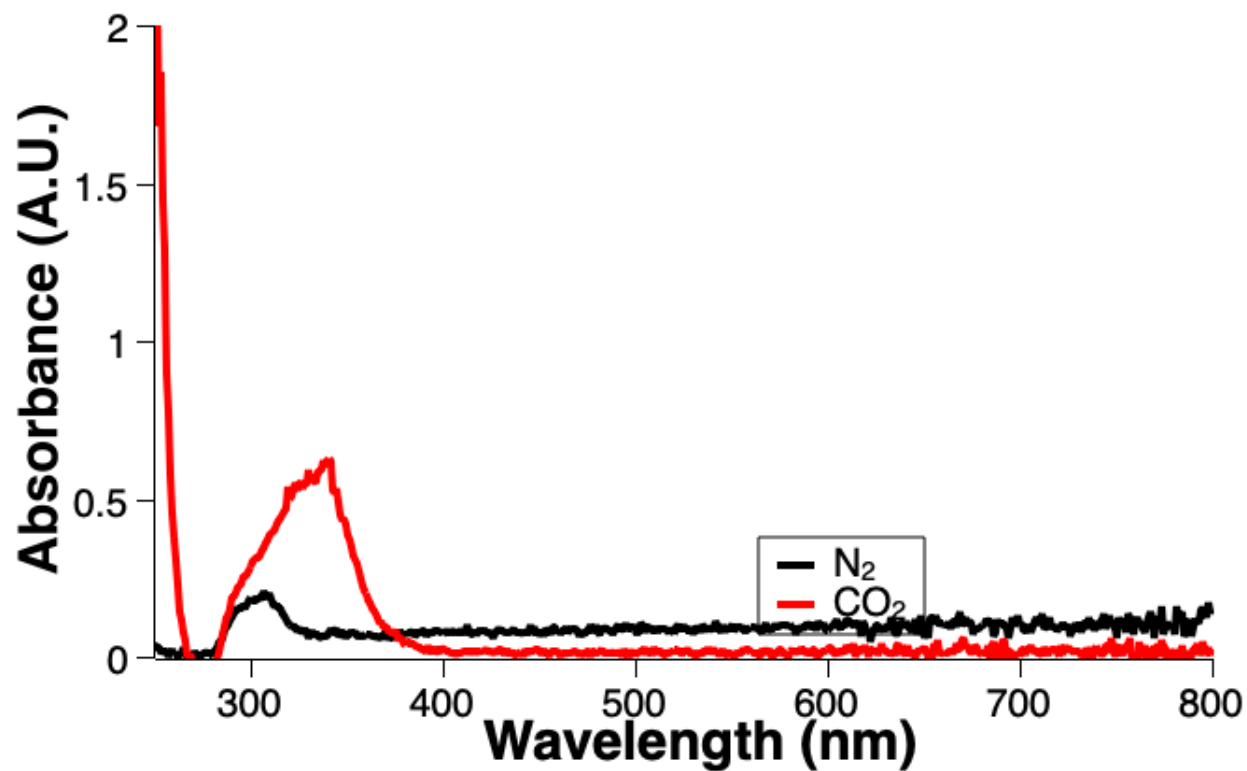
Figure 3.31. UV-visible spectra of Q4 dianion in Ca (OTf)$_2$ under N$_2$ (black trace) and CO$_2$ (red trace).
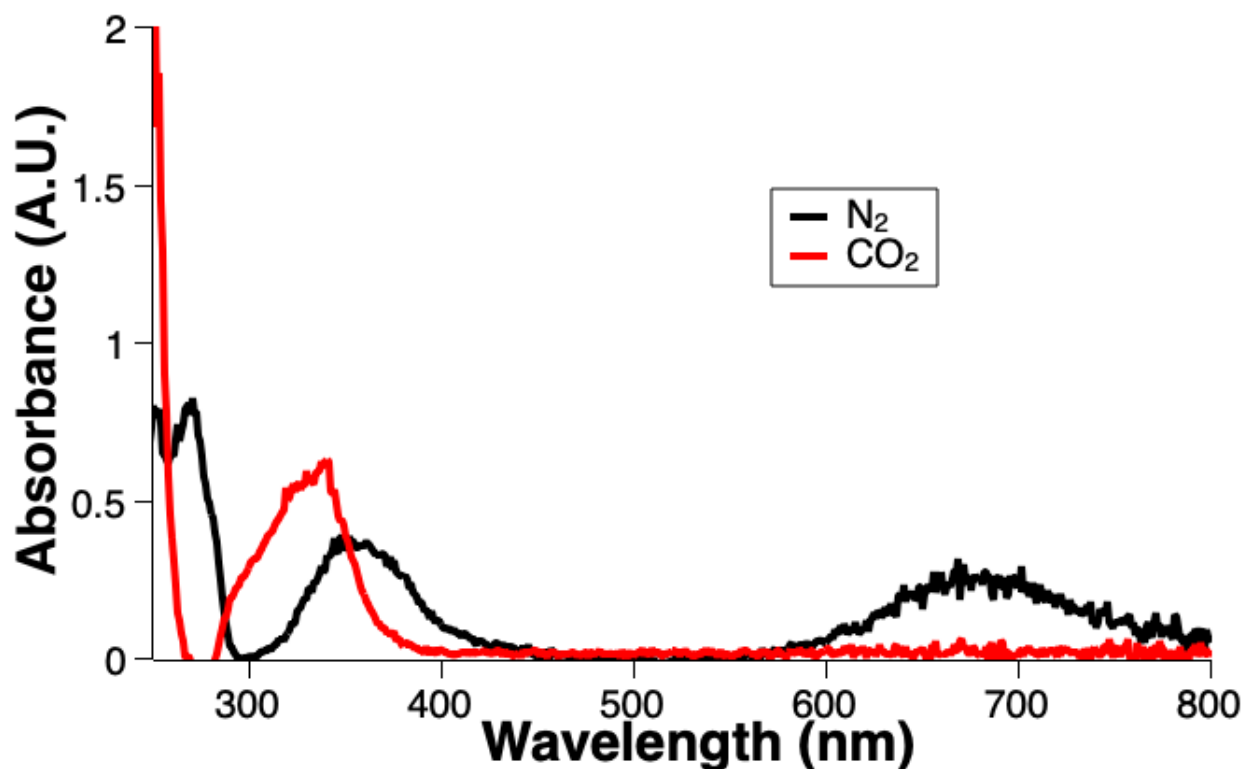
Figure 3.32. UV-visible spectra of Q6 dianion in Ca (OTf)$_2$ under N$_2$ (black trace) and CO$_2$ (red trace).

When barium trifluoromethanesulfonate was used as a supporting electrolyte, the cyclic voltammograms of Q1 and Q4 did not have changes that indicated a clear shift of reduction potential in the presence of CO$_2$ (**Figure 3.34 and 3.35**). However, there was a new oxidative feature in Q4. The CVs of Q6 looked opposite to what is traditionally seen in the presence and absence of CO$_2$ (**Figure 3.36**). Under N$_2$, there was a broad reductive feature that separated into two features upon addition of CO$_2$. This indicates that some sort of reaction is occurring, but the data is inconclusive. When studied using spectroelectrochemical UV-visible spectroscopy, Q1 and Q4 both had a new, broad peak at 397 nm and 329 nm, respectively, in the presence of CO$_2$, indicating the formation of a CO$_2$ adduct (**Figure 3.37 and 3.38**). When the dianion of Q6 was formed *in-situ*, the UV-visible spectra in the presence and absence of CO$_2$ were completely

different, showing that a CO_2 formed (**Figure 3.39**). Under N_2, there was a broad peak at 373 nm

that was not at all present under CO_2, which had a peak at 326 nm.
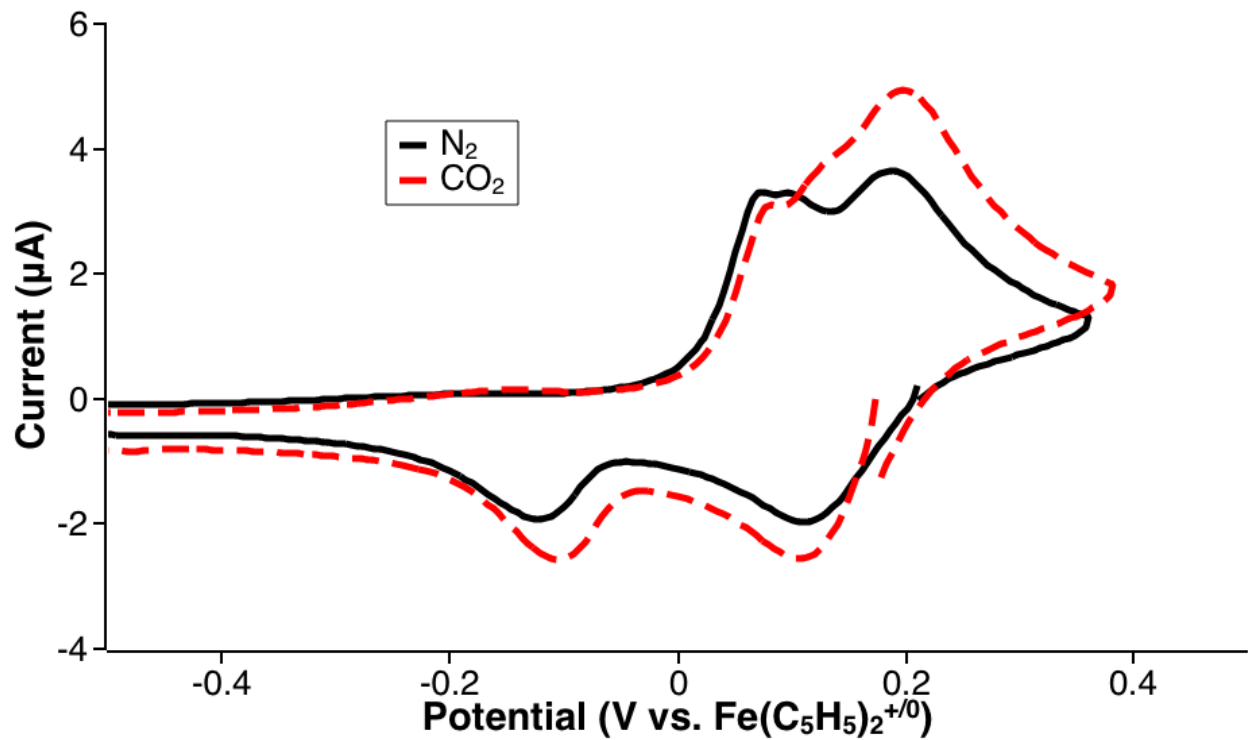
Figure 3.33. Cyclic voltammetry of 0.001M Q1 and 0.1M Ba $(OTf)_2$ in MeCN.
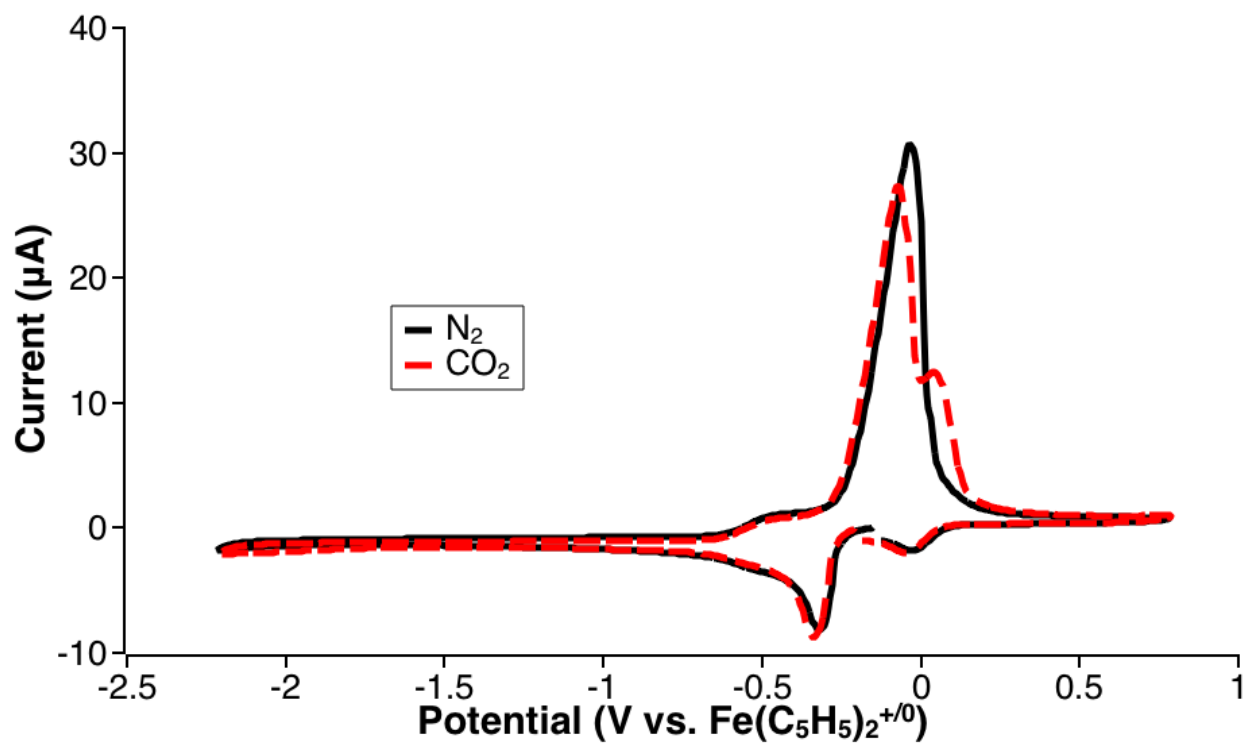
Figure 3.34. Cyclic voltammetry of 0.001M Q4 and 0.1M Ba (OTf)$_2$ in MeCN.
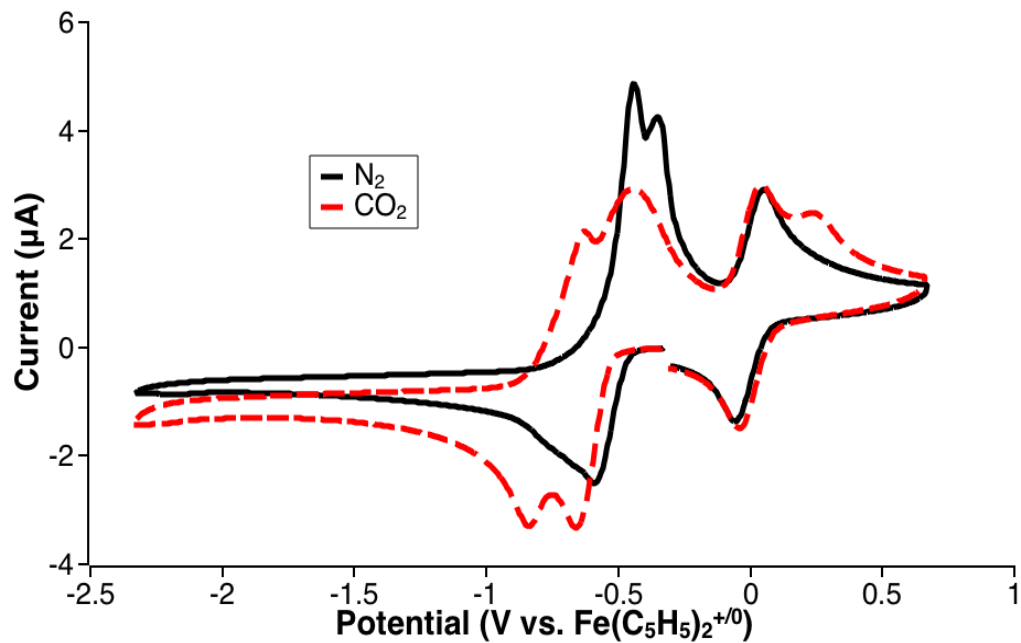
Figure 3.35. Cyclic voltammetry of 0.001M Q6 and 0.1M Ba (OTf)$_2$ in MeCN.
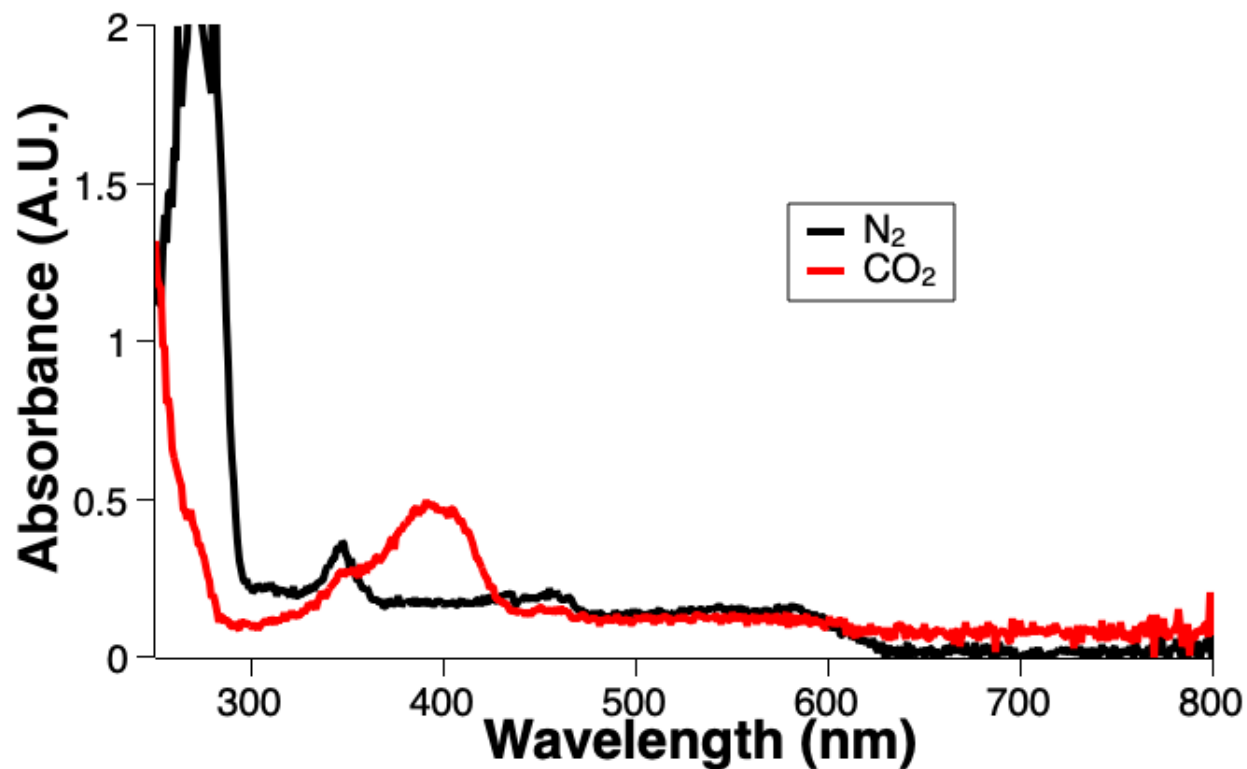
Figure 3.36. UV-visible spectra of Q1 dianion in Ba (OTf)$_2$ under N$_2$ (black trace) and CO$_2$ (red trace).
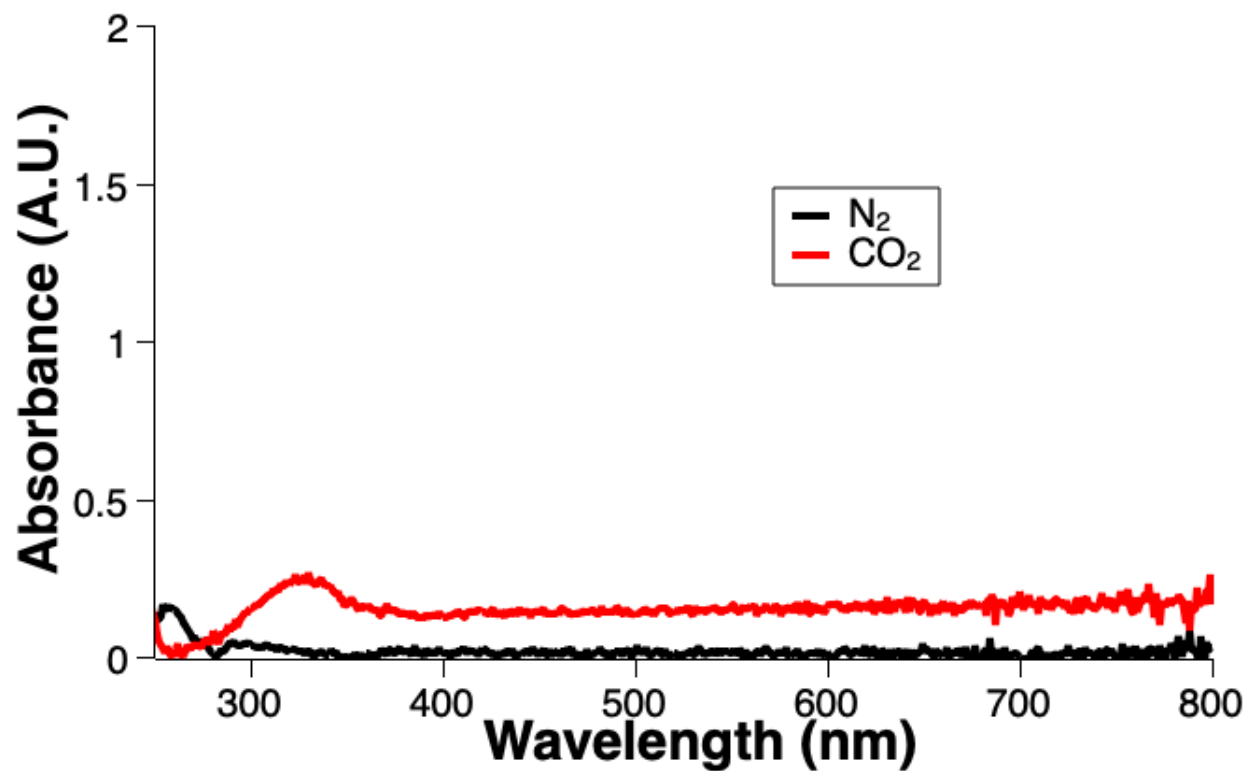
Figure 3.37. UV-visible spectra of Q4 dianion in Ba (OTf)$_2$ under N$_2$ (black trace) and CO$_2$ (red trace).
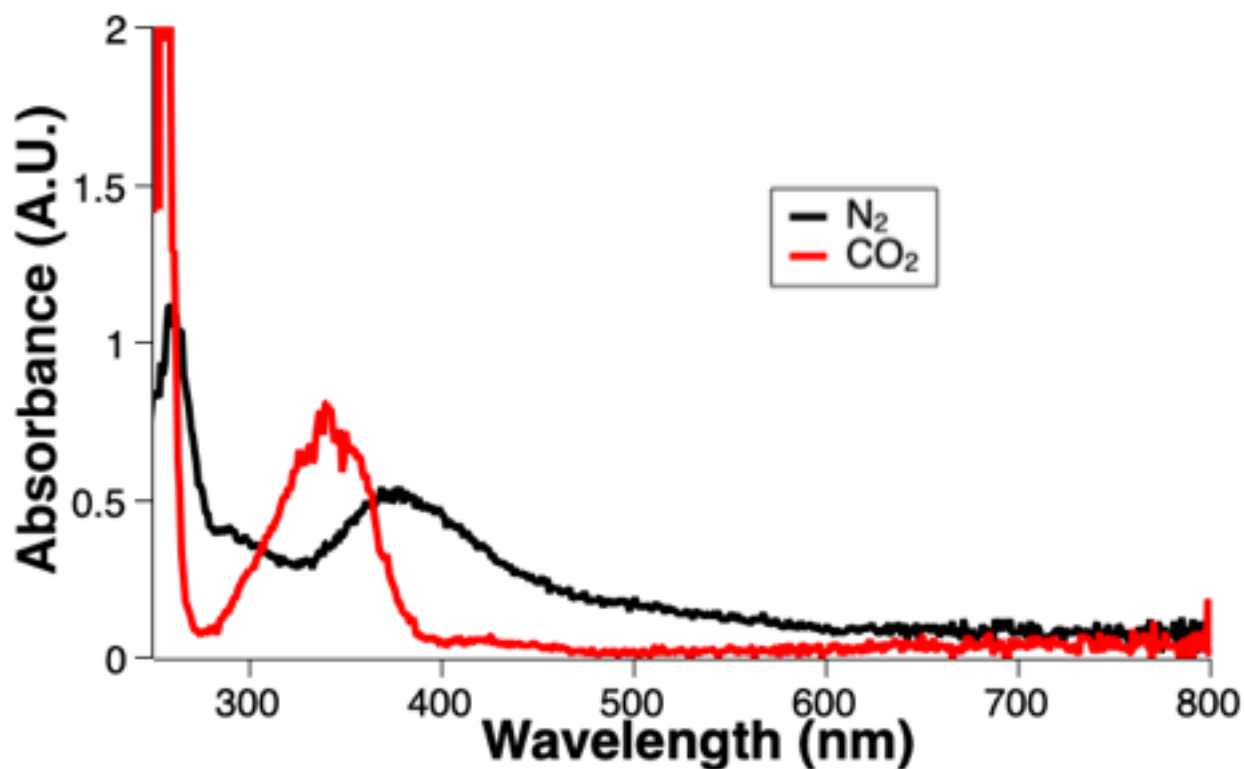
Figure 3.38. UV-visible spectra of Q6 dianion in Ba (OTf)$_2$ under N$_2$ (black trace) and CO$_2$ (red trace).

3.3 Conclusion

The variation of alkyl chain length on an alkylammonium supporting electrolyte breaks the previously-demonstrated linear free energy relationship between reduction potential and CO$_2$ binding affinity.[3] While the reduction potential shifts anodically in the case of shorter-chained alkylammonium supporting electrolyte, the CO$_2$ binding affinity is not notably affected. In the case of the longer-chained alkylammonium supporting electrolyte, the reduction potential shifts cathodically, though this effect is less pronounced. When Lewis acidic alkali and alkaline earth metals were used as the supporting electrolyte, there was a shift in the reduction potential that was indicative of binding of the Lewis acid, a phenomenon that has been studied previously.[15] However, despite this ion-pair interaction, there still appears to be an association with CO$_2$. This association is consistently to a lesser degree than the affinities found in the alkylammonium supporting electrolytes.

The intermolecular forces between the supporting electrolyte and the redox carrier can be used to tune the reduction potential by small amounts without major effects on the CO_2 binding affinity. This study shows that the substitution of the supporting electrolyte can have a direct effect on the capabilities of the system, similarly to what has been shown in Chapter 2 with the exchange of the solvent and the effect it had on the reduction potential and CO_2 binding affinity. In **Figure 3.40**, it is clear that the reduction potential steadily shifts positively with smaller cations in the supporting electrolyte. A shift of the reduction potential is indicative of association; however, the strength of that association must be sufficiently insignificant such that CO_2 binding is still favorable. In the case of Barlow et al., they found that the association of ethanol was sufficient to shift the reduction potential, but it did not negatively impact the CO_2 binding affinity.[10] Tetramethylammonium is small enough to stabilize the dianion without binding to the anionic oxygen atom and significantly decreasing the CO_2 binding affinity. Small ions such as sodium and lithium associate strongly enough to have a deleterious effect on the CO_2 binding affinity. In Chapter 2, it was determined that informed ring functionalization is likely not sufficient for breaking the linear free energy relationship between the reduction potential and CO_2 binding

affinity. However, the use of additives in addition to informed ring functionalization has been shown to be an effective strategy toward designing redox carriers for oxygen stable CO_2 capture.

3.4 Experimental Procedures

3.4.1 General Methods

All salts and solvents were rigorously dried using vacuum and molecular sieves,

Figure 3.39. A comparison of reduction potential and CO_2 binding affinities when different chain lengths of alkylammonium are used as supporting electrolyte. Error in the reduction potential is too small to be seen in this graph. Error in binding affinity was determined using the standard deviation of multiple CO_2 concentrations.
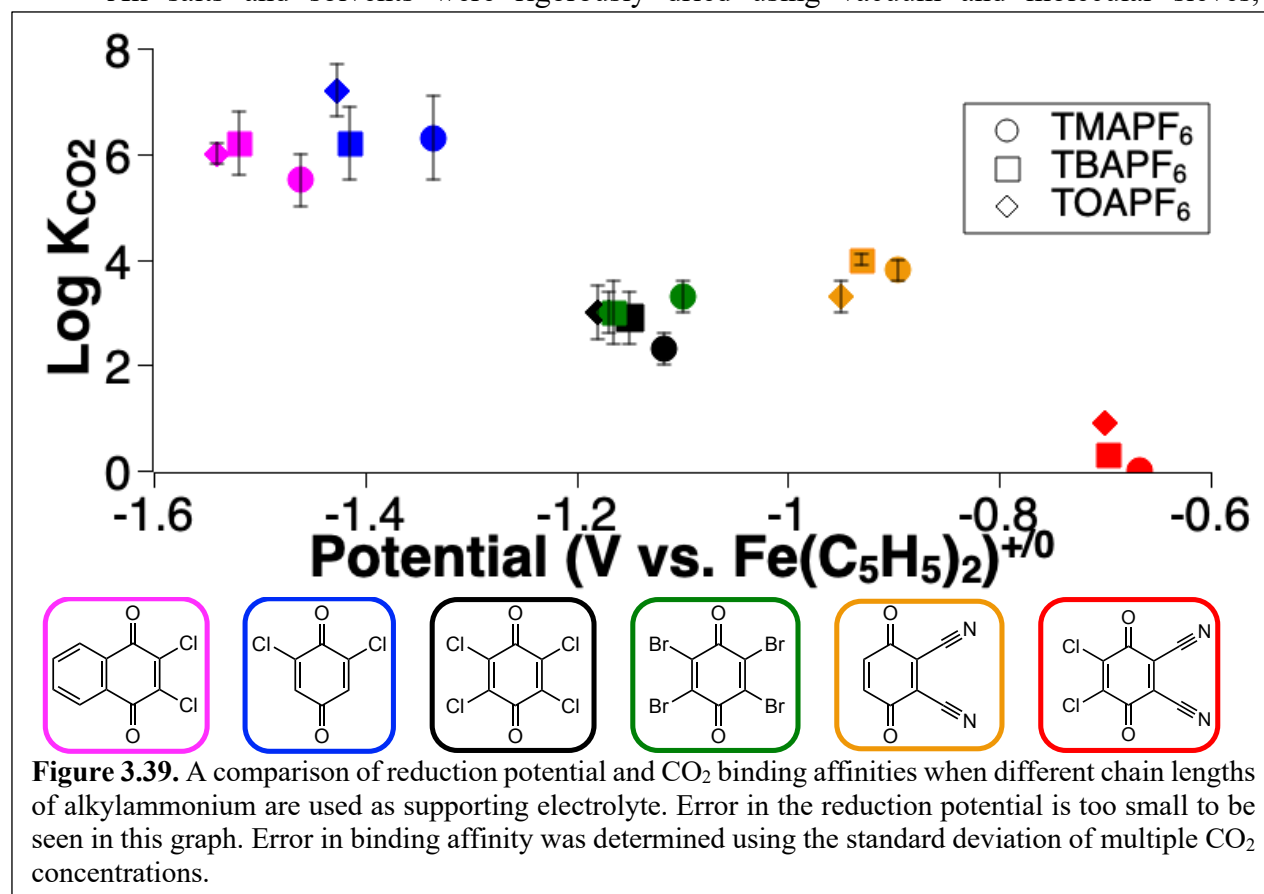
respectively. 2,3-dichloro-5,6-dicyano-p-benzoquinone, 2,6-dichloro-p-benzoquinone, 2,3-dichloro-p-naphthoquinone, tetrachloro-p-benzoquinone, and tetrabromo-p-benzoquinone were purchased and used without further purification. Ammonium hexafluorophosphate, tetramethylammonium hexafluorophosphate, and tetrabutylammonium hexafluorophosphate were all recrystallized 2-3 times with hot ethanol and rigorously dried before use.

Synthesis of bis-tetrabutylammonium 2,3-dicyano-p-benzoquinone dianion: Under an inert atmosphere in the absence of light, 0.013 g (8.2 x 10^{-5} mol) of 2,3-dicyano-p-hydroquinone was added to 5 mL of acetonitrile. 0.3 mL of 0.55 M tetrabutylammonium methoxide (1.6 x 10^{-4} mol) was added to the solution and, after 15 minutes, solvent was removed *in vacuo*. The resulting solid was used without further purification.

Synthesis of tetraoctylammonium hexafluorophosphate: 4.00 g (7.3 mmol) of tetraoctylammonium bromide was added to 100 mL of toluene. 1.35 g (7.3 mmol) of potassium hexafluorophosphate was added to the solution, and it was stirred for 1 hour. It was filtered and the solid was washed three times with dichloromethane. The combined organic filtrates were concentrated, and the resulting solid was recrystallized from hot ethanol three times.

3.4.2 Electrochemical Methods

All electrochemical measurements were performed using a Pine WaveDriver 10 bipotentiostat. Cyclic voltammograms were conducted with a 1 mm diameter glassy carbon disc working electrode, a silver wire pseudoreference electrode, and a glassy carbon rod counter electrode. All electrochemical measurements were performed in nonaqueous solvents and referenced to an internal standard of ferrocenium/ferrocene couple ($Fe(C_5H_5)_2^{+/0}$) at 0.00 V or cobaltocenium hexafluorophosphate. All experiments were performed in dry and degassed organic solvents using 1 mM analyte with 100 mM concentration of tetrabutylammonium hexafluorophosphate (TBAPF$_6$) supporting electrolyte. For electrochemical studies performed under CO_2 conditions, samples were prepared by sparging the analyte solution with carbon dioxide gas for 10 min prior to measurement. CO_2 binding affinity was determined using cyclic voltammetry, as described in reference 6.

UV-visible spectroelectrochemistry experiments were conducted in a commercially available UV-vis spectroelectrochemistry kit from Pine Instrument with Au honeycomb working electrode, Au counter electrode and Ag wire pseudo reference electrode. This electrode allows for the collection of UV-visible data during electrolysis; the honeycomb portion of the electrode is equipped with holes such that the laser of the UV-visible spectrophotometer can pass through it while the interconnected web of the honeycomb acts as a working electrode. This allows for the UV-visible monitoring of the species as it is being reduced. All UV-visible spectroscopy was performed within a glovebox that was connected to the instrument using fiber optics. The usage of the honeycomb electrode and the fiber optics induces noise within the data that cannot be avoided. For each run, a UV-visible spectrum was taken of the neutral quinone species, then a cyclic voltammogram was taken of the solution using a honeycomb spectroelectrochemical electrode. Because this setup uses a pseudo reference electrode in an aprotic solvent, a cyclic voltammogram must be taken before each electrolysis to ensure that the electrolysis is held at the appropriate potential. Then, a controlled potential electrolysis was performed. While the electrolysis was occurring, UV-visible spectra were collected to monitor the change upon reduction. All spectra shown in this chapter are of the dianion species that were formed *in-situ* electrochemically.

3.5 References

(1)   IPCC. *Climate Change 2022: Mitigation of Climate Change. Contribution of Working Group III to the Sixth Assessment Report of the Intergovernmental Panel on Climate Change*; Cambridge, UK and New York, NY, 2022. https://doi.org/10.1017/9781009325844.

(2)   Kennedy, G. *W. A. Paris Post-Combustion CO2 Capture and Sequestration Demonstration*

Project (Final Technical Report); 2020. https://doi.org/10.2172/1608572.

(3)   Bell, W. L.; Miedaner, A.; Smart, J. C.; DuBois, D. L. Synthesis and Evaluation of Electroactive CO2 Carriers. *SAE Technical Paper Series*. 1988, pp 1–10. https://doi.org/10.4271/881078.

(4)   Meng, Y.; Jiang, J.; Aihemaiti, A.; Ju, T.; Gao, Y.; Liu, J.; Han, S. Feasibility of CO2 Capture from O2-Containing Flue Gas Using a Poly(Ethylenimine)-Functionalized Sorbent: Oxidative Stability in Long-Term Operation. *ACS Appl. Mater. Interfaces* **2019**, *11* (37), 33781–33791. https://doi.org/10.1021/ACSAMI.9B08048.

(5)   Schimanofsky, C.; Wielend, D.; Kröll, S.; Lerch, S.; Werner, D.; M. Gallmetzer, J.; Mayr, F.; Neugebauer, H.; Irimia-Vladu, M.; Portenkirchner, E.; et al. Direct Electrochemical CO2 Capture Using Substituted Anthraquinones in Homogeneous Solutions: A Joint Experimental and Theoretical Study. *J. Phys. Chem. C* **2022**, *126* (33), 14138–14154. https://doi.org/10.1021/acs.jpcc.2c03129.

(6)   Zito, A. M.; Bím, D.; Vargas, S.; Alexandrova, A. N.; Yang, J. Y. Computational and Experimental Design of Quinones for Electrochemical CO2 Capture and Concentration. *ACS Sustain. Chem. Eng.* **2022**, *10* (34), 11387–11395. https://doi.org/10.1021/ACSSUSCHEMENG.2C03463.

(7)   Dubois, D. L.; Miedaner, A.; Bell, W.; Smart, J. C. Electrochemical Concentration of Carbon Dioxide. In *Electrochemical and Electrocatalytic Reactions of Carbon Dioxide*; Sullivan, B. R., Ed.; Elsevier: Amsterdam, 1993; pp 94–117.

(8)   Nagaoka, T.; Nishii, N.; Fujii, K.; Ogura, K. Mechanisms of Reductive Addition of CO2 to Quinones in Acetonitrile. *J. Electroanal. Chem.* **1992**, *322* (1–2), 383–389. https://doi.org/10.1016/0022-0728(92)80090-Q.

(9)   Connelly, N. G.; Geiger, W. E. Chemical Redox Agents for Organometallic Chemistry. *Chem. Rev.* **1996**, *96* (2), 877–910. https://doi.org/10.1021/cr940053x.

(10)   Barlow, J. M.; Yang, J. Y. Oxygen Stable Electrochemical CO2 Capture and Concentration with Quinones through Alcohol Additives. *J. Am. Chem. Soc.* **2022**, *144* (31), 14161–14169.

(11)   Koval, C.; Poshusta, J.; Scovazzo, P.; Noble, R.; DuBois, D. Electrochemical Separation and Concentration of <1% Carbon Dioxide from Nitrogen. *J. Electrochem. Soc.* **2003**, *150* (5), D91–D98. https://doi.org/10.1149/1.1566962.

(12)   Gurkan, B.; Simeon, F.; Hatton, T. A. Quinone Reduction in Ionic Liquids for Electrochemical CO2 Separation. *ACS Sustain. Chem. Eng.* **2015**, *3* (7), 1394–1405. https://doi.org/10.1021/acssuschemeng.5b00116.

(13)   Liu, Y.; Ye, H.-Z.; Diederichsen, K. M.; Van Voorhis, T.; Hatton, & T. A. Electrochemically Mediated Carbon Dioxide Separation with Quinone Chemistry in Salt-Concentrated Aqueous Media. *Nat. Commun.* **2020**, *11* (2278). https://doi.org/10.1038/s41467-020-16150-7.

(14)   Delgado, M.; Wolf, R. E.; Hartman, J. R.; McCafferty, G.; Yagbasan, R.; Rawle, S. C.; Watkin, D. J.; Cooper, S. R. *Redox-Active Crown Ethers. Electrochemical and Electron Paramagnetic Resonance Studies on Alkali Metal Complexes of Quinone Crown Ethers*; 1992; Vol. 114.

(15)   Nagaoka, T.; Okazaki, S.; Fujinaga, T. Ion-Pair Effects on the Electroreduction of Carbonyl Compounds in N,-Dimethylformamide. *J. Electroanal. Chem.* **1982**, *133* (1), 89–99. https://doi.org/10.1016/0022-0728(82)87008-3.

(16)   Kim, Y. R.; Kim, R. S.; Kang, S. K.; Choi, M. G.; Kim, H. Y.; Cho, D.; Lee, J. Y.; Chang, S. K.; Chung, T. D. Modulation of Quinone PCET Reaction by Ca2+ Ion Captured by Calix[4]Quinone in Water. *J. Am. Chem. Soc.* **2013**, *135* (50), 18957–18967. https://doi.org/10.1021/ja410406e.

(17)   Peover, M. E.; Davies, J. D. The Influence of Ion-Association on the Polarography of Quinones in Dimethylformamide. *J. Electroanal. Chem.* **1963**, *6* (1), 46–53. https://doi.org/10.1016/0022-0728(63)80116-3.

(18)   Eggins, B. R. Interpretation of Electrochemical Reduction and Oxidation Waves of Quinone-Hydroquinone System in Acetonitrile. *J. Chem. Soc. D Chem. Commun.* **1969**, No. 21, 1267–1268. https://doi.org/10.1039/C29690001267.

(19) Kieslich, G.; Sun, S.; Cheetham, A. K. An Extended Tolerance Factor Approach for Organic–Inorganic Perovskites. *Chem. Sci.* **2015**, *6* (6), 3430–3433. https://doi.org/10.1039/C5SC00961H.

(20) Bonetti, M.; Nakamae, S.; Roger, M.; Guenoun, P. Huge Seebeck Coefficients in Nonaqueous Electrolytes. *J. Chem. Phys.* **2011**, *134* (11), 114513. https://doi.org/10.1063/1.3561735.

(21) Guin, P. S.; Das, S.; Mandal, P. C. Electrochemical Reduction of Quinones in Different Media: A Review. *Int. J. Electrochem.* **2011**, *2011*, 1–22. https://doi.org/10.4061/2011/816202.

(22) Hudnall, P. M. Hydroquinone. *Ullmann's Encycl. Ind. Chem.* **2000**. https://doi.org/10.1002/14356007.A13_499.

(23) Rõõm, E. I.; Kütt, A.; Kaljurand, I.; Koppel, I.; Leito, I.; Koppel, I. A.; Mishima, M.; Goto, K.; Miyahara, Y. Brønsted Basicities of Diamines in the Gas Phase, Acetonitrile, and Tetrahydrofuran. *Chem. – A Eur. J.* **2007**, *13* (27), 7631–7643. https://doi.org/10.1002/chem.200700097.

(24) Alligrant, T. Mechanistic Studies on the Electrochemistry of Proton Coupled Mechanistic Studies on the Electrochemistry of Proton Coupled Electron Transfer and the Influence of Hydrogen Bonding Electron Transfer and the Influence of Hydrogen Bonding Downloaded from Dow, Virginia Commonwealth University, 2010.

(25) Li, X.; Zhao, X.; Liu, Y.; Hatton, T. A.; Liu, Y. Redox-Tunable Lewis Bases for Electrochemical Carbon Dioxide Capture. *Nat. Energy 2022 711* **2022**, *7* (11), 1065–1075. https://doi.org/10.1038/s41560-022-01137-z.

Chapter 4

Transition Metal Complexes for Electrochemical

Carbon Dioxide Capture and Concentration

4.1 Introduction

Cobalt tetradentate macrocyclic amine complexes have been studied for electrocatalytic carbon dioxide reduction and nitrate reduction to ammonia.[1–4] Durand and coworkers observed a positive shift of the reversible $Co^{II/I}$ redox couples of a series of tetraazamacrocyclic cobalt complexes (Co[14]diene) upon the addition of CO_2.[2] The observed shifts of reduction potential indicate reversible CO_2 binding to the metal center. The shift of the half-wave potential, $\Delta E_{1/2}$, and the concentration of CO_2 in solution were used to find the binding constant, K_{CO2}, using a relationship derived from the Nernst equation and equilibrium constant expression (described in Chapters 1 and 2)

Subsequent work by Lewis and coworkers measured the reduction potentials and CO_2 binding affinities of various cobalt tetraazamacrocycles.[5] The reduction potentials required to form the CO_2-active species for the cobalt macrocycles are notably more negative than the reduction of dioxygen in aprotic solvents, which occurs at –1.2 V vs. $Fe(C_5H_5)_2^{+/0}$ (**Figure 4.1**). Changing the structure of the macrocycle and exchanging the cobalt for nickel did not result in significant changes in CO_2 binding affinity. Therefore, it is unlikely that these complexes will be applicable for an industrial system.

Figure 4.1. A comparison of reduction potentials and K_{CO2} values for quinone and cobalt tetraazamacrocycles. Values for the cobalt complexes can be found in ref. 6; all quinone values can be found in **Table 1.1**.

Quinones, however, have tunable redox and CO_2 binding properties through intramolecular interactions. Barlow et al. demonstrated that the reduction potential of tetrachloro-*p*-benzoquinone is shifted positively upon the addition of ethanol to the electrolyte solution and does not negatively impact the CO_2 binding affinity. Chapter 3 discussed the effect of changing the size of the cation of the supporting electrolyte. While small cations stabilize the dianion and shift the reduction potential positive, the CO_2 binding affinity decreases. Non-redox active metals, such as Zn, also induced anodic shifts redox-active ligands.[6,7] However, the effect on the CO_2 binding affinity of a quinone bound to a transition metal complex is unknown.

Herein, two approaches to using metal complexes for electrochemical carbon dioxide capture and

Figure 4.2 Cobalt macrocycles (a) Co(SIM) and (b) Co(TIM) as well as (c) quinone phd and (d) 2,2'-bipyridine are compounds of interest for this work.
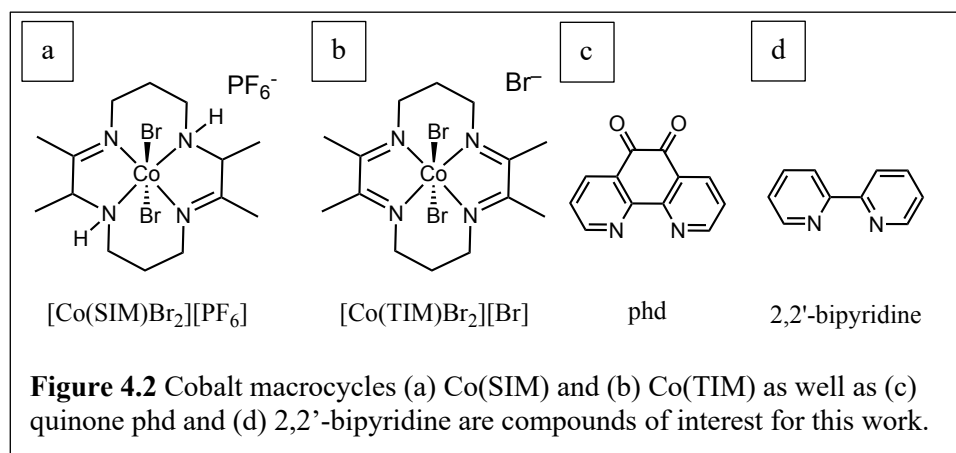
concentration are described. The first study attempted the use of the $[Co(SIM)Br_2][PF_6]$ (SIM = 2,3-dimethyl-1,4,8,11-tetraazacyclotetradeca-1,8-diene) complex (**Figure 4.2a**) as a model system for electrochemical cycling of CO_2. $[Co(SIM)Br_2][PF_6]$ has a sufficiently high binding constant to bind and release carbon dioxide from a simulated flue gas stream (12% CO_2 in N_2).[5] This compound is not air stable in its reduced form; thus it was be only used as a model system to learn about the capture system. The second study aimed to use Zn as a non-redox active stabilizer for the anion form of phd (phd = 1,10-phenanthroline-5,6-dione, **Figure 4.2b**). Phd is of interest because of its similarity to 9,10-phenanthrenequinone, a quinone that has been well-characterized

for CO_2 binding activity with a reduction potential in acetonitrile of -1.96 V vs. $Fe(C_5H_5)_2^{+/0}$ and a log K_{CO2} of 9.0.[8] Phd has also been used as a ligand for various transition metals including zinc, cobalt, and ruthenium.[9,10]

4.2 Results and Discussion

4.2.1 X-ray Crystallography of [Co(SIM)Br$_2$][PF$_6$]

After synthesizing [Co(SIM)Br$_2$][PF$_6$] (described further in **Section 4.4**), crystals suitable for single X-ray diffraction analysis were grown through vapor diffusion of diethyl ether into an acetonitrile solution. A solid-state structure of [Co(SIM)Br$_2$][PF$_6$] was solved by Dr. Tyler Kerr (**Figure 4.3**). The crystal structure can be directly compared to the previously reported crystal structure of the starting material, [Co(TIM)Br$_2$][Br],[11] for evidence that the double
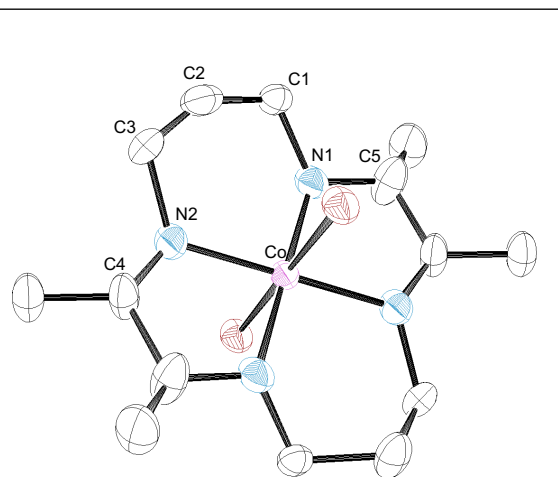
Figure 4.3. Solid state structure of [Co(SIM)Br$_2$][PF$_6$], asymmetric unit contains half of the molecule, other half generated by inversion around Co; thermal ellipsoids drawn at 50%; hydrogen atoms and PF$_6$ anion omitted for clarity. Brown spheres correlate to bromide atoms.

bond character of the ligand framework has changed in the new structure (**Figure 4.2b**). **Table**

Table 4.1. Selected Bond Distances (Å) of [Co(TIM)Br$_2$][Br][11] and [Co(SIM)Br$_2$][PF$_6$]			
Atom 1	Atom 2	[Co(TIM)Br$_2$][Br] Bond Length (Å)	[Co(SIM)Br$_2$][PF$_6$] Bond Length (Å)
Co	N1	1.9210(13)	1.940(5)
Co	N2	1.9208(13)	1.948(5)
N1	C1	1.288(2)	1.566(16)
N1	C5	1.472(2)	1.329(8)
N2	C3	1.286(2)	1.511(18)
N2	C4	1.469(2)	1.380(8)

4.1. summarizes the metrical parameters of [Co(SIM)Br$_2$][PF$_6$] and [Co(TIM)Br$_2$][Br]. Both structures include an octahedral coordination environment in which the cobalt is bound to four nitrogen atoms and two bromine atoms. However, for [Co(SIM)Br$_2$][PF$_6$], the N2–C4 bond (1.380 Å) exhibits less double bond character than the N1–C5 bond (1.329 Å), and both exhibit a loss in double bond character overall. These crystallographic data indicate that the double bonds formed in the macrocycle are *trans* in relation to one another.

4.2.2 Electrochemical Analysis of [Co(SIM)Br$_2$][PF$_6$]

Electrochemical studies were carried out to probe [Co(SIM)Br$_2$]PF$_6$ as a redox carrier for electrochemical CO$_2$ capture and concentration. To determine the ideal solvent for use in the gas capture system, the electrochemical properties of [Co(SIM)Br$_2$][PF$_6$] were

Figure 4.4. Cyclic voltammogram of 0.001M [Co(SIM)Br$_2$]PF$_6$ (pictured) with 0.1 M tetrabutylammonium hexafluorophosphate in THF.
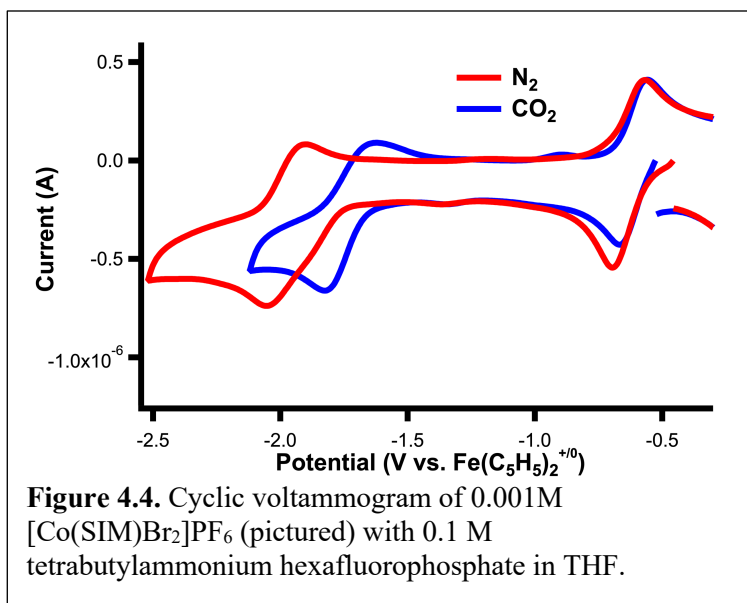
investigated in various organic solvents using cyclic voltammetry under an atmosphere of N$_2$ and CO$_2$. Five solvents were tested: acetonitrile, DMF, dimethylsulfoxide (DMSO), propylene carbonate, and tetrahydrofuran (THF). THF was the only solvent that exhibited a reversible Co$^{II/I}$ reduction under N$_2$ and CO$_2$ (**Figure 4.4**). Its binding constant was measured using cyclic voltammetry to be sufficient for CO$_2$ capture from flue gas ($K_{CO2} = 6.1 \pm 0.1$ x 10^4 M^{-1}), and its reduction potential was -1.97 V vs. Fe(C$_5$H$_5$)$_2^{+/0}$.

[Co(SIM)Br$_2$]PF$_6$ was also tested in an electrochemical gas capture apparatus. Seven attempts to bulk electrolyze [Co(SIM)Br$_2$]PF$_6$, along with the specific challenges, are detailed below (**Table 4.2**). All were performed in THF, with 0.1M TBAPF$_6$ (saturated), and the working and counter electrodes were glassy carbon while the reference electrode was Ag/Ag$^+$ jacketed electrode.

Table 4.2. A description of all of the attempts of electrochemically capturing and releasing CO$_2$ using [Co(SIM)Br$_2$]PF$_6$. Further details of the electrochemical cycling apparatus can be found in Appendix A.

Bulk No.	**Description** (all done in THF, with 0.5M TBAPF$_6$)	**Suspected Problem**
1	~0.025M Co^{III}(SIM), 100% CO$_2$; sparged with N$_2$ throughout duration of bulk	CVs only showed 1 peak (expected 2); would have taken 64 hours (crossover/leaking concerns)
2	0.05M Co^I(SIM), 100% CO$_2$, 5% ketjenblack; sparged with N$_2$ throughout duration of bulk	2 reversible peaks by CV; ran 5 hours, saw change in pressure but inconclusive results (did not have CO$_2$ meter yet)
3	0.025M Co^{III}(SIM), 0.05M decamethylcobaltocene (CoCp*); 0.025M CoCp; 5% ketjenblack; 100% CO$_2$; sparged with N$_2$ throughout duration of bulk	Used CoCp* to get to Co^I(SIM); THF condensed in both bubblers; attempts to fix this led to inconclusive results
4	0.025M Co^{III}(SIM); 0.0875M CoCp*; 5% ketjenblack; 100% CO$_2$; sparged with N$_2$ before and after bulk	CoCp* cannot reduce Co^{III} to Co^I (see solid form)
5	0.025M Co^I(SIM); 0.05M CoCp*; 5% ketjenblack; 10% CO$_2$; sparged with N$_2$ before and after bulk	Very little current passed; working electrode seemed to have something deposited on it
6	0.03M Co^I(SIM); 10% CO$_2$; sparged with N$_2$ before and after bulk	Saw 3 peaks in CV (expected 2); went all the way to the end, detected no CO$_2$
7	0.025 M Co^I(SIM); 0.05 M cobaltocene (counter); 10% CO$_2$; sparged with N$_2$ before and after bulk	No rise in CO$_2$ was detected by the CO$_2$ meter

Initially, Co^{III}(SIM) was electrochemically reduced to form the Co^I species that binds CO$_2$ capture, however, due to limited solubility, the timescale of this process resulted in leaks in the cell. Ketjenblack was added in an attempt to increase conductivity within the solution. While the

addition of ketjenblack decreased the time required to reduce or oxidize the solution, the effect was not sufficient to decrease the timescale of the experiment.

Attempts were then made to synthesize the Co^I species chemically. Decamethylcobaltocene was added to the Co^{III} solution in an attempt to produce the Co^I species *in situ.* In additional experiments, potassium graphite, KC_8, was used to attempt to form the Co^I species before introduction to electrolyte. However, the Co^I species was not stable for the hours-long electrolyses that were required of a CO_2 redox carrier. This was investigated by stopping the electrolysis and taking a cyclic voltammogram of the solution. The cyclic voltammograms after the electrolysis included a loss of the reversibility of the $Co^{II/I}$ redox couple. Attempt were made to isolate and characterize the Co^I species that was formed chemically; characterization by NMR and X-ray crystallography were unsuccessful.

Through these cycling attempts, it became apparent that the setup required a form of amplification of the conductivity of the solution, which was done through changing the electrolyte and the addition of ketjenblack. The addition of cobaltocene (CoCp) to the counter compartment of the electrolysis cell served as a sacrificial reductant, which led to a shorter time period required for electrolysis.[12] The conclusion that was found from this data was that the $[Co(SIM)Br_2]PF_6$ was not cyclable. Further crystallographic investigation performed by Dr. Tyler Kerr suggests that the reduced cobalt compound may dimerize in the solid state.

Spectroelectrochemistry was performed to investigate the Co species formed *in situ* upon reduction at –2.1 V vs. $Fe(C_5H_5)_2^{0/+}$ under N_2 and CO_2 in THF, which is the potential required to perform a two-electron reduction. The spectroelectrochemical results were compared to chemically reduced Co^I species under N_2 and CO_2 in THF. The spectra indicates that these species are not the same (**Figure 4.5a and b, Figure 4.6**), suggesting that the Co^I species synthesized chemically and electrochemically were different. Further attempts were made to isolate the Co^I species and the CO_2 adduct to investigate via NMR and X-ray crystallography; however, these attempts led to

Figure 4.5. Spectroelectrochemical UV-visible spectra of the reduction of $[Co(SIM)Br_2]PF_6$ in THF with $TBAPF_6$ supporting electrolyte under N_2 (a) and CO_2 (b) show very little change. It is expected that a CO_2-bound compound would have a different UV-visible spectrum.
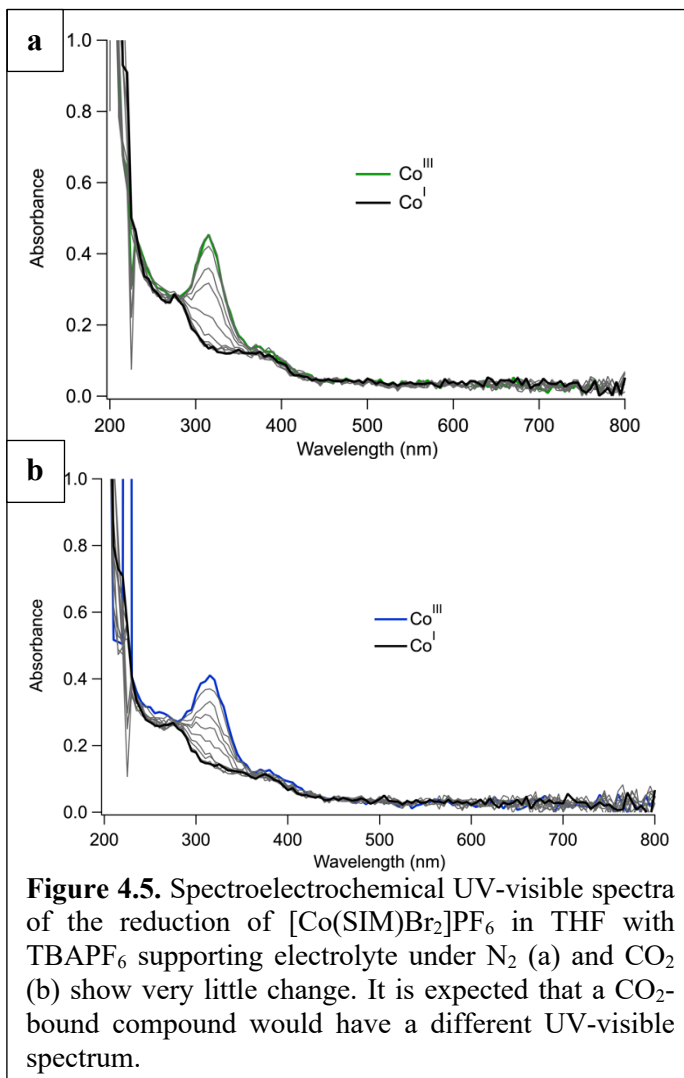
unextractable materials and crystals that could not be diffracted due to size and/or instability.

Figure 4.6. UV-Vis measurements of the chemically-synthesized Co^I species taken in THF were different from the electrochemically-formed spectra in **Figure 4.5.**
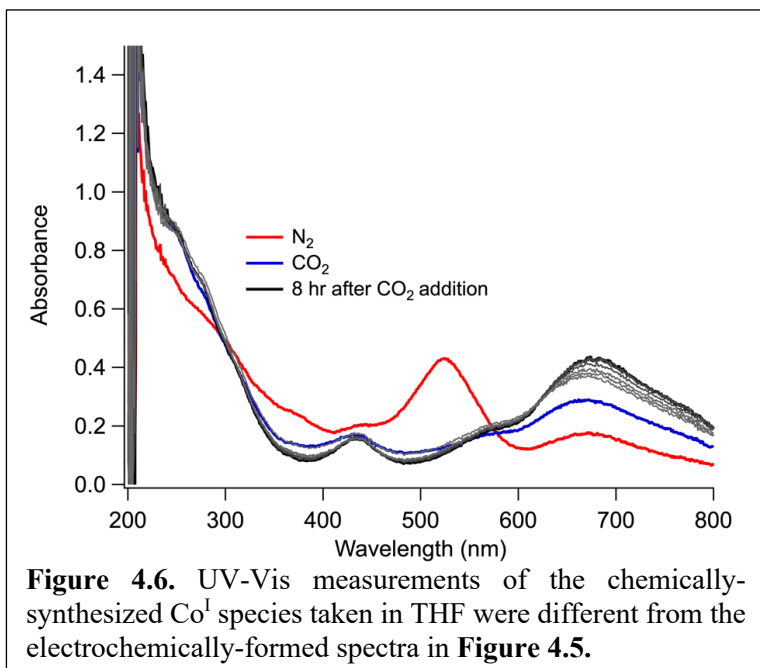
After multiple failed attempts at cycling, it was determined that $[Co(SIM)Br_2]PF_6$ was not stable enough to be used as a model compound for cycling.

4.2.3   X-ray   Crystallography   of [Zn(phd)₃][(PF₆)₂]

After synthesizing $[Zn(phd)_3][(PF_6)_2]$ (described further in **Section 4.4**), crystals suitable for single crystal X-ray analysis were grown through vapor diffusion of pentane into an acetonitrile solution. A solid-state structure was solved by Dr. Joseph Ziller and can be seen in **Figure 4.7.** The unit cell differed but the bond lengths are the same as a previously reported compound.[13]

The bond lengths for the Zn complex can be seen in **Table 4.3**.

Figure 4.7. Crystal structure of $[Zn(phd)_3][(PF_6)_2]$. Hydrogen atoms, counteranions, and solvent molecules are omitted for clarity; ellipsoids are shown at 50% probability. Asymmetric unit contains one third of the molecule, other two thirds generated by inversion around Zn; Black, red, blue, and brown spheres represent carbon, oxygen, nitrogen, and zinc, respectively.
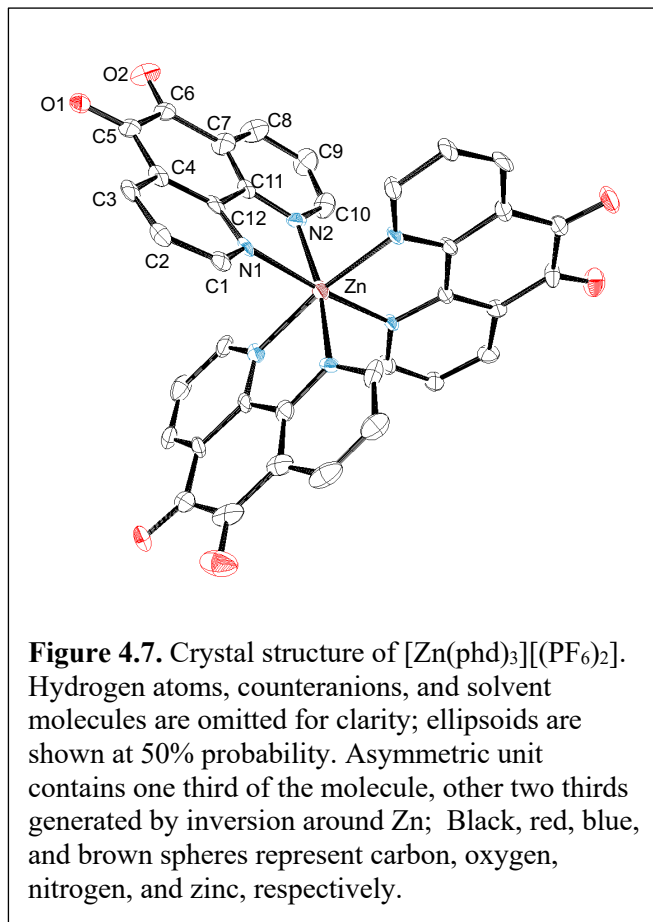
Table 4.3 Selected bond distances for [Zn(phd)₃][(PF₆)₂]

Atom 1	Atom 2	[Zn(phd)$_3$][(PF$_6$)$_2$] Bond Length (Å)
Zn	N1	2.074(7)
Zn	N2	2.105(8)
O1	C5	1.187(13)
O2	C6	1.216(14)
N1	C1	1.336(12)
N1	C12	1.361(12)
N2	C10	1.324(3)
N2	C11	1.342(12)
C1	C2	1.378(14)
C2	C3	1.388(19)
C3	C4	1.382(17)
C4	C12	1.395(14)
C4	C5	1.507(17)
C5	C6	1.546(18)
C6	C7	1.482(15)
C7	C8	1.357(16)
C7	C11	1.430(13)
C8	C9	1.361(17)
C9	C10	1.417(15)
C11	C12	1.472(14)

4.2.4 Electrochemical Analysis of phd and [Zn(phd)₃][(PF₆)₂]
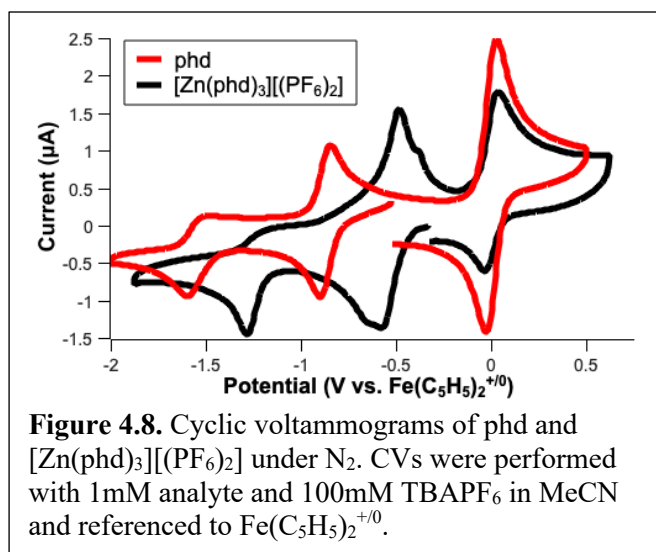
Figure 4.8. Cyclic voltammograms of phd and [Zn(phd)$_3$][(PF$_6$)$_2$] under N$_2$. CVs were performed with 1mM analyte and 100mM TBAPF$_6$ in MeCN and referenced to Fe(C$_5$H$_5$)$_2^{+/0}$.

Phd and [Zn(phd)$_3$][(PF$_6$)$_2$] were studied using cyclic voltammetry in acetonitrile. The coordination of the phd to the Zn resulted in the positive shift of the reduction potentials associated with the phd ligand. The E$_{pc}$ for the formation of the dianion of the free phd is −1.60 V vs.

Fe(C$_5$H$_5$)$_2$$^{+/0}$; upon coordination to Zn, the E$_{pc}$ for the dianion is –1.28 V vs. Fe(C$_5$H$_5$)$_2$$^{+/0}$ (**Figure 4.8**).

Figure 4.9. Binding affinity measurement for (a) phd and (b) [Zn(phd)$_3$][(PF$_6$)$_2$] using different concentrations of CO$_2$.
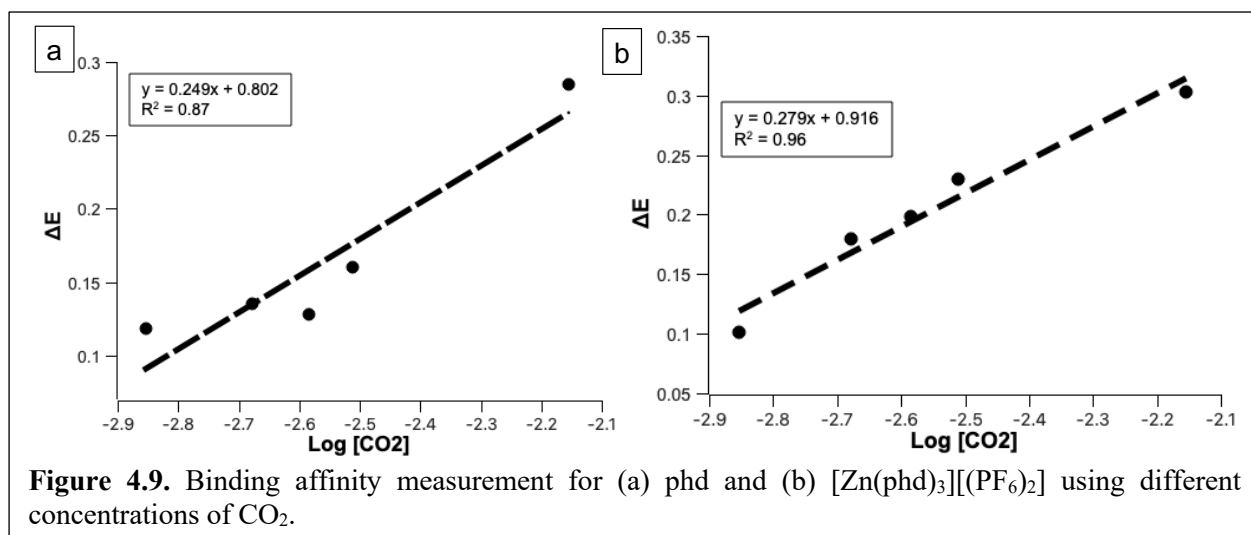
Upon addition of CO$_2$, only one reduction event is observed, which is often seen in compounds that have high CO$_2$ binding affinities. To further probe the CO$_2$ binding affinity, CO$_2$ was sparged into the analyte solution in different concentrations and the potential shift of the E$_{pc}$ of the dianion was monitored. The linear relationship between the change in potential and the log of the concentration of CO$_2$ and was used to calculate the CO$_2$ binding affinity (**Figure 4.9a and b**). From the y-intercept values and standard deviation of the linear fit, phd dianion has a log K_{CO2} value of 15.5 ± 1.4 and fully reduced [Zn(phd)$_3$][(PF$_6$)$_2$] has a log K_{CO2} value of 14 ± 2. The slope of this relationship indicates that each molecule of phd captures 2.1 ± 0.4 molecules of CO$_2$, while each molecule of Zn(phd)$_3$ can capture 4.7 ± 0.5 molecules of CO$_2$. I hypothesize the binding likely occurs at each of the oxygen atoms, similar to what has been previously reported by Mizen and Wrighton,[8] with a weaker interaction at the nitrogen atoms. Though, this interaction may not be occurring, as indicated by the error in the slope of the linear relationship used to calculate the number of CO$_2$ atoms bound.

To further investigate the theory that the nitrogen atoms of the free phd ligand participates in CO_2 binding, the CO_2 binding affinity of 2,2-bipyridine was probed (**Figure 4.2d**). The CV indicates one reversible couple (**Figure 4.10a**), and the CO_2 binding affinity was measured by sparging different concentrations of CO_2 into the analyte solution and measuring the change in the E_{pc} (**Figure 4.10b**). From the y-intercept of the linear relationship, the log K_{CO2} value is 2.9 ± 0.2,

Figure 4.10. (a) Cyclic voltammetry of 2,2-bipyridine under N_2. (b) Binding affinity measurement for 2,2'-bipyridine using different concentrations of CO_2.
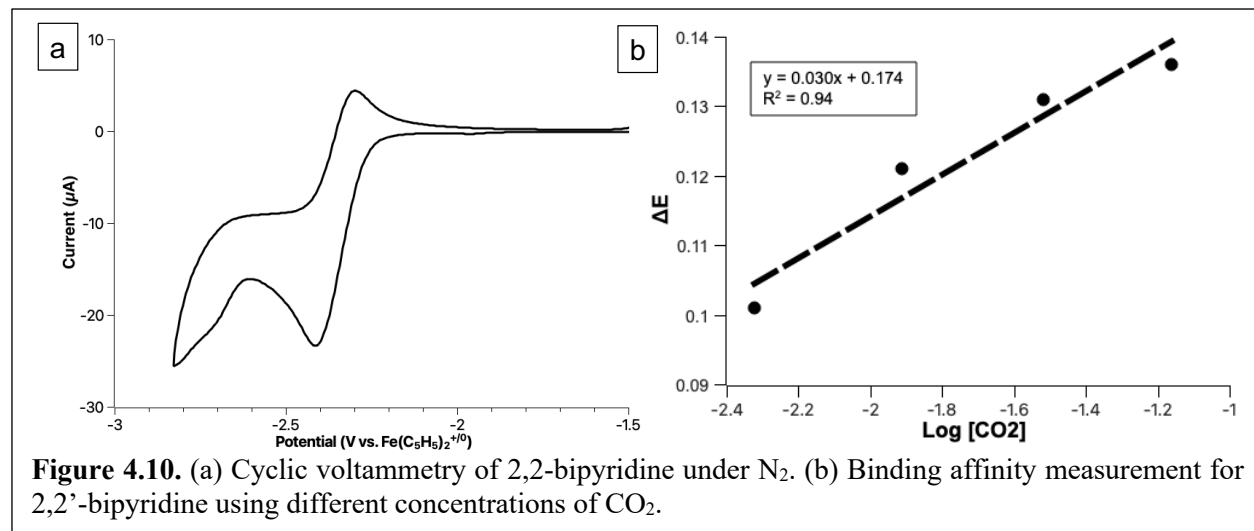
and the reduction potential is -2.41 V vs. $Fe(C_5H_5)_2^{+/0}$. The slope of the linear relationship indicates that each 2,2'-bipyridine captures 0.50 ± 0.09 molecules of CO_2. The binding mode of the CO_2 molecule to 2,2'-bipyridine is expected to be similar to the studies performed Ranjan et al. on 4,4'-bipyridine, in which the CO_2 is bound to one of the nitrogen molecules on either end.[14]

4.3 Conclusion

A cobalt tetraazamacrocycle was synthesized and crystallographically characterized. Attempts were made to use $[Co(SIM)Br_2]PF_6$ as a model system for continuous electrochemical capture and release of carbon dioxide. Problems arose with stability of the Co^I complex, which is the oxidation state required for CO_2 capture; the complex was not able to be used for the electrochemical cycling experiments.

1,10-phenanthroline-5,6-dione (phd) was appended to Zn to stabilize the dianion, resulting in a positive shift of its reduction potential. The Phd was also investigated as an independent CO_2 capture redox carrier. electrochemical activity and CO_2 binding affinities were probed, and nearly identical CO_2 binding affinities was observed. It binds to more than 2 CO_2 molecules per molecule to doubly reduced phd. To investigate the unexpected binding of greater than 2 CO_2 molecules for the free phd ligand, 2,2'-bipyridine was used as a model compound. 2,2'-bipyridine weakly binds 0.5 molecules per molecules of CO_2, indicating both the oxygen atoms and the nitrogen atoms may be interacting with CO_2.

Figure 4.11. A comparison of reduction potentials and K_{CO_2} values for quinone and cobalt tetraazamacrocycles as well as the values from this chapter. Values for the cobalt complexes can be found in ref. 6; all quinone values can be found in **Table 1.1**. Green dashed line indicates the minimum K_{CO_2} value for capture from flue gas and the brown dashed line indicates the minimum K_{CO_2} value for capture from air.

Though coordination of phd to zinc resulted in a decreased CO_2 binding affinity, the potential is more positive. Both phd and Zn(phd)$_3$ have some of the highest recorded CO_2 binding affinities at relatively mild potentials (**Figure 4.11**). Notably, the zinc complex is capable of capture from air and has a reduction potential that is ~80 mV from the dioxygen reduction. With the addition of hydrogen bond donors or a weak Lewis acid, this reduction potential may shift without causing a significant decay in CO_2 binding affinity.

125

4.4 Experimental Methods

General Methods: Synthesis and manipulation of compounds were carried out in open air unless otherwise mentioned. For air- and moisture-sensitive procedures, manipulations were carried out using standard Schlenk techniques or in a glovebox under an inert atmosphere of dinitrogen. All reagents and solvents were used as received without further purification unless otherwise noted. Deuterated solvents were purchased from Cambridge Isotopes Laboratories, Inc. and were used as received without further purification. Electrochemical studies were performed using high purity (99.999%) carbon dioxide passed through a VICI carbon dioxide purification column to eliminate residual H_2O, O_2, CO, halocarbons, and sulfur contamination.

Physical Methods: ^1H and ^{13}C NMR spectra were taken with a 500 MHz Bruker DRX500 spectrometer with either a BBO probe or a TCI cryoprobe as standard. All NMR spectra were acquired at room temperature. All spectra were referenced to residual ^1H or ^{13}C resonances of the deuterated solvent (^1H: $CDCl_3$, δ 7.26; CD_3CN, δ 1.94) (^{13}C: CD_3CN, δ 118.26)[15] and reported as parts per million. Electrospray ionization mass spectrometry was performed using an ESI LC-TOF Micromass LCT. Elemental analysis was taken on a PerkinElmer 2400 Series II CHNS elemental analyzer. Infrared spectroscopy was performed using a ThermoScientific Nicolet iS5 spectrophotometer with an iD5 ATR attachment. UV-Visible absorption spectra were collected using an Agilent Technologies Cary 60 UV-Vis. Chemical reduction of $[Co(SIM)Br_2][PF_6]$ was performed in a glovebox using two equivalents of KC_8.

Electrochemistry: All electrochemical measurements were performed using a Pine Wavedriver 10 bipotentiostat. Cyclic voltammograms were taken with a 1 mm diameter glassy carbon disc working electrode, a silver wire pseudoreference electrode, and a glassy carbon rod counter electrode. Bulk electrolyses were taken using either glassy carbon or carbon cloth working and

counter electrodes with a Ag/Ag+ reference electrode. Open circuit potential measurements were taken using a 1 mm diameter glassy carbon disc working electrode, a Ag/Ag+ reference electrode, and a glassy carbon counter electrode. OCP was taken over 15 seconds and values were average All electrochemistry was done in non-aqueous solvents and was therefore referenced to ferrocene as an internal standard $(Fe(C_5H_5)_2^{+/0})$ at 0.00 V. All experiments were performed in dry and degassed organic solvents using 1 mM analyte with 100mM tetrabutylammonium hexafluorophosphate (TBAPF$_6$) supporting electrolyte concentrations. For electrochemical studies performed under an atmosphere of CO_2, samples were prepared by sparging the analyte solution with carbon dioxide gas for 10 minutes prior to measurement. CO_2 concentrations were controlled using the gas mixer (explained in Appendix A). Spectroelectrochemistry was performed with a Pine Platinum honeycomb spectroelectrochemical electrode chip and a 1.7 mm thin-film quartz cuvette.

[Co(2,3,9,10-tetramethyl-1,4,8,11-tetraazacyclotetradeca-1,8-diene)Br₂]PF₆

([Co(SIM)Br₂]PF₆): Co(TIM)Br$_2$PF$_6$ (1.694 g, 0.003 mol) was added to 120 mL methanol with stirring. Hypophosphorous acid (2.64 mL, 0.02 mol) was added, and a bright green precipitate formed immediately. The product was recrystallized by vapor diffusion of diethyl ether into an acetonitrile solution of the complex. Yield 40%. ESI+ *m/z* calculated for $[C_{14}H_{28}Br_2CoN_4]^+$: 471.0. Found: 471.0. ^{1}H NMR (500MHz, CD$_3$CN, ppm): 5.23 (broad s, 2 H, N–H), 3.91 (s, 2H, C–H), 3.87 (s, 4H, C=N–CH$_2$), 3.11 (t, 4H, NH–CH$_2$), 2.68 (m, 2H, –CH$_2$–), 2.40 (s, 2H, –CH$_2$–), 2.34 (s, 6H, N=C=CH$_3$), 1.61 (d, 6H, –CH$_3$). IR cm^{-1}: 3200 w $\nu_{N–H}$, 1650 s $\nu_{C=N}$. Anal. Calcd. for C$_{14}$H$_{28}$Br$_2$CoF$_6$N$_4$P: C, 27.29; H, 4.58; N, 9.09. Found: C, 27.26; H, 4.58; N, 9.05.

[Zn(tris-1,10-phenanthroline-5,6-dione)](PF₆)₂ ([Zn(phd)₃][(PF₆)₂]): 1,10-phenanthroline-5,6-dione (phd, 0.47 g, 2.2 mmol) was added to 125mL ethanol with stirring. ZnCl$_2$ (0.1 g, 0.73 mmol)

was added, and the reaction was stirred at room temperature for 8 h. A tan precipitate was formed and collected using a fine frit and washed with diethyl ether. The solid was added to 75 mL water and ammonium hexafluorophosphate was added. The reaction was stirred overnight. A brown-tan precipitate was formed and collected using a fine frit. The product was recrystallized by vapor diffusion of pentane into an acetonitrile solution of the complex. Yield 49%. ^{1}H NMR (500MHz, CD$_3$CN, ppm): 8.75 (dd, J = 7.9, 1.2 Hz, 1H), 8.20 (d, J = 4.5 Hz, 1H), 7.84 (dd, J = 7.9, 5.2 Hz, 1H). IR cm^{-1}: 1706 w $\nu_{C=O}$, 1576 s ν_{C-N}.

A Note on the NMR Spectroscopy of [Co(SIM)Br$_2$][PF$_6$]

[Co(SIM)Br$_2$][PF$_6$] was analyzed by ^{1}H and ^{13}C NMR spectroscopy (CD$_3$CN, 25 ºC). Heteronuclear and ^{1}H-^{1}H correlation NMR were used to confirm the peak assignments of both the ^{1}H and ^{13}C NMR spectra. HSQC (**Figure 4.11**) indicated that the proton signals at 2.40 ppm and 2.68 ppm correspond to the same carbon. Through HMBC and COSY it can be noted that these protons are not equivalent via NMR. The likely cause of this is one hydrogen is pointed toward the axial bromine while the other is pointed away. The HSQC indicated that the proton signal seen at 5.23 ppm does not correlate to a carbon. Analysis of the COSY and HMBC spectra indicates that the signal at 5.23 corresponds to the protons associated with the two amine protons and that these amines are *trans* in relation to one another.
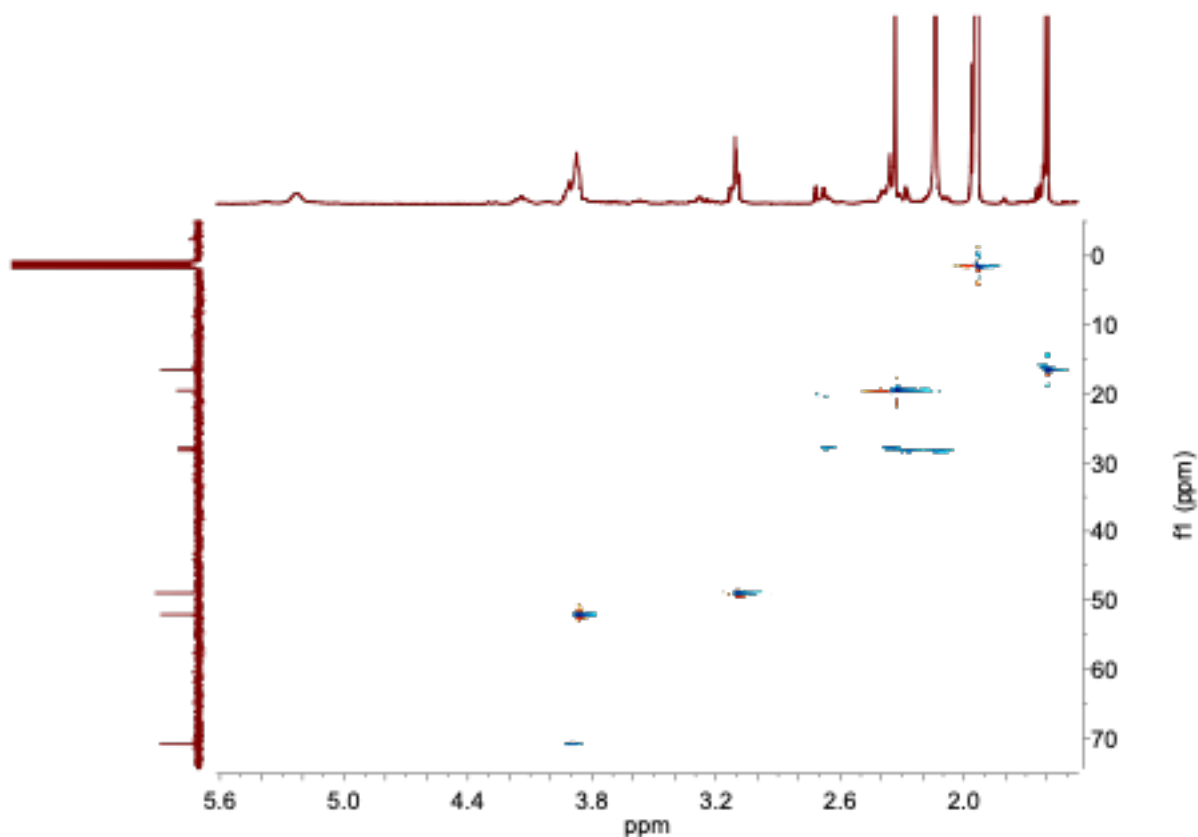
Figure 4.12. HSQC of [Co(SIM)Br$_2$][PF$_6$]

X-ray Data Collection, Structure Solution and Refinement for [Co(SIM)Br$_2$][PF$_6$]

The data for jyy183_cc_a were collected from a shock-cooled single crystal at 88(2) K on a three-circle diffractometer. The diffractometer was equipped with a low temperature device and used MoK α radiation (λ = 0.71073 Å). All data were integrated with SAINT and a multi-scan absorption correction using SADABS was applied.[16,17] The structure was solved by direct methods using SHELXT and refined by full-matrix least-squares methods against F^2 by SHELXL-2018/3.[18,19] All non-hydrogen atoms were refined with anisotropic displacement parameters. All C-bound hydrogen atoms were refined isotropic on calculated positions using a riding model with their U iso values constrained to 1.5 times the U eq of their pivot atoms for terminal sp^3 carbon

atoms and 1.2 times for all other carbon atoms. Disordered moieties were refined using bond lengths restraints and displacement parameter restraints. Crystallographic data for the structures reported in this paper have been deposited with the Cambridge Crystallographic Data Centre.[20] This report and the CIF file were generated using FinalCif.[21]

X-ray Data Collection, Structure Solution and Refinement for [Zn(phd)₃][(PF₆)₂]

An orange crystal of approximate dimensions 0.250 x 0.265 x 0.276 mm was mounted on a glass fiber and transferred to a Bruker SMART APEX II diffractometer system. The APEX2[22] program package was used to determine the unit-cell parameters and for data collection (25 sec/frame scan time). The raw frame data was processed using SAINT[16] and SADABS[23] to yield the reflection data file. Subsequent calculations were carried out using the SHELXTL[24] program package. The diffraction symmetry was $2/m$ and the systematic absences were consistent with the monoclinic space groups $P2_1$ and $P2_1/m$. It was later determined that space group $P2_1$ was correct. The structure was solved by direct methods and refined on F^2 by full-matrix least-squares techniques. The analytical scattering factors[25] for neutral atoms were used throughout the analysis.

Hydrogen atoms were included using a riding model. Disordered atoms were included using multiple components with partial site-occupancy-factors. There were three molecules of acetonitrile solvent present.

Least-squares analysis yielded wR2 = 0.1919 and Goof = 1.091 for 650 variables refined against 8640 data (0.82 Å), R1 = 0.0727 for those 8442 data with I > 2.0σ (I). The structure was refined as an inversion twin. Further information about the refinement parameters can be found in **Table 4.4**.

Table 4.4. Crystallographic data and refinement parameters for [Co(SIM)Br$_2$][PF$_6$] and [Zn(phd)$_3$][(PF$_6$)$_2$].

Complex	[Co(SIM)Br$_2$][PF$_6$]	[Zn(phd)$_3$][(PF$_6$)$_2$]
Formula	C$_{14}$H$_{28}$Br$_2$CoN$_4$PF$_6$	C$_{36}$H$_{18}$N$_6$O$_6$Zn(PF$_6$)$_2$(C$_2$H$_3$N)$_3$
Molar Mass	616.12	1109.03
Crystal System	Monoclinic	Monoclinic
Space Group	C2/c	$P2_1$
T[K]	88(2)	93(2)
a[Å]	12.5082	11.969(2)
b[Å]	10.9843(6)	14.563(3)
c[Å]	15.0528(8)	13.158(3)
α[°]	90	90
β[°]	94.085(1)	94.981(4)
γ[°]	90	90
V[A^3]	2062.91(19)	2284.7(8)
Z	4	2
D(calcd) [Mgm^{-3}]	1.984	1.612
μ(Mo-Kα) [mm^{-1}]	4.845	0.715
Index Range	$-17 \leq h \leq 17$ $-15 \leq k \leq 15$ $-21 \leq l \leq 21$	$-14 \leq h \leq 14$ $-17 \leq k \leq 17$ $-16 \leq l \leq 16$
Reflections Collected	15998	41665
Independent Reflections	3118	8640
Data/Restraints/Parameters	3118/66/161	8640/2/650
R$_1$, wR$_2$ [I > 2σ(I)]	R$_1$ = 0.0650 wR$_2$ = 0.1609	R$_1$ = 0.0727 wR$_2$ = 0.1910
R$_1$, wR$_2$ [all data]	R$_1$ = 0.0915 wR$_2$ = 0.1765	R$_1$ = 0.0738 wR$_2$ = 0.1919
GOF	1.074	1.091

4.5 References

(1)   Tait, A. M.; Busch, D. H. Reactions of Coordinated Ligands. Selective Hydrogenation of α-Diimine Linkages in Complexes of Cobalt(III) with Macrocyclic Ligands. *Inorg. Chem.* **1977**, *16* (4), 966–968. https://doi.org/10.1021/ic50170a057.

(2)   Gangi, D. A.; Durand, R. R. Binding of Carbon Dioxide to Cobalt and Nickel Tetra-Aza Macrocycles. *J. Chem. Soc., Chem Commun.* **1986**, 697–699. https://doi.org/10.1039/C39860000697.

(3)   Xu, S.; Ashley, D. C.; Kwon, H. Y.; Ware, G. R.; Chen, C. H.; Losovyj, Y.; Gao, X.;

        Jakubikova, E.; Smith, J. M. A Flexible, Redox-Active Macrocycle Enables the

        Electrocatalytic Reduction of Nitrate to Ammonia by a Cobalt Complex. *Chem. Sci.* **2018**,

        9 (22), 4950–4958. https://doi.org/10.1039/c8sc00721g.

(4)   *Electrochemical and Catalytic Reactions of Carbon Dioxide*; Sullivan, B. R., Ed.;

        Amsterdam, 1993. https://doi.org/10.1002/9783527630295.fmatter.

(5)   Schmidt, M. H.; Miskelly, G. M.; Lewis, N. S. Effects of Redox Potential, Steric

        Configuration, Solvent, and Alkali Metal Cations on the Binding of Carbon Dioxide to

        Cobalt(I) and Nickel(I) Macrocycles. *J. Am. Chem. Soc.* **1990**, *112* (9), 3420–3426.

        https://doi.org/10.1021/ja00165a027.

(6)   Das, S.; Mondal, R.; Chakraborty, G.; Kumar Guin, A.; Das, A.; Paul, N. D. Zinc

        Stabilized Azo-Anion Radical in Dehydrogenative Synthesis of N-Heterocycles. An

        Exclusively Ligand Centered Redox Controlled Approach. **2023**, *21*, 41.

        https://doi.org/10.1021/acscatal.1c00275.

(7)   Nguyen, A. I.; Blackmore, K. J.; Carter, S. M.; Zarkesh, R. A.; Heyduk, A. F. One-and

        Two-Electron Reactivity of a Tantalum(V) Complex with a Redox-Active Tris(Amido)

        Ligand. *J. Am. Chem. Soc.* **2009**, *131* (9), 3307–3316. https://doi.org/10.1021/JA808542J.

(8)   Mizen, M. B.; Wrighton, M. S. Reductive Addition of CO2 to 9,10-Phenanthrenequinone.

        J. Electrochem. Soc. **1989**, *136* (4), 941. https://doi.org/10.1149/1.2096891.

(9)   Satyanarayana, S.; Dabrowiak, C.; Chaires, J. B. Tris(Phenanthroline)Ruthenium(II)

        Enantiomer Interactions with DNA: Mode and Specificity of Binding. *Biochemistry* **1993**,

        32, 18.

(10)   Silva, T. F. S.; Smoleński, P.; Martins, L. M. D. R. S.; Silva, M. F. C. G. da; Fernandes,

A. R.; Luis, D.; Silva, A.; Santos, S.; Borralho, P. M.; Rodrigues, C. M. P.; et al. Cobalt and Zinc Compounds Bearing 1,10-Phenanthroline-5,6-Dione or 1,3,5-Triaza-7-Phosphaadamantane Derivatives – Synthesis, Characterization, Cytotoxicity, and Cell Selectivity Studies. *Eur. J. Inorg. Chem.* **2013**, *2013* (21), 3651–3658. https://doi.org/10.1002/EJIC.201300197.

(11)   El-Ghamry, H.; Issa, R.; El-Baradie, K.; Masaoka, S.; Sakai, K. Dibromido(2,3,9,10-Tetra-Methyl-1,4,8,11-Tetra-Azacyclo-Tetra-Deca-1,3,8, 10-Tetra-Ene)Cobalt(III) Bromide. *Acta Crystallogr. Sect. E Struct. Reports Online* **2009**, *65* (11). https://doi.org/10.1107/S160053680904166X.

(12)   Liu, J.; Lu, L.; Wood, D.; Lin, S. New Redox Strategies in Organic Synthesis by Means of Electrochemistry and Photochemistry. *ACS Cent. Sci.* **2020**, *6* (8), 1317–1340. https://doi.org/10.1021/acscentsci.0c00549.

(13)   Rezvani, A. R.; Saravani, H.; Hadadzadeh, H. Synthesis, Crystal Structure, Electrochemical and Fluorescence Studies of a Novel Zn(II)-Fluorophore, 1,10-Phenanthroline-5,6-Dione (Phen-Dione). *J. Iran. Chem. Soc.* **2010**, *7* (4), 825–833. https://doi.org/10.1007/BF03246075.

(14)   Ranjan, R.; Olson, J.; Singh, P.; Lorance, E. D.; Buttry, D. A.; Gould, I. R. Reversible Electrochemical Trapping of Carbon Dioxide Using 4,4′-Bipyridine That Does Not Require Thermal Activation. *J. Phys. Chem. Lett.* **2015**, *6* (24), 4943–4946. https://doi.org/10.1021/acs.jpclett.5b02220.

(15)   Fulmer, G. R.; Miller, A. J. M.; Sherden, N. H.; Gottlieb, H. E.; Nudelman, A.; Stoltz, B. M.; Bercaw, J. E.; Goldberg, K. I. NMR Chemical Shifts of Trace Impurities: Common Laboratory Solvents, Organics, and Gases in Deuterated Solvents Relevant to the

Organometallic Chemist. *Organometallics* **2010**, *29* (9), 2176–2179.

https://doi.org/10.1021/om100106e.

(16)   Bruker. SAINT, V8.34A. Bruker AXS Inc.: Madison, Wisconsin, USA 2013.

(17)   Krause, L.; Herbst-Irmer, R.; Sheldrick, G. M.; Stalke, D. Comparison of Silver and

Molybdenum Microfocus X-Ray Sources for Single-Crystal Structure Determination. *J.*

Appl. Cryst. **2015**, *48*, 3–10. https://doi.org/10.1107/S1600576714022985.

(18)   Sheldrick, G. M.; IUCr. Crystal Structure Refinement with SHELXL. *urn:issn:2053-2296*

2015, *71* (1), 3–8. https://doi.org/10.1107/S2053229614024218.

(19)   Sheldrick, G. M.; IUCr. SHELXT – Integrated Space-Group and Crystal-Structure

Determination. *urn:issn:2053-2733* **2015**, *71* (1), 3–8.

https://doi.org/10.1107/S2053273314026370.

(20)   Groom, C. R.; Bruno, I. J.; Lightfoot, M. P.; Ward, S. C. The Cambridge Structural

Database. *urn:issn:2052-5206* **2016**, *72* (2), 171–179.

https://doi.org/10.1107/S2052520616003954.

(21)   Kratzerts, D. FinalCif, V113 https://dkratzert.de/finalcif.html (accessed Mar 5, 2023).

(22)   APEX2 Version 2014.11-0. Bruker AXS Inc.: Madison, Wisconsin, USA 2014.

(23)   Sheldrick, G. M. SADABS, Version 2014/5. Bruker AXS Inc.: Madison, Wisconsin, USA

2014.

(24)   Sheldrick, G. M. SHELXTL, Version 2014/7. Bruker AXS Inc.: Madison, Wisconsin,

USA 2014.

(25)   *International Tables for Crystallography 1992, Vol. C.*; Dordrecht: Kluwer Academic

Publishers.

Chapter 5

Study of Benzoquinone Di-Imines as Redox Carriers

Electrochemical CO_2 Capture

5.1 Introduction

The ideal redox carrier for a flue gas capture system has a CO_2 binding affinity of at least 10^4 M^{-1} and a reduction potential for the formation of the active species positive of -1.2 V vs. $Fe(C_5H_5)_2^{+/0}$, which is the reduction potential of dioxygen to superoxide in most aprotic solvents. The previously measured reduction potentials and K_{CO_2} values do not fall within these parameters (green box, **Figure 5.1**).

Figure 5.1. Reduction potentials and CO_2 binding affinity values that have been previously published. Currently, there are no redox carriers that have reduction potentials positive of the dioxygen reduction and have sufficient K_{CO_2} values for capture from flue gas or air, represented by the green box.
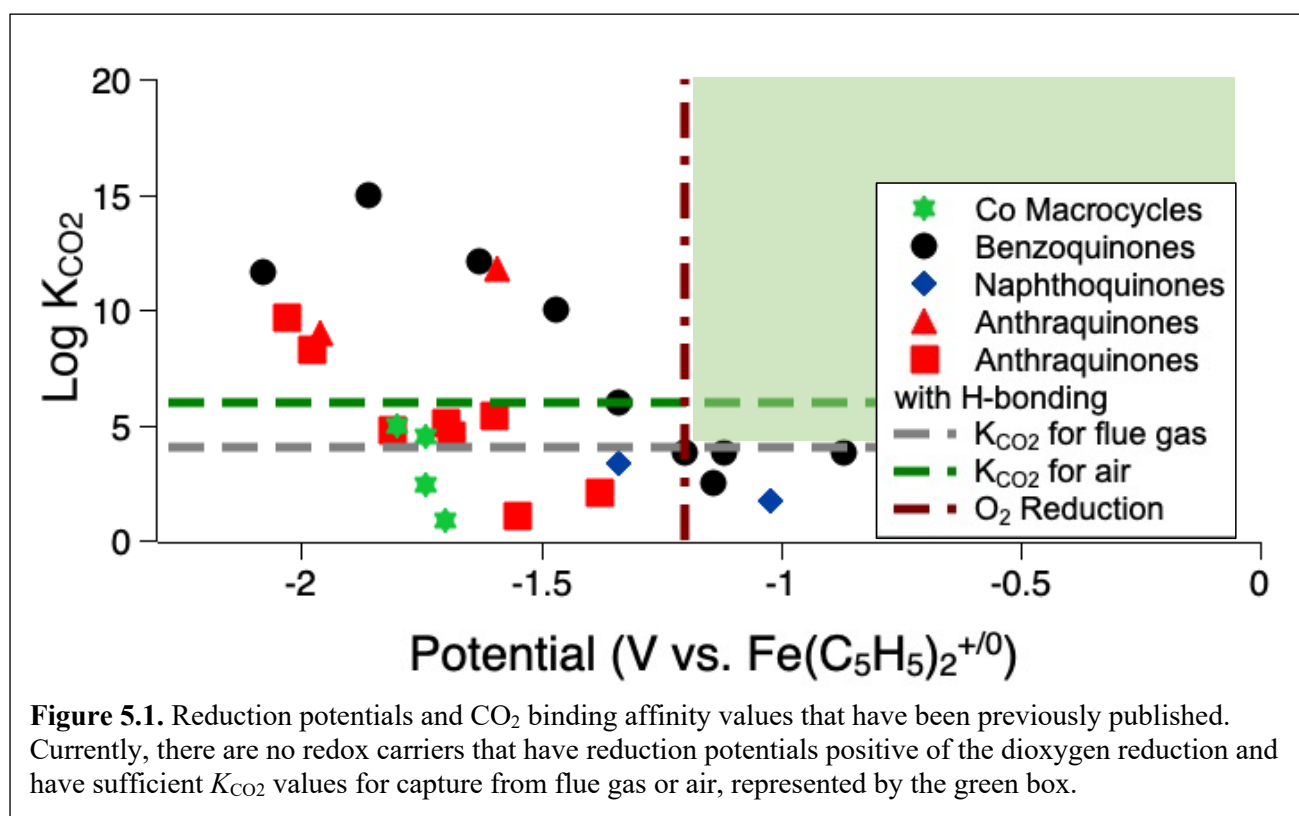
The first redox carriers probed for electrochemical carbon dioxide capture and concentration were benzoquinones and metal complexes, which were discussed in detail in Chapters 1-4.[1] The former is compelling because quinones can generate a dianionic species whose nucleophilic oxygen atoms can reversibly bind to CO_2. After Dubois and coworkers' initial studies, many additional studies used quinones as redox carriers to study their CO_2 binding affinity.[2–4] Beyond quinones, Ranjan et al. found that 4,4'-bipyridine had the capability to bind to CO_2 upon

a one-electron reduction, though no binding affinity value was reported.[5] This work inspired later work by Xing Li et al., who investigated CO_2 interactions with sp^2 nitrogen centers.[6]

Benzoquinone di-imines are a class of molecules that have not yet been probed for CO_2 capture capabilities. Much like benzoquinones, benzoquinone di-imines undergo two one-electron oxidations to form a nucleophilic, dianionic species in aprotic solvent. However, instead of only functionalizing the aromatic ring, in benzoquinone di-imines, the nitrogen atoms can be functionalized. Functionalization of the nitrogen atom is expected to have a more significant effect on the reduction potential and K_{CO_2} than functionalization of the C–H bonds in the benzoquinone ring.

Herein, the characterization of five benzoquinone di-imine compounds is detailed. A variation of electron withdrawing and electron donating groups were used to determine whether the properties of these compounds follow the same linear free energy relationship as seen in benzoquinones. The electron withdrawing groups are the tosyl (**Figure 5.2a**),

Figure 5.2. General structure for a benzoquinone imine which were functionalized with (a) tosyl, (b) methoxy tosyl, (d) phenyl, and (e) naphthyl groups.

methoxy tosyl (**Figure 5.2b**), and pivaloyl (**Figure 5.2c**). Since the effect of the function group is expected to be notable, weakly electron donating groups of phenyls (**Figure 5.2d**) and naphthyl (**Figure 5.2e**) were chosen.

5.2 Results

Figure 5.3. Cyclic voltammograms of compounds **a-e** under N_2 and CO_2.
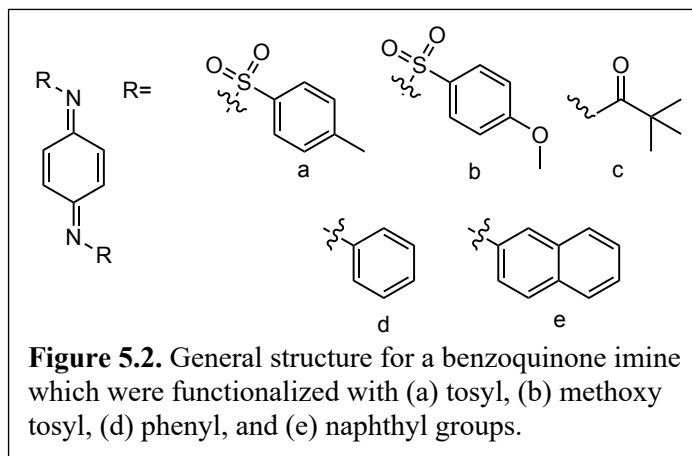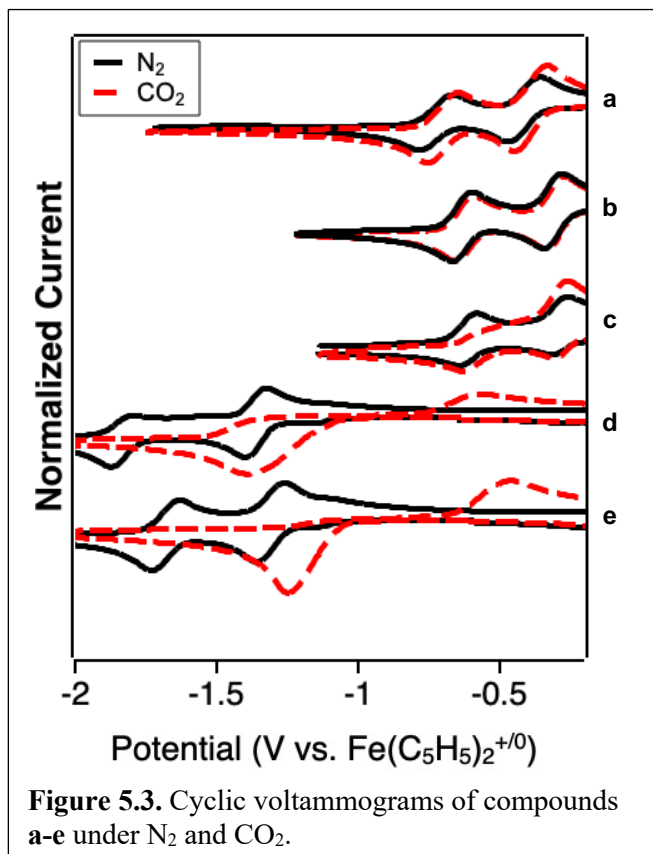
Compounds a-e were synthesized. Their properties were studied using electrochemistry. The measured reduction potentials and K_{CO_2} values are reported in **Table 5.1**. For compounds **a, b** and **c**, the K_{CO_2} was determined using cyclic voltammetry (CV). By CV, the addition of CO_2 does not impact the first reduction to the semiquinone. However, the second reductive peak (**Figure 5.3**) to form the dianion shifts anodically, indicating the species reacts with CO_2 in a chemical step. These voltametric data indicate an EEC mechanism (electron transfer, electron transfer, chemical reaction). The shift of the half-wave potential ($\Delta E_{1/2}$) to form the dianion between a N_2 and CO_2 atmosphere and the concentration of ($[CO_2]$) was used to find the binding constant, as described in Chapter 2. For compounds with a K_{CO_2} value of <100 M^{-1}, a slightly different equation was used (equation 5.1) where the number of CO_2 molecules bound to the redox carrier is assumed to be 1.[7]

$$\Delta E = \frac{0.0592}{n} \log \left(K_{CO2}[CO_2] + 1 \right) \qquad (5.1)$$

Similar to compounds studied in Chapters 2 and 3, compounds **d** and **e** did not exhibit a second reductive peak in the presence of CO_2 (**Figure 5.3**). This voltametric behavior is believed

to be indicative of an ECEC binding mechanism (electron transfer, chemical reaction, electron transfer, chemical reaction).[8]

In these cases, the K_{CO_2} values were measured by sparging the solution with dilute streams of CO_2 counterbalanced with N_2 and taking the open circuit potential of the solution, as described in Chapter 2. The change in the potential with varying concentrations of CO_2 was plotted versus log $[CO_2]$ (**Figures 5.4 and 5.5**). From this plot, the y-intercept and the standard deviation can be used to calculate K_{CO_2} and its associated error, based on the modified Nernst equation (eq. 2.2). The OCP binding constant plot for compound **d** is featured in **Figure 5.4**
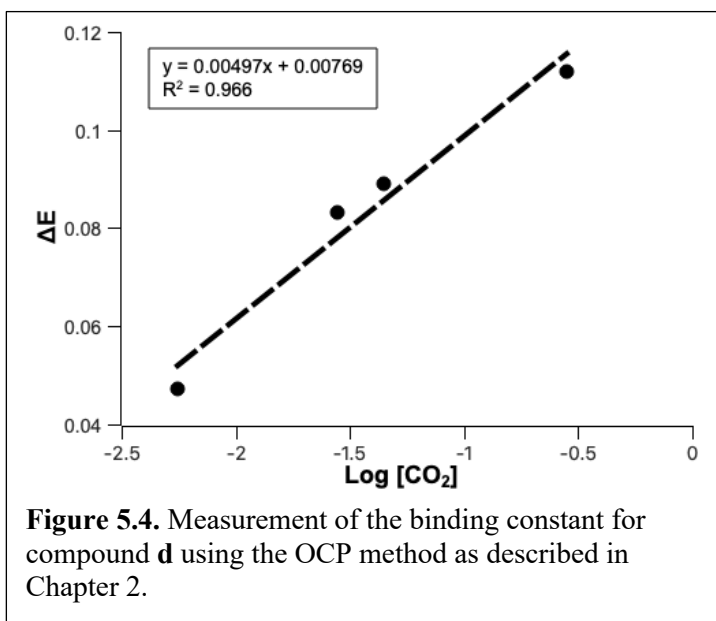
Figure 5.4. Measurement of the binding constant for compound **d** using the OCP method as described in Chapter 2.

and the OCP binding constant plot for compound **e** is featured in **Figure 5.5**.
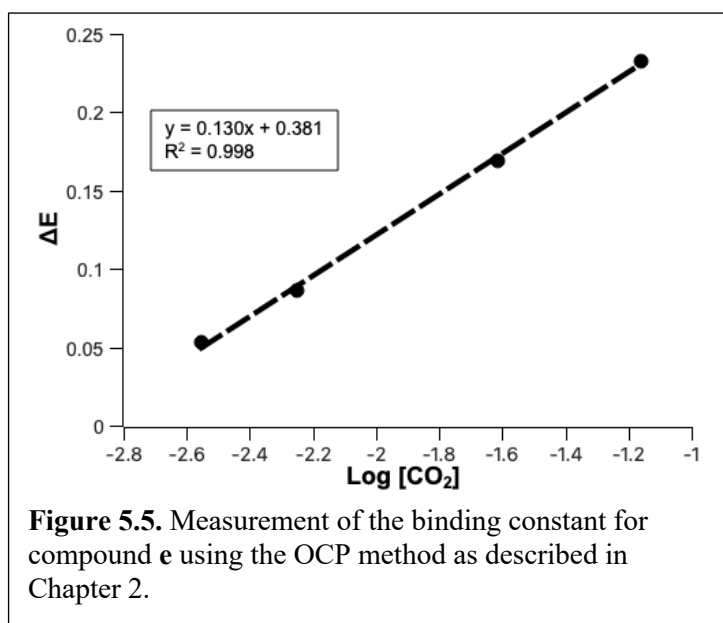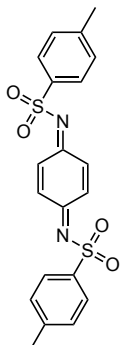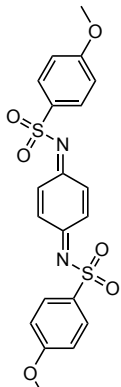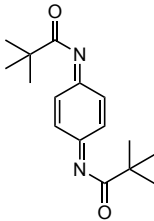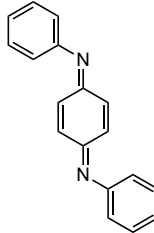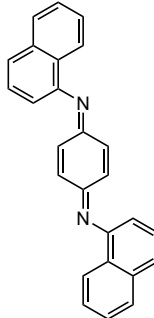
Figure 5.5. Measurement of the binding constant for compound **e** using the OCP method as described in Chapter 2.

Table 5.1. Reduction potentials and CO_2 binding affinities of benzoquinone di-imines synthesized and studied in this work.

Compound	Structure	$E_{1/2}$ [V] (vs. Fe$(C_5H_5)_2^{+/0}$)	log (K_{CO_2})	Solvent
a		-0.71	1.1	Dichloromethane
b		-0.62	0.77	Acetonitrile
c		-0.60	0.87	Acetonitrile
d		-1.81	2.5 ± 0.2	Acetonitrile
e		-1.67	6.4 ± 0.1	Acetonitrile

5.3 Discussion

Electronic effects dictate the measured reduction potential and CO_2 binding affinities. While Hammett parameters are not directly applicable to a benzoquinone di-imine system, they offer insight into relevant electronic effects. Generally, the σ_p for carbonyl is 0.50, whereas the σ_p for tosyl is 0.28 and the σ_p for phenyl is -0.01.[9,10]

The pivaloyl group in compound **a** has the most positive reduction potential, which was expected, as the pivaloyl group was expected to be the most electron withdrawing substituents studied, bearing similarity to a carbonyl group. Compound **b** had methoxy tosyl substituents that resulted in a very similar reduction potential to that of compound **a.** Both methyl and methoxy groups are considered electron donating groups, with methoxy generally considered to be a stronger electron donor. However, compound **b** had a notably more positive reduction potential than compound **c**. Methoxy groups that are not directly appended to the ring can have a lesser electron donating effect than methyl groups. For example, the σ_p for a $-CH_2OMe$ group is 0.01 and the σ_p for an ethyl group is -0.15. Since the methoxy is attached to the tosyl group, it is apparent that the methoxy tosyl substituted benzoquinone di-imine has more electron withdrawing character. Additionally, while phenyl and naphthyl are considered weakly electron donating groups, naphthalene is considered more reactive than benzene. The reactivity differences translate into a more positive reduction potential for compound **e** in comparison to compound **d**.

The benzoquinone di-imines with electron withdrawing substituents (compounds **a**, **b**, and **c**) have small K_{CO_2} values, which aligns with the linear free energy relationship between the reduction potential and K_{CO_2} (**Figure 5.6**). The reduction potentials and log K_{CO_2} values of compounds **b** and **c** were comparable to 2,3-dicyano-5,6-dichlorobenzoquinone, which has a reported reduction potential of -0.65 V vs. $Fe(C_5H_5)_2^{+/0}$ and log K_{CO_2} of 0.56. Similarly, the

reduction potential of the naphthyl-substituted benzoquinone di-imine mirrored the quinones with similar reduction potentials, and it has similar binding constants to anthraquinones with substituents that could hydrogen bond to the nucleophilic oxygen. While a naphthyl group is not expected to be a hydrogen bond donor, the naphthyl group stabilizes the dianion more than the phenyl group. This stabilization may reduce the nucleophilicity of the nitrogen atom.

Figure 5.6. The relationship of the log of the CO_2 binding affinity versus the reduction potential correlates with electronic character for the benzoquinone di-imines measured within this chapter.
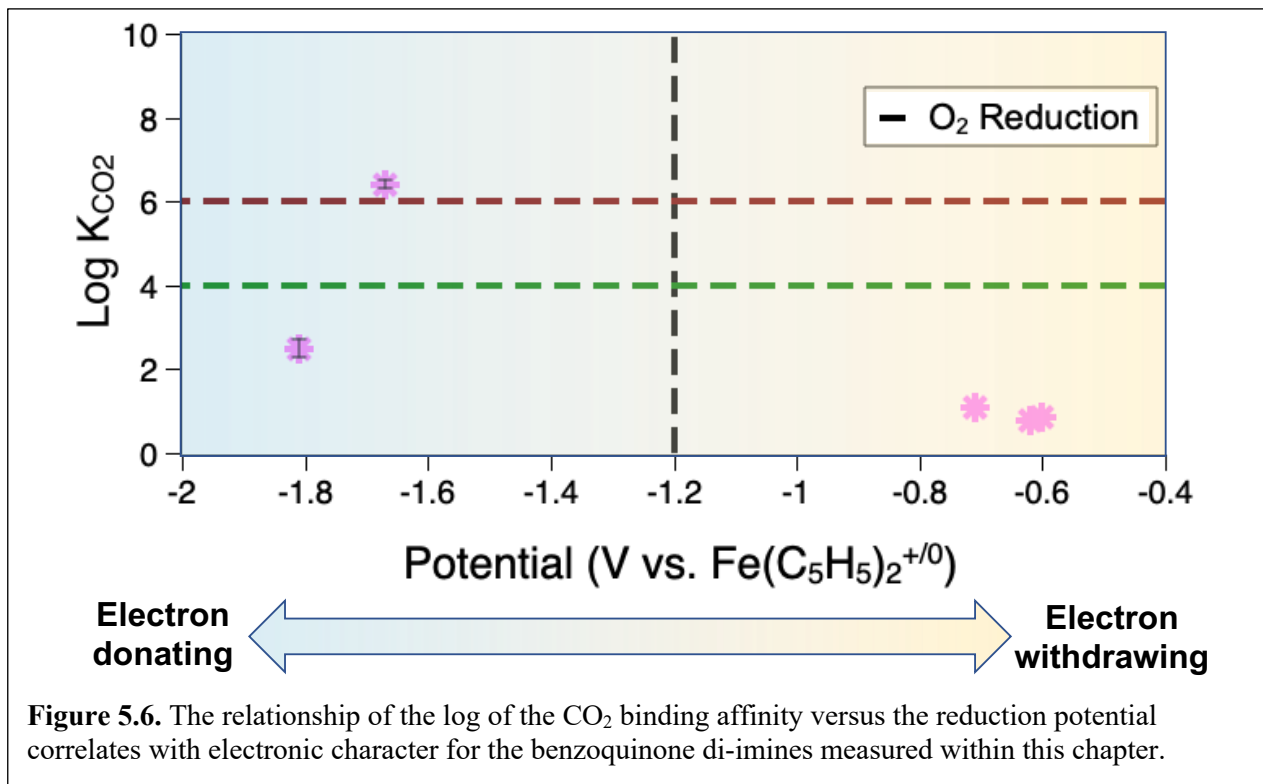
5.4 Conclusion

The characterization of a new class of redox carriers to be used for CO_2 capture is described. Five benzoquinone di-imines were synthesized and studied using electrochemistry in the presence and absence of CO_2 to learn about them as redox carriers. The benzoquinone di-imines functionalized with electron withdrawing groups have two reversible one-electron redox couples that are positive of the dioxygen to superoxide reduction potential. The species that

combines the structures of a benzoquinone and a benzoquinone di-imine to form an asymmetric molecule (**Figure 5.8**) could be an effective solution for breaking the linear free energy relationship between reduction potential and K_{CO_2}. Specifically, functionalizing the imine as well as the ring may offer the opportunity to specifically tune parameters of interest for the electrochemical carbon dioxide capture and fuel cell communities.

Figure 5.7. General structure for an asymmetric benzo-quinone imine.
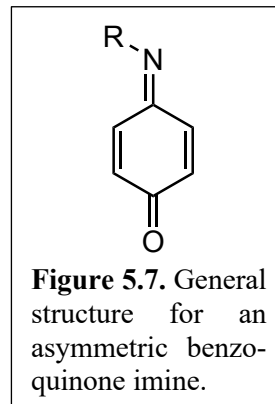
5.5 Experimental Methods (Sections 5.2 and 5.3 were performed with Jesus Galeana)

General Methods: Synthesis and manipulation of compounds were carried out in open air unless otherwise mentioned. For air- and moisture-sensitive procedures, manipulations were carried out using standard Schlenk techniques or in a glovebox under an inert atmosphere of dinitrogen. All reagents and solvents were used as received without further purification unless otherwise noted. Deuterated solvents were purchased from Cambridge Isotopes Laboratories, Inc. and were used as received without further purification. Electrochemical studies were performed using high purity (99.999%) carbon dioxide passed through a VICI carbon dioxide purification column to eliminate residual H_2O, O_2, CO, halocarbons, and sulfur contamination. Compounds a and b were synthesized in two steps.[11,12] Compound c was synthesized as the hydroquinone,[11] and subsequently deprotonated using 2 equivalents of tetrabutylammonium methoxide in the same manner as described in Chapter 3. Electrochemical characterization was performed on the dianion for compound c. Compounds d and e were synthesized by oxidation of the hydroquinone forms, which were commercially available.[12]

Electrochemistry: All electrochemical measurements were performed using a Pine Wavedriver 10 bipotentiostat. Cyclic voltammograms were taken with a 1 mm diameter glassy carbon disc

working electrode, a silver wire pseudoreference electrode, and a glassy carbon rod counter electrode. Bulk electrolyses were taken using either glassy carbon or carbon cloth working and counter electrodes with a Ag/Ag^+ reference electrode. Open circuit potential measurements were taken using a 1 mm diameter glassy carbon disc working electrode, a Ag/Ag^+ reference electrode, and a glassy carbon counter electrode. OCP was taken over 15 seconds and values were average All electrochemistry was done in non-aqueous solvents and was therefore referenced to ferrocene as an internal standard $(Fe(C_5H_5)_2^{+/0})$ at 0.00 V. All experiments were performed in dry and degassed organic solvents using 1mM analyte with 100 mM tetrabutylammonium hexafluorophosphate $(TBAPF_6)$ supporting electrolyte concentrations. Compounds **b, c, d,** and **e** were all studied in acetonitrile while compound **a** was studied in dichloromethane because it was not solubile in acetonitrile. For electrochemical studies performed under CO_2 conditions, samples were prepared by sparging the analyte solution with carbon dioxide gas for 5 minutes prior to measurement. CO_2 concentrations were controlled using the gas mixer (explained in Appendix A).

5.6 References

(1)   Bell, W. L.; Miedaner, A.; Smart, J. C.; DuBois, D. L. Synthesis and Evaluation of Electroactive CO2 Carriers. *SAE Technical Paper Series*. 1988, pp 1–10. https://doi.org/10.4271/881078.

(2)   Namazian, M.; Zare, H. R.; Yousofian-Varzaneh, H. Electrochemical Behavior of Tetrafluoro-p-Benzoquinone at the Presence of Carbon Dioxide: Experimental and Theoretical Studies. *Electrochim. Acta* **2016**, *196*, 692–698. https://doi.org/10.1016/J.ELECTACTA.2016.02.159.

(3)   Nagaoka, T.; Nishii, N.; Fujii, K.; Ogura, K. Mechanisms of Reductive Addition of CO2

to Quinones in Acetonitrile. *J. Electroanal. Chem.* **1992**, *322* (1–2), 383–389. https://doi.org/10.1016/0022-0728(92)80090-Q.

(4)   Schimanofsky, C.; Wielend, D.; Kröll, S.; Lerch, S.; Werner, D.; M. Gallmetzer, J.; Mayr, F.; Neugebauer, H.; Irimia-Vladu, M.; Portenkirchner, E.; et al. Direct Electrochemical CO2 Capture Using Substituted Anthraquinones in Homogeneous Solutions: A Joint Experimental and Theoretical Study. *J. Phys. Chem. C* **2022**, *126* (33), 14138–14154. https://doi.org/10.1021/acs.jpcc.2c03129.

(5)   Ranjan, R.; Olson, J.; Singh, P.; Lorance, E. D.; Buttry, D. A.; Gould, I. R. Reversible Electrochemical Trapping of Carbon Dioxide Using 4,4′-Bipyridine That Does Not Require Thermal Activation. *J. Phys. Chem. Lett.* **2015**, *6* (24), 4943–4946. https://doi.org/10.1021/acs.jpclett.5b02220.

(6)   Li, X.; Zhao, X.; Liu, Y.; Hatton, T. A.; Liu, Y. Redox-Tunable Lewis Bases for Electrochemical Carbon Dioxide Capture. *Nat. Energy 2022 711* **2022**, *7* (11), 1065–1075. https://doi.org/10.1038/s41560-022-01137-z.

(7)   Schmidt, M. H.; Miskelly, G. M.; Lewis, N. S. Effects of Redox Potential, Steric Configuration, Solvent, and Alkali Metal Cations on the Binding of Carbon Dioxide to Cobalt(I) and Nickel(I) Macrocycles. *J. Am. Chem. Soc.* **1990**, *112* (9), 3420–3426. https://doi.org/10.1021/ja00165a027.

(8)   Mizen, M. B.; Wrighton, M. S. Reductive Addition of CO2 to 9,10-Phenanthrenequinone. *J. Electrochem. Soc.* **1989**, *136* (4), 941. https://doi.org/10.1149/1.2096891.

(9)   Hansch, C.; Leo, A.; Taft, R. W. A Survey of Hammett Substituent Constants and Resonance and Field Parameters. *Chem. Rev.* **1991**, *91* (2), 165–195. https://doi.org/10.1021/cr00002a004.

(10)   Stang, P. J.; Anderson, A. G. Hammett and Taft Substituent Constants Hammett and Taft Substituent Constants for the Mesylate, Tosylate, and Triflate Groups. *J. Org. Chem* **1976**, *41* (5), 781.

(11)   Ito, A.; Sakamaki, D.; Ino, H.; Taniguchi, A.; Hirao, Y.; Tanaka, K.; Kanemoto, K.; Kato, T. Polycationic States of Oligoanilines Based on Wurster's Blue. **2009**. https://doi.org/10.1002/ejoc.200900403.

(12)   Bhatnagar, I.; George, M. V. Oxidation with Metal Oxides. III. Oxidation of Diamines and Hydrazines with Manganese Dioxide. *J. Org. Chem.* **1968**, *33* (6), 2407–2411. https://doi.org/10.1021/JO01270A052.

Chapter 6

Redox Carrier Development for Electrochemical CO$_2$ Capture Using Intermolecular and Intramolecular Interactions

Portions of this chapter were performed with Dr. Carina Jette.

6.1 Introduction

Secondary sphere interactions have a direct effect on the reduction potential and CO_2 binding affinity, as has been discussed at length in chapters 1, 3, and 4. While many quinones have been studied for CO_2 binding, none have broken the linear free energy relationship. Intermolecular and intramolecular interactions may be able to more finely tune the reduction potentials and, consequently, CO_2 binding affinities compared to modifying the electronic structure by altering the functional groups on the quinone.

The identity of the supporting electrolyte results in notable changes in the electrochemical properties of the quinones (Chapter 3). Additional studies using intermolecular and intramolecular interactions have been performed and described in this chapter to find a system that could capture and release carbon dioxide from air in the presence of dioxygen. This condition requires a CO_2 binding affinity (K_{CO2}) of ~6 M^{-1} and a reduction potential positive of -1.2 V vs. $Fe(C_5H_5)_2^{+/0}$. Beyond changing the cation of the supporting electrolyte as described in Chapter 3, there were efforts made to install alkali metals within a crown attached to the quinone. Installation of non-redox active cations into the crown ether entity of transition metal complexes result in anodic shifts in the reduction potential of the transition metal.[1–3] A quinone with an appended crown ether was investigated to determine the effect of a cation in the crown entity on CO_2 binding affinity. Additional efforts were made to study the effect of intermolecular and intramolecular hydrogen bonding on quinone reduction potential. Anthraquinones with hydrogen bond donating and hydrogen bond accepting groups in the 1, 4, 5, and 8 positions were probed to study the effect of these groups on the reduction potential of the dianion. Quinones with phenylsulfonyl groups were probed to study the effect of a hydrogen bond accepting group on the aromatic ring. The dual effect of a hydrogen bond accepting phenylsulfonyl group installed on the aromatic ring and in ethanol,
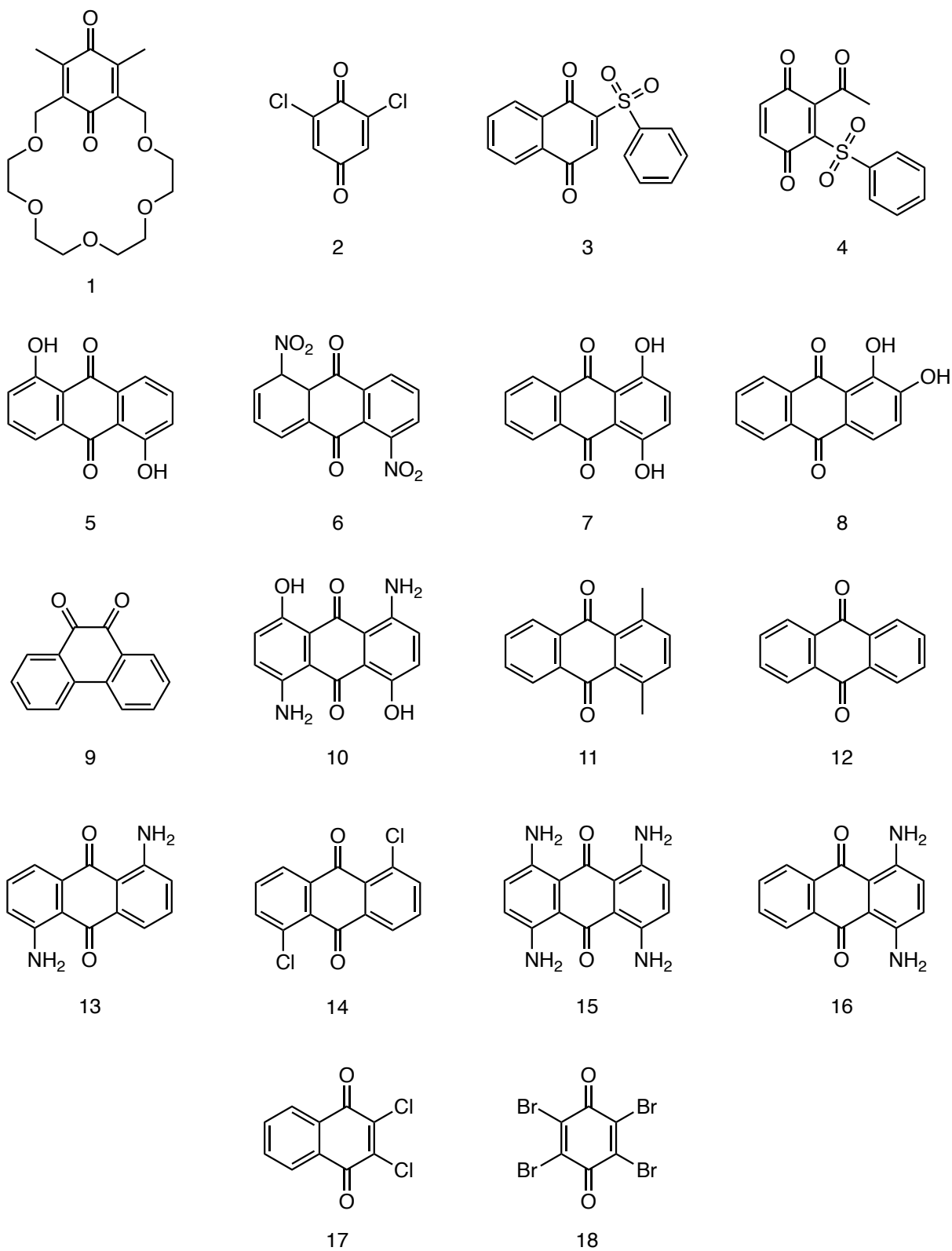
Figure 6.1. All quinones studied within this chapter.

which is also a hydrogen bond donor, was studied. Also, multiple intramolecular hydrogen bond

donor-quinone systems were studied for their effect on CO_2 binding and reduction potential. All compounds studied within this chapter are depicted in **Figure 6.1**.

6.2 Results and Discussion

6.2.1 Quinone Crown Ether

Previous studies have found that inserting alkali metals into the crown of a redox-active quinone crown ether results in more anodic reduction potentials.[4] 6QC (**1**) was synthesized and studied electrochemically. CVs were taken of 6QC without an cation, and upon addition of lithium, sodium, and potassium. A described in prior work, the CV of 6QC has two quasi-reversible reduction events to form the radical anion and dianion species.[4] However, in the presence of cations, only one redox couple is observed. We were able to reproduce these reduction events. However, there was no observed shift in the presence of CO_2. As previously mentioned in Chapter 3, the absence of a shift under CO_2 is likely due to the coordination of the alkali metals to the dianion. As a result, this system would not be desirable for CO_2 binding.

6.2.2 18-Crown-6 as an Additive

Figure 6.2. CVs of a 1mM solution of 2,6-dichloro-p-benzoquinone upon titration of 18-crown-6 under N_2 (a) and CO_2 (b).
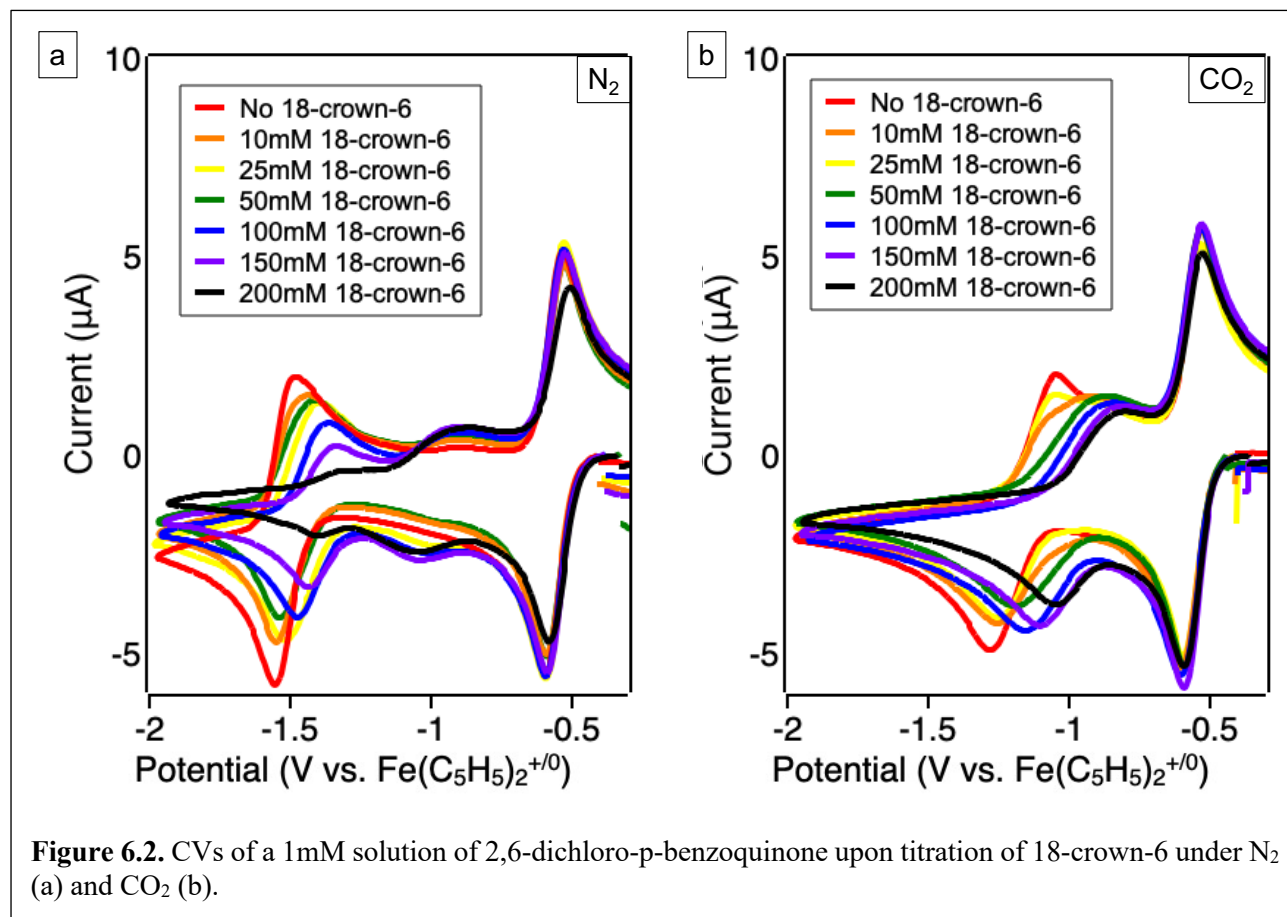
In Chapter 3, the addition of alkali and alkaline earth metals were discussed as a non-redox active additive for stabilization of the quinone dianion. This concept was inspired by the work with 6QC. To study the role of the empty crown in dianion stabilization, 18-crown-6 was titrated into a 1mM solution 2,6-dichloro-p-benzoquinone (**2**) with 100mM $TBAPF_6$ in DMF. It is not expected that the empty 18-crown-6 would have any effect on the reduction potential, as 18-crown-6 is redox-innocent. However, titration of 18-crown-6 resulted in the gradual growth of an additional redox feature more positive of the dianion formation with gradual disappearance of the redox couple associated with formation of the dianion under N_2 (**Figure 6.2a**). For the CO_2-sparged solution, addition of the crown resulted in a positive shift the redox event associated with formation

of the dianion. However, the additional redox feature that appears at –1 V vs. $Fe(C_5H_5)_2^{+/0}$ with increasing concentration of 18-crown-6 was not witnessed (**Figure 6.2b**).

By comparing the CVs between 2,6-dichloro-p-benzoquinone in the presence and absence of CO_2, the presence of 18-crown-6 appears to inhibit CO_2 binding (**Figure 6.3**). An alkali metal such as sodium or potassium, may be a contaminant, causing a shift of the reduction potential. Since the addition of 18-crown-6 hindered CO_2 binding under these conditions, this project was not further investigated.

6.2.3 Phenylsulfonyl-substituted Quinones

After the studies described in Chapter 2, attempts were made to identify a weakly electron withdrawing group that could be appended to a quinone to form a species that had a reduction

Figure 6.3. A direct comparison of the CVs of 2,6-dichloro-p-benzoquinone without 18-crown-6 (top) and with 200 equivalents of 18-crown-6 (bottom). Addition of 18-crown-6 appears to inhibit CO_2 binding.

potential and CO_2 binding affinity with appropriate properties to capture CO_2 from air. One such weakly electron withdrawing group is a phenylsulfonyl group. Two compounds of interest were synthesized and studied for CO_2 binding character.

2-phenylsulfonyl-p-naphthoquinone (3)
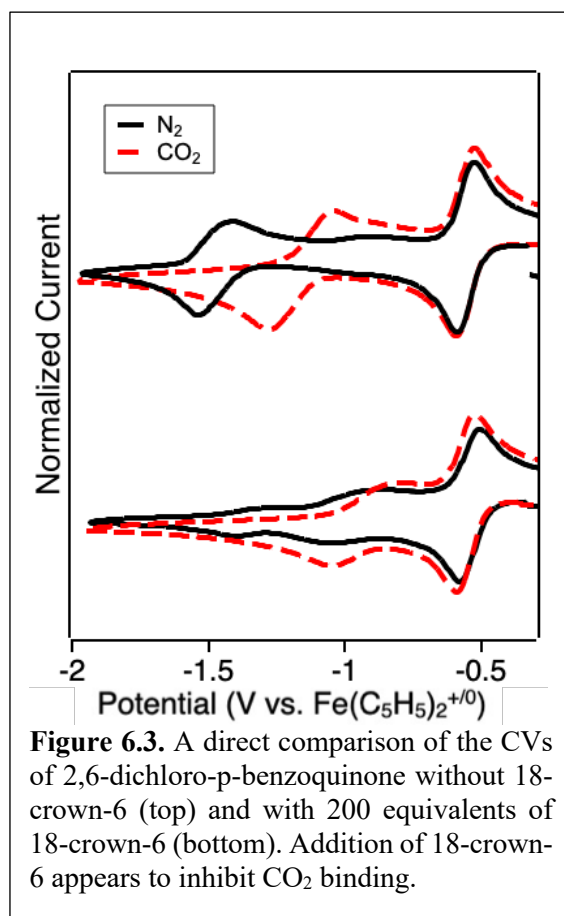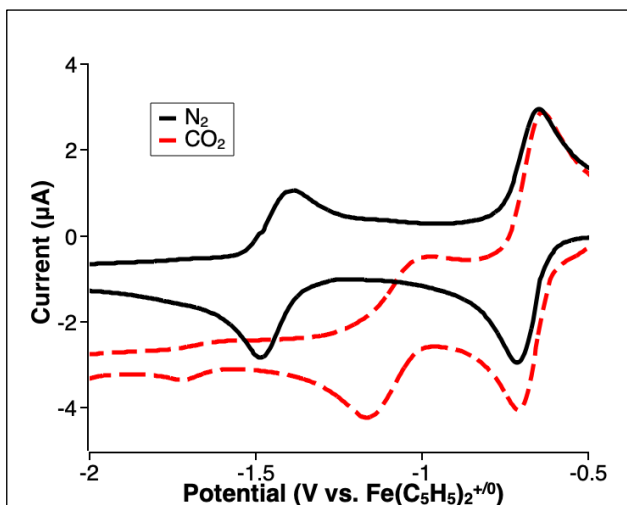
Figure 6.4. CV of 2-phenylsulfonyl-p-naphthoquinone under N_2 and CO_2. Performed in acetonitrile.

The first compound was 2-phenylsulfonyl-p-naphthoquinone. It was characterized by CV to have a reduction potential of -1.45 V vs. $Fe(C_5H_5)_2^{+/0}$ and a log K_{CO2} of 6.6 in acetonitrile (**Figure 6.4**).

2-acetyl-3-phenylsulfonyl-p-naphthoquinone (4)

The second compound, 2-acetyl-3-phenylsulfonyl-p-benzoquinone was synthesized by Dr. Carina Jette following a literature procedure.[5] The reduction potential for this compound is -1.33 V vs. $Fe(C_5H_5)_2^{+/0}$ and the log K_{CO2} was ~4. Under CO_2, the second reduction feature became quasi-reversible. Ethanol was added to investigate the effects of an intramolecular hydrogen bond donor on the reduction potential of the quinone (**Figure 6.5**). Upon the addition of 100 equivalents of ethanol to a 1 mM solution of 2-acetyl-3-phenylsulfonyl-p-benzoquinone and 100 mM $TBAPF_6$ in acetonitrile, an anodic shift in potential positive of

Figure 6.5. CV of 1 mM solution of 2-acetyl-3-phenylsulfonyl-p-benzoquinone with 100 mM $TBAPF_6$ in acetonitrile with increasing equivalents of ethanol as an intramolecular hydrogen bond donor. Reduction potentials sufficiently positive of dioxygen reduction is observed after adding 100 equivalents of ethanol.

the dioxygen reduction was seen. Upon the addition of CO_2, the CO_2 binding affinity did not significantly change.

6.2.4 Anthraquinones with Intermolecular Hydrogen Bonding Substituents

In an attempt to install charge or electronic stabilization within the backbone of the quinone and study the effect these substituents would have on the reduction potential, twelve anthraquinones were studied electrochemically (**Table 6.1**). The quinones with hydrogen bond donating hydroxyl substituents had notably positive reduction potentials in comparison to anthraquinone by itself. The presence of hydrogen bond accepting amino substituents on the backbone of the anthraquinone resulted in notably negatively shifted reduction potentials.

Table 6.1. A table of the twelve anthraquinone probed electrochemically in acetonitrile and their associated reduction potentials required to form the dianion.

Anthraquinone (AQ)	$E_{1/2}^2$ (V vs. $Fe(C_5H_5)_2^{+/0}$)
Anthrarufin (1,5-dihydroxy-AQ) (**5**)	-1.44
1,5-dinitro-AQ (**6**)	-1.57
Quinizarin (1,4-dihydroxy-AQ) (**7**)	-1.59
Alizarin (1,2-dihydroxy-AQ) (**8**)	-1.69
PAQ (9,10-phenanthrenequinone) (**9**)	-1.69
1,5-diamino-4,8-dihydroxy-AQ (**10**)	-1.73
1,4-dimethyl-AQ (**11**)	-1.87
Anthraquinone (**12**)	-1.96
1,5-diamino-AQ (**13**)	-2.04
1,5-dichloro-AQ (**14**)	-2.11
Disperse Blue (1,4,5,8-tetraamino-AQ) (**15**)	-2.13
1,4-diamino-AQ (**16**)	-2.18

As reported in work by Dubois and coworkers and noted in Chapter 2, electron withdrawing groups result in more positively shifted reduction potentials. In comparison to

anthraquinone, the reduction potential of anthrarufin (1,5-dihydroxy-anthraquinone) is about 500 mV more positive. This value, however, is not sufficient to avoid favorable electron transfer with dioxygen. 1,4-diamino-anthraquinone, however, has a reduction potential over 200 mV more negative of the unsubstituted anthraquinone, demonstrating the electronic effects with an electron donating substituent. There is also a 140 mV difference between the 1,4-diamino-anthraquinone and the 1,5-diaminoanthraquinone. This drastic potential change between two compounds with the same substituents in slightly different positions offers insight into the interactions between the nucleophilic oxygen and the nearby functional groups.

6.2.5 Intramolecular Hydrogen Bond Donors

Initial work performed by Dr. Jeffrey Barlow demonstrated that addition of intramolecular hydrogen bond donors offered promising stabilization of the dianion without inhibiting CO_2 binding.[6] His work was the first demonstrated redox carrier system that had a CO_2 binding affinity sufficient for flue gas capture with a reduction potential that avoided the dioxygen reduction. He used tetrachloro-p-benzoquinone with ethanol as a hydrogen bond donating additive in a DMF system. Tetrachloro-p-benzoquinone is extremely light sensitive, and studies on capture and release CO_2 over multiple cycles were not successful due to decomposition that occurs upon the second attempted reduction or oxidation. The work herein describes three of the most promising attempts to use intramolecular hydrogen bond donors with quinones that are expected to be more robust in hopes of identifying a cyclable system.

2,6-dichloro-p-benzoquinone with ethanol

Figure 6.6. CV of 1 mM solution of 2,6-dichloro-p-benzoquinone with 100 mM TBAPF$_6$ in DMF with increasing concentrations of EtOH. A shift positive of the dioxygen reduction is only observed after adding 500 equivalents of ethanol.
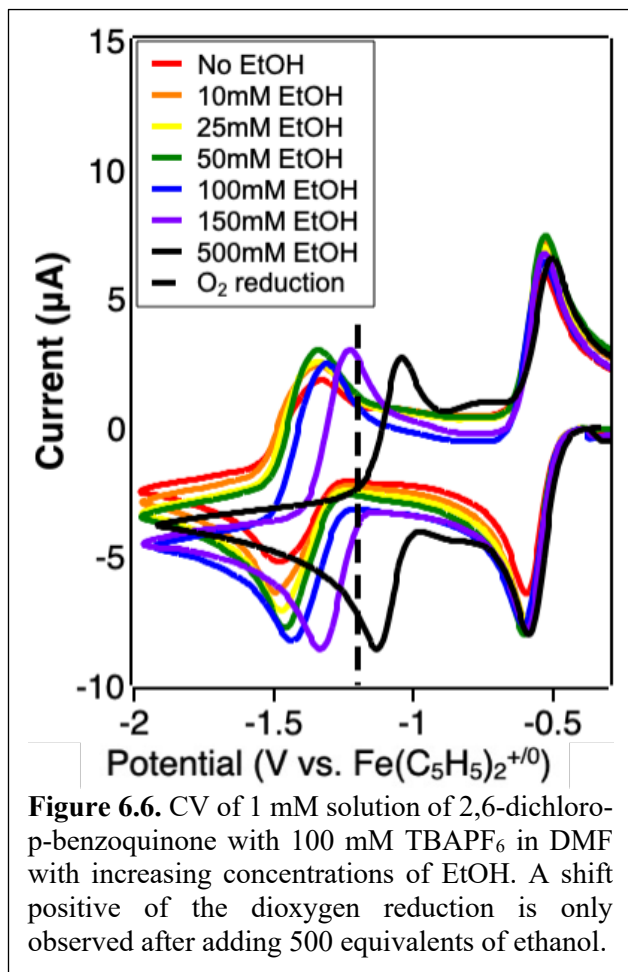
The first compound studied for ethanol addition was 2,6-dichlorobenzoquinone due to its high log K_{CO2} value of 6. The impact on the reduction potential upon titration of ethanol was studied by cyclic voltammetry. The addition of ethanol results in a positive shift in the reduction potential. After 500 equivalents, the reduction potential is positive of the dioxygen to superoxide reduction potential (**Figure 6.6**). CVs taken in the presence of 500 equivalents of ethanol and under an atmosphere of CO$_2$ indicate that the CO$_2$ binding constant does not significantly decrease in the presence of ethanol. The

reduction potential under N$_2$ shifts from –1.39 V vs. Fe(C$_5$H$_5$)$_2^{+/0}$ without ethanol to –1.07 V vs. Fe(C$_5$H$_5$)$_2^{+/0}$ in the presence of 500 equivalents of ethanol. 2,6-dichloro-p-benzoquinone is not expected to be as sensitive to light. Based on the high binding constant and more anodic reduction potential, this system may be interesting for testing for direct air capture, which requires a log K_{CO2} of ~6, depending on the solvent.

2,3-dichloro-p-naphthoquinone with ethanol

Another compound of interest is 2,3-dichloro-p-naphthoquinone (**17**). Naphthoquinones tend to have more negative reduction potentials compared to benzoquinones; however, since they

Figure 6.7. CVs of a 1 mM solution of 2,3-dichloro-p-naphthoquinone with 100 mM TBAPF$_6$ in DMF with added ethanol as a hydrogen bond donor. Upon addition of 500 equivalents of ethanol, the reduction potential to the dianion is shifted positive by 360 mV.
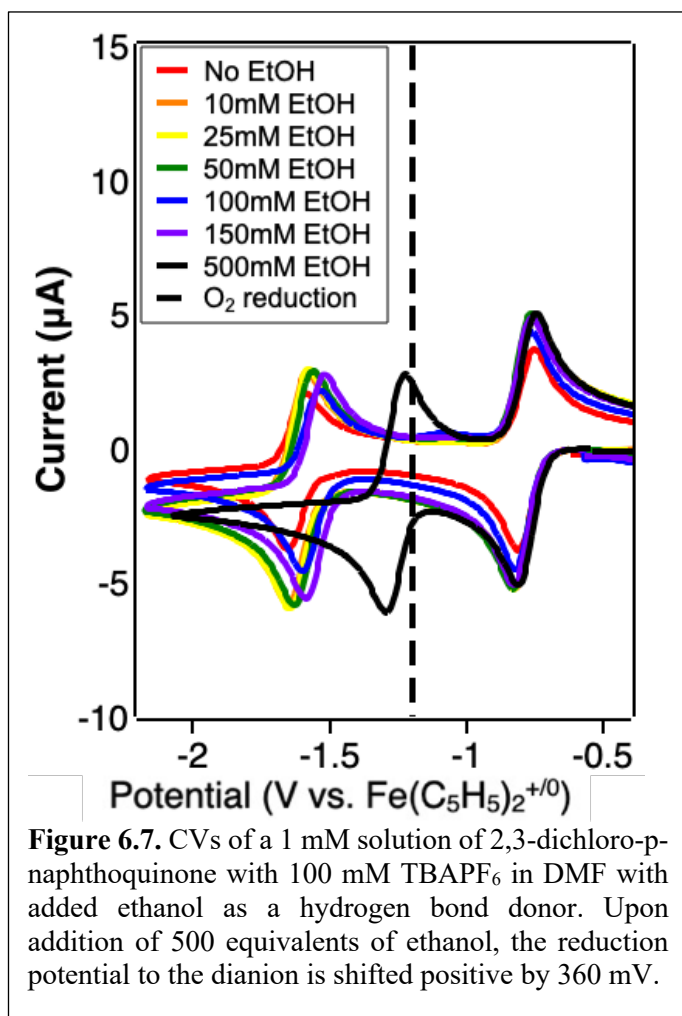
have a second aromatic ring, they tend to be less susceptible to the Kolbe-Schmitt decomposition reaction.[7] Under N$_2$, 2,3-dichloronaphthoquinone has a reduction potential of –1.61 V vs. Fe(C$_5$H$_5$)$_2^{+/0}$ in DMF. The addition of 500 equivalents of ethanol results in a reduction potential of –1.25 V vs. Fe(C$_5$H$_5$)$_2^{+/0}$ (**Figure 6.7**). CO$_2$ binding was probed, but the peaks merged into one upon the addition of ethanol.

Tetrabromo-p-benzoquinone with ethylene glycol

In a flow system, solvents with lower vapor pressures are preferred. The vapor pressure of ethanol at 20º C is 5.95 kPa. The first demonstration of an electrochemical carbon capture system capable of capture in the presence of dioxygen used ethanol.[6] However, in an attempt to use a hydrogen bond donor with a lower vapor pressure, ethylene glycol was used for CV studies in propylene carbonate. Ethylene glycol has a vapor pressure of 0.007 kPa, and propylene carbonate has a vapor pressure of 0.04 kPa. Tetrabromo-p-benzoquinone (bromanil, **18**) was used as a model compound because it should be capable of electrochemical capture from flue gas, with a measured reduction potential of -1.28 V vs. Fe(C$_5$H$_5$)$_2^{+/0}$ and a log K_{CO2} value of 3.3 in DMF (Chapter 2).

In propylene carbonate, tetrabromo-p-benzoquinone has a reduction potential of -1.21 V vs. $Fe(C_5H_5)_2^{+/0}$. Upon the addition of 100 equivalents of ethylene glycol, the reduction potential shifts to -1.03 V vs. $Fe(C_5H_5)_2^{+/0}$ while remaining reversible. This 180 mV difference results in a reduction potential positive of dioxygen

Figure 6.8. CVs were taken of a 1 mM solution of bromanil 100 mM TBAPF$_6$ in DMF upon titration of ethylene glycol as a hydrogen bond donor. Upon addition of 100 equivalents of ethylene glycol, the reduction is positive of the dioxygen reduction.
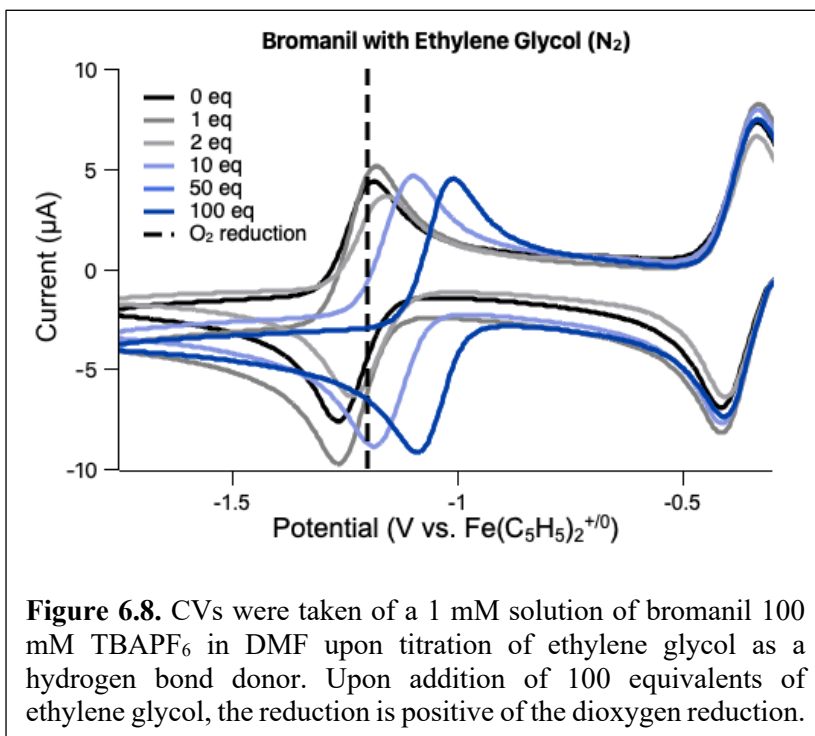
reduction (**Figure 6.8**). Upon the addition of CO_2, the log K_{CO2} for tetrabromo-p-benzoquinone in propylene carbonate is 2.9; with 100 equivalents of ethylene glycol, the log K_{CO2} is estimated to be the same. Ethylene glycol is an alternative hydrogen bond donor that could work well in flow systems.

6.3 Conclusion

Intermolecular and intramolecular interactions can affect the reduction potential of the redox carrier; however, depending on the type of interaction, it may significantly decrease the CO_2 binding affinity. Installation of cations into a quinone crown ether entity arrests CO_2 binding. It is expected that the absence of CO_2 binding is attributed to more favorable binding to the cation in the crown ether entity. Though the crown was assumed to be innocent, the effect of titration of 18-crown-6 was investigated using 2,6-dichloro-p-benzoquinone. It appears that there is an interaction

of the 18-crown-6 with the dianion, however, upon addition of CO_2, this does not inhibit binding. There is a possibility that the crown is not empty and contains a cation such as sodium, and the shift seen in **Figure 6.2** is due to an interaction with a crown-bound cation.

Substituting quinones with phenylsulfonyl groups resulted in more anodic dianion reduction potentials. However, the weakly electron withdrawing functional group addition did not break the linear free energy relationship between K_{CO2} and reduction potential.

Intermolecular hydrogen bond donors installed in the anthraquinone backbone arrested CO_2 binding, while intermolecular hydrogen bond acceptors installed in the anthraquinone backbone enhanced CO_2 binding. Unfortunately, neither of these effects resulted in the ideal parameters for CO_2 capture from flue gas.

The addition of intramolecular hydrogen bond donors results in positive shifts of the reduction potential without significant effects on CO_2 binding. Future directions of interest for this work would include investigation of a combined system of 2,6-dichloro-p-benzoquinone and ethanol or 2-acetyl-3-phenylsulfonyl-p-benzoquinone and ethanol for electrochemical cycling of CO_2 capture and release.

6.4 Experimental Methods

6.4.1 General Methods

All salts and solvents were rigorously dried using vacuum and molecular sieves, respectively. 2,6-dichloro-p-benzoquinone (**2**), anthrarufin (**5**), 1,5-dinitro-anthraquinone (**6**), quinizarin (**7**), alizarin (**8**), 9,10-phenanthrenequinone (**9**), 1,5-diamino-4,8-dihydroxy-anthraquinone (**10**), 1,4-dimethyl-anthraquinone (**11**), anthraquinone (**12**), 1,5-diamino-anthraquinone (**13**), 1,5-dichloro-anthraquinone (**14**), disperse blue (**15**), 1,4-diamino-

anthraquinone (**16**), 2,3-dichloro-p-naphthoquinone (**17**), and tetrabromo-p-benzoquinone (**18**) were purchased and used without further purification. 6QC (**1**),[4] 2-phenylsulfonyl-naphthoquinone (**3**),[5] and 2-acetyl-3-phenylsulfonyl-p-benzoquinone (**4**)[5] were synthesized using literature procedures. Tetrabutylammonium hexafluorophosphate were all recrystallized 2-3 times with hot ethanol and rigorously dried before use.

6.4.2 Electrochemical Methods

Cyclic voltammetry was performed on a Pine Wavedriver 10 bipotentiostat with AfterMath software, using a 1 mm diameter glassy carbon disc working electrode and glassy carbon rod counter electrode. A $Ag^{+/0}$ pseudo-reference electrode containing a silver wire submerged in 0.1 M tetrabutylammonium hexafluorophosphate (TBAPF$_6$) separated from the bulk solution by a Vycor tip was used in addition to an internal $Fe(C_5H_5)_2^{+/0}$ reference. TBAPF$_6$ was recrystallized three times from hot ethanol and dried in a vacuum oven before use. Scans included iR drop compensation and $Fe(C_5H_5)_2^{+/0}$ was added as an internal reference and each CV was carefully referenced individually. A scan rate of 100mV/s was used for all cyclic voltammetry. For electrochemical studies performed under CO_2 conditions, samples were prepared by sparging the analyte solution with carbon dioxide gas for 5 minutes prior to measurement.

6.5 References

(1)   Chantarojsiri, T.; Reath, A. H.; Yang, J. Y.; Hantarojsiri, T. C.; Reath, A. H.; Ang, J. Y. Y. Cationic Charges Leading to an Inverse Free-Energy Relationship for N−N Bond Formation by Mn[VI] Nitrides. *Angew. Chemie Int. Ed.* **2018**, *57* (43), 14037–14042. https://doi.org/10.1002/ANIE.201805832.

(2)   Kang, K.; Fuller, J.; Reath, A. H.; Ziller, J. W.; Alexandrova, A. N.; Yang, J. Y. Installation

of Internal Electric Fields by Non-Redox Active Cations in Transition Metal Complexes †. **2019**. https://doi.org/10.1039/c9sc02870f.

(3)   Léonard, N. G.; Chantarojsiri, T.; Ziller, J. W.; Yang, J. Y. Cationic Effects on the Net Hydrogen Atom Bond Dissociation Free Energy of High-Valent Manganese Imido Complexes. *J. Am. Chem. Soc.* **2022**, *144* (4), 1503–1508. https://doi.org/10.1021/JACS.1C09583.

(4)   Delgado, M.; Wolf, R. E.; Hartman, J. R.; McCafferty, G.; Yagbasan, R.; Rawle, S. C.; Watkin, D. J.; Cooper, S. R. *Redox-Active Crown Ethers. Electrochemical and Electron Paramagnetic Resonance Studies on Alkali Metal Complexes of Quinone Crown Ethers*; 1992; Vol. 114.

(5)   Bruce, J. M.; Lloyd-Williams, P. Benzoquinones and Related Compounds. Part 6. Addition of Benzenesulfinic Acid to Substituted 1,4-Quinones. *J. Chem. Soc., Perkin Trans. 1* **1992**, 2877–2884. https://doi.org/10.1039/P19920002877.

(6)   Barlow, J. M.; Yang, J. Y. Oxygen Stable Electrochemical CO_2 Capture and Concentration with Quinones through Alcohol Additives. *J. Am. Chem. Soc.* **2022**, *144* (31), 14161–14169.

(7)   Dubois, D. L.; Miedaner, A.; Bell, W.; Smart, J. C. Electrochemical Concentration of Carbon Dioxide. In *Electrochemical and Electrocatalytic Reactions of Carbon Dioxide*; Sullivan, B. R., Ed.; Elsevier: Amsterdam, 1993; pp 94–117.

Appendix A

Development of a Cyclable Gas Capture System

A.1 Introduction

Testing the feasibility of using a redox carrier for repeated electrochemical capture and release of CO_2 requires the implementation of a gas capture apparatus. This apparatus differs from a catalytic system because CO_2 detection must be performed throughout the experiment. The goals of the gas capture apparatus are to (1) mix known quantities of CO_2 and N_2 for introduction to the electrolysis cell; (2) run electrolysis using a variable stationary cell setup; (3) detect the concentration of CO_2 in the headspace or outstream. To achieve these goals, the gas capture system is comprised of three main parts: the gas mixer, the stationary electrolysis cell, and the gas capture and analysis system. In attempts to optimize the system, multiple gas capture systems were developed and tested.

The first part of this appendix will provide insight into some of the attempts that were made to electrochemically cycle CO_2 using a redox carrier and the lessons learned from these attempts. There was variation of the stationary electrolysis cell, membrane or separator, electrodes, and modes for analysis of captured CO_2. The remainder of the appendix will explain each portion of the gas capture apparatus and provide information about how each portion can affect the overall electrochemical cycling experiments.

A.2 Results and Discussion

A.2.1 Attempts to Cycle and Lessons Learned

The first attempts to electrochemically bind and release CO_2 were done using 2,6-di-tert-butyl-benzoquinone (DtBBQ). DtBBQ was chosen because it had been used to concentrate a dilute stream of CO_2 previously by Scovazzo et al. (further described in Chapter 1).[1]

Figure A.1. (a) First iteration of electrolysis used for attempted electrochemical cycling and (b) H-cell used for subsequent electrochemical cycling. The electrodes marked in red represent the carbon working electrodes; electrodes with the gray cylinders represent the Ag reference electrodes; and the electrodes marked with the green cylinders represent the counter electrodes. Each cell was equipped with a stir bar in each compartment, and gas was sparged in through one of the openings in the cell. The additional opening in cell (a) was used for the addition of the redox carrier.

Two different electrochemical cells were used to attempt to reproduce the electrochemical reduction and oxidation of DtBBQ in the presence of CO_2. The first was an electrolysis cell that held ~100mL in the main chamber, and the counter electrode was in a smaller, separate chamber (**Figure A.1a**). The electrodes used were a glassy carbon rod for a working electrode (red, **Figure A.1a)**, Ag/AgCl for the reference electrode (gray, **Figure A.1a)**, and the counter electrodes had

been glassy carbon, vitreous carbon foam, platinum wire, or nichrome wire (generally represented by the green cylinder, **Figure A.1a**).

No attempts to electrochemically cycle using the cell in **Figure A.1a** were successful, so analysis of collected CO_2 was never performed. The failure of this system likely had a few causes. The separate counter electrode chamber led to uneven pressure within the cell. The volume of the cell was high, and all electrodes had a small surface area, leading to slower electrolyses than what were later achieved. There were problems with counter electrode choice, as well. It was found that the platinum wire did not have a sufficiently high surface area to be used as a counter electrode and the nichrome wire appeared to react during the electrolysis. We found that we were unable to amend the problems with uneven pressure in the counter electrode chamber and the high volume was leading to very long singular step runs (over 24 hours for an electrochemical reduction), so this cell was no longer used for cycling attempts.

All additional attempts to cycle DtBBQ were run using an H-cell; either an H-cell with a total volume of ~25mL and a medium frit as a permanent separator between the cells (**Figure A.1b**) or an H-cell with a total volume of ~20mL that was held together with a clamp and an o-ring such that a replaceable separator could be used. The electrodes used were a glassy carbon rod or vitreous working electrode (red, **Figure A.1b)**, Ag/Ag$^+$ for the reference electrode (gray, **Figure A.1b)**, and the counter electrodes had been glassy carbon, vitreous carbon foam, platinum wire, and nichrome wire (generally represented by the green cylinder, **Figure A.1b**).

Electrochemically cycling DtBBQ was generally unsuccessful. Using the exact concentrations described in Scovazzo et al.'s work proved to be difficult because they had used very high concentrations of analyte and electrolyte (0.3M DtBBQ and 0.75M TBAPF$_6$ in

propylene carbonate). These high concentrations combined with electrodes of limited surface area led to difficulties with compliance voltage. The Pine Wavedriver 10 bipotentiostat that we used was found to have too low of a compliance voltage at ±16.5 V. A Princeton Applied Research PARSTAT 2273 Advanced Electrochemical System was used since it has a ±100 V compliance voltage. Changing the potentiostat led to successful a controlled potential electrolysis, but unfortunately, with the high concentrations of analyte and the low surface area glassy carbon electrodes, we were still unable to run short electrolyses, and we ultimately saw decomposition of our redox carrier. The vitreous carbon foam offered a higher surface area but contact between the vitreous carbon and the potentiostat as inconsistent and the brittle vitreous carbon would crumble.

The lessons learned from experimental electrochemical cycling of DtBBQ were about volume and the importance of high surface area electrodes. When high volumes were used with low surface area electrodes, one electrolyses required a long period of time. Instead of hours for each reduction or oxidation, these systems would take multiple days or weeks. In a system where the goal is to electrochemically reduce and oxidize many times, this was not time-efficient, and therefore it was decided that only volumes of less than 25mL were of interest for future experiments. High surface area electrodes were also of particular interest because we were seeing problems with compliance voltage upon using a low surface area electrode such as glassy carbon. These lessons led to the implementation of carbon fabric as an electrode material and ketjenblack as an additive to the solution.

Cobalt tetraazamacrocycle

Additional attempts to electrochemically cycle were performed using a cobalt tetraazamacrocycle, and these electrochemical experiments are detailed in Chapter 4. The lessons

learned from these cycling attempts are described herein. When using a small concentration of redox carrier or a small volume, the amount of CO_2 that is expected to freeze out is not sufficient for detection using a pressure change. A CO_2 IR analyzer was implemented to allow for continuous monitoring of the headspace. It was also found that having a sacrificial oxidant in the counter compartment of the H-cell was helpful, though the sacrificial oxidant often crossed over into the working compartment, leading to losses in Faradaic efficiency that could not be quantified.

Tetrachloro-p-benzoquinone

Initial attempts to electrochemically cycle tetrachloro-p-benzoquinone were performed with Dr. Jeffrey Barlow. All of these were performed using an H-cell that had a permanent, porous frit installed between the compartments. The electrodes used were either carbon fabric or glassy carbon rods used with ketjenblack in solution. Tetrachloro-p-benzoquinone was known to be a particularly sensitive molecule, with sensitivities to light and oxygen in the dianionic form. Thus, electrochemical cycling experiments were performed entirely in the absence of light and in the glovebox. Continuous monitoring of the CO_2 concentration of the headspace was determined to be helpful for monitoring both CO_2 capture and release. However, there were initial problems with the speed of the pump on the CO_2 IR analyzer, which resulted in uneven pressure across the electrochemical cell.

The lessons learned from these experiments concerned the choice of oxidant for the counter compartment, the use of the CO_2 IR analyzer pump, and the importance of solvent choice. While ferrocene/ferrocenium was used as a sacrificial reductant/oxidant, the crossover was negatively impacting the Faradaic efficiency, so a symmetric cell was used. Tetrachloro-p-hydroquinone was deprotonated and used in the counter compartments as a sacrificial oxidant that, upon oxidation,

could be used as a sacrificial reductant for the next chemical step. The change to the dianionic quinone improved the Faradaic efficiencies and inhibited formation of non-quinone side products. Additionally, the CO_2 IR analyzer pump was too strong, so to mitigate this problem, the pump was only used at specific time points. Only using the pump at specific time points did not allow for continuous headspace monitoring, which is of interest for future cycling, however, since this was a fully closed system, this was the only option. Lastly, for all of the previous cycling experiments, solvents have been chosen mostly based on the solubility of the redox carrier within the solvent, and they have varied from acetonitrile to DMF to propylene carbonate. It has been found that for running multiple cycling experiments that include sparging of the solution, it is important to have some sort of gas-liquid contact before sparging into the analyte solution. Initial attempts to include gas-liquid contact have been through using a bubbler that contains the solvent of interest.

A.2.2 The Anatomy of the Gas Capture Apparatus

Gas Mixer

The gas mixer was built using four Cole-Parmer flow tubes. One CO_2-specific. It was found that in order to mix the gases so the CO_2 output could be controlled to be 0.5-10% CO_2, a 374 mL/min air tube must be used for the CO_2 inlet and a 500 mL/min nitrogen tube must be used for the nitrogen. These gases are then mixed in an 814 mL/min air tube, which leads to a correlated flow tube that allows for control of the mixed gas flowrate. The reliability of this setup as well as CO_2 headspace concentrations was tested through the use of an ExplorIR-W 100% CO_2 IR sensor. This sensor was combined with a motorized pump so the headspace could be cycled through the meter, allowing for more accurate measurement. An additional flow tube specified for O_2 mixing has been appended to the gas mixer as well such that oxygen-containing flue gas can be simulated.

Stationary Electrochemical Cell

A number of electrochemical cell setups were probed for usage in this system, as described in Section A.2.1. The first iterations used a 100-mL electrochemical cell that had a separate, fritted chamber for the counter electrode (**Figure A.1a**). This system was found to require too much material and had problems with pressure regulation, so a smaller, 20-mL H-cell was used. This H-cell was held together using a clamp and o-rings, which allowed for the usage of a membrane. Additionally, this H-cell had ground glass joints that could be used with septa but could not support three electrodes and a gas sparging/sampling system while remaining sealed, so this cell was not ideal for our needs. A 25-mL fritted H-cell was then employed (**Figure A.1b**). While this system is an improvement, there was significant crossover between the chambers. The last iteration of an H-cell that was used has a volume of 15mL and two separate chambers that are separated by a removable membrane.

Stationary Electrochemical Cell: Membranes and Separators

Scovazzo et al. reports using a Nafion membrane with aprotic solvents in their electrochemical setup.[1] We attempted to use a Nafion membrane when attempting to reproduce Scovazzo et al.'s demonstration, and we found that the Nafion membrane introduced water into the system. Most of the current capture systems mentioned in this thesis require dry solvent, so the Nafion membrane was left out of future iterations of the setup. If Nafion is to be used, solvent exchanges must be performed to ensure that the porous material. For further information about the intercalation of aprotic solvent into Nafion membranes and the effect is will have on conductivity, it is recommended to look at work by Yu et al.[2]

Many of our cycling attempts used an H-cell that had a frit that was not removable. It had medium porosity, which was deemed too high for our work and resulted in significant crossover between chambers. If a permanent frit is to be used, it has been recommended that a very fine or ultra fine frit is used to discourage crossover as much as possible. If a two-chamber H-cell is being used that does not have a permanent frit, then Celgard 2500 can be used as a membrane. Celgard is robust to all solvents expected to be used for these systems (acetonitrile, methanol, ethanol, propylene carbonate, DMF) and can be dried using a vacuum line before use in a water-sensitive reaction.
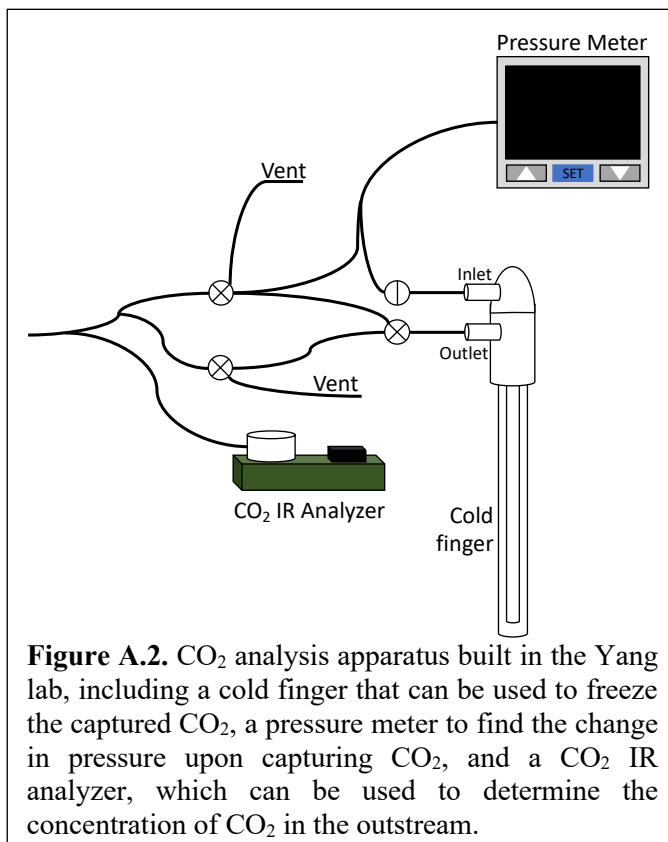
Electrode Choice

Initially, platinum wire and nichrome wire were used as counter electrodes. However, it was found that the surface area of the platinum wire was not sufficient, and the nichrome wire decomposed. Glassy carbon rods were then used as working and counter electrodes. However, it was found that the surface area limited contact with the redox carrier, especially redox carriers with limited solubility. This led to the calculated time to completion for all bulk electrolyses to be about a week for a single electrochemical reduction or oxidation. Vitreous carbon was next used for the working and counter electrodes, and it was found that the vitreous carbon electrodes were having problems with conductivity and were extremely brittle. It is believed that the problems with conductivity stemmed from the process used to make the electrodes. Carbon fabric was also used as an electrode material, and this led to a significantly increased contact in comparison to the glassy carbon rod. Lastly, a porous carbon material called ketjenblack was added directly to the solution to increase the conductivity of the working and counter electrodes in solution. The addition of ketjenblack assisted in cutting the timetables to only 6-8 hours for a single bulk reduction or

oxidation and can cut further depending on the redox carrier's reduction potential and the size of the stationary electrolysis cell.

CO$_2$ Analysis

Initially, analysis of CO$_2$ capture was to be done using a GC equipped with a column capable of CO$_2$ detection. However, for a system that is electrochemically capturing and concentrating continuously, CO$_2$ concentration within the headspace must be monitored throughout the experiment. Dr. Jeffrey Barlow and I made a system that was equipped to freeze the captured CO$_2$; this was the system that was used in the Co(SIM) studies described in Chapter 4 and can be seen in **Figure A.2**. The pressure meter could be used to quantify changes in the

Figure A.2. CO$_2$ analysis apparatus built in the Yang lab, including a cold finger that can be used to freeze the captured CO$_2$, a pressure meter to find the change in pressure upon capturing CO$_2$, and a CO$_2$ IR analyzer, which can be used to determine the concentration of CO$_2$ in the outstream.

system's pressure and was expected to be helpful for determining a change in pressure upon concentration of CO$_2$. One of the labeled vents was attached to a solenoid that would release if the pressure reached a certain threshold. The other vent could be used for gas sampling. The cold finger could be used to freeze and isolate the CO$_2$ that had been concentrated. After isolation, the frozen, captured CO$_2$ could thaw and be quantified by the pressure meter. Lastly, the CO$_2$ IR analyzer was used. Our CO$_2$ IR analyzer was made by CO2meter.com, and it was the GC-0016 model. It could be connected to a pump to push gas through the analyzer, or it could be freely connected to the cell. Connection to the pump is best for a closed system in which the solution is

only sparged before the oxidation of the redox carrier and release of CO_2. For an open system in which there is constant gas flow throughout the duration of the experiment, it has been suggested that a two CO_2 meter system is used to monitor the concentration of CO_2 entering the cell and the concentration of CO_2 exiting the cell such that capture and release can be continuously monitored.

A.3 Conclusion

Electrochemical CO_2 capture and concentration cycling has been attempted with various redox carriers. Each of these experiments helped inform the current design of the gas capture apparatus. While the design of a gas capture apparatus has been informed by experimental study, it can be further optimized. Suggestions for further optimization include but are not limited to investigation of different membranes and separators, gas-liquid contact methods, solvent choice, and electrode choice.

The membranes and separators used previously still allowed for crossover between the working and counter compartments, which decreased Faradaic efficiency. Investigations into proton and/or anion exchange membranes may be of interest for increase Faradaic efficiency. Gas-liquid contact methods have been studied in the field, and implementation of a gas-liquid contactor beyond a bubbler would be of interest in the industrialization of electrochemical cycling. Choice of solvent can have a notable effect on the CO_2 capture capabilities, as solvents have a fixed CO_2 solubility, volatility, and ability to solubilize the redox carrier. For homogeneous electrochemical capture, it is vital that the redox carrier have a higher solubility than CO_2 in the chosen solvent. Ideally, the solvent also has a low vapor pressure (less than 0.1 kPa, though this depends on the gas-liquid contactor) such that there are not significant solvent losses. The electrode must have a

notably high surface area and be robust after multiple cycling experiments. While carbon electrodes have been investigated, other electrodes may be useful as well. Appending the quinone to the electrode may be of interest for making the process heterogeneous, however, it will likely have an impact on efficiency. Hatton and coworkers have studied use of a heterogeneous quinone system for electrochemical capture and concentration,[3] and attempts have been made to understand the fundamental thermodynamic difference between a homogeneous and heterogeneous system.[4]

A.4 References

(1)   Koval, C.; Poshusta, J.; Scovazzo, P.; Noble, R.; DuBois, D. Electrochemical Separation and Concentration of <1% Carbon Dioxide from Nitrogen. *J. Electrochem. Soc.* **2003**, *150* (5), D91–D98. https://doi.org/10.1149/1.1566962.

(2)   Voropaeva, D. Y.; Novikova, S. A.; Kulova, T. L.; Yaroslavtsev, A. B. Solvation and Sodium Conductivity of Nonaqueous Polymer Electrolytes Based on Nafion-117 Membranes and Polar Aprotic Solvents. *Solid State Ionics* **2018**, *324*, 28–32. https://doi.org/10.1016/J.SSI.2018.06.002.

(3)   Voskian, S.; Hatton, T. A. Faradaic Electro-Swing Reactive Adsorption for CO_2 Capture. *Energy Environ. Sci.* **2019**, *12*, 3530–3547. https://doi.org/10.1039/c9ee02412c.

(4)   Shaw, R. A.; Hatton, T. A. Electrochemical CO_2 Capture Thermodynamics. *Int. J. Greenh. Gas Control* **2020**, *95* (June 2019), 102878. https://doi.org/10.1016/j.ijggc.2019.102878.